FERMILAB-TM-2169
May 2002

Fermilab

PROTON DRIVER STUDY II
PART 1

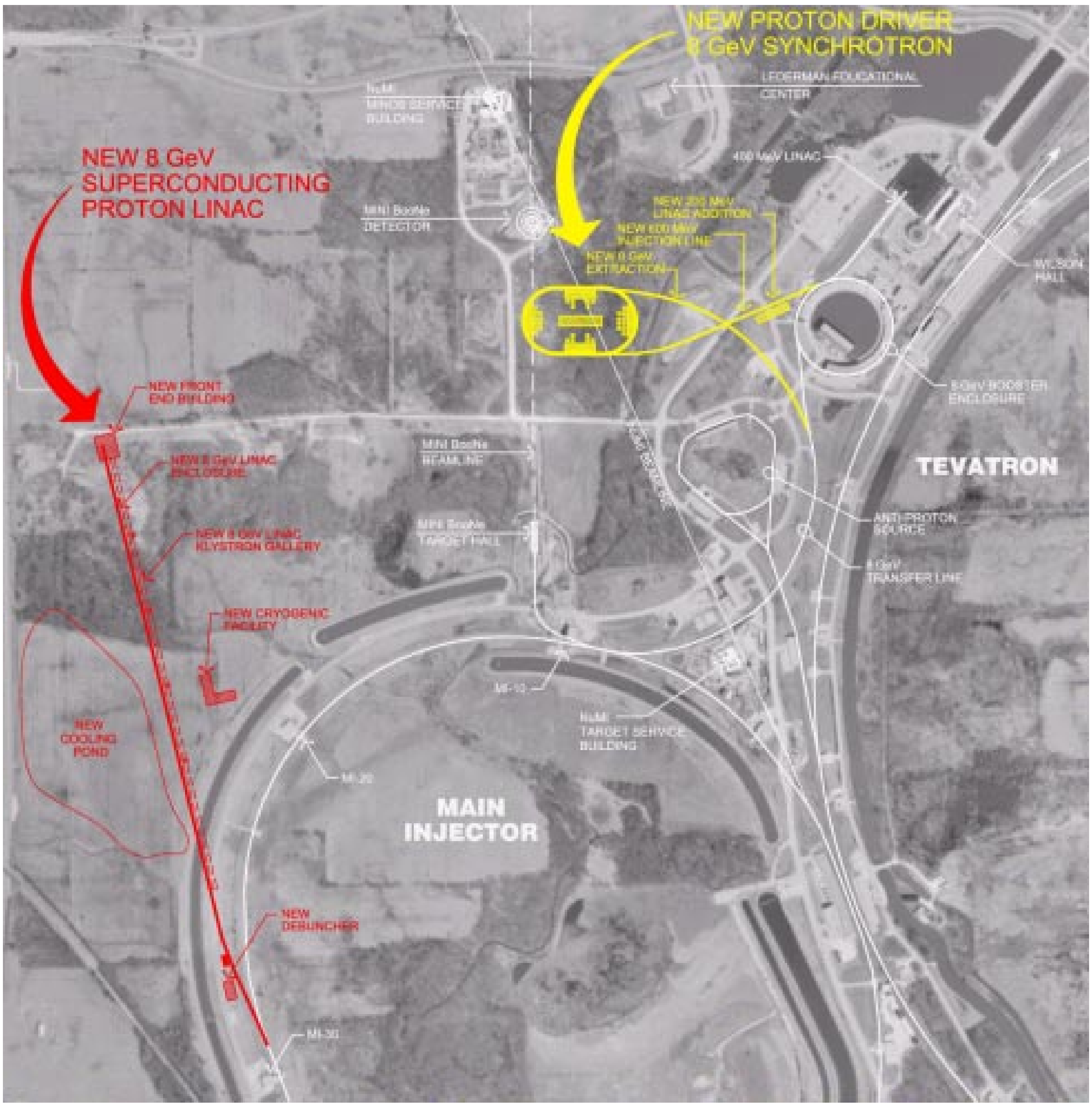

Fermilab

FERMILAB-TM-2169

Proton Driver Study II (Part 1)

Edited by G.W. Foster, W. Chou, and E. Malamud

for the

Proton Driver Study II Group

Russ Alber
Terry Anderson
Chuck Ankenbrandt
Dixon Bogert
Chuck Brown
John Carson
Alex Chen
Weiren Chou
Don Cossairt
Jim Crisp
Joe DiMarco
Sasha Drozhdin
Vadim Dudnikov
Matt Ferguson
Bill Foster
Al Garren (UCLA)
Norman Gelfand
Henry Glass
Bob Goodwin
Jim Griffin
Nancy Grossman
David Harding
Debbie Harris
Jeff Holmes (ORNL)
Cezary Jach
Chris Jensen
Carol Johnstone
Vladimir Kashikhin
Paul Kesich
Kiyomi Koba
Mikhail Kostin
Ioanis Kourbanis
Jim Lackey
Tom Lackowski
Jim MacLachlan
Sasha Makarov
Ernie Malamud
Alberto Marchionni
Phil Martin
Elliott McCrory
Leo Michelotti
Douglas Moehs
Nikolai Mokhov
Al Moretti
Bill Ng
Sho Ohnuma (U. Hawaii)
Francois Ostiguy
Milorad Popovic
Chris Prior (RAL)
Zubao Qian
Grahame Rees (RAL)
John Reid
Dave Ritson (Stanford U.)
Phil Schlabach
Mike Shea
Jeff Sims
Iouri Terechkine
Ray Tomlin
Kamran Vaziri
Bob Webber
Dave Wildman
Dan Wolff
Don Young

May 2002

Table of Contents

Executive Summary

In a charge dated January 10, 2002 (Appendix 3), the Fermilab Director requested a design study for a high average power, modest energy proton facility. As pointed out in the Director's charge, the HEPAP Subpanel report identified such a facility as a possible candidate for a construction project in the U.S. starting in the middle of this decade. The worldwide renaissance in neutrino physics gives added impetus to this call. An intensity upgrade to Fermilab's 120-GeV Main Injector represents an attractive concept for such a facility, which would leverage existing beam lines and experimental areas and would greatly enhance physics opportunities at Fermilab and in the U.S. The key technical element in such an upgrade is the replacement of the 8-GeV Booster, which provides beam to the Main Injector. This new machine, dubbed the "Proton Driver", has potential for a significant stand-alone physics program in addition to its primary mission of providing input beams for the Main Injector.

This report is not yet complete and is being issued now in a preliminary version with limited distribution. When completed the report will be in three parts. Part A describes an 8-GeV synchrotron-based proton driver. Part A is a continuation and extension of Proton Driver Study I (PD1), completed in December 2000 and documented in FERMILAB-TM-2136. Part B describes modifications and upgrades of the Main Injector (MI) and associated beam lines. Part C describes an 8-GeV superconducting proton linac, an interesting alternative option to the synchrotron-based injector. Part A, the description of a synchrotron-based proton driver is complete. The material for part C is not yet finished. When part C is finished it will be incorporated into this report, and part B, will be expanded to cover the impact on the Main Injector and beam lines of either proton driver option.

A physics study focusing on applications of the Proton Driver is completed at Fermilab and a report is published elsewhere. [1]

The previous study, PD1, described a 16-GeV Proton Driver synchrotron as one option for such a facility. The current study, PD2, presents another option, an 8-GeV Proton Driver. Compared to PD1, the 8-GeV option would fit better into the Fermilab accelerator complex and be focused on improving the performance of existing machines and diversifying the research program.

In Part A of this report, the design of an 8-GeV synchrotron-based Proton Driver is presented. Compared with the 16-GeV design, it reduces the up front cost by about 1/3. The 8-GeV synchrotron is the same size as the present Booster (474.2-m circumference) but with a beam power 10 times higher (0.5-MW). A future upgrade to 2-MW is also possible because a large space (254-m) has been reserved between the linac and the ring for a future linac energy upgrade to as high as 1.9-GeV.

Many design features of the 8-GeV synchrotron are similar to the 16-GeV machine in PD1: a transition-free lattice having zero-dispersion straight sections and large dynamic aperture; an injection scheme employing transverse painting to reduce space charge effects; a power supply using a dual-harmonic resonant system (15 Hz plus 12.5% of 30 Hz component), thereby lowering the peak rf power requirement by 25%; main magnets employing external vacuum skins like those in the Booster, with large apertures like those in the Fermilab Accumulator, and equipped with metallic perforated liners to provide a low-impedance environment for the beam; a sophisticated 2-stage beam collimation system collecting about 99% of the lost particles in a small areas around the circumference, thereby allowing hands-on maintenance in the rest of the enclosure. On the other hand, there are also some important differences between PD1 and PD2. For example, PD2 uses a new doublet lattice with racetrack geometry. The stranded conductor coils adopted in PD1 are replaced by solid conductor coils with parallel connections. In this report, we highlight the differences in the two designs and recommend reading the PD1 and PD2 (Part A) reports side-by-side in order to get a complete picture of the design.

Part A also includes a chapter on related improvements and upgrades of the H^- source and the present Linac. The main goals are to increase the linac energy by 200 MeV for a total of 600 MeV and to increase the beam transverse brightness by a factor of four. The former is necessary to reach the required beam intensity (2.5×10^{13} particles per cycle) in the Proton Driver, and the latter to control linac beam losses during high intensity operation.

In Part B, a 2-MW Main Injector is described. The baseline design parameters of the present Main Injector are 3×10^{13} particles per cycle, 1.867-sec cycle time (6-batch operation) and 0.3-MW beam power. With a Proton Driver, either synchrotron-based or linac-based, the beam intensity of the MI is expected to be increased by a factor of five to 1.5×10^{14} particles per cycle. Accompanied by a shorter cycle (1.533-sec), the beam power would reach 1.9-MW. This would make the MI a more powerful machine than either of the two large accelerator projects currently under construction: the SNS (1.4-MW) and the JHF (2 rings, 1-MW and 0.75-MW, respectively). Moreover, the high beam energy (120-GeV) and the tunable energy range (8 - 120 GeV) of the MI are unique features compared to any other high power proton facilities.

The main upgrade required to operate the Main Injector with 2 MW beam power is the radiofrequency (rf) system. The number of power amplifiers driving each cavity needs to double and two more cavities need to be added. In addition, one needs a γ_t-jump system, several large aperture quadrupoles, passive dampers and active feedback systems, a collimation system, large aperture kickers, and modest upgrades in power supplies, beam dump and rf cooling system. These upgrades are discussed in detail in the relevant chapters of Part B. Each of them (perhaps with the exception of the rf) is of a scale that can be accomplished via an accelerator improvement project (AIP).

Part B also discusses the modifications and upgrades of the NuMI, MiniBooNE and other beam lines. With modest investments, both the NuMI and MiniBooNE beam lines are able to take full advantage of the high beam power from the Proton Driver and MI upgrade.

A construction cost estimate of the synchrotron-based 8-GeV Proton Driver and a cost estimate for the MI and beam line upgrades are presented in Appendix 1. An R&D program is outlined in Appendix 2.

Part C of this report, when completed will describe an 8-GeV superconducting linac. A possible siting for this facility is shown on the cover of this report. The linac is largely based on replicating successful technologies from other projects. This minimizes the R&D required. The linac front end and DTL are based on commercially available designs. Superconducting linac cavities similar to those of the SNS would be used up to 1.2 GeV. TESLA-style cryomodules operating at 1207.5 MHz would be used to accelerate the proton beam from 1.2 to 8 GeV. This would be followed by H^- stripping injection into the Main Injector.

The 8 GeV linac on alternate cycles can accelerate H^-, protons or electrons. Therefore besides its primary mission of injecting into the MI, the many unused cycles could be used for other physics missions. This provides many potential benefits for the US HEP program.

There would be major benefits to the neutrino and fixed-target programs; proton economics problems would be solved. An 8 GeV superconducting linac using TESLA technology would be a 1.5% scale demonstration of TESLA economics and would establish a stronger U.S. position in linear collider technology. Clearly, there would be benefits to the muon collider and neutrino factory R&D programs, e.g. a CEBAF-style recirculating linac could be made. An XFEL driver and antiproton deceleration are other interesting possible uses for the facility.

A group of accelerator physicists and engineers from Fermilab's Beams Division, Technical Division, and FESS and ES&H sections contributed to this study. A number of physicists from University of California in Los Angeles (UCLA), Oak Ridge National Laboratory, University of Hawaii, Stanford University and Rutherford Appleton Laboratory in England also participated and played important roles. The Editors express our thanks to them for their commitment and contributions to this study.

References:

[1] A draft version of the Proton Driver Physics Study Report can be found on the web: http://projects.fnal.gov/protondriver/

Chapter 1. Introduction

W. Chou

1.1. Overview

The Proton Driver Study II (PD2) explores two possible upgrade options for the Fermilab accelerator chain: an 8-GeV high intensity proton synchrotron, or an 8-GeV proton linac. Part A of this report (Chapters 1 - 12) explores the synchrotron-based design.

The design study of the Proton Driver I (PD1) was completed in December 2000 and documented in Ref. [1]. The central part of that study was a 16-GeV rapid cycling synchrotron, generating 1.2 MW proton beams. The beam dynamics, technical systems design, civil construction and ES&H issues were described in detail in that document. In this PD2 report, we do not attempt to repeat all the work that has been done in the previous study. Rather, we will only highlight the differences in the two designs due to changes in major parameters. We recommend reading the PD1 and PD2 reports side-by-side in order to get a complete picture of the design.

A major objective in the PD2 study is to reduce the up front cost. In PD1, three major cost drivers were identified: the magnets, the power supplies, and the civil construction. (The rf is relatively cheap because the existing Booster rf system will be reused.) Each one of these three items represents about 1/4 of the total project cost. The cost of the magnets and power supplies scales with the stored magnetic energy and the number of magnets. The cost of civil construction scales with the machine size. Therefore, an effective way to reduce the cost is to lower the beam energy and reduce the machine size.

The charge from the Director (Appendix 3) clearly reflects this objective. The design goals for the synchrotron specified in the charge are: 8 GeV, 2.5×10^{13} protons per cycle, 0.5 MW. Table 1.1 compares the main parameters in PD1 and PD2.

Table 1.1. Comparison of PD1 and PD2 Parameters

Parameters	**PD1**	**PD2**
Ring circumference (m)	711.3	474.2
Linac energy (MeV)	400	600
Synchrotron peak energy (GeV)	16	8
Protons per cycle	3×10^{13}	2.5×10^{13}
Protons per bunch	2.4×10^{11}	3×10^{11}
Repetition rate (Hz)	15	15
RF frequency (MHz)	53	53
Normalized transverse emittance (mm-mrad)	60π	40π
Beam power (MW)	1.2	0.5

Because the acceptance of the Main Injector at 8 GeV is 40π, the normalized transverse beam emittance is also chosen to be 40π in PD2, smaller than the 60π in PD1 (Note: PD1 could allow a larger emittance because its extraction energy is higher, either 12 or 16 GeV, which is also the MI injection energy.) In the meantime, the number of protons per bunch in PD2 is higher (see Table 1.1). In order to compensate the space charge effects, the linac energy is increased from 400 MeV to 600 MeV.

A logical choice for the size of an 8-GeV machine is 474.2-m, the same as the present Booster. This makes the circumference ratio between the Proton Driver and the Accumulator 1:1 and the ratio between the Proton Driver and the Main Injector 1:7. This simplifies beam transfers between machines.

1.2. PD2 *vs.* PD1

Based on differences between the PD2 and PD1 major parameters, the PD2 design includes the following changes:

1. A completely new lattice is designed. This lattice is transition-free (γ_t = 13.8) and has zero-dispersion long straight sections. It is a racetrack with 2-fold symmetry. Although a triangle was the preferred shape in PD1, it is difficult to design a triangular lattice in PD2 with all the necessary features, in particular, enough usable straight section space and the desired phase advance per module. The PD2 lattice employs a doublet structure instead of a singlet one as in PD1. A main advantage of the doublet lattice is that it reduces the number of dipoles, of which the ends occupy a large portion of the drift space. It also reduces the number of quadrupole families and thus simplifies the lattice structure. This lattice is described in Chapter 3.
2. Transverse and longitudinal beam dynamics studies are redone using the PD2 parameters. (Chapter 4)
3. The designs of most technical systems are similar to PD1 and are consolidated into one chapter (Chapter 5). An exception is the magnet design, which includes significant changes. In particular, stranded conductor coils adopted in PD1 are replaced by solid conductor coils. This is possible because the eddy current loss in the coils is reduced thanks to smaller sizes of the magnets and the coils. To keep the voltage-to-ground under control, several coils are connected in parallel for reducing number of turns per pole.
4. The beam loss and shielding are recalculated and the collimators redesigned. (Chapter 6)
5. The injection and extraction systems are redesigned using the new lattice. (Chapter 7)
6. The linac new front-end design is simplified by using one RFQ and no alpha-magnets. (PD1 uses two RFQs and one alpha-magnet.) There is also a section describing the design of a new 200 MeV linac extension. (Chapter 8)
7. The two beam transport lines are redesigned. In PD1, they were 400-MeV and 12/16-GeV. In PD2, they are 600-MeV and 8-GeV, respectively. (Chapter 9)

8. The civil construction is revised using the PD2 footprint. Also a section on a 200 MeV linac extension gallery is added. (Chapter 10)
9. The ES&H considerations are reviewed. (Chapter 11)

1.3. PD2 vs. the Present Booster

1.3.1. Problems of the Present Booster

There are three fundamental problems that prevent the present Booster from being a high intensity proton machine.

a) The magnet aperture is too small (vertical 1.6/2.2 inches in the D/F magnet, respectively, horizontal good field region ~2 inches).
b) The linac is too close to the ring (no room for a linac energy upgrade except by using higher gradient accelerating structures).
c) The tunnel is not deep enough (13.5 ft.). Furthermore, there are office buildings on top of the tunnel. The radiation level on the surface from beam losses is a major concern.

These three limitations existed even during the design of the Booster more than 30 years ago. This was probably because Fermilab's main interest at that time was in high energy rather than high intensity. These problems make it virtually impossible to increase the Booster beam intensity by any significant amount, unless one replaced all the magnets, and/or relocated the linac, and/or moved the Booster deeper. Any of these measures would require building a new machine.

In addition to these problems, the present Booster has several other features that also make an intensity increase difficult:

d) There is transition crossing during the cycle ($\gamma_t = 5.45$).
e) The lattice beta-function and dispersion are quite large (maximum at 33.7 m and 3.2 m, respectively), which lead to large beam sizes.
f) The rf cavity has a small aperture (2-1/4 inches).
g) The rf cavities are in the dispersive region.
h) There is no rf shield inside the magnets.
i) Orbit correction capability is limited.

Although actions are being taken to improve the situation (e.g., R&D effort to increase the rf cavity aperture, implementation of ac orbit correctors, addition of a gamma-t jump, etc.), room for improvement is limited.

1.3.2. Design Considerations of the Proton Driver

In the Proton Driver design, the three fundamental problems and other problems of the present Booster are addressed:

a) The magnets have large aperture. The good field region is 4 in $\times$ 6 in.

b) Space has been reserved between the linac and the ring for a future linac energy upgrade. (The 600-MeV beam transport line is 254-m long.)
c) The tunnel is twice as deep (27 ft.).
d) The lattice has no transition crossing (γ_t = 13.8).
e) The lattice has smaller beta-functions and dispersion (max β_x = 15.1 m, max β_y = 20.3 m, max D_x = 2.5 m).
f) The rf cavity aperture is increased to 5 inches.
g) The lattice has zero-dispersion long straight sections for the rf.
h) There is a perforated metal liner shielding the beam from the magnet laminations.
i) The correctors (steering magnets and trim quads) are ac powered and have sufficient strength to make corrections through the full acceleration cycle.

In addition, the following measures have been adopted in the PD2 design that will further help improve the performance:

- The linac energy is increased from 400 MeV to 600 MeV. (The space charge scaling factor $\beta\gamma^2$ is increased by ~50%).
- The injected beam will be painted in transverse phase space to reduce space charge effects.
- The resonant power supply system is dual-harmonic (15 Hz plus a 12.5% 30 Hz component). This reduces the required peak rf power by 25%.
- A carefully designed 2-stage collimator system that will collect 99% of the uncontrolled beam loss.

With these measures, it is believed that the Proton Driver can have a factor of 5 more beam intensity than the present Booster (from 5×10^{12} to 2.5×10^{13} protons per cycle) while keeping the beam loss under control.

References

[1] "The Proton Driver Design Study," FERMILAB-TM-2136. (December 2000)

Chapter 2. Machine Layout and Performance

R. Alber, W. Chou

2.1. Overview

The synchroton based Proton Driver design includes the following items:

1. A new 8 GeV rapid cycling synchrotron (the Proton Driver) in a new enclosure.
2. A new linac extension of 200 MeV (to bring the total linac energy to 600 MeV) in a new gallery and enclosure.
3. A new 400 MeV beam transport line connecting the existing Linac and the new linac extension.
4. A new 600 MeV beam transport line in a new enclosure.
5. A new 8 GeV beam transport line extending from the existing MI-8 line.
6. A modest improvement of the H^- source and the existing 400 MeV Linac.

The layout of this new accelerator complex is shown in Figure 2.1.

The H^- beam will be extracted from the present Linac to the 400 MeV transport line via the Linac access way. This beam is injected into the new linac extension and accelerated to 600 MeV. It is then transported via the 600 MeV beam line and injected into the Proton Driver in the same way as in the present Booster, namely, through a charge exchange process, in which the electrons are stripped by a foil and dumped. The H^+ (proton) beam will then be accelerated to 8 GeV in about 38 ms and extracted to the 8 GeV transport line. It is then injected into the MI-10 section of the Main Injector.

The new 400 MeV beam line is about 90-m long. It includes a vertical drop from the existing linac level (near surface) to the new linac level (13.5 ft. deep). The new linac extension has five CCL modules for a total length of 45-m. The 600 MeV beam line is about 254-m long. This leaves room for a future linac energy upgrade. This beam line also includes a vertical drop from the new linac level to the Proton Driver level (27 ft. deep). It has a bend near the end where a beam dump can be placed.

The Proton Driver has a circumference of 474.2-m, the same as the present Booster. It is racetrack in shape and has 2-fold symmetry as shown in Figure 2.2. It has two arcs (P10 and P30) and two long straight sections (P20 and P40). Each arc is about 161.66 m-long and each straight section about 75.44-m long. Of the two straight sections, P20 is used for injection and rf, P40 for extraction and rf. A number of trim magnets and diagnostics can also be located in these straight sections in addition to available slots in the arcs. Details of the lattice structure are in Chapter 3.

The 8 GeV extraction beam line has a total length of about 900-m. It consists of two sections. The upstream section, about 420-m, connects the synchrotron to the present MI-8 enclosure. It is followed by a 480-m section in the MI-8 enclosure. This beam line uses permanent combined function magnets, as in the present MI-8 line.

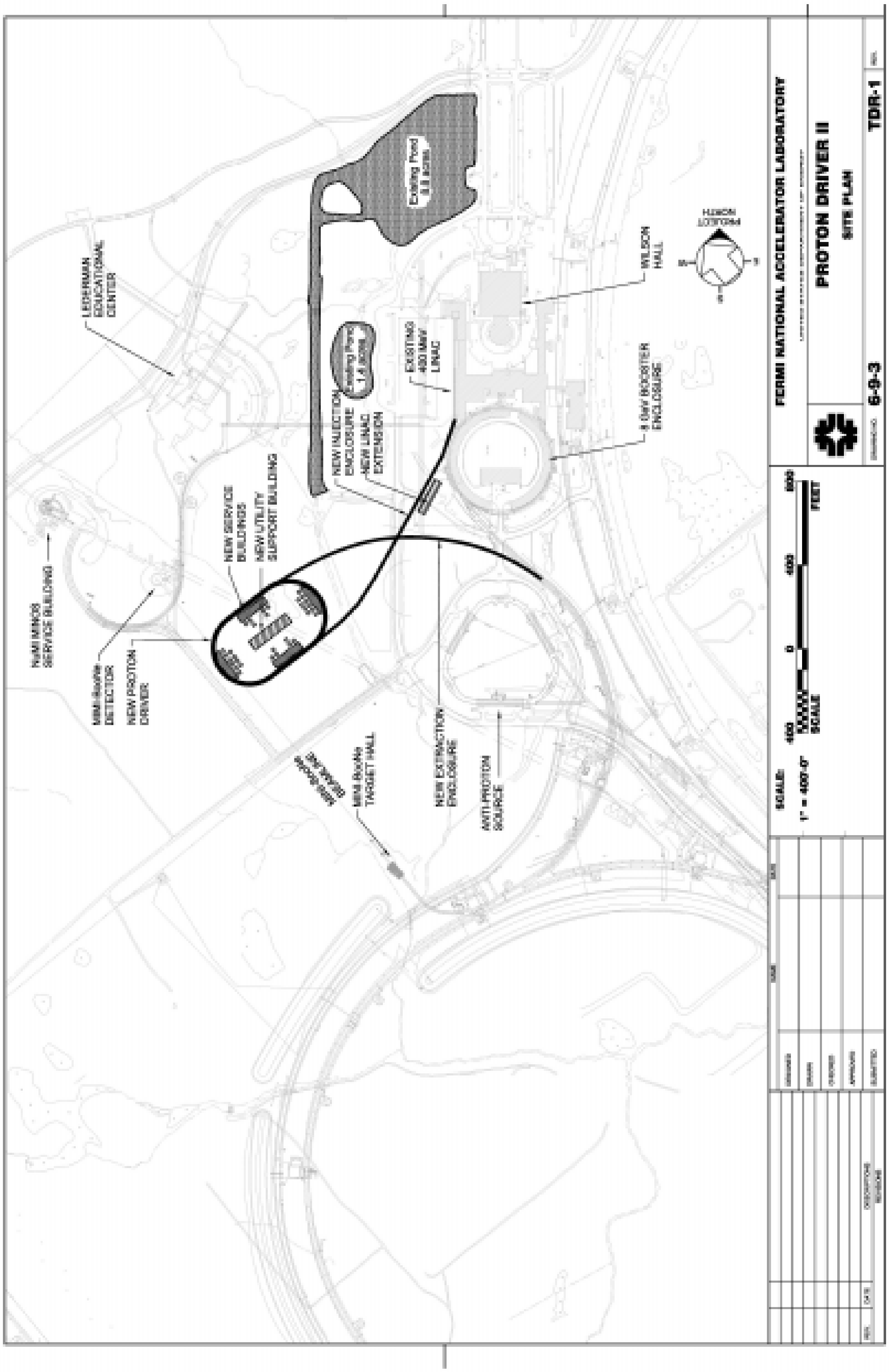

Figure 2.1. Layout of the 8-GeV Synchrotron-based Proton Driver Accelerator Complex.

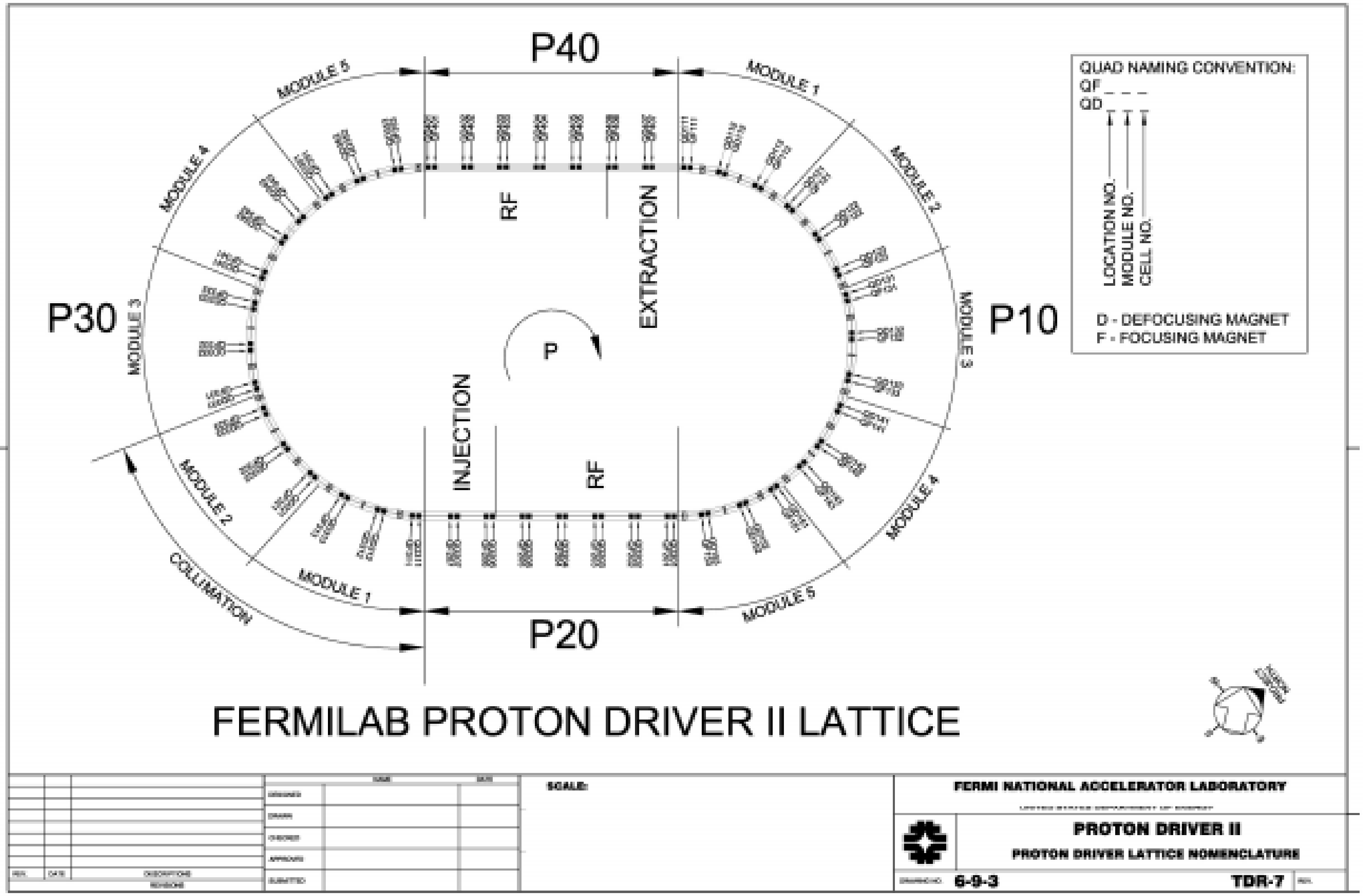

Figure 2.2. Layout of the PD2 8-GeV Synchrotron Ring.

2.2. Siting

Based on PD1, the site of the Proton Driver is chosen at the west side of Kautz Road (see Figure 2.3). The elevation of the Proton Driver is the same as that of the Main Injector. This ensures adequate radiation shielding. The NuMI beam line is deeper so the NuMI line and the Proton Driver do not intersect. Although the Proton Driver intersects the neutrino beam from the MiniBooNE target, this is not a problem. The location of this site in a wetland area raises concerns addressed in Chapter 11.

Another possible location for a racetrack type Proton Driver is in the vicinity of the MI-8 beam line, between the MI-8 and MI-10 buildings. This would shorten the lengths of the 600 MeV and 8 GeV beam lines and reduce their cost. However, it has a number of disadvantages because the new linac extension would have to be in the present MI-8 enclosure: (1) Although the CCL modules can fit into the MI-8 enclosure, it would be crowded. The transportation of hardware in the enclosure would be difficult. (2) A curved linac structure is not preferred. (3) The installation of the new modules would interrupt the ongoing RunII program. (4) Because only the permanent magnet portion of the MI-8 enclosure has room for a new linac, the usable space for a future linac upgrade would be limited. Therefore, this siting option is rejected at this time.

2.3. Major Design Parameters

The main differences of the PD2 parameters from PD1 are: lower energy (8 GeV *vs.* 16 GeV) and lower beam power (0.5 MW *vs.* 1.2 MW). The major PD2 design parameters are listed in Table 2.1 and compared with the parameters of the present Proton Source.

The linac maximum beam energy is increased from 400 MeV to 600 MeV. The required beam intensity is 50 mA, usable pulse length 90 μsec, and repetition rate 15 Hz, all achievable in the present Linac. These numbers correspond to 2.8×10^{13} protons per pulse injected into the Proton Driver. Allowing reasonable beam losses during the cycle (10% at injection, 1% during ramp and at extraction), the design value is 2.5×10^{13} protons per pulse extracted from the Proton Driver. At 15 Hz and 8 GeV, the beam power is about 0.5 MW.

It should be pointed out that the injection beam power from the Linac is only 40 kW, much lower than the output beam power from the Proton Driver. This is a main advantage of using a synchrotron to obtain high beam power, compared with, say, the approach adopted by the Spallation Neutron Source, which uses a full energy linac and an accumulator.

Table 2.1. Parameters of the Present Proton Source and the Proton Driver (PD2)

Parameters	Present Proton Source	Proton Driver (PD2)
Linac (operating at 15 Hz)		
Kinetic energy (MeV)	400	600
Peak current (mA)	40	50
Pulse length (μs)	25	90
H^- per pulse	6.3×10^{12}	2.8×10^{13}
Average beam current (μA)	15	67
Beam power (kW)	6	40
Booster (operating at 15 Hz)		
Extraction kinetic energy (GeV)	8	8
Protons per bunch	6×10^{10}	3×10^{11}
Number of bunches	84	84
Protons per cycle	5×10^{12}	2.5×10^{13}
Protons per second	7.5×10^{13}	3.75×10^{14}
Normalized transverse emittance (mm-mrad)	15π	40π
Longitudinal emittance (eV-s)	0.1	0.2
RF frequency (MHz)	53	53
Average beam current (μA)	12	60
Beam power (MW)	0.1(*)	0.5

(*) Although originally designed for 15 Hz operations, the present Booster has never delivered beam at 15 Hz continuously. In the past it has run at 2.5 Hz. In the near future it will run at 7.5 Hz for the MiniBooNE experiment.

Table 2.2 lists the parameters of the PD2 8-GeV synchrotron. A major feature in the design is that it employs a lattice that is transition-free ($\gamma_t = 13.8$) and has zero-dispersion straight sections. This is important for reducing beam loss and emittance dilution. The required good field region is determined by the following aperture criterion:

$$A = \{3\ \varepsilon_N \times \beta_{max} / \beta\gamma\}^{1/2} + D_{max} \times \Delta p/p + \text{c.o.d.}$$

in which A is the required half-aperture, ε_N the normalized emittance, $\beta\gamma$ the relativistic factor at injection, β_{max} the maximum beta-function, D_{max} the maximum dispersion, c.o.d. the closed orbit distortion, generously assumed to be 10 mm. The factor of 3 is for accommodating the beam halo, which has been observed in high intensity proton machines. Using the parameters in Table 2.2, the required good field region is (rounded up to) 4 in × 6 in. The dynamic aperture should be at least three times as large as the beam emittance so that it is consistent with the good field criterion.

Table 2.2. Parameters of the PD2 8-GeV Synchrotron

Circumference (m)	474.2
Super-periodicity	2
Number of straight sections	2
Length of each arc (m)	161.66
Length of each straight section (m)	75.44
Injection kinetic energy (MeV)	600
Extraction kinetic energy (GeV)	8
Injection dipole field (T)	0.2
Peak dipole field (T)	1.5
Bending radius (m)	19.77
Peak quad gradient (T/m)	10
Good field region	4 in × 6 in
Number of dipoles	
Long (5.646 m each)	20
Short (1.188 m each)	10
Number of quads (44 × 1.261 m, 44 × 1.126 m)	
In the arcs	60
In the straight sections	28
Max β_x, β_y (m)	15.14, 20.33
Min β_x, β_y (m)	4.105, 4.57
Max D_x in the arcs (m)	2.52
Dispersion in the straight sections	0
Transition γ_t	13.8
Horizontal, vertical tune ν_x, ν_y	11.747, 8.684
Natural chromaticity ξ_x, ξ_y	-13.6, -11.9
Revolution time at injection, extraction (μs)	2.0, 1.6
Injection time (μs)	90
Injection turns	45
Maximum Laslett tune shift	0.24
Normalized transverse emittance ε_N (mm-mrad)	
Injection beam (95%)	3 π
Circulating beam (100%)	40 π
Longitudinal emittance (95%, eV-s)	
Injection beam	0.1
Circulating beam	0.2
Extracted bunch length σ_t (rms, ns)	1
Momentum acceptance $\Delta p/p$	±1%
Dynamic aperture	> 120 π

2.4. Operation Modes

Three possible operation modes of the Proton Driver have been considered.

1. *Main Injector 120 GeV fixed target experiments: (NuMI, KaMI, CKM, other Meson Area beams, etc.)*
   The Main Injector will take six Proton Driver batches to fill its ring. Each batch gives 2.5×10^{13} protons. So the Main Injector will operate at 1.5×10^{14} protons per cycle, a factor of five higher than its baseline design intensity (3×10^{13} protons per cycle). The required modifications and upgrades of the Main Injector and the associated beam lines for such an intensity increase are discussed in detail in part B of this report (chapters 13 through 21). The upgraded cycle time of the Main Injector in NuMI operation will be 1.533 seconds (23 PD cycles, see Ch. 13) and therefore will use 6/23 of the protons available from the Proton Driver. The other 17/23 of the protons can be used for the other programs (see below).

2. *Proton Driver fixed target experiments: (MiniBooNE, etc.)*
   The MiniBooNE experiment uses the 8 GeV beam from the present Booster with a beam power of about 30 kW. When the Proton Driver replaces the Booster, this beam power will be increased by an order of magnitude. Seventeen out of every twenty-three Proton Driver cycles can be dedicated to this experiment. This gives an average proton flux of 2.8×10^{14} per second or 0.36 MW beam power to this experiment. In addition to MiniBooNE (or a full BooNE), it is also possible to establish new physics programs based on the stand-alone capabilities of the Proton Driver that can be carried out in parallel to the Main Injector experiments. The high intensity secondary particle beams produced by the proton beams will enable a rich class of physics programs based on muon, kaon, neutron, and neutrino beams.

3. *Antiproton production:*
   In this mode, the Main Injector will take one Proton Driver batch every 1.467 seconds (22 PD cycles). Each Proton Driver batch contains 2.5×10^{13} protons, five times more than the present Booster batch (5×10^{12}). This means the antiproton production rate would be increased by a factor of five, provided that the production target, the cooling systems in the Debuncher and Accumulator, and the acceptance of the associated beam lines would be upgraded accordingly. This mode of operation can be performed simultaneously with operation mode 1.

In the long run, the Proton Driver also serves as the first stage in a staged implementation of a neutrino factory and/or a muon collider. It could provide neutrino superbeams to the detectors, or high intensity muon beams that would be phase rotated, cooled, accelerated and stored in the next stages of such a project. This is because the beams from the Proton Driver have not only high intensity, but also a short bunch structure. The latter is essential for a neutrino factory.

Figure 2.3. Synchrotron-based Proton Driver Site Plan.

Chapter 3. Optics

A.Drozhdin, A.Garren, N.Gelfand, C.Johnstone,
L.Michelotti, S.Ohnuma, G.Rees, D.Ritson

The lattice chosen for PD2 differs from that of PD1 in several respects: saliently, (a) it is a superperiod 2 racetrack, instead of a superperiod 3 triangle, (b) it has 2/3 the circumference, and (c) its kinetic energy range is less than half. In this chapter we describe its optics. Conclusions drawn from this material must be tempered with the understanding that "optics" refers to the behavior of one and only one proton traversing a fixed, static electromagnetic environment. It especially refers to those features of particle orbits that scale with the ratio of magnetic field to momentum. Consideration of other phenomena, such as space charge and impedance effects, is relegated to other chapters.

The structure of this chapter is similar to that of its counterpart in the PD1 Report [1], which is assumed as background. Some information that can be found there is not repeated here. The first section contains a list of constraints under which lattice designs and ideas were considered. Descriptions of the arcs and straight sections of the PD2 lattice is provided in Section 3.2. Further examination of its optical properties, including discussions of resonance excitation and errors, is postponed to Section 3.3.

Several possible designs were considered before settling upon one, but the decisions that were made may not be final. They are, nonetheless, the ones under which this study was conducted. A few promising alternatives will be presented in Section 3.4.

3.1. Requirements, Constraints, and Features

Design of the PD2 lattice was constrained and influenced by a number of criteria, ranging from requirements to desiderata. These included:

Length The Proton Driver's circumference was set to 474.2 m, to match that of Fermilab's Booster. This constraint severely limits the amount of space available for utility hardware. If considered desirable or necessary, it could be enlarged in a later revision, either (a) by adding cells to the straight sections or (b) by increasing the length of its standard cell (see below). In the latter case, focusing must also increase to maintain the Driver's optical properties.

Energy range For PD2, injection energy of the Proton Driver was raised from 400 MeV to 600 MeV, and extraction energy lowered from 16 GeV to 8 GeV, for transfer into the Main Injector. At the Driver's length of 474.2 m, the protons' revolution frequency will thus vary from 501 kHz (2.00 μsec) to 629 kHz (1.59 μsec).

Transition We avoid transition effects in the Proton Driver by requiring γ_t to be beyond the reach of the extraction energy. Thus, it is required that $\gamma_t > 9.5$, or, equivalently, that the momentum compaction $\alpha = 1/\gamma_t^2 < 0.011$.

Momentum acceptance The large momentum acceptance of $\pm$ 2.5 % used in PD1 was predicated on using the Driver as front end to a neutrino factory or muon collider. In this study, the required acceptance has been reduced to $\pm$ 1 %, suitable for transfer to the Main Injector.

Transverse acceptance Tune spread within the beam due to space charge can be as large as 0.25. In order to make this as small as possible, painting will be used to flatten the transverse charge distribution. We require that transverse beam emittance, after painting and including space charge effects, be no larger than 40 π mm-mr (normalized, 95%). The Proton Driver must accept 40π mm-mr invariant emittance in both planes. To achieve this, emphasis was placed on minimizing the maximum values of lattice functions, β_x and β_y, and horizontal dispersion, D. In the course of the study, a criterion was informally established that set upper bounds of $\beta \leq 20\,\mathrm{m}$ and $D \leq 2.5\,\mathrm{m}$. Together, these assure a maximum horizontal excursion of $\approx \pm 5\,\mathrm{cm}$ from the closed orbit, evenly divided between dispersion and emittance.

Phase advance Although it has not been observed in proton machines, it is prudent to avoid any possibility of synchro-betatron coupling resonances [2], especially in view of a relatively large value of synchrotron frequency, ($\nu_s \approx 0.06$), at low energies. This is done by zeroing the chromaticity with sextupoles in the arcs and the dispersion in the straight sections, where RF cavities will be placed. To assure this, the horizontal phase advance through an arc was required to be a multiple of 2π.

Dynamic aperture The dynamic aperture of the Proton Driver, calculated with chromaticity sextupoles powered but no other significant sources of nonlinearity, is required to exceed $3 \times 40\pi$ mm-mr (invariant, transverse) emittance for the entire momentum spread range of $\pm 1\%$.

Straight sections Two long straight sections will be used for injection, extraction, and acceleration. Collimation will be done in the arcs. Considerations given to the design of the two long straight sections included:

Superperiodicity Trim quads in the straight sections will be used to tune the Proton Driver to a good working point. It is highly recommended that they be powered symmetrically across the Driver so as to maintain its superperiodicity.

Injection The beam's size at the stripping foil should be large enough to prevent excessive temperatures. At the same time, large β functions at the foil contribute to emittance growth, due to multiple Coulomb scattering. The compromise choice of $\beta_x \approx \beta_y \approx 10\,\mathrm{m}$ satisfies these requirements. In the doublet lattice of the straight section the foil can be located between the focusing and defocusing quadrupoles of a doublet. This permits the use of a defocusing quadrupole for injection and circulating beams separation, upstream of the foil, at the injection Lambertson magnet, and it permits the use of a focusing quadrupole for separation of the H^0 component and of circulating beam behind the foil at the entrance to the neutral beam dumper. Drift spaces between the adjacent doublets upstream and downstream must be large enough to accommodate both H^- injection and dumping of the H^0 component. The phase advance between the first and last kicker magnets for painting, located on each side of the foil, should be close to 180° so that the required kicker strength is not excessive.

Extraction The phase advance between kickers and septa as well as lattice functions at various extraction devices should be chosen carefully in order not to make excessive demands on magnets. The system should be able to accommodate at least twice the 95% beam emittance, $\varepsilon_{\text{inv}} = 40\pi$ mm-mr, so that no halo scraping occurs in any extraction magnet.

RF It is intended to reuse RF cavities from the current Fermilab Booster in the Proton Driver's straight sections. The cavities are 2.35 m long, and at least 21 will be needed, requiring 49.35 m of empty space. If there is at least 7.05 m between quadrupoles, three of these cavities can be placed within a straight section cell.

Collimation Large β functions and dispersion are necessary at the primary collimators. The phase advance over the collimation system should not be less than 180° in both directions.

Magnets We will write criteria for magnetic field errors in Section 3.3.4. Here, we touch upon three properties.

Peak fields In order that quadrupoles and dipoles track well during the ramp, while avoiding both saturation and excessive power loss, it was decided early to limit the maximum field in dipoles to 1.5 T and the peak gradient of quadrupoles to 10 T/m. Further, a maximum kick angle of 5 mrad is imposed for dipole correctors.

Spacing Because of fabrication requirements for magnet ends and bellows, minimal spacings between quadrupoles and dipoles were established: the minimum space between the quadrupoles of a doublet was set to 47 cm; the minimum space between a quadrupole and a dipole, to 85 cm.

Edge focusing To mitigate the sagitta problem, dipoles will be bent into an arc corresponding to the radius of curvature of the closed orbit. However, the faces of a dipole will remain parallel. The impact of vertical edge focusing on lattice functions and tune must be taken into account in designing the Proton Driver.

3.2. Lattice Description

Based primarily on considerations of available space and the size of lattice functions, a racetrack configuration was chosen for PD2: two 75.44 m straight sections connected by two 161.66 m, 180° arc sections, making its circumference of 474.20 m identical to the current Fermilab Booster's, as required. The racetrack structure leads to longer straight sections and ability to design arcs that give higher transition energy. In this section we'll describe the pieces of this lattice.

3.2.1. Overview

The Proton Driver is partitioned into forty-four 10.777 m cells, 15 for an arc and 7 in a straight section. Each cell contains a defocusing (D) and focusing (F) quadrupole doublet on the main bus and a corresponding pair of independently powered trim quads. Their peak gradients, at 8 GeV extraction (kinetic) energy, are $\pm$ 10 T/m. The F quad is 1.262 m long, the D quad, 1.126 m, and they are separated by 47 cm. Trim quads, positioned just outside the doublet, are 20 cm long; each is separated by 19 cm from its counterpart.

This leaves about 7.1 m of empty space in each cell. In the arcs, they will be filled with dipoles and collimation hardware; in the straight sections, with hardware for injection, extraction, and acceleration. Additional diagnostic and control devices – beam position monitors, orbit correctors, dampers, and the like – must fit into whatever space remains.

3.2.2. Arc module

Each arc is organized into 5 modules of 3 cells, 15 cells in all. Quadrupole lengths were chosen so as to produce a phase advance per module of $(\Delta\psi_x, \Delta\psi_y)|_{\text{module}} = (8\pi/5, 6\pi/5)$ which sets the average phase advance per cell to be $(\Delta\psi_x, \Delta\psi_y)|_{\text{cell}} = (8\pi/15, 2\pi/5)$ $= (96^\circ, 72^\circ)$. A horizontal phase advance close to 90° is convenient for injection and extraction. Because the total phase advance across an arc is $(\Delta\psi_x, \Delta\psi_y)|_{\text{arc}} = (8\pi, 6\pi)$, it is, to first order, optically transparent: its 4×4 transfer matrix is the identity. Thus, the arcs will preserve lattice functions, including zero dispersion, across the straights. If the phase advance per cell were exactly repeated throughout the racetrack, the Proton Driver's tunes would be $(\nu_x, \nu_y) = (11.73, 8.80)$.

The two outer cells of an arc module contain a large dipole (5.646 m, 16.2° bend) and the inner cell a small one (1.188 m, 3.4° bend). Their lengths were chosen so as to create a first order achromatic bend, thus zeroing the dispersion between modules. As a stand-alone periodic unit, the lattice functions of a single arc module would be as shown in Figure 3.2.1.

Four chromaticity correcting sextupoles are placed in each arc module. To conserve space, they replace the four trim quadrupoles closest to the short dipole. Alternatively, it may be possible, and perhaps preferable, to build a correction package consisting of quadrupole and sextupole. If not, then we must rely on two trim quads to control the phase advance through each module.

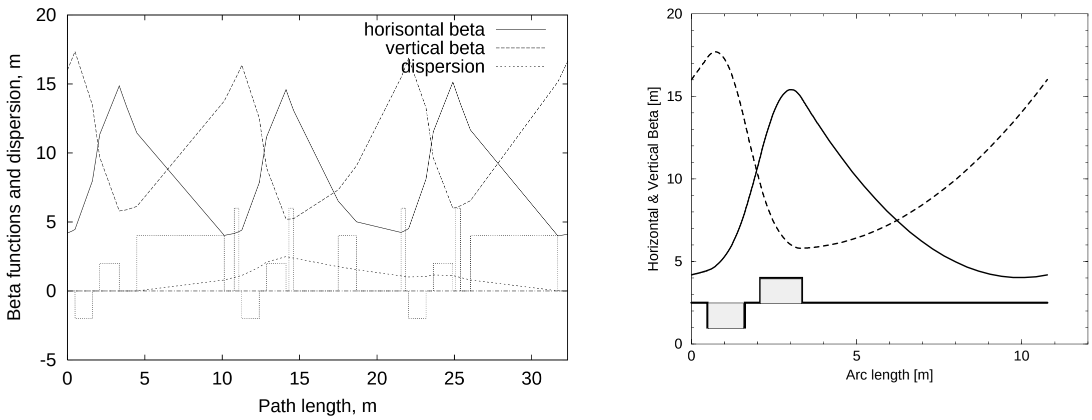

Figure 3.2.1. Lattice functions of (a) an arc module and (b) a straight section's cell, treating each as a periodic unit.

3.2.3. Straight section

The seven cells in each straight section do not contain dipoles, and the absence of edge focusing distorts the lattice functions (esp., β_y) slightly. Lattice functions for a single straight section cell, treated as a periodic unit, are shown in Figure 3.2.1.; its phase advance is $(\Delta\psi_x, \Delta\psi_y)|_{\text{cell}} = (8\pi/15, 0.96 \cdot (2\pi/5))$. In fact, these *are* its lattice functions in the base configuration, because of the arcs' optical transparency.

3.2.4. Hardware and space allocations

The use of similar cells in the arcs and long straight sections, identical except for the presence of dipoles in the arcs, allows for just four kinds of magnets powered on the main bus: 2 quadrupoles, and 2 dipoles. The F and D quadrupole strengths are equal and opposite; the two dipoles likewise have equal fields, but all four have different lengths. It is possible to obtain a reasonable beta function match between the arcs and straight sections while minimizing the number of magnets with different lengths.

The magnetic hardware and their space usage in the PD2 lattice are tabulated below. Only magnetic lengths are included in this table; they do not include the physical ends of elements. Using these numbers, dipoles take up 26.32% of the lattice, main bus quads, 22.16%, chromaticity correcting sextupoles, 2.53%, and trim quadrupoles, 2.02%.

3.2.5. Nomenclature

In order to identify the components in the Proton Driver a system of nomenclature has been devised so that the location, and to some extent the function, of an element can be inferred

Lattice	Element	Name	Number	Length [m]		Field	
PD2	DIPOLES	B1	2x5x2 = 20	5.646	B =	1.49	T
		B2	5x2 = 10	1.188		1.49	
	QUADRUPOLES	QF	(3x5+7)x2 = 44	1.262	B' =	10.02	T/m
		QD	(3x5+7)x2 = 44	1.126		-10.02	
		QDT<N>	(5+7)x2 = 24	0.200	B' =	0.00	T/m
		QFT<N>	(5+7)x2 = 24	0.200		0.00	
	SEXTUPOLES	SF	2x5x2 = 20	0.300	B''=	49.10	T/m^2
		SD	2x5x2 = 20	0.300		-71.05	
	FREE (total)			222.728			

Table 3.2.1. Hardware and space usage in the PD2 lattice.

from its name. The direction of the beam is clockwise and our naming system will follow the direction of the beam. It will be easier to follow the description below by referring to the graphical layout of the Proton Driver contained in Chapter 2.

The system involves dividing the ring into four logical groupings, or sectors, of the elements. The first sector is an arc, denoted as P10, consisting of five modules of three cells. Each cell contains a quadrupole doublet and a bending magnet. The quadrupoles will be assigned a name that reflects (a) their horizontal focusing properties, QD or QF, (b) the sector, (c) the module, and (d) the cell. Thus, QDijk will mean a horizontally defocusing quadrupole in the k^{th} cell of the j^{th} module in the i^{th} sector: the first quadrupoles in the first sector will be named QD111 and QF111, and the last quadrupoles in this sector will be QD153 and QF153.

The arc, P10, is followed by a straight section, P20, consisting of 7 cells, each with a quadrupole doublet. To resolve the superperiod 2 ambiguity, we identify P20 as the sector containing injection hardware, in addition to RF cavities. The quadrupoles will be assigned a name that reflects (a) their horizontal focusing properties, QD or QF, (b) the sector number, (c) 0 for the module number, (d) and the cell number. QD$i0k$ will mean a horizontally defocusing quadrupole in the k^{th} cell in the i^{th} sector. Thus, the first quadrupoles in the second sector will be named QD201 and QF201. The last quadrupoles in this sector will be QD207 and QF207.

The injection straight P20 is followed by the arc sector P30 where collimation takes place. As in the arc P10 there are 5 modules each consisting of 3 cells. The naming convention is the same as in P10 except that the magnet names have the value of 3 for the sector number. The ring is completed with another straight section P40 that contain RF and extraction elements. Its naming scheme is similar to that of section P20.

3.3. Analysis

The complete lattice functions for half of the racetrack, with one arc joined to one straight section, are shown in Figure 3.3.2. The vertical beta wave is caused by edge focusing in the dipoles, or, alternatively, its absence in the straight section cells. The arcs' optical transparency confines the wave; it does not propagate into the straight sections. The actual tunes associated with the base configuration are shifted from $(11.73, 8.80)$ to $(11.747, 8.684)$. That point is shown as a dark circle in Figure 3.3.3., wherein are drawn the sum resonance lines up to fourth order.

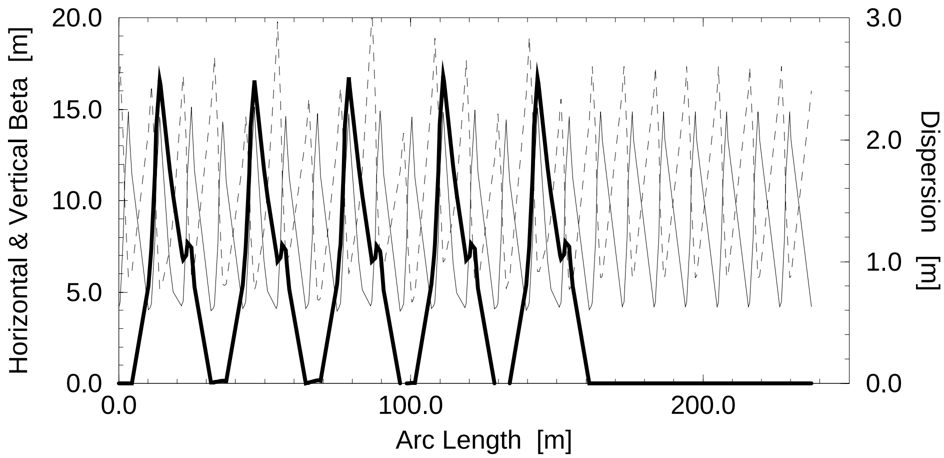

Figure 3.3.2. Lattice functions for half the racetrack: β_x is plotted as a solid line, β_y as a dashed line, and D as a dark solid line.

As an exercise, families of trim quadrupoles in the straight section were used to move the tunes to $(11.880, 8.850)$, the point shown as an open circle in Figure 3.3.3., without breaking superperiodicity. In the sections to follow, we will refer to this as the "tuned configuration." Lattice functions are, of course, perturbed slightly in the process. Tuning was done in such a way that the vertical beta wave was transferred from the arcs to the straight sections.

The tunes identified in Figure 3.3.3. refer to single particle optics. In reality, space charge will reduce the tunes of particles in the core of the beam by an amount that will depend on painting. (See Chapter 4.) Protons undergoing large amplitude oscillations will be less affected by space charge, but their tunes will increase (slightly) due to the presence of chromaticity correcting sextupoles, as will be discussed on page 3 - 9. The combined effects of space charge and sextupole fields (and octupole error fields) will spread the tunes away from the displayed points in opposite directions. The single particle "optical tune," the "working point," acts as a reference for this distribution. Maximum spread will occur at injection. As the beam's energy increases, the distribution will collapse into the working point. Space charge forces will decrease, as $v/c \to 1$, shrinking the distribution

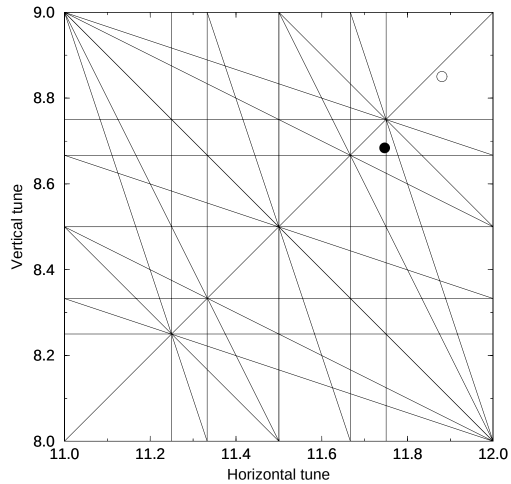

Figure 3.3.3. Tune diagram. The Proton Driver's base lattice (dark circle) has tunes (11.747,8.684). A possible tuned lattice (white circle) is shown with tunes (11.880,8.850).

from below, and the sextupole/octupole tune spread will decrease, as emittances become smaller, shrinking the distribution from above.

3.3.1. Chromatic properties

The natural chromaticities of the PD2 base configuration – normalized as $\Delta\nu = \xi\Delta p/p$ – are $(\xi_x, \xi_y) = (-13.61, -11.88)$. These are zeroed by powering the sextupoles placed in the arc modules to $B'' = 49$ T/m^2, near the F quad, and $B'' = -71$ T/m^2, near the D quad. (In the tuned configuration these values are only slightly different: $B'' = 50$ T/m^2 and $B'' = -73$ T/m^2.) Chromaticity in the actual Proton Driver undoubtedly will not be set to zero but to some small negative value, since the machine will run below transition. Thus, the actual values of B'' will be marginally smaller, mitigating somewhat the magnitude of effects discussed in the rest of this report.

Because each module is a first order achromat, dispersion is small in the vicinity of its two outer dipoles. The contribution from the shorter, central dipoles to the momentum compaction can be estimated by assuming a horizontal dispersion of 1.7 m at that location.

$$\langle D/\rho \rangle \approx \frac{1.7\,\mathrm{m}}{29.7\,\mathrm{Tm}/1.49\,\mathrm{T}} \cdot \frac{1.19\,\mathrm{m}\cdot(5\cdot 2)}{474.2\,\mathrm{m}} = 0.0021$$

This accounts for 40% of the total momentum compaction, which is $\alpha = 0.00528$, making $\gamma_t = 13.8$, comfortably larger than 9.5.

The chromaticities, ξ_x, ξ_y, considered not as constants but as functions of $\Delta p/p$, are plotted in Figure 3.3.4. for the extended range $|\Delta p/p| \leq 0.02$. ξ_y is nearly flat for negative

$\Delta p/p$, with a variation of less than 0.5 over the entire range. On the other hand, ξ_x increases monotonically, only slightly faster than linearly, by more than 2.5. The overall variation across $\pm$ 1% is small.

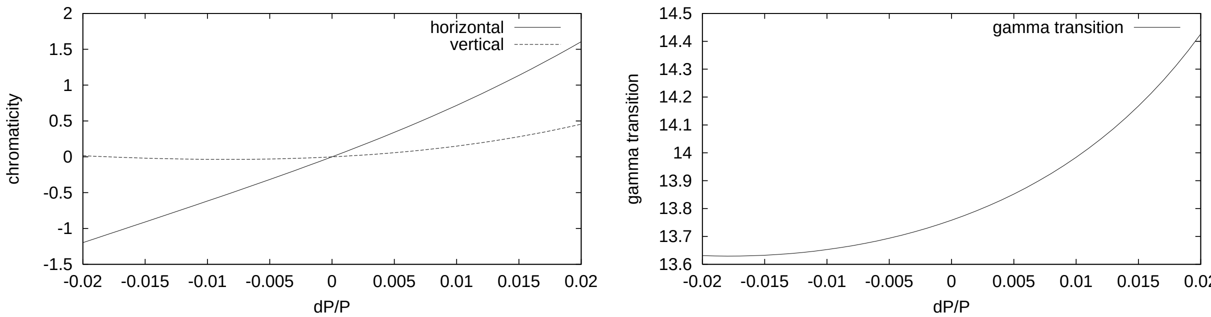

Figure 3.3.4. Proton Driver chromaticity and γ_t.

The corresponding plot of γ_t vs. $\Delta p/p$ is the almost exponential looking curve displayed on the right in Figure 3.3.4. Its variation is of little concern, because all of these values are larger than required.

Lattice functions, β_x, β_y, and D, take on perturbed values when $\Delta p/p \neq 0$. Their maxima are plotted, as functions of $\Delta p/p$, in Figure 3.3.5. The variations of $\beta_{y,\max}$ and $D_{\max}$ are

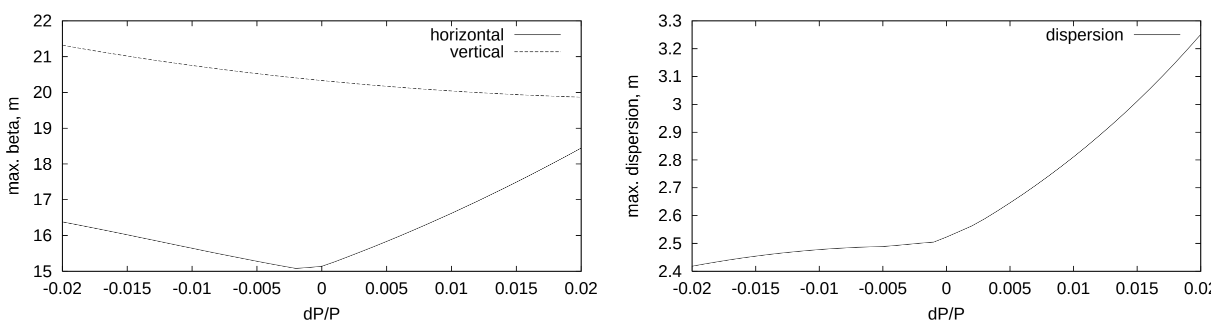

Figure 3.3.5. Proton Driver maximum β functions and dispersion.

monotonic, while $\beta_{x,\max}$ goes through a minimum near $\Delta p/p = 0$. As in the previous figures, there is larger variation for positive than negative $\Delta p/p$. Estimates of the closed orbit based on the value $D|_{\Delta p/p=0}$ should be increased by $\approx$ 12% at the momentum acceptance limit, $\Delta p/p = 1\%$.

3.3.2. Tune footprint

The sextupoles used to zero chromaticity will produce an amplitude dependent tune shift proportional to the square of their excitation. Second order perturbation theory predicts, for the PD2 base configuration,

$$\begin{aligned}\Delta\nu_x &= 0.120\,\varepsilon_x/\pi + 0.114\,\varepsilon_y/\pi \\ \Delta\nu_y &= 0.114\,\varepsilon_x/\pi + 0.230\,\varepsilon_y/\pi\ ,\end{aligned}$$

where $\Delta\nu$ is given in units of 10^{-3} and ε is in mm-mr.[1] For the tuned configuration, the coefficients are somewhat larger.

$$\begin{aligned}\Delta\nu_x &= 0.126\,\varepsilon_x/\pi + 0.397\,\varepsilon_y/\pi \\ \Delta\nu_y &= 0.397\,\varepsilon_x/\pi + 0.384\,\varepsilon_y/\pi\end{aligned}$$

The upper limit on transverse emittance is $\varepsilon_{\mathrm{inv}} \leq 40\pi$ mm-mr, so that

$$\begin{aligned}\varepsilon/\pi = \frac{\varepsilon_{\mathrm{inv}}/\pi}{\beta\gamma} &\leq \frac{40}{9.47} = 4.22\ \ \mathrm{mm\text{-}mr}\quad \text{at extraction} \\ &\leq \frac{40}{1.30} = 30.8\ \ \mathrm{mm\text{-}mr}\quad \text{at injection.} \qquad (3.1)\end{aligned}$$

Even at injection into the tuned configuration, the vertical tune spread resulting from sextupole excitation will only be about 0.02.

3.3.3. Dynamic aperture

The dynamic aperture of the PD2 lattice has been estimated by tracking. Only the dipoles, quadrupoles, and chromaticity sextupoles have been included. Again, this is single particle tracking within a static magnetic environment: it does not include space charge, synchrotron oscillations (with or without non-zero chromaticities), or magnet ramping; also not included are systematic or random error fields. The results obtained should be considered an upper bound on the actual dynamic aperture. Fortunately, it turns out to be a large upper bound. Its actual (theoretical) value will have to be determined by more detailed studies, especially including space charge and RF.

Since "dynamic aperture" is an ambiguous concept, we will first describe the procedure that was used. A particle was launched from a point $(x,y), x,y \gg 0$, with $x' = y' = 0.0$. If the particle failed to complete 10^5 turns, the value of y was reduced and the tracking started again. When the particle survived for 10^5 turns the initial point, (x, y_{max}), was considered inside the dynamic aperture. Once a stable orbit was found, x was decreased, y was reset to a large value, and the entire process was repeated, down to $x = 0$. The set of pairs $\{(x, y_{\mathrm{max}})\}$ were then converted into normalized emittances using the values of the lattice functions at the initial point.

The results, at the injection energy of 600 MeV, where dynamic aperture is smallest, are shown in Figure 3.3.6. Along the diagonal, the dynamic aperture is at $\varepsilon_{\mathrm{inv}} \approx 10 \times 40\pi$ mm-

[1] This is written using "emittance" notation, ε, but, since we are dealing with a single particle, ε is more properly interpreted as an action (or amplitude) coordinate, I, according to $\varepsilon/\pi = 2I$.

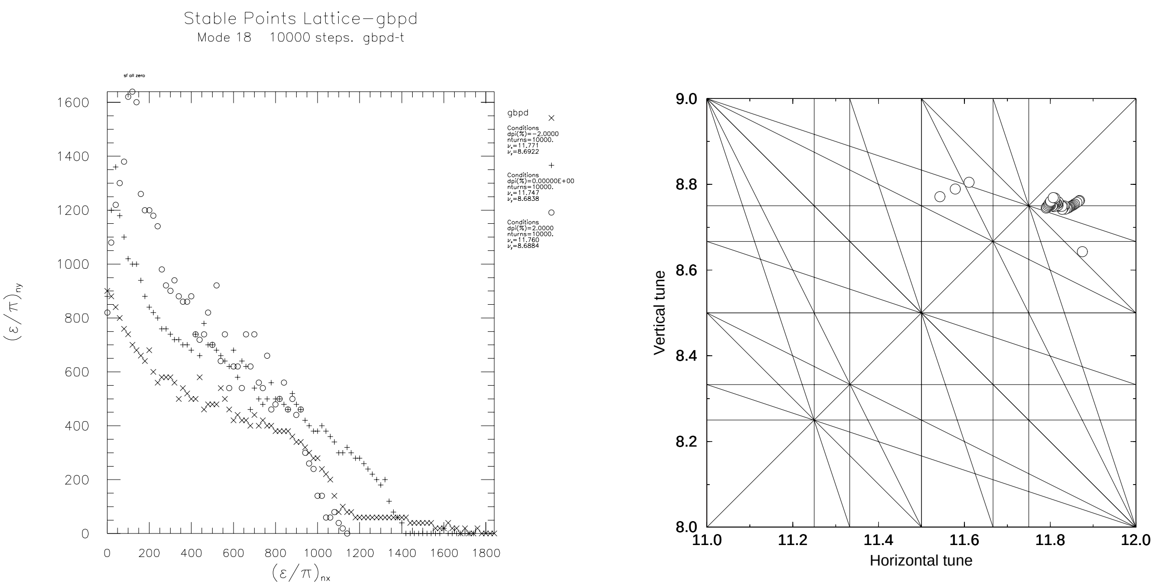

Figure 3.3.6. Dynamic aperture: (a) Scatter plot of largest amplitude stable orbits at $\Delta p/p = 0$ and $\pm 2\%$. (b) Tunes of orbits at the boundary of the dynamic aperture.

mr. For purely horizontal orbits it increases to $\varepsilon_{\rm inv} \approx 25 \times 40\pi$ mm-mr, and for mostly vertical orbits[2] it is slightly less, $\varepsilon_{\rm inv} \approx 20 \times 40\pi$ mm-mr. The interior of this region was scanned further to make certain that the stable orbits defining the dynamic aperture were not caused fortuitously by isolated stable regions (islands) in an otherwise unstable portion of phase space.

Peaks of the tune spectra were calculated for all orbits just inside the dynamic aperture. The right hand side of Figure 3.3.6. shows a scatterplot of these values superposed on the tune diagram of Figure 3.3.3. Clearly, there is a clustering about the line $4\nu_y = 35$, which is excited at second order in the strength of sextupoles. The chromaticity sextupoles both excite this resonance and provide the necessary tune spread to put it within the reach of very large amplitude orbits, as will be discussed in Section 3.3.4.

3.3.4. Errors

We will assume the same estimates for positioning errors that were made in the PD1 Report [1, p.3-12]:

1) transverse quadrupole misalignments: $\sigma_X = \sigma_Y = 0.2$ mm.
2) dipole roll: $\sigma_\Theta = 0.2$ mrad; this will be relaxed to 0.5 mrad.
3) integrated dipole field uniformity: $|\Delta B/B| < 2 \times 10^{-4}$; this will be relaxed to 5×10^{-4}.

[2] Because of the sextupoles, pure vertical orbits are impossible.

These estimates were based on criteria set for alignment of the Antiproton Accumulator. Those which are to be "relaxed" were considered too difficult to achieve reliably.

With regard to field quality, a "flatness criterion" was established in PD1,

$$\text{flatness at } x = x_0 \;\equiv\; \left| \frac{\int dz B_y(x = x_o, y = 0, z)}{\int dz B_y(x = 0, y = 0, z)} - 1 \right| \quad \text{for dipoles.}$$

For quadrupoles, replace B_y with $B' = G = \partial B_y / \partial x$ in the integrals. Upper bounds for flatness were specified in the PD1 Report [1, p.3-14] at an offset of $x_o = 4$ inches. We adjust them here to an offset of $x_o = 3$ inches: 3×10^{-4} for dipoles and 3×10^{-3} for quadrupoles. In terms of isolated multipoles, this is equivalent to:

dipoles:	$\lvert B^{(2)}/B \rvert$	< 0.1	m^{-2}	$= 0.3$	units
	$\lvert B^{(4)}/B \rvert$	< 214	m^{-4}	$= 0.04$	units
quadrupoles:	$\lvert G^{(2)}/G \rvert$	< 1	m^{-2}	$= 3$	units
	$\lvert G^{(3)}/G \rvert$	< 41	m^{-3}	$= 1$	units

where "unit" refers to the Fermilab convention of "$\times 10^{-4}\,\text{inches}^{-n}$." For now, we continue to accept these as achievable estimates of field quality.

The use of multipoles is complicated by the fact that dipoles are to be bent into an arc. In a straight magnet, the vector potential of the error field – the quantity appearing in Hamiltonian resonance calculations – is expanded in the midplane as,

$$A_3/B = \frac{1}{2} b_1 x^2 + \frac{1}{3} b_2 x^3 + \cdots \quad .$$

When the magnet is bent, curvature terms are added to these coefficients. [3, p.177]

$$A_\phi/B = \frac{1}{2}(b_1 - 1/\rho)x^2 + (b_2/3 - b_1/6\rho + 1/2\rho^2)x^3 + \cdots$$

For the Proton Driver, $1/\rho = 1.5\,\mathrm{T}/29.7\,\mathrm{Tm} = 13 \times 10^{-4}\,\mathrm{in}^{-1}$, or 13 "units." Its interference with b_1 is already accounted for by linear theory. Using the specifications given above, $b_2/3$ will be ≈ 0.1 units, while the curvature terms contribute 0.009 units to the x^3 coefficient. Unless dipoles are constructed extraordinarily well, their error fields will dominate over curvature effects.

3.3.4.1. Closed orbit

To first order, the closed orbit error at point i caused by a kick error, $\Delta x'$, at point j is given by the matrix element [4, p.92],

$$\partial x_i / \partial \Delta x'_j \equiv M_{ij} = \frac{1}{2 \sin \pi\nu} \sqrt{\beta_i \beta_j} \cos(\psi_i - \psi_j - \pi\nu) \;\; ,$$

where we assume $0 \le \psi_i - \psi_j < 2\pi\nu$. If the errors are random and uncorrelated,

$$\sigma^2(x_i) = \sum_j M_{ij}^2 \sigma^2(\Delta x'_j)$$

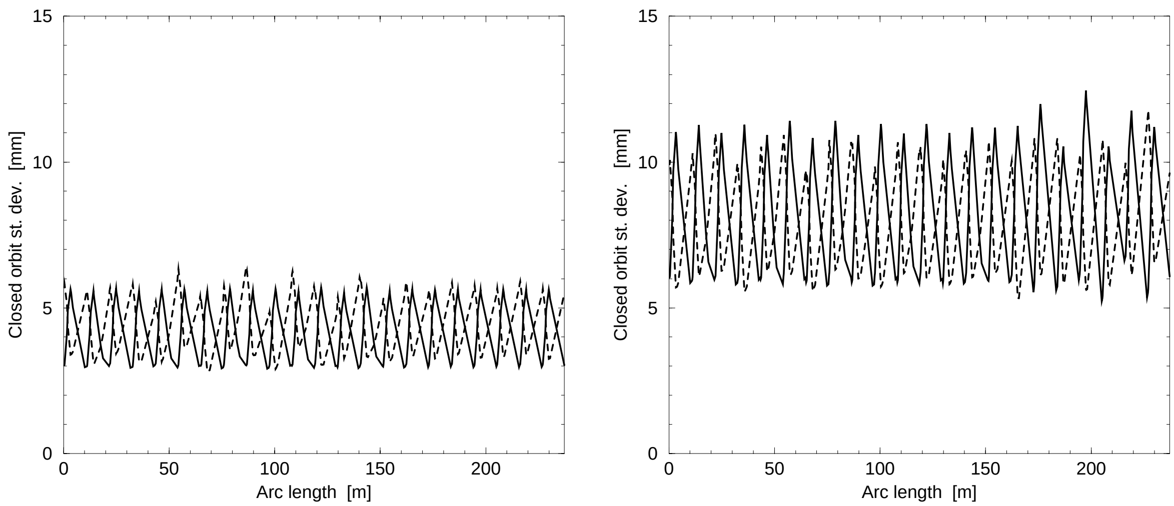

Figure 3.3.7. Closed orbit error standard deviation: base (left) and tuned (right) lattices. Only half the racetrack is shown.

(Ab)using the misalignment errors listed in Section 3.3.4., we can estimate the relevant standard deviations as follows.

$$\begin{aligned}
\text{(a) quad misalignment}: \quad \sigma_{\Delta x'} &= \frac{B'l}{B\rho}\sigma_X \\
\text{(b) dipole roll (small)}: \quad \sigma_{\Delta x'} &= \frac{Bl}{B\rho}\sigma_\Theta \\
\text{(c) field uniformity}: \quad \sigma_{\Delta x'} &= \frac{Bl}{B\rho}\sigma_{\Delta B/B}
\end{aligned}$$

The horizontal closed orbit is affected by (a) and (c); the vertical, by (a) and (b). Results of inserting these into Eq.(3.3.4.) and performing the calculation on the base configuration are shown on the left in Figure 3.3.7. The results for the tuned configuration are shown on the right. In both cases, only half of the racetrack is shown. The larger excursion in the tuned configuration arises (a) mostly from the $\sin\pi\nu$ in the denominator of Eq.(3.3.4.), (b) from slightly larger lattice functions, and (c) from the fact that the trim quads are contributing. The numbers are in reasonable agreement with our crude estimates. The difference in tunes accounts for most of the increase in going from the base lattice to the tuned lattice.

Steering magnets A system of correction dipoles will be necessary to reduce the expected 5-10 mm (or more) excursion of the closed orbit. The specification common to horizontal and vertical directions is that the maximum kick angle of each steering element should be 5 mr. The maximum horizontal and vertical deflections generated by this kick will be 50 mm and 77 mm, respectively. For horizontal kicks, there will be special windings in each dipole. The required kick angle is 1.8% of the bend angle of regular dipoles and 8.4% of short dipoles. Horizontal orbit correction is then possible up to the highest energy.

Vertically, the kick will be provided by 20 cm long steering magnets. A 5 mr vertical kick would require a field of 0.10 T at injection and 0.74 T at extraction. Imposing an upper bound on corrector strength would reduce the maximum (kinetic) energy at which such a kick could be done: e.g., 5.1 GeV for $B_{\max} = 0.5\,T$, 2.8 GeV for $B_{\max} = 0.3\,T$. Correcting an improbably bad vertical closed orbit beyond this energy would then require realigning quadrupoles. In such a case, it should be possible to select the optimum combination of a specified number of quadrupoles based on BPM readings of the established closed orbit.

There will be no room for correctors in the cells containing RF. Care must be taken to minimize the closed orbit deviation and its derivative at the boundaries of those regions.

3.3.4.2. Tunes

We consider here three isues regarding the Proton Driver's tunes: their adjustment away from the base configuration, linear horizontal-vertical coupling, and the tune footprint caused by chromaticity sextupoles.

Tune adjustment Arc quadrupoles will be responsible for maintaining the phase advance per module in arcs, while quadrupoles in long straights will be used to locate the working point at the optimum position in the tune diagram. It is impossible to predict what this will be. Experience gained in Accumulator and Main Injector operation indicates that, if magnets are constructed carefully, it is not necessary to have the flexibility to explore a wide range of tune values: something less than ± 0.3 may be sufficient. For the Proton Driver, tune adjustment will be needed for picking a good working point, maintaining the phase advance per module in the arcs, compensating for space charge detuning, and minimizing beam loss during extraction.

We make a representative estimate (at 8 GeV) of the tune correction obtained by powering one trim quad at 1 T/m. Ignoring the orthogonal plane, this is

$$(\Delta\nu_x, \Delta\nu_y) = \frac{1}{4\pi}\frac{B'l}{B\rho}\cdot(\,\beta_x, \beta_y\,) = \frac{1}{4\pi}\cdot\frac{1\,\mathrm{T/m}\cdot 0.2\,\mathrm{m}}{29.7\,\mathrm{Tm}}\cdot(\,14\,\mathrm{m}, 16\,\mathrm{m}\,) = (0.0075, 0.0086)$$

There are 24 trim quads of each type, but only the 14 in the straight sections would be used for tune control. This provides a tune reach of $(\pm 0.053, \pm 0.060)$ per T/m of excitation.

Tune adjustment can also be done by special windings in each quadrupole. If the gradient in a main bus (QD or QF) quadrupole is adjusted by 1%, the in-plane tune shift would be $\Delta\nu = 0.005$. The 14 main quads in the straight sections would then supply an additional tune reach of $\approx \pm 0.07$ (per 1% variation). Again, these estimates are made ignoring the influence of the orthogonal plane. Taking it into account would extend the reach.

Horizontal-vertical coupling Linear coupling is produced by skew quadrupole components, which can arise from field errors and from rolling normal quads. Its effects will be most pronounced when tunes are near the resonance condition, $\nu_x - \nu_y = n$, where, for the Proton Driver, $n = 3$. Near such resonance, the Hamiltonian is characterized by a dimensionless coupling,

$$g = \frac{1}{2\pi} \left| \sum \frac{B'_{\text{skew}} l}{B\rho} \sqrt{\beta_x \beta_y} e^{i(\psi_x - \psi_y - \delta \cdot \Theta)} \right| \quad ,$$

where $B'_{\text{skew}} = \partial B_x / \partial x$ is the skew coefficient, and $\delta = \nu_x - \nu_y - 3$. If a normal quad is rolled through a small angle, Θ, then $B'_{\text{skew}} = B' \cdot 2\Theta$. Following usual procedures, as was done in PD1, we will estimate this term by summing in quadrature, and use σ_Θ for Θ, with the result,

$$\begin{aligned}
\sigma_g &= \frac{1}{2\pi} \cdot 2\sigma_\Theta \left(\sum \left(\frac{B'l}{B\rho} \right)^2 \cdot \beta_x \beta_y \right)^{1/2} \\
&\approx \frac{1}{\pi} \cdot 5 \times 10^{-4} \cdot \left(44 \cdot \left(\frac{10\,\text{T/m} \cdot 1.26\,\text{m}}{29.7\,\text{Tm}} \right)^2 \cdot 13\,\text{m} \cdot 7.5\,\text{m} \right. \\
&\qquad \left. + 44 \cdot \left(\frac{10\,\text{T/m} \cdot 1.13\,\text{m}}{29.7\,\text{Tm}} \right)^2 \cdot 6.0\,\text{m} \cdot 15.3\,\text{m} \right)^{1/2} \\
&= 5.9 \times 10^{-3} \quad .
\end{aligned}$$

The coupling into transverse amplitudes is $(1 + (\delta/g)^2)^{-1/2} \approx (1 + (\delta/\sigma_g)^2)^{-1/2}$. For the base configuration, (11.747,8.684), this is about 9%. That is, if the horizontal excursion of the beam is 1 cm, the estimated (r.m.s.) excursion in the vertical direction generated by coupling will be 0.9 mm. This is large enough to consider introducing a few skew quad correctors, to reduce the value of g, or tuning farther from the diagonal, to increase the value of δ.

Sextupole errors in dipoles The contribution of a local sextupolar field to chromaticity is approximated as

$$(\Delta\xi_x, \Delta\xi_y) = \frac{1}{4\pi} \cdot \left(\frac{B''l}{B\rho} \right) \cdot D \cdot (\beta_x, -\beta_y) \quad .$$

If $\langle |B''/B_o| \rangle < 0.1\text{m}^{-2}$ in the dipoles, then their contributions to the chromaticity will be

$$\begin{aligned}
(|\Delta\xi_x|, |\Delta\xi_y|) &\approx 20 \times (0.006, 0.009), \ \text{for long dipoles,} \\
&\approx 10 \times (0.02, 0.03), \ \text{for short dipoles.}
\end{aligned}$$

These values are negligible compared with the natural chromaticities of (-14, -12).

With the phase advance per arc module set at $(\Delta\psi_x, \Delta\psi_y)|_{\text{module}} = (8\pi/5, 6\pi/5,)$ contribution of the dipoles' average sextupole field to the $3\nu_x = 35$ resonance will cancel across one arc, but its contribution to the $\nu_x + 2\nu_y = 29$ resonance will build maximally across an arc, while cancelling across the ring. This cancellation depends on good adherence to superperidiocity, as will be discussed below.

3.3.4.3. Resonances

As suggested by Figure 3.3.3., it will be important to pick a good working point for the Proton Driver. We will discuss here the possible effects of two third integer resonances close to the working point of the base configuration, $\nu_x + 2\nu_y = 29$ and $3\nu_y = 26$, and (briefly) the $4\nu_y = 35$ resonance, which was seen in Figure 3.3.6. to be important in determining the dynamic aperture. In addition, see the discussion of phase advance in Section 3.4.

The effect of the $\nu_x - \nu_y = 3$ resonance on the tuned configuration was discussed in Section 3.3.4. A driver of the $2\nu_x - 2\nu_y = 6$ resonance will be space charge, a variant of the so-called "Montague resonance." Discussion of space charge effects is postponed to Chapter 4.

Most of the discussions in this section, and some in the preceding sections, are carried out using rough approximations. Applying isolated resonance theory validly requires satisfaction of many conditions. At the least, particle tunes must be very close to one and only one active resonant line, and no detuning must occur, apart from what is done by the resonance source itself. We will ignore the extent to which these conditions are violated.

$\underline{\nu_x + 2\nu_y = 29}$ The phase advance of $(\Delta\psi_x, \Delta\psi_y) = (8\pi/5, 6\pi/5)$ across an arc module means that the sextupoles' contribution to the $\nu_x + 2\nu_y = 29$ resonance driving term will add in phase from one module to the next. This is mitigated by the fact that 29 is an odd number, so that whatever resonance driving term is produced by one of the arcs should be cancelled by the other. Nonetheless, trusting in cancellations across opposite sides of a ring is risky. Superperiodicity of the lattice can be broken by the tuning quads in the straight sections, or simply because of field errors. A phase error between the two arcs will certainly arise. Estimating the effect of this resonance must take that into account.

A (moderately) "safe region" for the $\nu_x + 2\nu_y$ resonance is bounded by the curves [3, pp.233-238]

$$
\begin{aligned}
\frac{1}{8}\left(\frac{\delta}{g}\right)^2 &= \frac{1}{4}\frac{\varepsilon_y}{\pi} + 2\left(\sqrt{\frac{\varepsilon_x}{2\pi}} - \frac{1}{4}\frac{|\delta|}{g}\right)^2 \quad , \\
\text{and} \quad -\frac{1}{4}\left(\frac{\delta}{g}\right)^2 &= 2\,\frac{\varepsilon_x}{\pi} - \frac{\varepsilon_y}{\pi} \quad , \\
\text{where} \quad g &= \frac{\sqrt{2}}{8\pi}\left|\sum \frac{B''l}{B\rho}\sqrt{\beta_x}\beta_y e^{i(\psi_x + 2\psi_y - \delta\cdot\theta)}\right| \quad ,
\end{aligned}
$$

and $\delta = \nu_x + 2\nu_y - 29 = 0.12$. If sextupoles existed in all three of an arc module's cells, the value of g for one module would almost vanish, because $\langle \Delta(\psi_x + 2\psi_y)|_{\text{cell}} \rangle = (2/3)\cdot 2\pi$. However, for the base configuration as given, with sextupoles in two of the three cells, the value of g for one arc module is $\approx 1.36\ \text{m}^{-1/2}$. If we ignore the contribution from $\delta\cdot\theta$ in the exponent, then $g \approx 6.82\,\text{m}^{-1/2}$ across an arc, since $\Delta(\psi_x + 2\psi_y)|_{\text{module}} = 4\pi$. Let the phase error between arcs be $\Phi \equiv \Delta\psi_x + 2\Delta\psi_y \pmod{2\pi}$. Then,

$$g_{\text{racetrack}} = 2\,|\,\sin(\Phi/2)\,|\,g_{\text{arc}} \quad .$$

The "safe regions" are plotted in Figure 3.3.8. for $\Phi \in \{\,45°, 90°, 135°, 180°\,\}$. Two squares

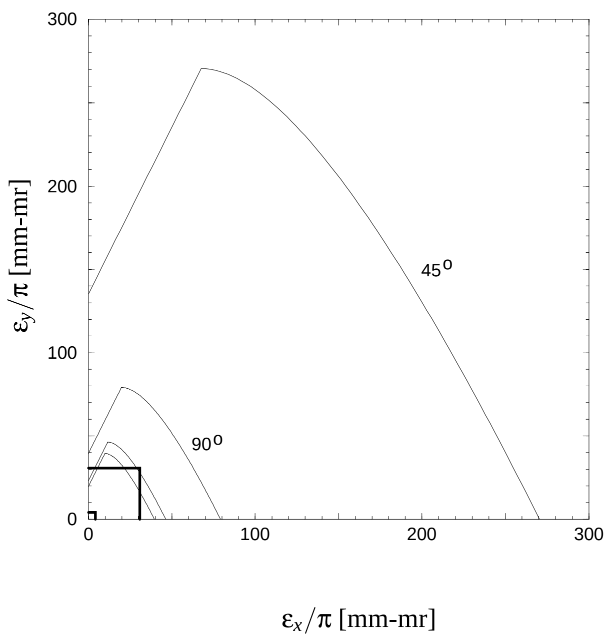

Figure 3.3.8. "Safe regions" for the $\nu_x + 2\nu_y$ resonance, in the base configuration, when $\Phi \in \{\,45°, 90°, 135°, 180°\,\}$, with invariant emittance of 40π mm-mr shown at injection and extraction. Ignoring space charge and second order sextupole effects, the injected beam is within the boundary provided $\Phi \ll 105°$.

in the lower left corner show the beam emittances at injection and extraction. (See Eq.(3.1).) The boundary crosses the injected beam at $\Phi \approx 105°$. Superperiodicity must be preserved to a value smaller than that.

This optimistic statement does not take into account the effects of space charge and (to second order) sextupoles in distributing tunes throughout the beam. How small, for example, must Φ be in order to reduce the "tune width" to $\delta \le \pm 0.01$ for all particles at injection? Answering this is complicated by the fact that the largest tune shifts will occur near the core of the beam. For the sake of argument, let us say that 10% of the beam (emittance) gets shifted within reach of the resonance line. Then, we require that superperiodicity be preserved at the level $\Phi < 24°$ or better, significantly more restrictive than the optical value of $105°$. However, it is possible that space charge detuning could limit the instability produced by the resonance. [5] If the PD2 base configuration is seriously considered, this issue should be studied thoroughly. Near extraction, where particle tunes will be closer to the reference point, $\Phi < 21°$ should be sufficient to allow moving the entire beam within ± 0.01 of the resonance line, although there is no reason to do so.

$3\nu_y = 26$ Even in the absence of field errors, the $3\nu_y = 26$ resonance can be excited in the base configuration by a roll misalignment of chromaticity sextupoles. The maximum vertical emittance contained within a (0,3) separatrix is,[3]

$$\begin{aligned} \varepsilon_{\max} &= \frac{2}{\sqrt{3}}\left(\frac{\delta}{g}\right)^2 , \text{ where} \quad (3.2) \\ \delta &\equiv 3\nu_y - 26 , \text{ and} \\ g &\equiv \frac{1}{12\sqrt{2}\,\pi}\left| \sum \left(\frac{B''_{\text{skew}} l}{B\rho}\right) \beta_y^{3/2} e^{i(3\psi_y - \delta\cdot\theta)} \right| . \end{aligned}$$

The sum is taken over all sources of skew sextupole: $\delta = 3\nu_y - 26$, assumed to be small, is the distance to the resonance line, g is the resonance coefficient, $\theta = s/R$ is the azimuthal coordinate around the ring, while β_y and ψ_y are vertical lattice functions at θ. When δ is sufficiently small, we can set $\delta = 0$ in the exponent of the integrand. If the field arises from a dipole error, then $B''_{\text{skew}} = 2Ba_2$, where B is the dipole field and a_2 is the skew sextupole coefficient; if it arises from rolling a normal sextupole through a small angle, Θ, then $B''_{\text{skew}} = B'' \cdot 3\Theta$. Thus, we can rewrite Eq.(3.2) as,

$$g = \frac{1}{12\sqrt{2}\,\pi}\left| \sum_{\text{dipoles}} 2a_2 \cdot \phi \cdot \beta_y^{3/2} e^{i(3\psi_y - \delta\cdot\theta)} + \sum_{\text{sextupoles}} \left(\frac{B''l}{B\rho}\right) \cdot (3\Theta) \cdot \beta_y^{3/2} e^{i(3\psi_y - \delta\cdot\theta)} \right| ,$$

where ϕ is the bend angle of a dipole. A systematic error is of little concern, because the phasors cancel remarkably well across an arc: $3\Delta\psi_y|_{\text{module}} = 18\pi/5 \simeq (-1/5)\cdot 2\pi$. To estimate the effect of random errors, we do the summation in quadrature.

$$\sigma_g^2 = \frac{1}{8\pi^2}\left[\frac{1}{9}\left(\sum_{\text{dipoles}} \phi^2 \beta_y^3\right) \sigma_{a_2}^2 + \frac{1}{4}\left(\sum_{\text{sextupoles}} \left(\frac{B''l}{B\rho}\right)^2 \beta_y^3\right) \sigma_\Theta^2 \right]$$

We concern ourselves here only with the term arising from chromaticity sextupoles. For 20 of the 40 sextupoles, $B''l/B\rho \approx 0.50\,\text{m}^{-2}$ and $5.3\,\text{m} < \beta_y < 6.8\,\text{m}$, with a median value of 6.2 m; for the other 20, $B''l/B\rho \approx -0.72\,\text{m}^{-2}$ and $14.2\,\text{m} < \beta_y < 19.8\,\text{m}$, with a median value of 16.7 m. Thus we estimate,

$$\sigma_g^2\,[m^{-1}] = \frac{1}{32\pi^2} \cdot 20 \cdot \left(0.5^2 \cdot 6.2^3 + 0.72^2 \cdot 16.7^3\right) \cdot 0.0005^2 = 3.9 \times 10^{-5}$$

Putting this number into Eq.(3.2) we see that, at injection, maximum amplitude particles ($\varepsilon \approx 31\pi$ mm-mr) will feel the effect of this resonance when $\delta < 5.7 \times 10^{-5}$, a number too small to be considered threatening.

$4\nu_y = 35$ The tune diagram of Figure 3.3.6. suggests that the dynamic aperture is "seeded" [3, pp.281-284] upon the $4\nu_y = 35$ resonance. Since no octupoles were included in either the base or tuned configurations models, this line is excited by the sextupoles with a strength quadratic in $B''/B\rho$. The same sextupoles shift the tunes of large amplitude particles onto the line. (See page 3 - 9.) The importance of a $4\nu_y$ resonance and its effect on beam loss in ISIS has already been discussed in the PD1 Report. [1, p.3-18]

[3] One can choose from several rough approximations to develop this argument. The one used here employs the area of an equilateral triangle with vertices at the resonant orbits. To use the triangle's in-circle instead, replace "$2/\sqrt{3}$" with "$\pi/9$."

3.4. Alternative Designs

Several alternative lattice designs were considered, although not all were studied thoroughly. Some may eventually be revisited and new ones developed. For now we content ourselves with simply recording a few of them for future reference. One, the possibility of using combined function magnets, was already discussed in PD1. The three we consider here are: (a) changing the phase advance through the arc module, (b) eliminating the small dipole from the central cell of the arc module (MM: missing magnet), and (c) using a triangular, transitionless lattice (IG: imaginary γ_t). For convenient reference, a summary of their optical properties is provided below. Information on their hardware and space

Property (Lengths in meters)	PD2	MM (racetrack)	IG
$\Delta\psi_{\text{cell}}$	$(8\pi/15, 2\pi/5)$	$(\pi/2, \pi/2)$	$(\pi/2,\pi/2)$
Cells/arc	$3\times 5 = 15$	$3\times 4 = 12$	N/A
Cells/straight	7	6	4
(ν_x,ν_y)	(11.747, 8.684)	(9.048, 8.784)	(8.366,7.805)
max (β_x,β_y)	(15.141, 20.332)	(19.225, 20.695)	(41.363, 36.120)
min (β_x,β_y)	(4.105, 4.570)	(5.578, 4.642)	(1.014, 1.252)
max D_x	2.523	4.334	2.809
min D_x	0.0	-0.061	-3.819
α	0.0053	0.0066	-0.006
γ_t	13.758	12.349	N/A

Table 3.4.2. Optical properties of alternative lattices.

usage is compiled in Table 3.4.3., which should be compared with Table 3.2.1.. Lattice files, in MAD input format, for all of these can be found on the Proton Driver web site, http://www-bd.fnal.gov/pdriver/8GEV .

3.4.1. Alternative Phase Advance Lattices

The phase advance per arc module of the PD1 lattice, with four modules in an arc, was $(\Delta\psi_x,\Delta\psi_y)|_{\text{module}} = (3\pi/2, 3\pi/2)$. When the number of modules was increased to five, the phase advance had to change to $(m_x\pi/5, m_y\pi/5)$, where m_x and m_y were integers. To zero the dispersion in the straight sections, (a) m_x should be even, and (b) each module should be a first order achromat. (If (b) is not satisfied, dispersion in the arcs won't be periodic across module boundaries.) The choice $m_x = 8$ assures that γ_t is comfortably above the energy reach of the Proton Driver; $m_x = 6$ results in insufficient horizontal focusing. For much of PD2 it was assumed that the average phase advance per cell was to be $(\Delta\psi_x,\Delta\psi_y)|_{\text{cell}} = (8\pi/15, \pi/3) = (96^\circ, 60^\circ)$, corresponding to $m_x = 8, m_y = 5$, and making the vertical phase advance across a three-cell arc module, $\Delta\psi_y|_{\text{module}} = (1/2)\cdot 2\pi$. However, when dipoles (with parallel edges) are introduced into the module, perturbations induced by the vertical edge focusing make it difficult to make the module a periodic, linearly stable unit in the vertical direction. It is sitting on top of the half-integer stop band.

Lattice	Element	Name	Number	Length [m]		Field	
MM	DIPOLES	B1	2x4x2 = 16	7.780	$B =$	1.49	T
	QUADRUPOLES	QF	(6+3x4)x2 = 36	1.059	$B' =$	10.29	T/m
		QD	(6+3x4)x2 = 36	1.059		-10.07	
	FREE (total)			273.401			
IG	DIPOLES	B2	3x2x3 = 18	7.88	$B =$	1.26	T
		B2145	2x2x3 = 12	2.95		1.26	T
	QUADRUPOLES	QFS+QFS	2x3 = 6	0.50	$B' =$	8.13	T/m
		QDS+QDS	1x3 = 3	0.50		-8.13	
		QDAF+QDS	2x3 = 6	0.50		-8.13	
		QDLBX	3x3 = 9	1.00		-8.13	
		QFLBX	3x2x3 = 18	1.00		8.13	
		QDLBY	2x2x3 = 12	0.72		-8.13	
		QFLBY	2x3 = 6	0.72		8.13	
		QDT	4x2x3 = 24	0.24		-2.03	
		QFT	2x3x3 = 18	0.24		2.03	
	SEXTUPOLES	HS1	2x3x3 = 18	0.25	$B'' =$	16.86	T/m^2
		VS1	2x3x3 = 18	0.25		-24.70	
		HS2	2x2x3 = 12	0.25		-16.86	
		VS2	2x2x3 = 12	0.25		24.70	
	FREE (total)			254.38			

Table 3.4.3. Hardware and space usage in two alternative designs: MM, the missing magnet lattice, and IG, the transitionless (imaginary γ_t) lattice.

Either the module is unstable vertically or its vertical lattice function, β_y, does not match well into the straight sections. Of course, *it is not necessary that the arc module be a linearly stable unit.* The arcs could act simply as beamlines connecting one straight section to the other. One design did, in fact, proceed in this manner, but not without using individually powered trim quads to control β_y in the arcs.

The choice was between (a) designs in which lattice functions in arcs and straight sections are automatically reasonably matched using the main bus quads, while trim quads are used for small perturbations, and (b) designs in which trim quads control lattice functions in the arcs, even in a "base" configuration. The phase advance was changed to $(\Delta\psi_x, \Delta\psi_y)|_{\text{module}} = (8\pi/5, 6\pi/5)$, corresponding to choice (a).[4] (As a bonus, the arcs were made optically transparent in both planes.) We have discussed the negative implications for the $\nu_x + 2\nu_y = 29$ resonance line when superperiodicity is broken. (See pp.3 - 16 *ff.*) If superperiodicity is preserved, tracking suggests that the most important resonance for determining dynamic aperture will be $4\nu_y = 35$, which could be excited by the $(8\pi/15, \pi/3)$ design as well. Finding a good working point will be an important operational consideration.

[4] A possibility that was not studied, but may be worth a look in the future, is $(\Delta\psi_x, \Delta\psi_y)|_{\text{module}} = (8\pi/5, 7\pi/5)$. The principle resonance of concern would then be $2\nu_x + 2\nu_y = 44$. Considering that there are 44 cells, and that the resonance can be driven by space charge, this numerology could be ominous.

3.4.2. Missing Magnet Lattice

In one variation of the PD2 design, the small dipoles are removed from the central cells of the arc modules. This increases the amount of free space in the arcs and eliminates about 40% of the momentum compaction (see page 3 - 8), raising transition gamma. Lengths and strengths of remaining elements are adjusted so that the arc module remains a linear achromat. The "missing magnet" design had the attractiveness of featuring only a single species of quadrupole and dipole, making it one of the simplest lattices considered. It was not pursued because its maximum dispersion of ≈ 3 m, with $\beta_{x,\mathrm{max}} \approx 26$ m and $\beta_{y,\mathrm{max}} \approx 30$ m, were too large to accomodate $\varepsilon_{\mathrm{inv}} = 40\pi$ mm-mr at injection.

3.4.3. Transitionless Lattice

One of the superperiod 3, triangular lattices considered is noteworthy in that it possesses a negative momentum compaction, α. It is a so-called "imaginary γ_t" lattice, which more correctly means that it is transitionless: there is no energy for which the slip factor, $\alpha - 1/\gamma^2$, becomes positive. Each arc contains three low β_x regions and two low β_y regions. Low β_y regions coincide with regions of negative dispersion, which make α negative. Unfortunately, small β in one location generally requires large β elsewhere. Like the missing magnet design, this one was not pursued because its maximum dispersion (magnitude) of ≈ 3.8 m was too large when combined with $\beta_{x,\mathrm{max}} \approx 41$ m and $\beta_{y,\mathrm{max}} \approx 36$ m.

3.4.4. References

[1] R. Alber, *et al.*, The proton driver design study. Technical report, Fermilab, December, 2000. Fermilab-TM-2136.

[2] A. Piwinski. Handbook of Accelerator Physics and Engineering, p.72. Edited by A. Chao and M. Tigner.

[3] L. Michelotti. *Intermediate Classical Dynamics with Applications to Beam Physics*. John Wiley & Sons, Inc., New York, 1995.

[4] D. A. Edwards and M. J. Syphers. *An Introduction to the Physics of High Energy Accelerators*. John Wiley & Sons, New York, 1993.

[5] I. Hofmann, A. Fedotov, and G. Franchetti. Space charge resonances in high intensity drivers. Presented at 20th ICFA Advanced Beam Dynamics Workshop: High Intensity High Brightness Hadron Beams. Fermilab., April 8-12 2002.

Chapter 4. Beam Dynamics

4.1. Space charge and beam stability

J. Holmes, K.Y. Ng, C. Prior

4.1.1. Tune shifts

The *betatron tunes* ν_z, $z=x$ or y, of transverse oscillations of charged particles in the beam moving with axial velocity $v=\beta c$, c being the velocity of light, are mainly determined by the applied focusing forces due to quadrupoles. With finite beam current the tunes are shifted, both by direct space charge and by image forces due to induced voltages in the surrounding structure impedances. At relativistic beam energies, the space charge forces are strongly reduced by a factor $\gamma^{-2}=1-\beta^2$ due to partial compensation of electric and magnetic forces. However, in the PD2 at 600 MeV injection energy, $\gamma=1.640$ and the space charge term is largely dominant.

The *coherent* and *incoherent tune shifts* of a beam with half width a_x and half height a_y consisting of N_p protons are [1]

$$\Delta\nu_{\mathrm{coh},z}=-\frac{N_pr_pR}{\pi\nu_z\gamma\beta^2}\left[\left(\frac{1}{\gamma^2B_f}+\beta^2\right)\frac{\xi_{1z}}{h^2}+\beta^2\frac{\epsilon_{1z}}{h^2}+\mathcal{F}\beta^2\frac{\epsilon_{2z}}{g^2}\right], \tag{4.1}$$

$$\Delta\nu_{\mathrm{incoh},z}=-\frac{N_pr_pR}{\pi\nu_z\gamma\beta^2}\left[\left(\frac{1}{\gamma^2B_f}+\beta^2\right)\frac{\epsilon_{1z}}{h^2}+\beta^2\frac{\epsilon_{1z}}{h^2}+\mathcal{F}\beta^2\frac{\epsilon_{2z}}{g^2}+\frac{2\epsilon_{\mathrm{spch},z}}{\gamma^2a_y(a_x+a_y)B_f}\right]. \tag{4.2}$$

where r_p is the classical radius, B_f is the bunching factor, and R is the mean radius of the accelerator ring. The *coherent Laslett image coefficients* $\xi_{1,2z}$ and *incoherent Laslett image coefficients* $\epsilon_{1,2z}$ describe the strength of image forces for a particular geometry. For a rectangular vacuum chamber of total height $2h=4$ in and width $2w=6$ in, the images coefficients are $\xi_{1x}=0.0887$, $\xi_{1y}=0.5737$, $\epsilon_{1x}=-\epsilon_{1y}=-0.1617$. For the magnet pole gaps, the geometry of two infinite plates separated by $2g=4$ in covering $\mathcal{F}=0.5$ of the ring is assumed, giving $\epsilon_{2x}=\epsilon_{2y}=-\pi^2/24$. Because of multi-turn injection, a uniform distribution in the transverse directions is assumed for the self-field in the last term in Eq. (4.2), giving the space charge coefficients $\epsilon_{\mathrm{spch},y}=a_y/(a_x+a_y)$ and $\epsilon_{\mathrm{spch},x}=a_y^2/[a_x(a_x+a_y)]$. The tune shifts are calculated at every moment of the ramp cycle and are plotted in Fig. 4.1. In the computation, the standard rf voltage table has been used, which assumes a fixed bucket area in the latter part of the ramp 20.3 ms into the cycle. The bunching factor B_f is computed from the bunch area which is assumed to increase linearly from 0.05 eV-s just after injection to 0.15 eV-s at extraction. The beam radii are computed from the 95% normalized emittance $\epsilon_{N95\%}=40\times10^{-6}$ πm. We see that the bunching factor, which is also plotted in a different scale, decreases rapidly as the beam is captured into the rf bucket adiabatically. As a result, the tune shifts assume their maximal values

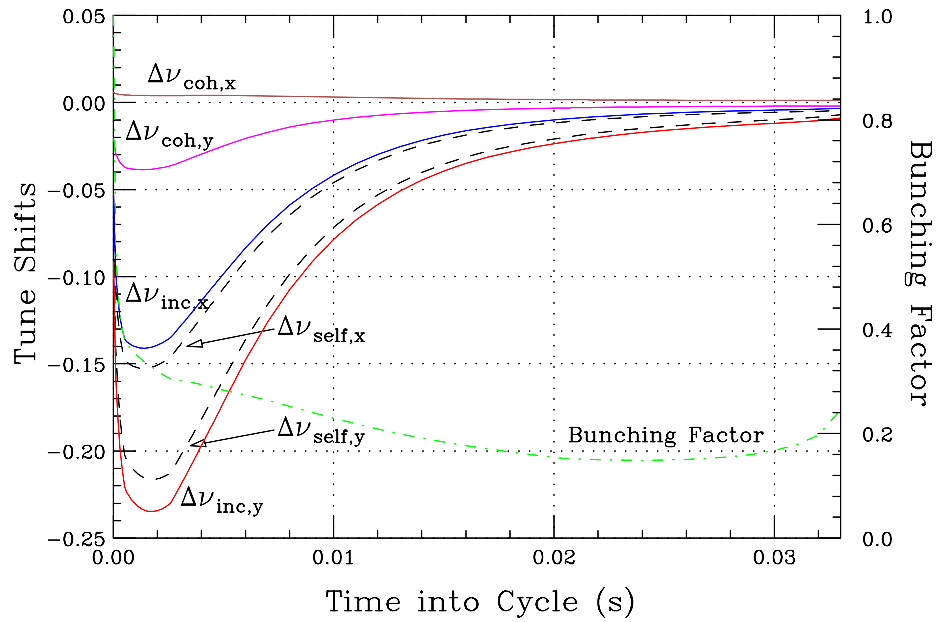

Figure 4.1. (color) Coherent and incoherent betatron tune shifts of the PD2.

about 8 ms into the cycle. The coherent tune shifts come from images in the vacuum wall and they are small. The incoherent tune shifts are dominated by the self-field contributions which are denoted by $\nu_{\text{self},x}$ and $\nu_{\text{self},y}$ in the figure. At their maximal values, we can write

$$\Delta\nu_{\text{incoh},x} = -0.153 + 0.013 = -0.140\,, \quad \Delta\nu_{\text{incoh},y} = -0.216 - 0.018 = -0.234\,, \tag{4.3}$$

where the first term in the middle corresponds to self-force contributions and the second term to image contributions. It is obvious that space charge dominates the incoherent tune shifts. However, it is well-known that only the coherent tune shifts are responsible for parametric resonances [2]. Although the space charge self-force does not contribute to the dipole coherent tune shifts, it contributes to the quadrupole coherent tune shifts. The symmetric coherent quadrupole mode will be shifted by $2 \times \frac{3}{4}$ of the incoherent dipole shift, or $\nu_{\text{quad}} = 2\big[\nu_{\text{dipole}} - \frac{3}{4}|\Delta\nu_{\text{incoh}}|\big]$. Therefore, $2\nu_y$ is shifted from 2×7.34 to 2×7.16 and $2\nu_x$ is shifted from 2×11.70 to 2×11.61. With the vertical and horizontal betatron bare tunes at $\nu_{y0} = 7.34$ and $\nu_{x0} = 11.7$, the equivalent vertical tune ν_y passes through the stopbands at 7.33, 7.25 and 7.20, while the equivalent horizontal tune ν_x passes through the stopband at 11.67.

4.1.2. Space charge at Injection

The code TRACK-2D, developed in the Rutherford Laboratory in England [3], also includes transverse space-charge effects, making use of a nonlinear space-charge solver based on finite elements. The code has been applied to the parameters of the Proton Driver to study the evolution of particles in transverse phase space. The results are shown in Figs. 4.2 for the transverse plane (x, y). Reading from left to right and top to bottom, each plot shows a sequence of shots in the first 1, 5, 10, 15, 20, 25, 30, 35, 40, 45, and 51 revolutions. Al-

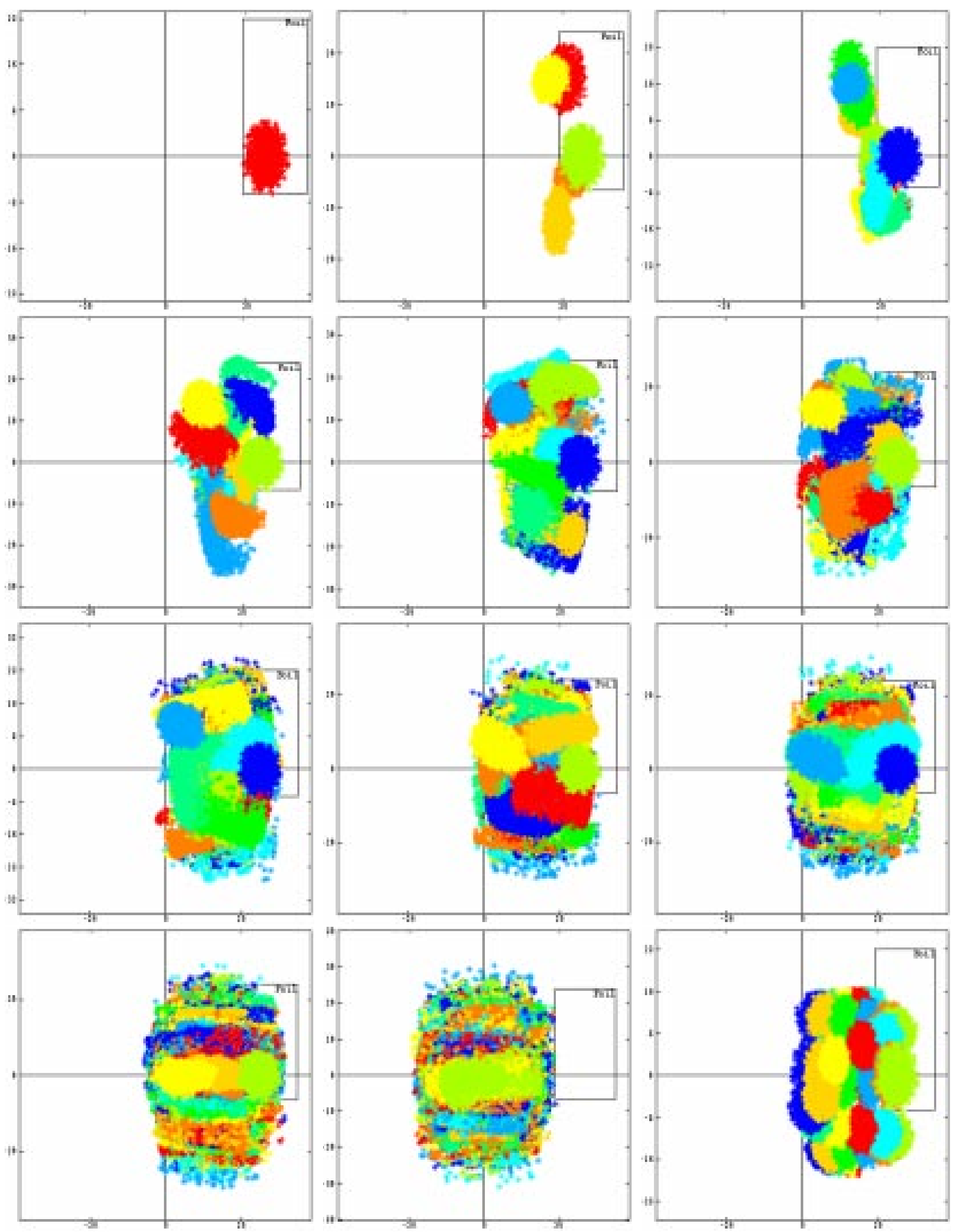

Figure 4.2. (color) Reading from left to right and top to bottom are x-y plots of the injection beam cross sections at stripping foil at the 1, 5, 10, 15, 20, 25, 30, 35, 40, 45, and 51 revolutions with the space charge force implemented. The last plot is at the 51 revolutions with the space charge force turned off. Note that the plots are on different scale. However, the stripping foil, depicted as a rectangle, should be of the same physical size.

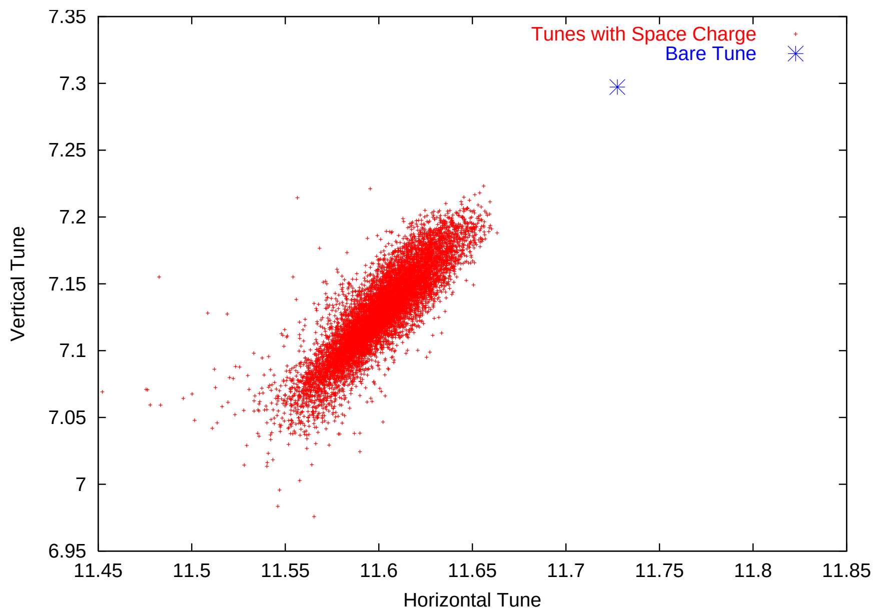

Figure 4.3. Tune foot-print after injection, showing the tunes of individual particles shifted by the space charge self-force from the bare values.

though these plots are on different scales, the transverse size of the injected beam can be inferred by comparison with the size of the stripping foil, which is depicted as a rectangle in every plot. The last plot is at the 51 revolutions with the space charge force turned off. It is clear by comparing this plot with the second last one that space charge does blow up the beam size.

A simulation of the injection was also performed with the transverse space charge force fully taken into account to determine the transverse locations of the beam particles [4]. The injection painting scheme follows the description in Sec. 7.1. Figure 4.3 shows the betatron foot-print just after injection. We see that the tunes are shifted from the bare values of $\nu_{y0} = 7.34$ and $\nu_{x0} = 11.7$ to the foot print that has the spreads of $\Delta\nu_y \sim 0.15$ and $\Delta\nu_x \sim 0.10$. The amounts of shifts closely resemble what were predicted in Fig. 4.1. In Fig. 4.4, the fractional number of particles that have exceeded a certain normalized emittance. For example, only $\sim 5\%$ full outside 30×10^{-6} πm, and this number becomes negligibly small at 40×10^{-6} πm.

4.1.3. Single Bunch Instability

Keil-Schnell limit for longitudinal microwave instability is [5]

$$\left|\frac{Z_0^{\|}}{n}\right| < \frac{|\eta| E_0}{e\beta^2 I_{\rm pk}} \left[\frac{\Delta E}{E_0}\right]^2_{\rm FWHM} F_{\|} \, , \tag{4.4}$$

where I_{pk} is the peak current, η is the slip factor, E_0 is the nominal beam energy, and the energy spread ΔE at FWHM is computed according to a parabolic distribution and the

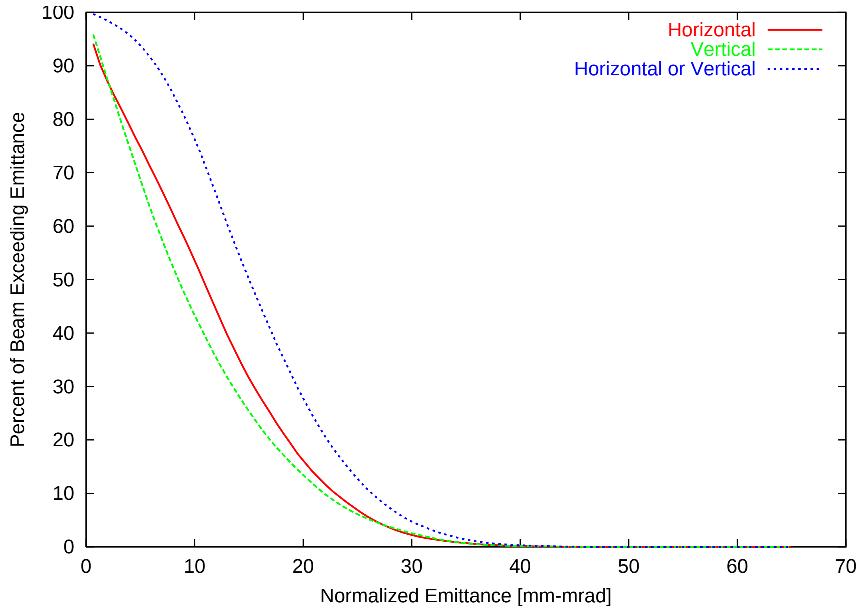

Figure 4.4. Plot showing the fractional number of particles falling outside a particular normalized emittance. The lowest curve is for vertical consideration only, the middle is for horizontal consideration only, and the uppermost one is regardless of vertical or horizontal.

form factor $F_{\|}$ is near unity for the real and inductive parts of the impedance, but is large for the capacitive part of the impedance. The stability limit is depicted in Fig. 4.5. Alongside, is also shown the space charge impedance of the beam inside the rectangular beam pipe,

$$\frac{Z_0^{\|}}{n} = i\frac{Z_0}{2\beta\gamma^2}\left[1 + 2\ln\left(\frac{4h}{\pi a}\tanh\frac{\pi w}{2h}\right)\right] , \tag{4.5}$$

where $Z_0 \approx 377\ \Omega$ is the free-space impedance and a is the beam radius.

The longitudinal resistive-wall impedance is

$$Z_0^{\|}\Big|_{\text{wall}} = [1 - i\,\text{sgn}(\omega)]\,\frac{\rho R}{h\delta_s}F_{\|}^{\text{wall}} , \tag{4.6}$$

where δ_{skin} is the skin depth for resistivity ρ and $F_{\|}^{\text{wall}} = 0.92698$ is a form factor which takes care of the fact that the beam pipe cross section is rectangular. The beam pipe will be constructed using Inconel with $\rho = 1.29 \times 10^{-6}\ \Omega$m. The real or imaginary part of the resistive-wall impedance amounts to $2.5\ \Omega$ at the revolution frequency. Since both the space charge and resistive-wall impedances are well below the Keil-Schnell limit, the beam should be stable against longitudinal microwave instability.

The Keil-Schnell-like limit for transverse microwave instability is [6]

$$|Z_1^{x,y}| < \frac{4\nu_{x,y}E_0}{e\beta R I_{\text{pk}}}\left[\frac{\Delta E}{E_0}\right]_{\text{FWHM}}|S_{x,y}|F_{x,y} , \tag{4.7}$$

where the *effective chromaticity* is $S_{x,y} = \xi_{x,y} + (\hat{n} - [\nu_{x,y}])\eta$, with $\xi_{x,y}$ the chromaticity, $\hat{n} = n + \nu_{x,y}^I$, n a revolution harmonic, $\nu_{x,y}^I$ and $[\nu_{x,y}]$ the integral and decimal parts of the

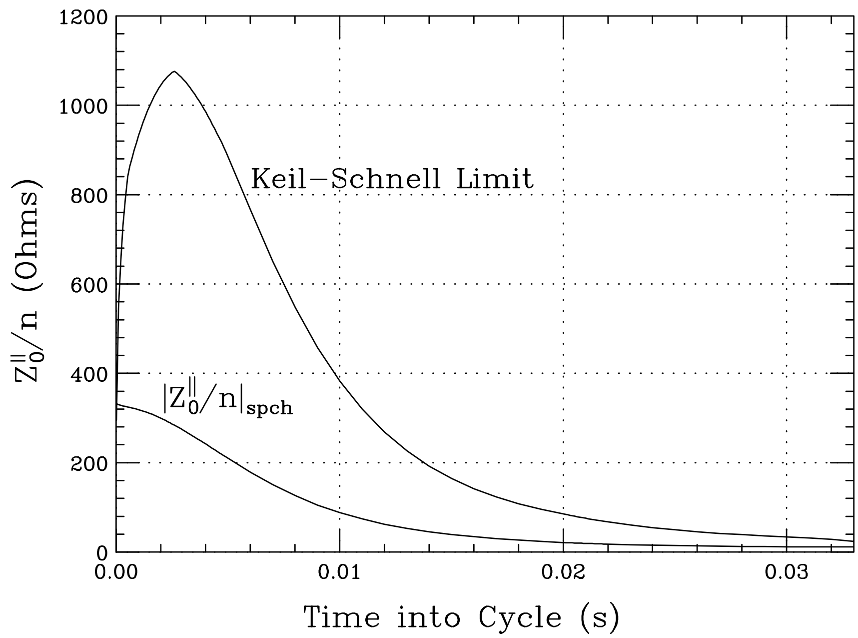

Figure 4.5. Keil-Schnell limits of longitudinal microwave instabilities for the PD2.

betatron tune. Instability occurs only for *slow waves* when $\hat{n} > [\nu_{x,y}]$. The form factor $F_{x,y}$ depends on the transverse particle distribution, about unity for the real part of the impedance but is large compared to unity for a space charge dominated impedance. Since this is a coasting-beam theory, it is applicable only when the wavelength of the perturbation is much less than twice the total bunch length. In the ramp cycle of this machine, the half bunch length is $\hat{\tau} \lesssim 5$ ns soon after adiabatic capture. Thus, the perturbation must have frequency larger than 50 MHz or revolution harmonic $n \gtrsim 100$. The slip factor η changes from -0.3668 at injection to -0.0058 at extraction (using $\gamma_t = 13.82$). The chromaticities will be negative both horizontally and vertically indicating that $S_{x,y}$ will not vanish. At injection, $S_{x,y} \approx 30$ is dominated by the slip-factor part. Near the end of the ramp, however, $S_{x,y}$ can be dominated by the chromaticity if the perturbation wavelength is as small as the bunch length. In other words, we should not expect $S_{x,y}$ to help much in the stability limit of Eq. (4.7). With $F_{x,y}|S_{x,y}| = 1$, the stability limits are depicted in Fig. 4.6. We see that, from injection to extraction, $|Z_1^y| < 0.31 \text{ to } 0.73\ \mathrm{M\Omega/m}\ |Z_1^x| < 0.49 \text{ to } 1.20\ \mathrm{M\Omega/m}$.

The transverse resistive-wall impedance is

$$Z_1^{x,y}\Big|_{\text{wall}} = \frac{2c}{h^2\omega} Z_0^{\|}\Big|_{\text{wall}} \frac{F_{x,y}^{\text{wall}}}{F_x^{\text{wall}}}\ , \tag{4.8}$$

with the form factors $F_x^{\text{wall}} = 0.40825$ and $F_y^{\text{wall}} = 0.81979$, leading to $|Z_1^y| = 0.07\ \mathrm{M\Omega}$/m and $|Z_1^x| = 0.14\ \mathrm{M\Omega}$/m at the revolution frequency. These are small compared with Eq. (4.7). On the other hand, the space charge contributions are $Z_1^y = i54$ to $i7.3\ \mathrm{M\Omega}$/m and $Z_1^x = i70$ to $i7.6\ \mathrm{M\Omega}$/m from injection to extraction, much larger than the limits quoted in Eq. (4.7). However, reactive impedance will not lead to instability if the resistive part can be controlled.

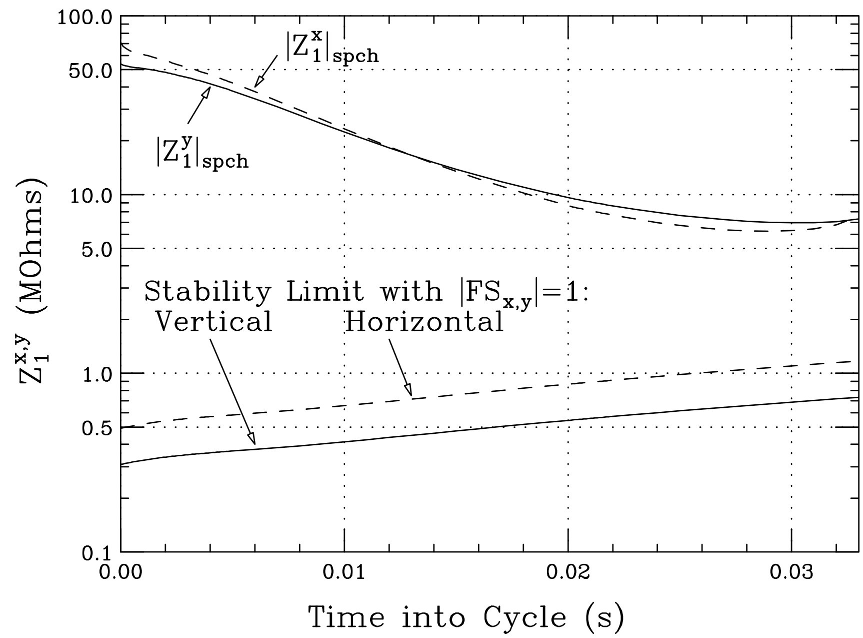

Figure 4.6. Keil-Schnell-like limits of transverse microwave instabilities for the PD2.

4.1.4. Coupled-bunch Instability

The resistive-wall impedance can drive transverse coupled-bunch instability with a growth rate

$$\frac{1}{\tau_\mu^{x,y}} \approx \frac{eMI_bc}{4\pi\nu_{x,y}E_0}\,\mathcal{R}e\, Z_1^{x,y}(\nu_{x,y}^c\omega_0)F\ , \tag{4.9}$$

where the form factor is $F \sim 0.811$ if sinusoidal modes are assumed and the instability is worst at injection. For $\nu_y = 7.34$, $[\nu_y] = 0.34$, $\nu_{x,y}^c = [\nu_{x,y}] - 1 = -0.66$ and $\mathcal{R}e\, Z_1^{x,y}(\nu_y^c\omega_0) = -0.088$ MΩ/m. The growth rate is $302\ \mathrm{s}^{-1}$ or growth time 3.30 ms or 1660 turns. This instability is hard to damp with chromaticity since $|\eta| = 0.3668$ at injection is not small. For example, with $\xi_y = -20$ and full bunch length $\tau_L = 10$ ns, $\omega_\xi\tau_L/\pi = 2f_0\xi_y\tau_L/|\eta| = 0.55$ and the form factor is reduced by only $\sim 5\%$. To damp this instability, one may need octupoles and/or a mode damper.

Coupled-bunch instabilities, longitudinal or transverse, driven by the higher-order modes of the rf cavities are quite different. This is because resonances from cavities have fixed frequencies. Since revolution frequency changes fast during ramping, these resonances will move through the revolution harmonics. In other words, a coupled-mode is driven for only a short time. Thus there will not be any growth at the early part of the cycle. For the driving frequency $f_r = \omega_r/(2\pi)$, define the resonant harmonic $n_r = f_r/(\beta f_\infty)$ where $f_\infty = c/(2\pi R)$. The drift rate at the harmonic n_r is $\dot\beta n_r f_\infty$. The time required to drift through the HWHM of the resonance with quality factor Q is

$$\Delta t = \frac{2\beta}{\dot\beta Q} = \frac{2\gamma^3\beta^2}{Q\dot\gamma}\ , \tag{4.10}$$

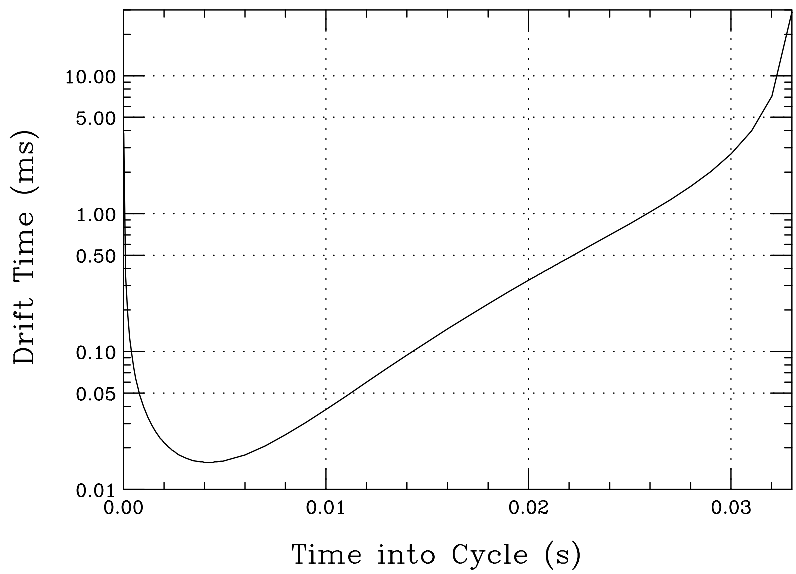

Figure 4.7. Time for a higher-order resonance of fixed frequency to drift through a harmonic line of the PD2.

implying that any coupled-bunch growth time $\gtrsim \Delta t$ cannot materialize. This is plotted in Fig. 4.7 for the situation of $Q = 5000$. Any coupled-bunch instabilities that occur during the latter part of the cycle will have similar behavior as those observed in the present booster; of course the growth rate will be faster. At this part of the cycle, the energy of the beam is much larger making the growth rates smaller. Since these couplings occur at high frequencies, the form factor drops as the bunch length increases; for example, at angular driving frequency ω_r, $F \sim e^{-(\omega_r \sigma_\tau)^2}$ for a Gaussian distribution with rms bunch length σ_τ.

4.2. Longitudinal Dynamics

James MacLachlan

The rf systems and longitudinal dynamics of the 8 GeV Proton Driver (PD2) relate most closely to the Phase I, Stage 1 description of the previous Proton Driver Design Study. Because of the smaller size and drastic change in lattice for the 8 GeV machine, however, few specific parameters carry over. Nonetheless, the design concepts are similar. The present study is like an addendum to the PD1 Design Study; what follows builds on Ch. 5. In common with the previous design, modified Booster cavities and a 15 Hz sinusoidal magnet ramp with a second harmonic are used. The usefulness of an inductive insert for space charge compensation remains an attractive but less crucial speculation. The parameters governing the longitudinal dynamics are summarized in Table 4.1.

Proton Driver 2 is fundamentally a high intensity injector or super booster for the MI. Accordingly, the use of modified Booster rf cavities is much less of a limitation than for

Table 4.1. 8 GeV Proton Driver specifications important for the rf design.

$E_{\rm inj}$	injection kinetic energy	600	MeV
	beam intensity	2.5×10^{13}	p/cycle
	cycle repetition rate	15	Hz
$E_{\rm ext}$	extraction kinetic energy	8	GeV
$R_{\rm eq}$	mean radius of equilibrium orbit	75.471	m
$f_{\rm rf}$	accelerating cavity frequency	42 – 53	MHz
h	harmonic number	84	
	number of populated buckets (at extraction)	81	
$\hat{V}_{\rm rf}$	maximum rf voltage	1.05	MV
	number of rf cavities	20	
ε_ℓ	95 % norm. longitudinal emittance (at extraction)	0.2	eVs
	bunch intensity	3×10^{11}	
	rms bunch length (at extraction)	1	ns
$\Delta E_{\rm inj}$	energy spread at injection	± 0.25	MeV
$\alpha_\circ$	momentum compaction	5.251×10^{-3}	
α_1	coefficient of $(\Delta p)^2$ in path length	-8.46×10^{-3}	
g	geometric factor for space charge	2.05	
$Z_\parallel/n$	high frequency broadband longitudinal impedance (estimate)	2	Ohm
	momentum acceptance	$\pm 1\%$	

the Phase 1, Stage 1 of the previous proposal. For example, a pure sinusoidal ramp is a cost saving option if the cavity count can be raised from 20 to 22. Also, inductive inserts are not necessary to achieve low losses.

Losses and emittance growth have been evaluated for three ramp options, a pure sinusoidal ramp like the present Booster and two using 12.5 % addition of second harmonic to reduce the maximum $\dot{p}$ (rate of change of momentum). One variant minimizes $\dot{p}$ early in the cycle; it is called here a “minimum $\dot{p}$ ramp” although partly it postpones the peak $\dot{p}$. The ramp which is called “minimum rf power” has a higher slope early in the cycle where the rf voltage is limited by tuner performance but has a lower maximum rf power. The $\dot{p}$ curves are plotted in Fig.4.8. In every case the maximum rf voltage has been limited to 1.05 MV; the twenty modified Booster cavities are expected to make this voltage, but the current capability is marginal for a pure sine ramp. Additional cavities are desirable to provide for reliable, stable operation.

The capture phase of the cycle is common to the three ramp variants. It has been optimized with perfectly conducting wall space charge taken into account with no other source of longitudinal impedance. Given that generally other $Z_\parallel$ is likely to have an inductive component, this condition is probably worst case for capture. Very small reduction in rf voltage in the first 5 ms produces significant losses; so the voltage specified includes little or no safety margin for operational variability. Practically some margin will be needed; if studies establish that an inductive insert is otherwise benign, a substantial safety margin for capture can be obtained inexpensively in this way. However, it is also possible that the modified cavities will provide sufficient voltage to cover reasonable operational variability. Failing positive results on both inductive insert and cavity gradient, another pair of cavities would be prudent.

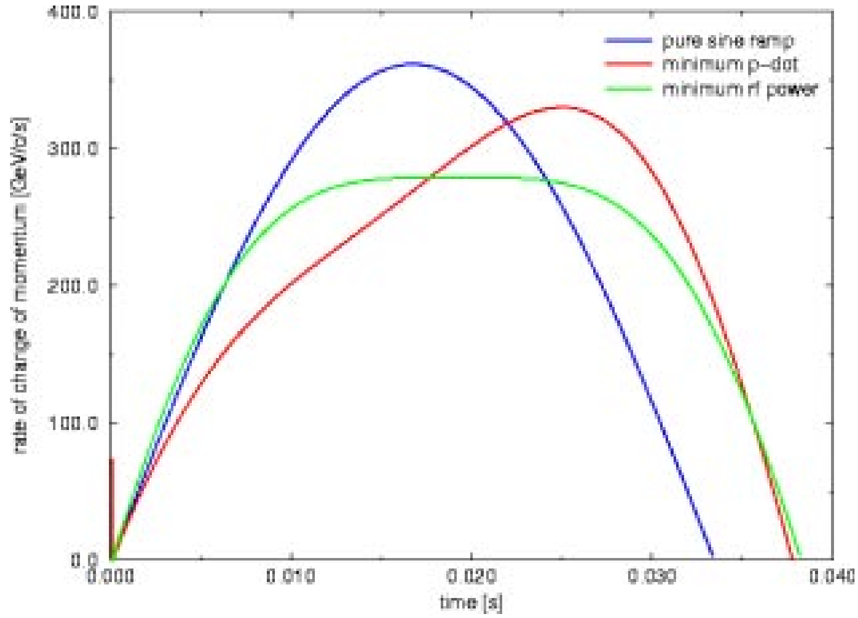

Figure 4.8. (color) Rate of change of momentum $\dot{p}$ [GeV/c/s] *vs*. time [s] for three ramp variants: pure sinusoidal ramp, ramp with second 12.5 % second harmonic phased for least $\dot{p}_{\rm max}$, ramp with 12.5 % second harmonic phased for least peak rf power.

Table 4.2 summarizes the basic results. Any of the quoted losses and final emittances would be acceptable if actually achieved, but the modeling is too idealized to support such an expectation. Rather one notes by comparison such details as the the tendency of the minimum rf power ramp toward higher loss because of faster ramp early in the cycle. Despite the clear appeal of the minimum rf power ramp, in an optimized design a different choice might be made based on a detailed tradeoff on RF power required and the frequency at which the peak power is required. Postponing the higher slope until later in the cycle may turn out to be beneficial because of better tuner performance at higher frequency. The rms and 95 % emittances at extraction don't appear to correlate closely. The rms values are more solid because the 95 % values are disproportionately affected by scraping with whatever loss there is and furthermore are not evaluated very precisely. However, all of the 95 % values have better than ten percent precision and exceed the Table 4.1 specification.

With respect to anticipated instabilities, the considerations of the PD1 Design Study

Table 4.2. Performance on variant ramps.

Ramp type $\rightarrow$	sine ramp	minimum $\dot{p}$	min. rf power
max. rate of momentum change [GeV/c/s]	361.4	329.9	278.8
accelerating voltage at $\dot{p}_{\rm max}$ [MV]	0.93	0.78	0.99
synchronous phase at $\dot{p}_{\rm max}$ [deg]	38	42	26
rf accelerating power at $\dot{p}_{\rm max}$ [MW]	1.4	1.3	1.1
95% longitudinal emittance at extraction [eVs]	0.07	0.10	0.08
rms longitudinal emittance at extraction [eVs]	0.0078	0.0077	0.0107
loss (all below 1.2 GeV)	<0.1 %	0.0	0.6 %
loss with inductive insert	0.0 %	0.0 %	0.0 %

remain generally relevant; however, the design beam current is 25 % higher because of the reduced circumference even though the number of protons has been reduced by 17 %. Controlling longitudinal coupled bunch instability will require not only a concerted effort on higher order mode suppression in the cavities but at least some level of active damping.

4.2.1. Extraction and Bunch rotation

The longitudinal matching of PD2 to the MI is practically the same as for the current Booster-MI transfer. About 90 kV in the PD matches a 0.8 eVs bucket generated by 1 MV or so in the MI. This bucket sounds a bit large, but it can not be reduced by much and still provide control and acceptable bucket shape distortion; it can be reduced a little if desired on the MI ramp.

Bunch rotation is not so important in PD2 as it was for the original Proton Driver design for two reasons. First of all, the momentum acceptance of the PD2 ring is only 40 % of the original, so path length dependence on momentum is less serious. It is accounted for to the first order correction in $\Delta p/p$. On the other hand, with advertised dynamic aperture of 250 π, path length dependence on betatron amplitude may be significant. This has not been accounted for in either study. Bunch rotation is also less important programmatically in the absence of a neutrino factory or μ storage ring. Neutrino beam users might make good use of tighter timing for gating and TOF discrimination. The result of a rotation on the ramp is shown in Fig. 4.9; the nonlinearity of the rotation is evident in the C-shaped bunch instead of the classic S and also in the up-down asymmetry of the bucket. However, the rms bunch width is only 0.2 ns with the rather reasonable symmetry about the mean shown in Fig. 4.10.

References

[1] L.J. Laslett, Proceedings of 1963 summer Study on Storage Rings, BNL-Report 7534, p. 324.

[2] F. Sacherer, *Transverse Space Charge Effect in Circular Accelerators*, Lawrence Rad. Lab. UCRL-18454 (PhD Thesis, University of California, 1968).

[3] C. Prior, Track-2D, private communication.

[4] J. Holmes, private communication.

[5] E. Keil and W. Schnell, CERN Report TH-RF/69-48 (1969); V.K. Neil and A.M. Sessler, Rev. Sci. Instr. **36**, 429 (1965).

[6] B. Zotter and F. Sacherer, *Transverse Instabilities of Relativistic Particle Beams in Accelerators and Storage Rings*, Proceedings of the First Course of the International School of Particle Accelerators of 'Ettore Majorana' Centre for Scientific Culture, Erice 10-22 November 1976, p. 175.

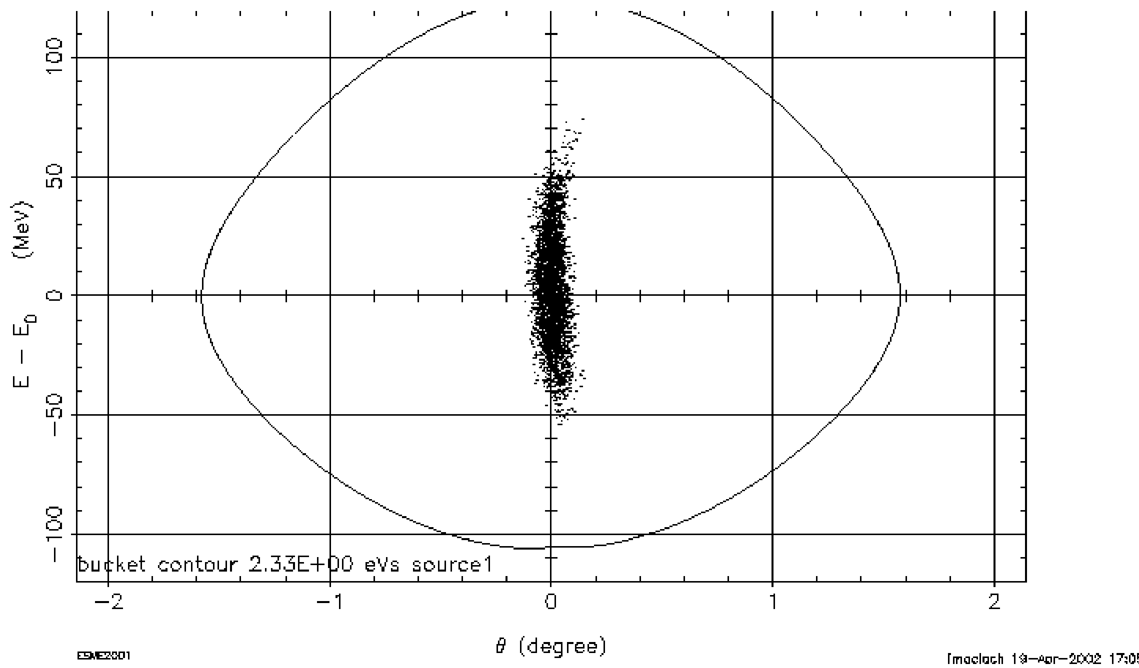

Figure 4.9. The phase space distribution of a bunch rotated with 1 MV of rf at the end of the minimum $\dot{p}$ ramp. The horizontal axis on this plot is just under 19 ns long; the units are $h = 1$ phase in degrees and energy in MeV. The momentum spread is about ± 0.8 %.

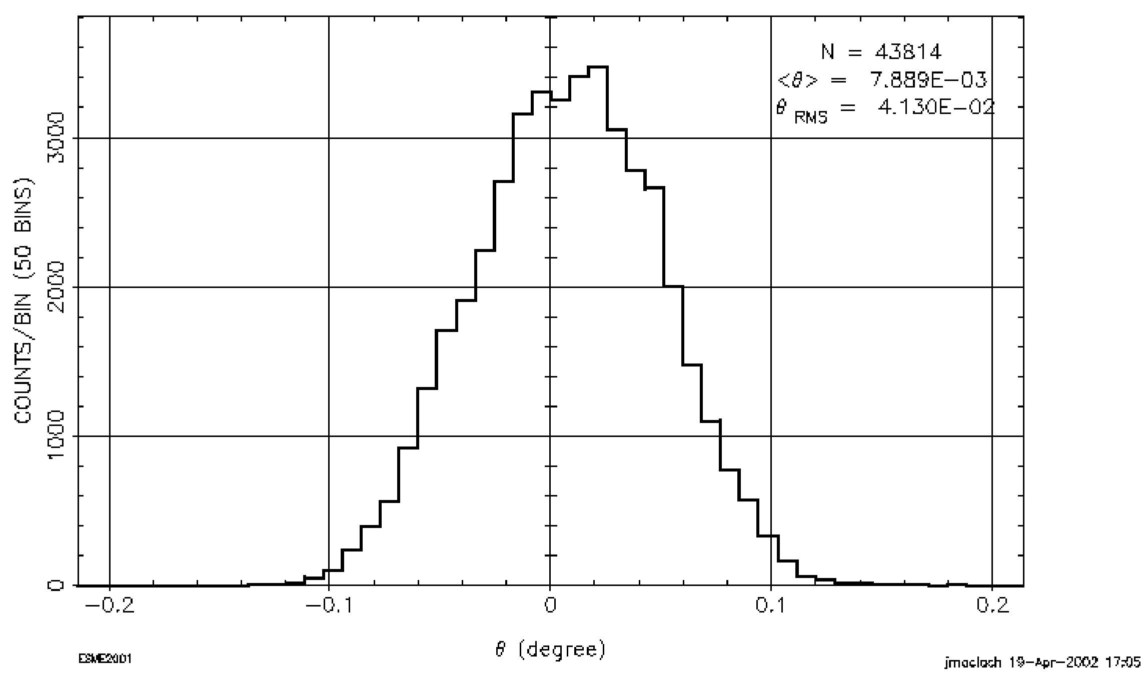

Figure 4.10. The bunch length profile plotted against h=1 phase in degrees; the horizontal axis corresponds to 1.9 ns.

Chapter 5. Technical Systems

5.1 RF

J. Griffin, J. Reid, D. Wildman

5.1.1 Accelerating rf System

Parameters for the PD2 8-GeV synchrotron are listed in Table 5.1.1. The required rf accelerating voltage per turn, $V\sin\varphi_s$, and the rf power delivered to the beam per turn, are derived directly from the rate of change of synchronous momentum, cp(t).

Table 5.1.1 Parameters for the PD2 8-GeV Proton Synchrotron

Mean orbit circumference	474.2	m
Cycle repetition rate	15	Hz
Injection kinetic energy	600	MeV
Extraction kinetic energy	8	GeV
Momentum acceptance (95%)	± 1%	
Harmonic number	84	
Occupied rf buckets	82	
Rf frequency range	42.0828 to 52.52	MHz
Protons per cycle	2.5×10^{13}	
Average rf power delivered to beam per cycle	444	kW
Injection longitudinal emittance per bunch (95%)	< 0.1	eV-s
Accelerated beam longitudinal emittance per bunch (95%)	< 0.2	eV-s
Transition gamma	13.82	

In Figure 5.1.1(a) the accelerating voltage $V\sin\varphi_s$, and the rf power delivered to the beam (as well as cp(t) and the kinetic energy T(t)), are shown for a sinusoidal 15 Hz magnet ramp. Figure 5.1.1(b) shows the same parameters for a 15 Hz magnet ramp to which a 12.5% second harmonic component has been added.

Addition of the second harmonic component to the acceleration ramp adds ~5 ms to the acceleration period, while reducing the peak amplitude of the rf power delivered to the beam from 1.42 MW to 1.06 MW. This distributes the power requirement more evenly over the cycle. The second type of the Robinson stability requirements in heavy beam loading conditions is that the power dissipated in the rf source be larger than that delivered to the beam. By distributing the beam power demand over the acceleration cycle, the rf cavity and amplifier dissipation may be equilibrated while still providing an adequate stability margin.

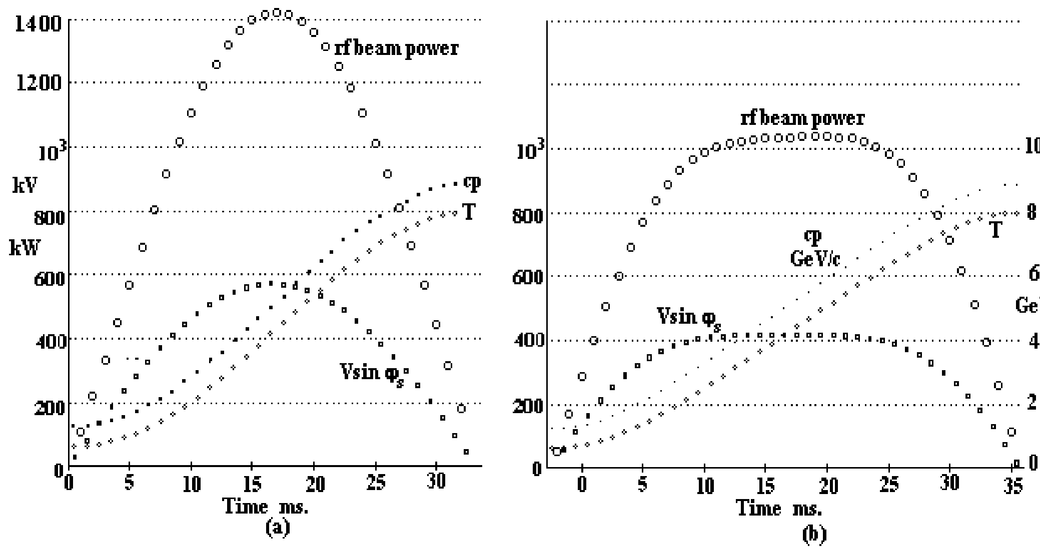

Figure 5.1.1. (a) and (b). Acceleration ramps without and with harmonic component.

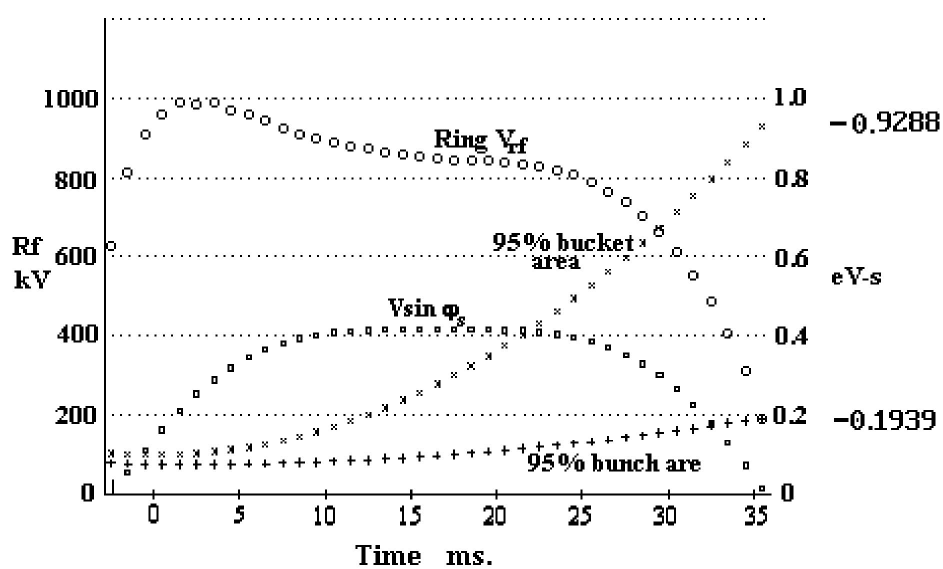

Figure 5.1.2. Rf ring voltage required for generating bucket area from 0.1 to 0.95 eV-s during the acceleration cycle.

In Figure 5.1.2 the ring rf voltage, rf bucket area, and an assumed bunch area consistent with ongoing simulation results are shown. For this calculation the plotted bucket-to-bunch area ratios and attendant bunch lengths are used to calculate the effect of space charge potential well distortion following injection. It is assumed that sufficient inductance has been introduced into the lattice so that the effective ring Z/n is inductive during acceleration, ranging from j30 Ω at injection to j5 Ω at extraction. The bunch longitudinal emittance reaches 0.19 eV-s at extraction. The plots are useful for evaluating cavity and amplifier performance at the maximum voltage point and at the maximum power demand point.

The peak rf ring voltage demand, ~ 1 MV per turn, occurs at about 5 ms (46.11.MHz). With twenty cavities, the effective voltage per cavity, V_c is 50 kV. The anode-to-each-gap voltage step-up ratio on the modified cavity is ~1.4 at 46 MHz. The effective cavity voltage is $V_c = 2V_g \sin(\Delta)$, where V_g is the voltage at each gap and 2Δ is the gap separation angle (136°). The step-up ratio from tube anode to effective gap voltage V_c is 2.6, so the anode rf voltage becomes 19.23 kV. The measured resonant anode load resistance of the modified cavities at 46 MHz is 5 kΩ, which transfers to effective cavity shunt impedance R_{sh} = 33.8 kΩ. The cavity power dissipation $V_c^2/2R_{sh}$ = 37 kW. At 46 MHz the accelerating voltage $V_c \sin\varphi_s$ is 253 kV (12.65 kV per cavity). With 50 kV gap voltage the phase angle $\varphi_s = 14.7°$.

With 82 of 84 buckets occupied with 3×10^{11} (4.88×10^{-8} Coulomb), the average dc beam current is ~2.25 A. The very small φ_s implies tightly bunched beam with large Fourier component. The Fourier component of rf beam image current i_i, will be ~4.5 A, capable of generating 152 kV at the effective cavity accelerating gap if the cavity is tuned to resonance. Through the use of a local phase-lock loop that compares the cathode drive current phase to the anode voltage phase, the cavities are detuned above beam resonance (below transition) so that a real load is presented to the power amplifier tube.

At 46 MHz the beam power requirement is 504 kW (25.4 kW per cavity). The amplifier grid bias, rf drive, and conduction angle may be set such that the anode dissipation is 120 kW. With correct detuning the amplifier will deliver 188 kW to a real load, with efficiency ~ 61%. Effective gap shunt impedance R_o representing the anode dissipation plus cavity losses is defined as $R_o \equiv V_c^2/2P_d$. An effective gap current representing total cavity losses, $i_o \equiv V_c/R_o$. The ratio of beam image current i_i to i_o is defined $Y \equiv i_i/i_o$. In this circumstance the detuning angle $\Theta = \arctan(Y\cos\varphi_s) = 34.7°$. The second of Robinson's criteria for beam loading stability is expressed in terms of these factors. The stability factor SF is required to be less than one. In this case SF = $Y\sin(\Theta)\cos(\Theta)/\cos(\varphi_s) = 0.347$.

At 23 ms (52.48 MHz), the beam rf power demand peaks at 1.039 MW (52 kW per cavity). At that point the ring voltage demand is 836 kV (41.8 kV per cavity), and $V\sin\varphi_s$ is 415 kV (20.8 kV per cavity). The phase angle φ_s is 29.8°. Again assuming that the power amplifier operating point is adjusted such that the anode dissipation is 120 kW, the detuning angle Θ becomes 31.9°. The amplifier delivers 198 kW at efficiency 62%. The stability factor SF = 0.37.

5.1.2 Large Bore (5-in diameter) Booster Cavity

The longitudinal bucket area and beam power requirements outlined above can be generated with reasonable efficiency and stability by the installation of twenty rf stations of the two-gap design presently installed in the FNAL Booster ring. The beam pipe aperture of the existing accelerating cavities is not adequate for the proposed accelerator. This problem has been addressed and modification of an existing cavity for larger aperture is well under way. [1] Measurements and specifications of the modified cavity are described in Chapter 5 of Ref. [2]. The modified cavities will use recently designed solid-state driver amplifiers. A discussion of the driver amplifier operation, with details of rf drive power, final amplifier screen power, and bias levels necessary to establish desired levels of anode efficiency and dissipation has been prepared by T. Berenc and J. Reid. [3]

The first welded prototype increased aperture cavity has been run at high power with two standard Booster tuners and one Main Injector tuner in the rf test station at MI-60. The high power tests were done without the required ceramic vacuum windows at each end of the cavity. This was a demonstration that the cavity would run with standard Booster frequency and anode voltage waveforms, making a nominal 55 KV peak accelerating volts (see Figure 5.1.3). The maximum voltage that can be achieved with this cavity is expected to be near 65 kV at 52 MHz due to a voltage breakdown limit of the existing ferrite tuner assembly. This limitation may be overcome by increasing the tuner stem connecting inductances, which will cause a slight reduction in the rf voltage at the tuners.

Detailed mechanical drawings for fabrication of a cavity that can be placed in the present Booster tunnel are being prepared. Most of the drift tube assembly has been detailed and dimension checking is presently under way before releasing drawings for fabrication of individual parts. The plan is to have one cavity assembled and ready for testing by late this year (2002). Six ceramic windows (two required per cavity) have been delivered and inspected.

At the relatively high beam current proposed in this upgrade, the most pressing problem in operation of the system will almost certainly be the longitudinal coupled bunch instability due to spurious resonances in the rf system or elsewhere in the ring. Special attention to spurious resonances will be required in the development of the modified aperture cavities. The double gap design of the cavities is particularly sensitive to end-to-end mode excitation, and careful design will be required to damp or eliminate this excitation mode. If these instability considerations can be overcome by a variety of damping techniques, there appears to be no serious barrier to successful installation and operation of these rf systems in the proposed accelerator upgrade scheme.

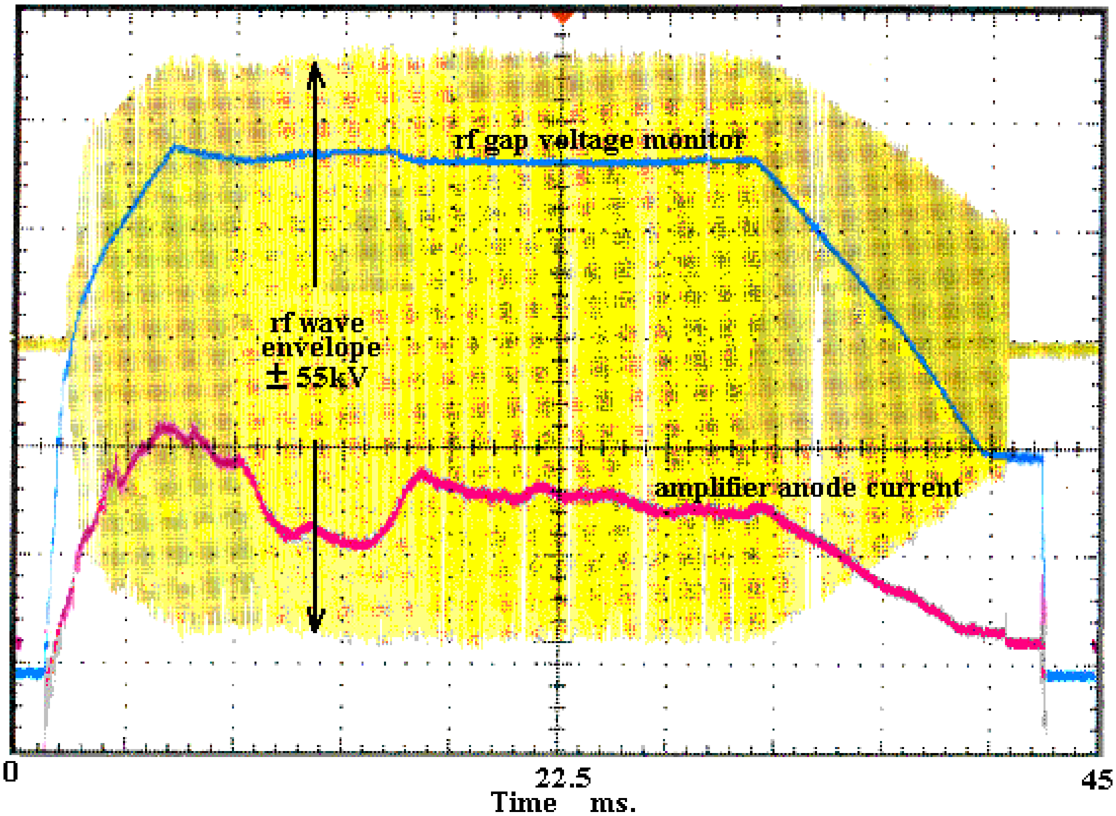

Figure 5.1.3. Large bore prototype cavity running a typical Booster waveform.

5.1.3 Passive Inductance Compensation for Space Charge Potential Well Distortion

In the present operation mode of the Booster approximately 65% of the beam loss on each cycle occurs within the 4-5 ms following injection. (This does not include another ~30% loss that occurs during the injection process.) It is conjectured that this loss results from a combination of transverse and longitudinal space charge effects. [4] It appears likely that this loss mode could increase to an unacceptable level with the proposed beam intensity increase. It has been proposed that longitudinal space charge potential well distortion effects can be eliminated through intentional introduction of inductance into the lattice. [5] Simulation studies of an earlier version of a high intensity proton driver (cf. Ref. [2], Ch.5-8, 9) have indicated that a dramatic reduction of losses during injection and acceleration are possible with insertion of appropriate values of inductance. The proposition has been tested experimentally in the LANL 800 MeV Proton Storage ring (PSR), and in the KEK 12 GeV proton synchrotron. [6,7] In each case dynamical predictions regarding effective rf focusing force were found to be correct.

The PSR operates at harmonic number one and rotation period ~358 ns, with gated injection bunches ~300 ns. The introduced inductance consisted of two tanks of $M_4C_{21}A$ Toshiba ferrite, each containing 30 cores and presenting inductance ~4 µH. This was originally thought to be about two-thirds of the inductance necessary to compensate exactly for the space charge induced longitudinal field seen by particles in the bunch. The goal of the exercise was to reduce particle leakage from the rf buckets into the space between bunches, where free protons may interact with trapped electrons causing e-p instability. The focusing force enhancement by the inductance is the result of interaction of the line charge derivative of the beam bunch with the inductance. The inductive reactance must be effective over a frequency range defined by the Fourier components of the charge distribution. Because of the relatively low rotation frequency and long bunches the frequency response of the introduced ferrite was well matched to the requirement.

The initial results of the exercise were sufficiently encouraging so that continued routine operation of the PSR with the installed inductances was initiated. However, at substantially increased intensity it was found that the inserts introduced a severe self-bunching instability near 72 MHz, preventing continued operation in this mode. Careful study of an equivalent ferrite geometry reveals a TM_{01} radial transmission line resonance near 84 MHz with Q ~ 4-5.

It has been further established that heating the ferrite to ~130° C increases the imaginary part of the permeability $j\mu''$ and reduces the Q of the resonance to a level near 1.5 - 2, at which level the PSR can be operated successfully. An added and serendipitous effect is that the required heating also increases the real part of the permeability μ' such that the introduced inductance equals or exceeds that necessary for exact compensation. The result is that the roughly rectangular injected charge distribution creates, in addition to the rf system field, self generated longitudinal barriers at each end of the injected distribution such that the length and amount of injected beam can be increased to near the rotation period. The net result is that the PSR is now capable of operation at a level near 9.6 μC per cycle, ~40% larger than the goal of the most recent rf system upgrade. [8]

In an initial attempt to address the cause of beam losses observed during the Fermilab Booster cycle, two inductive inserts similar to those in the PSR have been installed in the Booster. It is known, of course that, because the Booster accelerates from 400 MeV to 8 GeV using a harmonic number of 84, the frequency response of the introduced ferrite will not be well matched to the Fourier components of the beam.

Nevertheless, as a first step in evaluating their usefulness, it has been decided to install two inserts similar to those installed in the PSR. This is expected to compensate ~20% of the estimated space charge forces near injection. One real concern is the possibility that the inserts may excite a coupled-bunch instability driven by the known TM_{01} resonance at 73 MHz. At beam intensities up to 4.6×10^{12} no evidence has been observed of unusual signals near 73 MHz on the Booster resistive wall monitor. Unfortunately, no discernable improvement has been seen in the initial beam losses since the introduction of the inductive inserts in the Booster. One possible explanation is that the inductance of the two inserts is too low (about 10 μH) to show any effect. Six to eight more inserts will be added in the next step.

The PD2 is an ideal candidate for inductive inserts since the proton intensity will be five times greater than the present Booster. An R&D effort should be started to identify alternative higher frequency ferrites that would be a better match for the shorter PD2 bunches.

References

[1] J. Griffin, "Proposal to Rebuild Damaged Booster RF Cavity with Significant Improvement in Aperture, Gap Voltage, and Power Delivery Capability)," (1999).

[2] "The Proton Driver Design Study," FERMILAB-TM-2136 (Dec. 2000).

[3] T. Berenc and J. Reid, "A Solid-State Driven Power Amplifier Design for the Booster RF Cavities)," RFI Technote 023, (8-2001).

[4] M. Popovic and C. Ankenbrandt, "Space Charges in the Fermilab Booster," Space Charge Tune-Shift Workshop, AIP Proc. 448, 128, (1998).

[5] A. Sessler and V. Vaccaro, "Passive Compensation of Longitudinal Space-Charge Effects in Circular Accelerators - The Helical Insert," CERN 68-1, ISR Div. (1968).

[6] K. Koba et. al. "Longitudinal Tuner Using High Permeability Material," R.S.I. 70-7 (1999).

[7] J. Griffin, K.Y. Ng, Z.B. Qian and D. Wildman, "Experimental Study of Passive Compensation of Space Charge Potential Well Distortion at the Los Alamos National Laboratory Proton Storage Ring," Fermilab FN-661, (1977).

[8] R.J. Macek et. al, "Electron Proton Two-Stream Instability at the PSR," 2001 PAC Proceedings, Chicago, p.688, 2001.

5.2. Magnets

V. Kashikhin, A. Makarov and J. -F. Ostiguy

In the first design study (referred to as Study I) published in December 2000 [1], the Proton Driver was envisioned to be a machine capable of delivering 1 MW of beam power at 16 GeV. The design parameters assumed in this new study are more modest: 380 kW at 8 GeV. From a magnet standpoint, the principal change is a reduction in the good field aperture requirement from 12.7 cm $\times$ 22.86 cm (5 in $\times$ 9 in) to 10.16 cm $\times$ 15.25 cm (4 in $\times$ 6 in). This reduction leads to smaller magnets, lower overall stored magnetic energy and reduced operating costs. In Study I, we chose a special water-cooled stranded cable to suppress eddy currents in the conductors. While this remains an interesting solution, stranded cable is expensive. Furthermore, the technology for making electrically and mechanically reliable joints with this type of conductor is not well-established. For this iteration, we revisited our choice and concluded that conventional water-cooled conductor coils can be used. Both fabrication technology and costs are well-understood; the compromise is reduced operation efficiency.

One of the principal considerations in designing a high intensity proton synchrotron is to limit space charge induced tune shift and tune spread in order to ensure dynamic stability. This is accomplished in two ways: by keeping the machine circumference small and by spreading out the proton distribution transversely. The former strategy implies rapid cycling; the latter implies large aperture.

Aperture is a principal cost driver since magnet overall size, fabrication costs and power consumption and power supply costs are directly proportional to stored magnetic energy. Aperture is determined not only by space charge considerations, but also by the type of vacuum pipe employed. Additional aperture margin may also be needed to keep losses at a level compatible with safety requirements. Because of very substantial eddy current induced losses, a conducting beam pipe cannot be used. One possible solution is a ceramic beam tube with very thin conducting strips disposed on the inner surfaces to minimize beam impedance. This approach is costly in terms of physical aperture because ceramic walls have to be considerably thicker than metallic walls for mechanical reasons. The Proton Driver magnets use a strategy employed for the Fermilab Booster magnets : the entire magnet is put inside an evacuated enclosure. One drawback is that special care is needed in order to achieve satisfactory vacuum. This is important since beam loss induced activation is an important issue for a high intensity machine.

The Proton Driver is based on a separated function lattice with dipoles and quadrupoles on a common bus. The presence of a large energy dependent space charge tune shift and tune spread dictates the need for tight tune control during the entire acceleration cycle. For this reason, dipole/quadrupole tracking errors are a special concern. A tracking error is equivalent to momentum offset error and results in a tune shift of magnitude

$$\Delta\nu = \xi_{\text{uncorrected}} \left[\frac{\Delta G}{G} - \frac{\Delta B}{B} \right] = \xi_{\text{uncorrected}} \left[\frac{\Delta(G/B)}{(G/B)} \right] \tag{5.2.1}$$

where $\frac{\Delta G}{G}$ and $\frac{\Delta B}{B}$ are respectively the relative gradient and main dipole field errors. Note that the tune variation is proportional to $\xi_{\text{uncorrected}}$, the *uncorrected* chromaticity because, in the context of a quadrupole tracking error, there is no closed orbit error and the chromaticity correction sextupoles have no effect.

The magnitude of the tolerable tune shift is debatable. In the context of this study, we *conservatively* demand

$$\Delta\nu < 0.01 \tag{5.2.2}$$

during the *entire* cycle. This requirement is based on the ISIS experience, where the ability to control the tune at that level proved to be necessary to avoid specific resonances at extraction. It is conceivable that criterion (5.2.2) can be relaxed. Problematic resonances could be avoided; furthermore, space charge forces scales as $1/\gamma$ and tracking should be less critical an issue as time progresses during the acceleration cycle. Detailed simulations which are beyond the scope of this study would be necessary to validate relaxed tune control requirements.

Some rapid cyclic machines, like the Fermilab Booster, use combined function magnets to economize space. Good tracking is naturally obtained by operating far away from saturation (below 1 T). As already mentioned, the Proton Driver employs separate function magnets with bending dipoles operating at an aggressive 1.5 T peak field. The field strength is determined by two requirements. First, the circumference ratio between the Main Injector and the Proton Driver should be a simple rational fraction to allow synchronous beam transfers. Second, the total circumference should be as small as possible in order to minimize the space charge tune shift. While magnet transfer functions start deviating from linearity above 1 T, quadrupole and dipole magnets can be designed with matched saturation behaviors. The residual tracking error (on the order of a percent or two) is handled by an independently powered active quadrupole correction system. This system also has the ability to compensate for the tune shift dependence on energy during acceleration. Note that above 1.5 T, good dipole/quadrupole matching rapidly becomes more difficult.

5.2.1. Dipoles

The Proton Driver dipole is a conventional H-magnet design. Field homogeneity is preserved at high excitation by profiled pole edges and by the presence of circular holes in the center of the poles. The lamination cross-section is shown in Figure 5.2.1; a list of relevant parameters is presented in Table 5.2.1. The dipoles are excited so as to produce a magnetic field strength of the form

$$B(t) = B_0 - B_1 \cos(\omega t + \phi) + 0.125 B_1 \sin(2\omega t + 2\phi) \tag{5.2.3}$$

Table 5.2.1. Proton Driver II Main Dipole Magnet Parameters

Peak Dipole Field	1.5	Tesla
Good Field Aperture	101.6×152.4	mm^2
Physical Aperture	101.6×273.1	mm^2
Field Homogeneity	± 0.0005	
Magnet Length	5.72	m
Cycle Frequency	15	Hz
Peak Current	5170	A
Conductor Dimensions	20.2×15	mm^2
Conductor cooling hole diameter	10	mm
No of turns/pole (3 conductors & top/bottom coils in parallel)	12	
Lamination Thickness	0.35	mm
Lamination Material	Si-Fe M17	
Inductance	18	mH
DC Resistance	4.7	mOhm
Stored Energy	0.063	MJ
Coil Losses	115	kW
Core Losses	16.3	kW
Core mass	37,000	kg
Peak Terminal Voltage	4.85	kV
Water Pressure Drop	10	bar
Water Flow	1.7	l/s
Water Temperature Rise	17	deg C

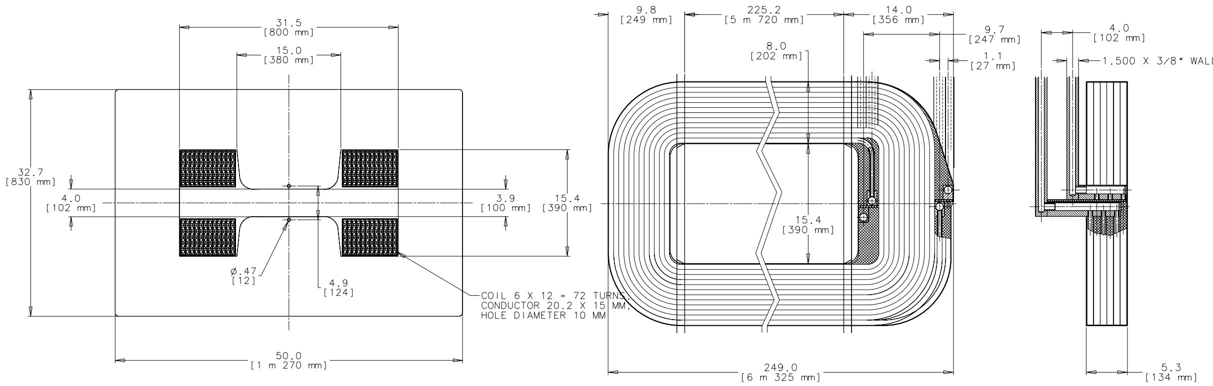

Figure 5.2.1. Proton Driver dipole cross-section and coil detail. Note the circular holes in the center of the poles. Note also the parallel connections at one of the coils extremities.

where B_0 is the injection field, B_1 is the magnitude of the fundamental component, $\omega/2\pi = f = 15$ Hz and *phi* is a constant phase factor. The second harmonic component is introduced to reduce the maximum value of dB/dt. Since the instantaneous RF accelerating voltage is proportional to dB/dt, the peak voltage required from the RF system cost is reduced, resulting in a substantial reduction in RF system costs. The magnetic field ramp and its derivative are shown in Figure 5.2.2.

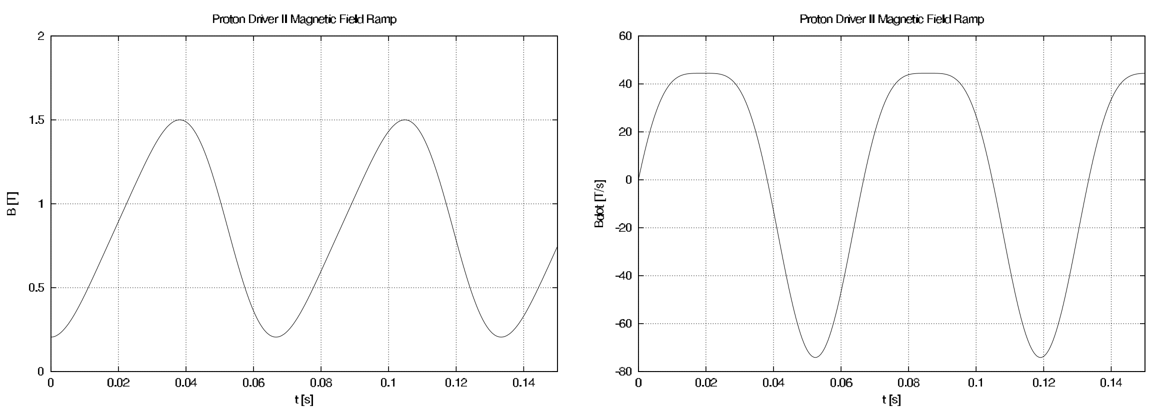

Figure 5.2.2. Magnetic field ramp and its derivative for 8 GeV operation ($B_0 = 0.853$ T, $B_1 = 0.629$ T).The RF accelerating voltage is proportional to the derivative of the magnetic field. The maximum of the derivative occurs on the down ramp. This value determines the maximum magnet terminal voltage although no beam is accelerated at that time.

In an iron dominated dipole, good field homogeneity can be achieved over the entire extent of the physical vertical aperture, that is, all the way to the pole surfaces. However, field homogeneity over the horizontal extent of the aperture requires a certain amount of pole overhang. For a given field homogeneity, the required horizontal extent of the physical aperture is minimized by shimming the pole pieces edges. A wide variety of shim geometries are possible. The optimality of a design can be accessed by comparing the achieved physical horizontal extent to a theoretical estimate developed by Klaus Halbach [2]. Referring to Figure 5.2.3, assume the origin of the x-axis is situated exactly at the pole edge and that the pole continues to infinity for $x > 0$. At any fixed horizontal position x and, in particular at $x = 0$, the complex field is an even function of the vertical position y can be expanded in a Fourier series of the form

$$H_y + jH_x = \sum_{n=-\infty}^{\infty} C_n \exp \frac{n\pi z}{g} \tag{5.2.4}$$

where g is the total vertical gap, the C_n are complex constant coefficients and $z = x + jy$. Since the field is finite, the coefficients C_n vanish for $n > 0$ and $C_0 = H_{y0}$ represents the field deep into the aperture region. Let d be the the pole overhang, as defined in Figure 5.2.3. Without shims, the first few low order harmonics dominate the field deviation from uniformity. Considering only the first $(n = -1)$ harmonic, the field error at the edge of the good field region is

$$\frac{\Delta B}{B} = \frac{\Delta H_y}{H_{y0}} \simeq \frac{1}{H_{y0}} \Re\{C_1\} = h_1 \exp \frac{-\pi d}{g} \tag{5.2.5}$$

With no shim, the first spatial harmonic dominates. A properly designed shim should suppress the first harmonic and the second harmonic dominates. Using these results, Halbach found that a simple two-parameter empirical relation of the form

$$\frac{\Delta B}{B} \simeq \lambda_1 \exp \frac{-\lambda_2 d}{g} \tag{5.2.6}$$

is generally an adequate predictor of field homogeneity. The values of λ_1 and λ_2 depend weakly on the pole geometry and are obtained by fitting results obtained numerically from two-dimensional calculations. Figure 5.2.1. shows the predicted amount of overhang necessary to achieve a field homogeneity $\frac{\Delta B}{B}$ for both shimmed and unshimmed magnets. For a given homogeneity, the amount of required overhang increases proportionally to the magnet gap. Thus, any increase in vertical aperture of the magnet – e.g. to accommodate a thick ceramic vacuum pipe – would result in a proportional increase in overall horizontal size. Figure 5.2.5 presents calculated field homogeneities achieved by the Proton Driver II dipole magnet. For this magnet, the ratio $d/w \simeq 0.6$ and we note that the achieved homogeneity is consistent with the prediction from Halbach's formula.

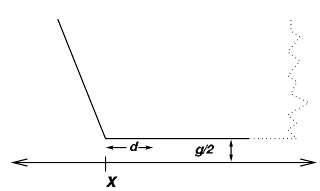

Figure 5.2.3. Idealized semi-infinite dipole magnet with pole overhang d and full gap g. The horizontal origin is exactly at the outer edge of the pole.

In a rapid cycling magnet, the presence of eddy currents is a source of potential technical difficulties. Eddy currents are induced both in the magnetic core and in the conductors. Eddy currents in the core are largely suppressed by the laminated core construction which

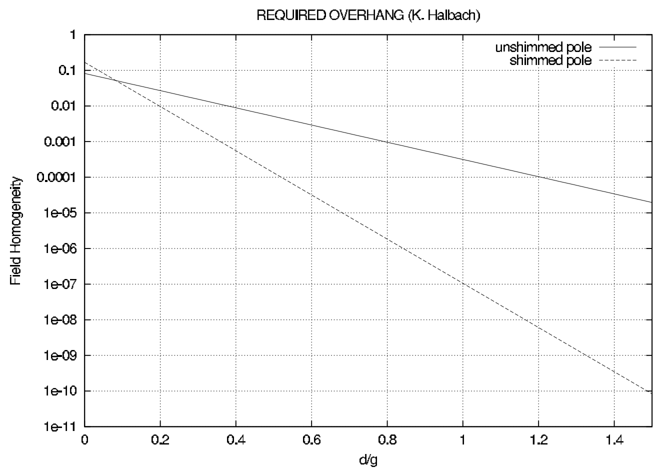

Figure 5.2.4. Amount of overhang required to achieve a given homogeneity as predicted by Halbach's formula.

impedes their flow in the longitudinal direction. As long as the lamination thickness is smaller than the skin depth, the principal effect of eddy currents in the core is to increase losses.

The Proton Driver magnet cores are assembled from 0.014 in (0.35 mm) thick isotropic Si-Fe laminations (M17 or M19). This material has a substantially higher resistivity than the low carbon steel used in low repetition rate synchrotron magnets. It offers a reduced coercivity which helps minimize remanent fields at injection. The main drawbacks are reduced high field permeability and saturation magnetization. At 15 Hz, the skin depth in electrical steel is $\delta \simeq 1$ mm = 0.040. One might question why even thinner laminations are not used. The answer is that very thin laminations are hard to handle and complicate the magnet assembly process. Furthermore, since laminations are coated with an insulator, thin laminations result in magnets with a less favorable stacking factor.

Core losses are difficult to compute and are usually estimated from experimental data. Virtually all data commonly supplied by manufacturers corresponds to measurements performed with a sinusoidal excitation at 50 or 60 Hz. Not only does the Proton Driver operate at 15 Hz, but the excitation also has a non-zero average component I_0, which renders the hysteresis loops asymmetric. As a reference, careful measurements were performed on a small core made out of M17 laminations. The results are summarized in Figure 5.2.7. For 0.014 in thick laminations with a DC bias equal to 50% of the maximum (1.5 T) field amplitude, the measured losses are on the order of 0.2 W/lb (0.44 W/kg).

Eddy currents induced in conductors are potentially problematic. Assuming that the total current circulating through each conductor is externally constrained, the sum of the induced currents over the conductor cross-section must add up to zero. However, the current distribution is not uniform, resulting in higher losses, or equivalently in a higher effective resistance. As long as the non-uniformity of the current distribution does not affect the

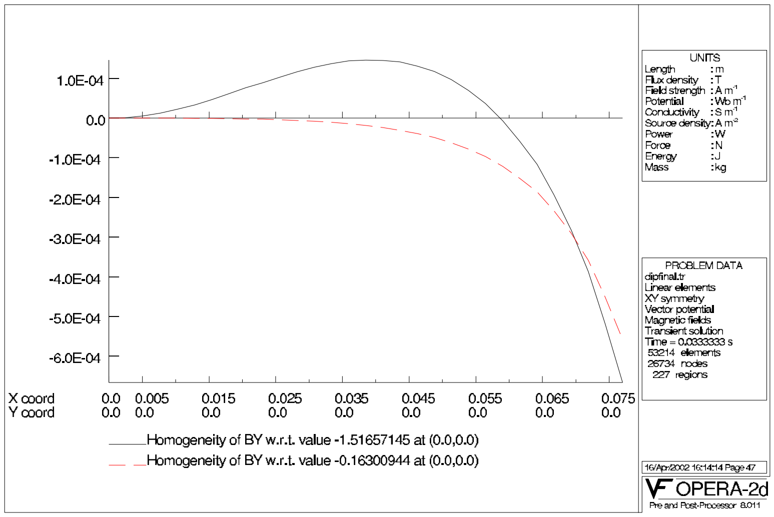

Figure 5.2.5. Proton Driver dipole field homogeneity at minimum and maximum excitations.

field homogeneity, the main issues are providing adequate cooling and minimizing operating costs.

For a rectangular conductor immersed in a uniform time-varying magnetic field $B_0 \sin(\omega t)$, it can be shown that the power losses are given by

$$P = \omega^2 B_0^2 A a^2 / 16\rho \tag{5.2.7}$$

where A is the conductor area, a is the conductor width and ρ is the resistivity. Eddy currents can be reduced either by reducing the conductor cross-section or by reducing the magnetic field in which it is immersed. Reducing the conductor area increases the number of turns N and therefore the magnet terminal voltage, since the inductance scales like N^2. To keep the voltage at a reasonable level it becomes necessary to connect multiple turns in parallel. The Proton Driver magnet coils use groups of three conductors connected in parallel. In addition, the coils from the top and bottom coils are also connected in parallel. The electrical and mechanical connections in the end regions are shown in detail in Figure 5.2.1. Note that the conductors are not transposed. Although transposition would reduce losses slightly, it would also render connections in the end region very complex and cumbersome.

In Study I, eddy current power loss problems were completely side-stepped by the use of a special water cooled stranded conductor. Because of the small strand cross-section, eddy currents where reduced to the level of a minor perturbation and could essentially be ignored. Aside from the technology required to produce reliable electrical and mechanical joints, the main drawback of the stranded conductor is its high cost, about an order of magnitude more expensive than conventional copper conductor. For this study, the possibility of using conventional solid water cooled conductors has been revisited. Figure 5.2.7 presents the result of an eddy current computation.

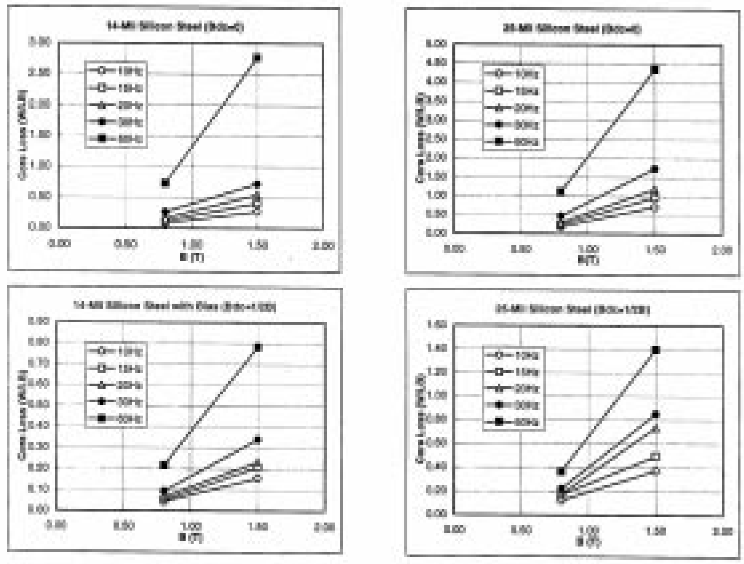

Figure 5.2.6. M17 Electrical steel loss measurements for 14 mil (0.35 mm) and 25 mil (0.64 mm) laminations. The measurements were performed from 10 to 60 Hz, with and without a 50% DC bias in the excitation.

Eddy current losses reach a substantial level in the conductors closest to the edge of the pole, in the fringe field region. To take advantage of the fact that the magnetic field is predominantly vertical in that region, a rectangular (as opposed to square) conductor is employed. Relatively high losses affect approximately 20% of the total coil cross section; however, localized heating should be prevented by good thermal contact between conductors. The relatively uniform coil temperature will determined by the total average power dissipation over the entire coil area. As already mentioned, conventional water-cooled solid copper coil is a well-understood technology. Compared with stranded conductors, the trade-off is reduced operational efficiency vs reduced up-front fabrication costs.

It is worth mentioning that in principle, the lossier conductors could be moved away from the highest field region. This can be accomplished by increasing the width of the area available for the coil or by constructing a specially shaped coil. Because of time constraints, this possibility was not explored. The solution adopted results in the simplest, easiest to fabricate coils.

5.2.2. Quadrupoles

The Proton Driver quadrupoles are four-fold symmetric magnets. The cross-section is shown in Figure 5.2.8. Both horizontal and vertical focusing quadrupoles are identical and the aperture radius is set to accommodate a rectangular good field region of the same size as the dipoles'. A common current bus is used to make the quadrupole gradient and

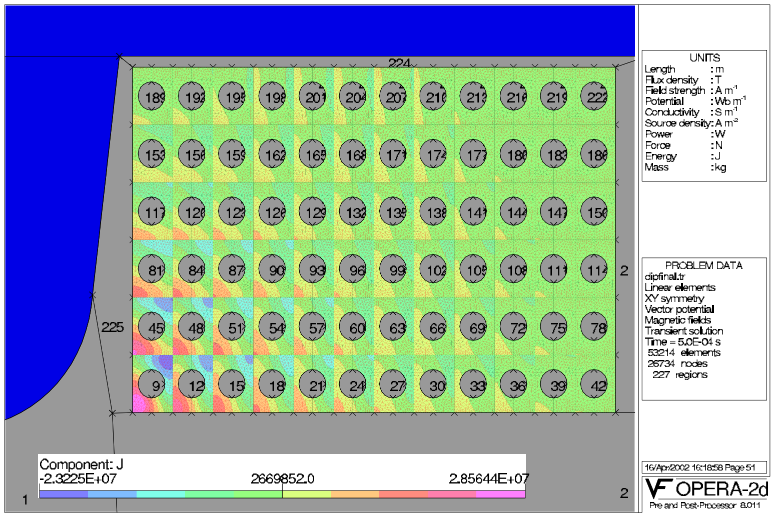

Figure 5.2.7. Eddy current distribution in the conductors. Note that the distribution is most uneven in conductors located near the pole edge.

dipole strength track dynamically. The number of turns and length of the quadrupole are selected so as to match optical and physical requirements at low field. In addition, at high field, the gradient/dipole strength ratio must remain as constant as possible. This requirement effectively limits the maximum achievable gradient. For the required aperture, when the quadrupole pole tip field reaches 0.84 T, the field at the edges of the truncated hyperbolic profile reaches approximately 1.5 T, and saturation begins to affect the linearity of the relation between quadrupole strength and excitation. Note that saturation in backleg region also affect nonlinearity; however, this effect can in principle be controlled by adjusting the backleg width. Note that for a four-fold symmetric quadrupole saturation does not adversely impact field quality since all harmonics except those of order 4n (8n-pole) are suppressed: the first allowed harmonic is the 12-pole. Figure 5.2.9 is a plot of the tracking error as a function of the excitation current. At 8 GeV, the deviation is on the order of 2.0%.

5.2.3. Other Magnets

The Proton Driver II sextupole magnets are six-fold symmetric with an aperture radius sufficient accommodate a rectangular region of dimensions 10.16×15.25 cm^2. They are grouped in families powered with independent programmable power supplies. No particular difficulties are anticipated.

Operational experience with machines such as ISIS demonstrates that in addition to good tune control, good orbit control during the entire acceleration cycle is one of the keys to loss minimization. This is not entirely surprising since small orbit changes typically result in small tune perturbations caused by change in overall orbit length and quadrupole

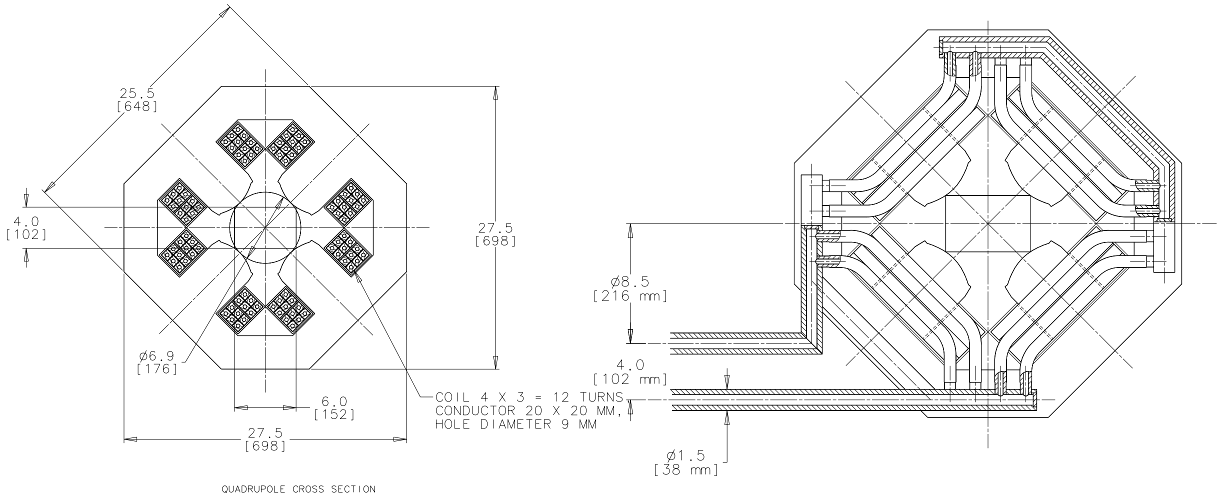

Figure 5.2.8. Proton Driver II quadrupole cross-section and coil detail.

Table 5.2.2. Proton Driver II Quadrupole Magnet Parameters.

Peak Gradient (8 GeV)	9.5626	Tesla/m
Pole Tip Field (8 GeV)	0.84	Tesla
Gradient Homogeneity	± 0.001	
Aperture (Inscribed circle radius)	8.8	cm
Peak Current	5170	A
Steel Length (F & D)	1.2	m
No of Turns/pole	6 (2 cond in parallel)	
Inductance	1.3-1.5	mH
Conductor Dimensions	20×20	mm^2
Conductor cooling hole diameter	9	mm
Coil Losses	31	kW
Max Terminal Voltage	0.4	kV
Lamination Area	0.24	m^2
Lamination Thickness	0.35	mm
Lamination Material	Si-Fe M17	
Core mass	2200	kg
Core losses	1	kW
Water Pressure Drop	10	bar
Water Flow	0.32	l/s
Water Temperature Rise	23	deg C

feed-down in sextupoles. The Proton Driver has a full complement of correctors and no particular difficulties are anticipated in building satisfactory magnets.

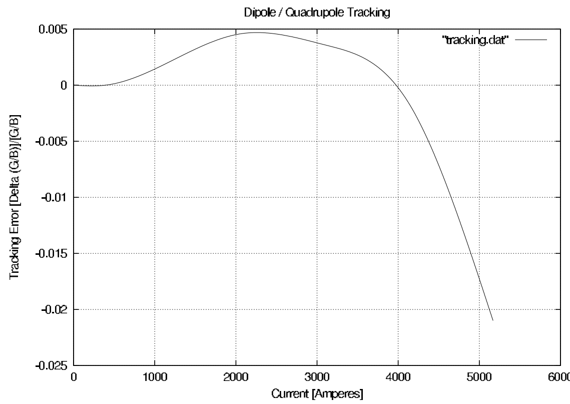

Figure 5.2.9. Normalized Quadrupole/Dipole strength tracking. At 8 GeV (common bus current of 5170 A), the deviation is approximately 2 %. This error is compensated by an independent active correction system.

5.2.4. AC Magnetic Measurements

Henry Glass

The goal of magnetic measurements for the proton driver dipole is to verify field homogeneity at 15 Hz operation. The usual tool for measuring field quality is the rotating harmonics coil. This is usually operated in DC mode; however there is some experience at Fermilab in using such coils to collect AC data. The most direct experience is in measurements of Booster gradient magnets being done in April-May of 2002. In this case a coil of length 1.0 m is installed within the magnet aperture to sample the field quality at various locations, e.g., within the body or at the magnet ends. Custom fixtures are built to support the probe at these locations. The coil has a tangential winding to measure the multipole components, and two pairs of bucking coils to subtract out dipole and quadrupole components. For the proton driver magnet, the situation is simplified by the use of separated function dipoles rather than gradient magnets. In dipoles, there is a greater tolerance of small probe positioning errors. Also, one only needs a pair of dipole bucking windings in addition to the tangential winding. Because of magnet sagitta, it is preferred to use a short coil with length in the range 0.5 - 1.0 m, rather than attempt to build a coil as long as the magnet. In this case, one sacrifices the ability to use the coil to measure total integrated field strength. However, one can measure the total strength using either a stretched wire system or, preferably, a coil wound on a rigid curved form matching the magnet axis curvature. The rotating coil diameter should be chosen as large as possible to have maximum sensitivity to high order harmonics. The constraint is the vertical aperture of 101.6 mm; the probe should be undersized by a few mm to allow for free rotation and probe support fixturing. Since the horizontal aperture is larger (152.4 mm), it is necessary to position the probe not only at the aperture center, but also displaced horizontally at about plus and minus 50 mm from the center to map the entire good field region.

Figure 5.2.10. AC Magnetic Measurement Setup used for a Booster Combined Function Magnet.

5.2.5. Research and Development

High voltage operation is a serious concern. The dipole magnets have a maximum terminal voltage on the order of 5 kV; in the proposed resonant configuration, the maximum voltage to ground reaches approximately 3.3 kV. Electrical insulation is an important issue for magnet long term reliability. Fermilab currently has limited experience with high voltage magnet fabrication and operation. Insulation weaknesses generally need to be spotted experimentally and corrected by trial and error; this can be both tricky and time-consuming. The ISIS synchrotron in operation at Rutherford Lab in the UK has been operating reliably at a significantly higher voltages ($\simeq$ 10 kV) than those envisioned for the Proton Driver. Active collaboration and exchanges with RAL would likely be beneficial.

Another source of concern in the fact that the entire magnet is be placed inside an evacuated enclosure. Special precautions will be needed during the assembly process to avoid degassing that would lead to poor vacuum.

The presence of metallic strips to reduce the beam impedance will perturb the field. While the perturbation can probably be predicted reliably through calculation, it should be carefully measured.

The new Proton Driver lattice uses two types of dipoles. The shortest one is approximately 1 m (1.06 m) long and would make a good candidate for an R&D prototype. Building such a magnet would lead to better understanding of coil fabrication high voltage insulation, and vacuum issues. Furthermore, power loss estimates and cooling effectiveness could be confirmed.

Although we opted not to use stranded water-cooled conductors in the context of this second study, this type of conductor remains an interesting option for rapid cycling synchrotrons. An R&D program should address the problem of making reliable electrical and mechanical joints and other aspects of coil fabrication using water-cooled stranded cable.

Finally, an interesting avenue for future R&D would be an investigation of super-ferric magnet technology. In recent years, a new generation of Nb-Ti superconducting cable has been developed for applications in power generation and transmission. The cable has insulated filaments with a diameter as small as 0.1 μm embedded in a Cu-Ni alloy matrix. Superconducting coils would result in substantial savings in overall magnet size and power consumption; these savings may be substantial enough to offset the additional costs and complexity engendered by the cryogenic system.

5.2.6. References

[1] The Proton Driver Design Study, Fermilab TM-2136, December 2000.

[2] A.W. Chao and M. Tigner Eds., *Handbook of Accelerator Physics and Engineering*, World Scientific, 1999.

5.3 Power Supplies

C. Jach, D. Wolff

In this section are described the power supplies required for the PD2 8-GeV synchrotron. A resonant network powers the main dipoles and quadrupoles of the synchrotron. The design is similar to that in Chapter 7, Ref. [1], namely, a dual-harmonic resonant system. It is a 15-Hz resonant circuit with a 12.5% second-harmonic (30-Hz) component. A detailed description of the system can be found in Ref. [1]. The dual-harmonic magnet current and voltage waveforms are shown in Figure 5.3.1.

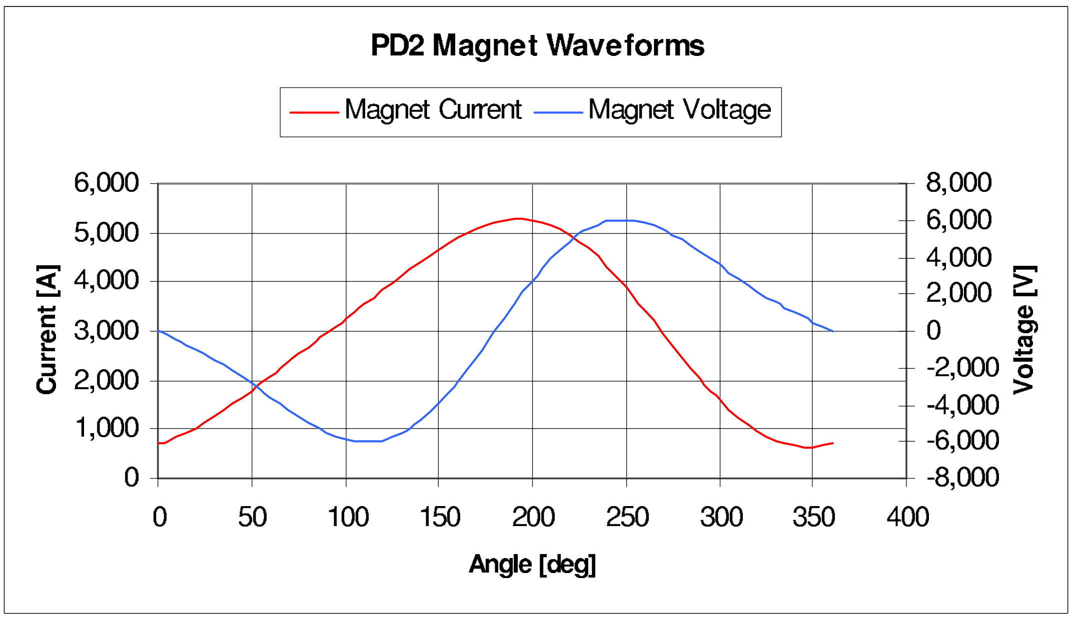

Figure 5.3.1. Magnet current and voltage waveforms.

This network consists of:

a. 10 resonant circuit cells with 1 long dipole, 1 short dipole, and a set of quads (D and F) with total inductance of 25.1 mH.
b. 10 resonant circuit cells with 1 long dipole, and 2 sets of quads with total inductance of 27.9 mH.
c. 2 resonant circuit cells with 7 sets of quads with total inductance of 19.6 mH

Each resonant circuit cell consists of an equivalent magnet (L_m), a main choke (L_{ch}), a main capacitor bank (C), an auxiliary choke (L_1), and an auxiliary capacitor bank (C_1). All resonant circuit cells are connected in series. Power supplies are inserted into the resonant network at or near virtual ground points. Figure 5.3.2 shows a typical resonant circuit cell. Table 5.3.1 lists the inductance and dc resistance of the magnets. Table 5.3.2

are the parameters of the power supply system. Figure 5.3.3 shows the dual-resonant frequencies at 15 and 30 Hz of this system.

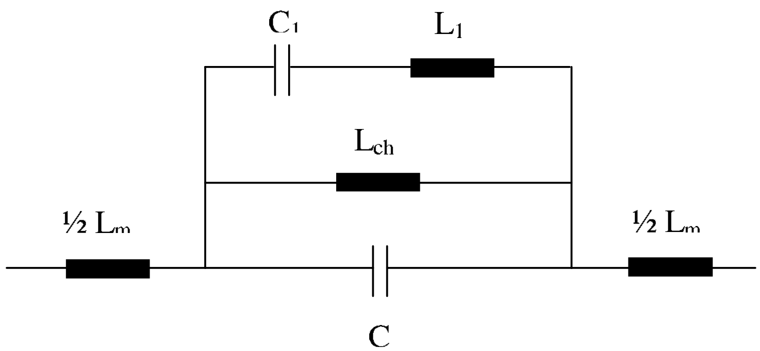

Figure 5.3.2. Typical resonant cell diagram.

Table 5.3.1. Magnet Load Parameters

Parameter	Unit	Value
Dipole, B1		
Length	m	5.646
Inductance	mH	18.9
DC resistance	mΩ	4.7
Total number		20
Dipole, B2		
Length	m	1.188
Inductance	mH	3.4
DC resistance	mΩ	0.9
Total number		10
Quadrupole, QF		
Length	m	1.261
Inductance	mH	1.5
DC resistance	mΩ	2.2
Total number		44
Quadrupole, QD		
Length	m	1.126
Inductance	mH	1.3
DC resistance	mΩ	2.2
Total number		44

Table 5.3.2. Main Magnet Power Supply Parameters

Parameter	Unit	Value
Magnet current:		
- peak	A	5,200
- dc	A	3,000
- ac, 15 Hz	A	2,200
- ac, 30 Hz	A	280
Total magnet inductance	H	0.535
Total magnet DC resistance	Ω	0.297
Magnet peak voltage to ground	V	3,050
Magnet peak stored energy	kJ	7,200
Number of resonant cells		22
Resonant cell main choke peak stored energy	kJ	318
Resonant cell aux. choke peak stored energy	kJ	72
Resonant cell main capacitor bank peak stored energy	kJ	133
Resonant cell aux. capacitor bank peak stored energy	J	107
Power supply voltage, peak	V	±2,000
Power supply current, peak	A	5,200
Number of power supplies		4

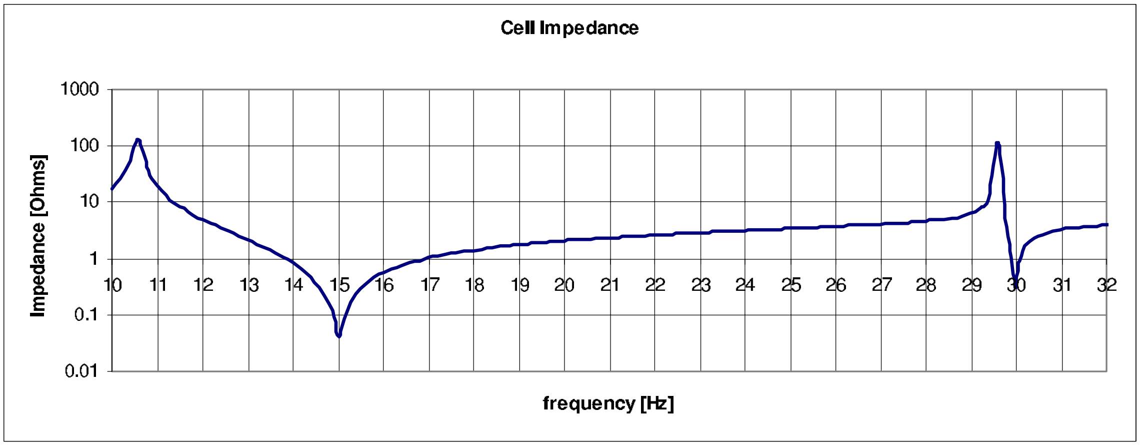

Figure 5.3.3. Single cell frequency response.

References

[1] "The Proton Driver Design Study," FERMILAB-TM-2136 (December 2000).

5.4. Vacuum

T. Anderson

5.4.1 Design Overview

The PD2 ring vacuum system is a 474-m continuous vacuum chamber composed of magnets, short sections of tubing, bellows, ion pumps, valves, and instrumentation. From a vacuum design standpoint there is little difference between the PD1 ring vacuum system and that of PD2. Both systems use the "canned magnet" design for the magnets and therefore system performance will be limited by the out-gassing rates we are able to achieve in the magnet laminations and coils. Table 5.4.1 below shows the primary system design parameters. These along with Chapter 8 of Fermilab-TM-2136, "The Proton Driver Design Study," are used as the basis for this design. The parameters are the same as in PD1 except for the average pressure, system length and aperture.

Table 5.4.1. Vacuum System Design Parameters

Average Pressure	$< 2 \times 10^{-7}$ Torr
Total System Length	474 m
Vacuum Aperture	4-in $\times$ 6-in
Maximum Pump Spacing	N/A
Primary Pump Type	Ion Pump, 800 l/s.
Roughing Pump Type	Turbo Molecular (500 l/s), w/10 CFM Dry Backing Pump.
Sector Pump-down Time	12 hr to rough vacuum, 72 hr bake-out to high vacuum.
Vacuum Gauging	Pirani, Ion Gauge and Ion Pump Read-back.
Beam Tube Material	Straight Sections and Magnets without Eddy Current Heating (Stainless Steel), Magnets with Eddy Current Heating (Inconel)
Vacuum Interface Type	Flanged with bellows.
Special Considerations	Dipoles and Quadrupoles of vacuum canned design (core and coils will be in the vacuum space).
Bake-out System	Magnet vacuum chambers will need low temperature (<150° C) bake-out capability.

As with PD1, all components that make up the vacuum system will need to be fabricated using ultra-high vacuum (UHV) practices and a low temperature bake-out system will need to be built into the magnets. It is premature at this time to lay out vacuum sector lengths, but in general they will need to be short enough to facilitate operational bake-outs. This will probably limit sector lengths to three or four long dipoles.

Most of the differences between the PD2 and PD1 vacuum systems are due to the changes in magnet properties and lengths. The quadrupoles used in PD2 are shorter and smaller in cross section than those used in PD1. This results in an 80% reduction in gas load for the PD2 quadrupoles and the number of 800 l/s ion pumps can be reduced form two to one per quadrupole. The same is true for the short dipoles except that the ion pumps are reduced from four to two. The long dipoles are longer but smaller in cross section than those used in PD1. As a result only a 10% reduction in gas load is achieved. Therefore, four 800 l/s ion pumps will still be required per long dipole. This makes a total of 188 ion pumps needed for PD2 verses 384 for PD1.

The other significant change between PD2 and PD1 is the number of vacuum interfaces. PD1 had two interfaces per magnet for a total of 288. In PD2 the F and D quadrupoles come as a set, thereby reducing the number of vacuum interfaces to one per quadrupole. PD2 would have a total of 148 vacuum interfaces.

5.4.2 Performance

In addition to the geometry and length changes noted above, the average pressure required for PD2 has been increased to 2×10^{-7} Torr from 1×10^{-7}. This is significant in that we are now in a pressure range that tests have shown are achievable. After the writing of the PD1 study, out-gassing tests were done on the lamination and coil materials. The results indicate that the total pressure at the long dipole pumps would be between 1×10^{-7} and 2×10^{-7} Torr several days after a bake out for PD1. This pressure range was based on out-gassing data taken two days after the samples had been baked at 150° C for two to three days. Experience shows us that the out-gassing rates will continue to decrease for many weeks after a bake-out. It is therefore reasonable to assume that the ultimate pressure will be less than that indicated by the tests. Table 5.4.2 shows the anticipated partial pressures for the component gases in the long dipoles for PD2 and PD1, using the out-gassing data from the tests.

Table 5.4.2. Partial Pressure for Component Gases in Long Dipoles

Gas	% Gas	Partial Pressure in PD1 (Torr)	Partial Pressure in PD2 (Torr)
H_2	58	6.8×10^{-8}	6.1×10^{-8}
CH_4	5	5.4×10^{-9}	4.9×10^{-9}
H_2O	15	1.8×10^{-8}	1.6×10^{-8}
CO	18	2.1×10^{-8}	1.9×10^{-8}
CO_2	4	4.2×10^{-9}	3.8×10^{-9}
Totals	100	1.2×10^{-7}	1.0×10^{-7}

5.5 Control System

M. Shea, J. Patrick

5.5.1 Fermilab Control System

The overall architecture of Fermilab control systems follows the standard design shown in Figure 5.5.1. Individual Front End Computers that control accelerator hardware are networked to each other, to console computers, and to various servers using a Local Area Network. The network connections contain 10 MHz, 100 MHz, and 1 GHz Ethernet segments along with switches and routers as needed, so that Control Room Consoles may access data for all the accelerators.

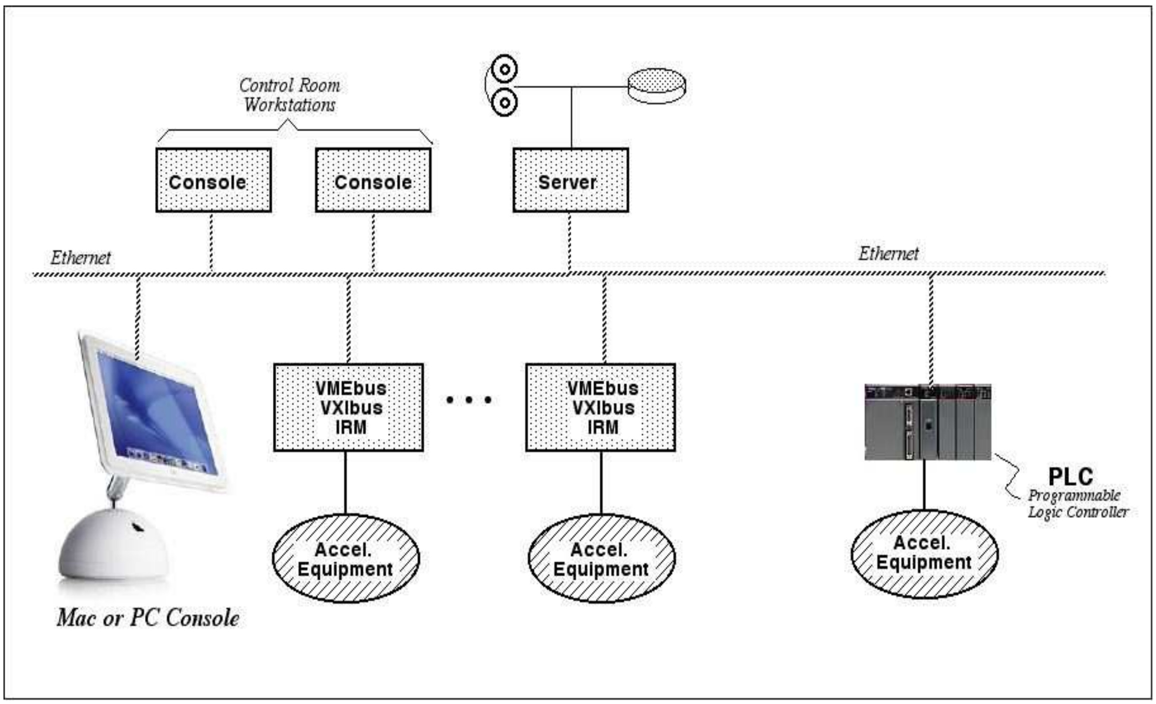

Figure 5.5.1. Control system architecture.

To the Fermilab Control System, the Proton Driver must appear as one more accelerator in the complex. It will be operated from the Main Control Room, and data from the Proton Driver will be presented on console displays along with data from other Fermilab accelerators.

The Control System architecture for PD2 will be essentially the same as that described in the PD1 design study, Fermilab-TM-2136. Because the machine operates at

15 Hz, the control system currently used for the Fermilab Linac, parts of the Booster, Tevatron and Main Injector will be used. This system is VMEbus-based, uses the Wind River vxWorks real time operating system and operates synchronously with the 15 Hz repetition rate of the accelerators. Both VMEbus crates and Internet Rack Monitors (IRMs) are used as Front End computers in the Fermilab ACNET control system. Operationally, the Proton Driver and its associated beam lines will appear as additional equipment to be controlled from ACNET consoles in the Main Control Room. The Front End computers connect to the accelerator hardware, collect raw data and make it available to ACNET.

5.5.2 PD2 Controls

The Control System for PD2 includes controls for the Linac, the synchrotron ring and the injection and extraction transport lines. Most of the controls for PD2 are similar to the controls needed for PD1. Because of that, the controls costs for many systems remain the same as those contained in the PD1 design study. The major change is due to the addition of a 200 MeV section of Linac although there are reductions in the requirements for the low energy end of the Linac and for the ring vacuum system.

5.5.2.1 PD2 Injection energy

The injection energy chosen for PD2 is 600 MeV, which requires the addition of 200 MeV of side-coupled cavity to be located in the injection tunnel. Five klystron stations are needed to provide the RF for this part of the Linac. Controls for this section of Linac will be similar to the high-energy end of the existing Linac. A VMEbus crate driving two HRMs will be used to control and monitor each of the five klystron stations. Beam diagnostics data will be collected using Quick Digitizer VMEbus modules. The beam diagnostics include wall current monitors, beam position detectors, wire scanners, and loss monitors. Except for the loss monitors, the beam diagnostic data will be acquired using 10 MHz snapshot digitizers.

5.5.2.2 Ion source and RFQ

The low energy part of the Linac for PD2 has been simplified compared with the system proposed for PD1. Instead of having two RFQ modules and the double alpha transport system, a single RFQ/ion source will be positioned very close to the input of the first Linac drift tube tank. This will reduce the RFQ system control costs, although an expanded offline test area would be needed to study the beam properties before mounting the assembly in place. Linac control costs have been reduced by about 30% to reflect this change.

5.5.2.3 Vacuum System

In the vacuum controls area, the PD2 controls costs will decrease. There are fewer ion pumps in the PD2 ring and so the vacuum controls will decrease by 20%.

5.5.4 R&D Program

During the R&D phase of the Proton Driver program, two VMEbus modules should be developed: an 8-channel 10-20 MHz Quick Digitizer module, and an 8-channel programmable waveform generator to be used to drive correction element power supplies.

Chapter 6. Beam Loss, Collimation and Shielding

A.I. Drozhdin, M.A. Kostin, N.V. Mokhov

6.1. Beam Loss and Shielding Design Strategy

A high beam power of 0.48 MW implies serious constraints on beam losses in the Proton Driver. As in the previous study [1], the design strategy is that the beam losses are localized and controlled as much as possible via the dedicated beam collimation system. This way, the source term for the radiation analysis is a derivative of the collimation system performance. A high loss rate is localized in the collimation section with components locally shielded to equalize prompt and residual radiation levels in the tunnel and drastically lower uncontrolled beam loss rates in the rest of the lattice [2, 3]. The radiation transport analysis is fundamentally important because of the impact on machine performance, conventional facility design, maintenance operations, and related costs. Results of this chapter are based on detailed Monte Carlo simulations with the STRUCT [4] and MARS [5] codes.

6.1.1. Regulatory requirements

1. Prompt radiation: the criterion for dose rate in non-controlled areas on accessible outside surfaces of the shield is 0.05 mrem/hr at normal operation and 1 mrem/hr for the worst case due to accidents [6]. Currently, the Fermilab Radiological Control Manual (FRCM) [6] requires that the machine designers describe and justify what a possible "credible worst case accident" is, and design the shielding—or modify operation of the machine—accordingly.

2. Hands-on maintenance: anywhere in the machine, residual dose rate P_γ $\leq$100 mrem/hr = 1 mSv/hr at 30 cm from the component surface, after 100 day irradiation at 4 hrs after shutdown. Averaged over all the components, $P_\gamma \leq$ 10 - 20 mrem/hr = 0.1 - 0.2 mSv/hr.

3. Ground-water activation: do not exceed radionuclide concentration limits $C_{i,reg}$ of 20 pCi/ml for ^{3}H and 0.4 pCi/ml for ^{22}Na in any nearby drinking water supplies. The sum C_{tot} of the fractions of radionuclide contamination (relative to regulatory limits $C_{i,reg}$) must be less than one for all radionuclides. Corresponding star density and hadron flux are strongly site and depth specific.

Additionally, one assumes the accumulated dose of 20 Mrad/yr or 400 Mrad over 20 years lifetime in the hot spots of machine components as a *radiation damage* limit for such materials as epoxy and cable insulation.

6.1.2. Normal operation and beam accident

The radiation analysis for the beam transport lines, arcs and long straight sections is performed both for normal operation and for accidental beam loss. The maximum shielding thickness from the both cases is put into the design as the tunnel shielding in that part of the machine.

In normal operation, the source term is based on the beam loss distributions calculated with a beam collimation system described in the next section. This system provides average rates in the arcs outside the collimation region of about 0.12 W/m at the top energy and less than 0.05 W/m at injection, although some peaks at the top energy are as high as several Watts per meter. This is to be compared to the tolerable beam loss rates for hands-on maintenance of about 0.25 W/m (bare beam pipes) and 3 - 10 W/m (magnets) for P_γ = 100 mrem/hr at local peaks and five times lower (0.05 and 0.6 - 2 W/m, respectively) for P_γ = 20 mrem/hr averaged over the lattice [1, 2]. At such rates, the peak accumulated dose in the coils is not a limiting factor. For ground-water activation a limiting rate is in the range of about 0.5 to 10 W/m depending on siting.

For accidental beam loss, a *credible* accident is considered: a point-like loss of 0.1% of the full beam intensity during one hour. This is about 10^{15} protons. Once such an accident happens, the machine is shut down within 1 second to analyze the cause and undertake appropriate measures.

6.2. Collimation System

6.2.1. Beam loss localization

With an assumed 1% (4.8 kW) of the beam lost at the top energy, the peaks (at some quadrupoles) in the beam loss distribution reach several kW/m, a few thousand times higher than the tolerable levels. Therefore, a three-stage beam collimation system is implemented into the lattice. Both of the two 75.4-m long straight sections are occupied by the RF cavities, injection and extraction systems. Due to space constraints, the collimation system is placed in the available drift spaces of the arc section in the slots upstream and downstream of the short dipoles. The system consists of horizontal and vertical primary collimators, four secondary collimators, and two supplementary ones as shown in Fig. 6.1 and Table 6.1.

Secondary collimators need to be placed at phase advances which are optimal to intercept most of particles out-scattered from the primary collimators during the first turn after the halo interaction with the primary collimator. Transverse phase space at the collimators is shown in Fig. 6.2. The optimal phase advances are around $k \cdot \pi \pm 30^o$. Phase advances between the primary and secondary collimators are presented in Table 6.1. The horizontal

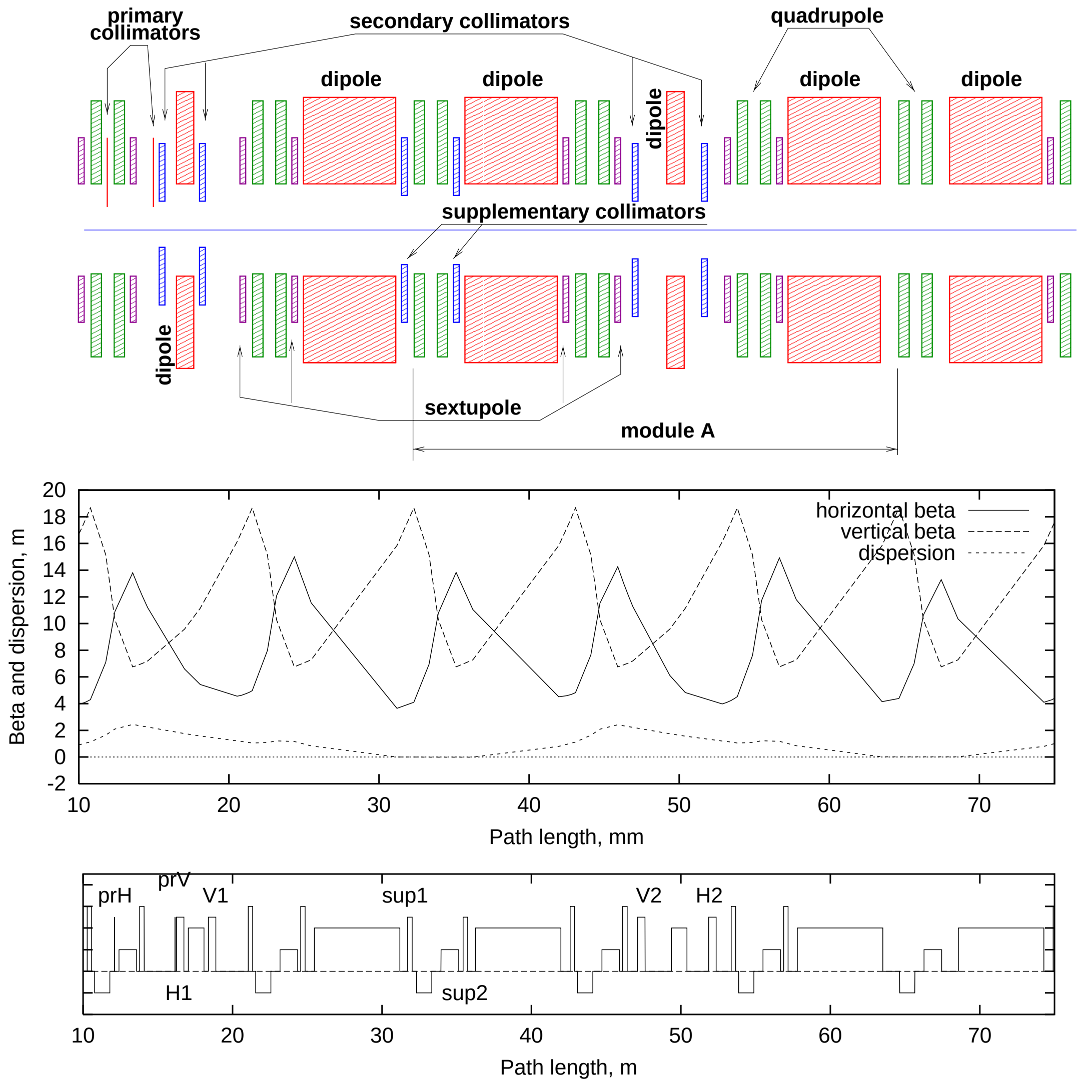

Figure 6.1. Beam collimation system (top) and beta functions and dispersion in the collimation section (bottom).

Table 6.1. β-functions, dispersion and phase advance between primary and secondary collimators.

Collimator	β-function (m)		Dispersion (m)	Phase advance between primary and secondary collimators (deg)	
	horizontal	vertical		horizontal	vertical
Horizontal primary	8.9	12.6	1.9	0	-
Vertical primary	8.0	8.5	1.9	-	0
Secondary H1	7.8	9.2	1.9	24	-
Secondary V1	5.2	12.6	1.5	-	14
Supplementary 1	3.9	17.9	0.0	176	84
Supplementary 2	12.2	7.0	0.0	203	105
Secondary V2	10.7	7.7	2.1	-	172
Secondary H2	4.0	15.0	1.4	348	-

and vertical primary collimators are placed at the edge of the beam after painting, with secondary collimators father from this position by an offset d. Beam loss distributions at injection and top energies are shown in Fig. 6.3 for the system with 0.3-mm thick tungsten primary collimators, four secondary collimators (0.5-m long stainless steel or copper) positioned at $d = 2$ mm and two 0.3-m long supplementary collimators at $d = 4$ mm. It is assumed in calculations that 10% of the beam is lost at injection and 1% at the top energy, and 2/3 of these amounts interact the horizontal primary collimator (a half for off-momentum protons with $\Delta p/p = \pm 0.002$ and a half for on-momentum protons) and 1/3 the vertical primary collimator. The β-function varies along the length of a secondary collimator, therefore the collimator apertures are assumed to be tapered to follow the beam envelope after painting.

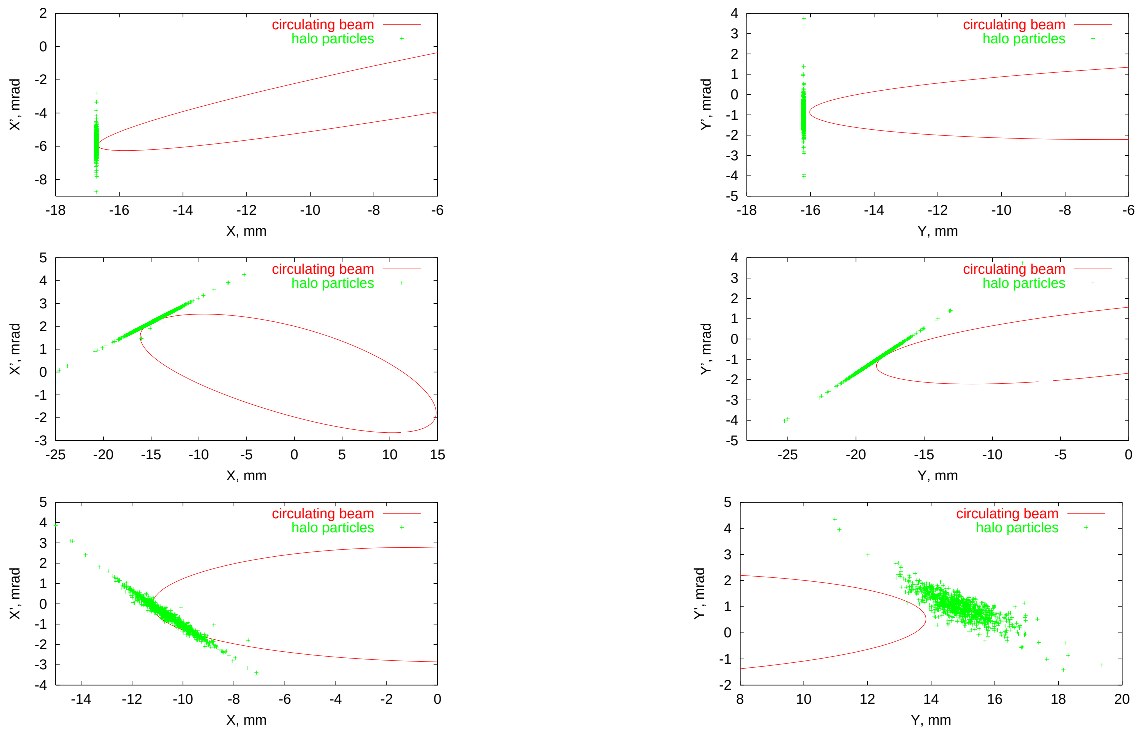

Figure 6.2. Horizontal (left) and vertical (right) phase space at the primary collimators (top), secondary collimators 1H and 1V (middle), and collimators 2H and 2V (bottom).

The right side of Fig. 6.3 shows details of beam loss in the collimation region. Secondary collimators generate out-scattered particles lost later in the lattice. One can reduce this component with a *3-stage collimation system*. Several *main* secondary collimators are positioned close to the beam to deal with protons scattered in the primary collimator and several *supplementary* collimators are farther from the beam to catch particles out-scattered from the main secondary collimators. A significant reduction of beam loss rates by introducing 2 supplementary collimators 0.3-m long positioned at $d = 4$ mm is seen by comparing the middle and bottom plots in Fig. 6.3. Total beam losses in the collimation section and in the rest of the machine along with the peak loss rates are presented in

Table 6.2 for both top and injection energies. Results are given for the machine without collimators and for the collimation system with primary collimators of various thicknesses t, secondary collimators at d = 2 mm and with and without two supplementary collimators at offset of d = 4 mm with respect to the primary collimators.

With the proposed system, $\sim$99% of the beam halo energy is intercepted in the 58-m long arc section. About 1% is lost in the rest of the machine along 416-m length with mean rate of 0.12 W/m. At several locations the beam loss is noticeably higher, exceeding the tolerable rates. Such "hot" locations need special care. Beam loss rates in the collimation system section itself are very high requiring a special shielding design (see next section).

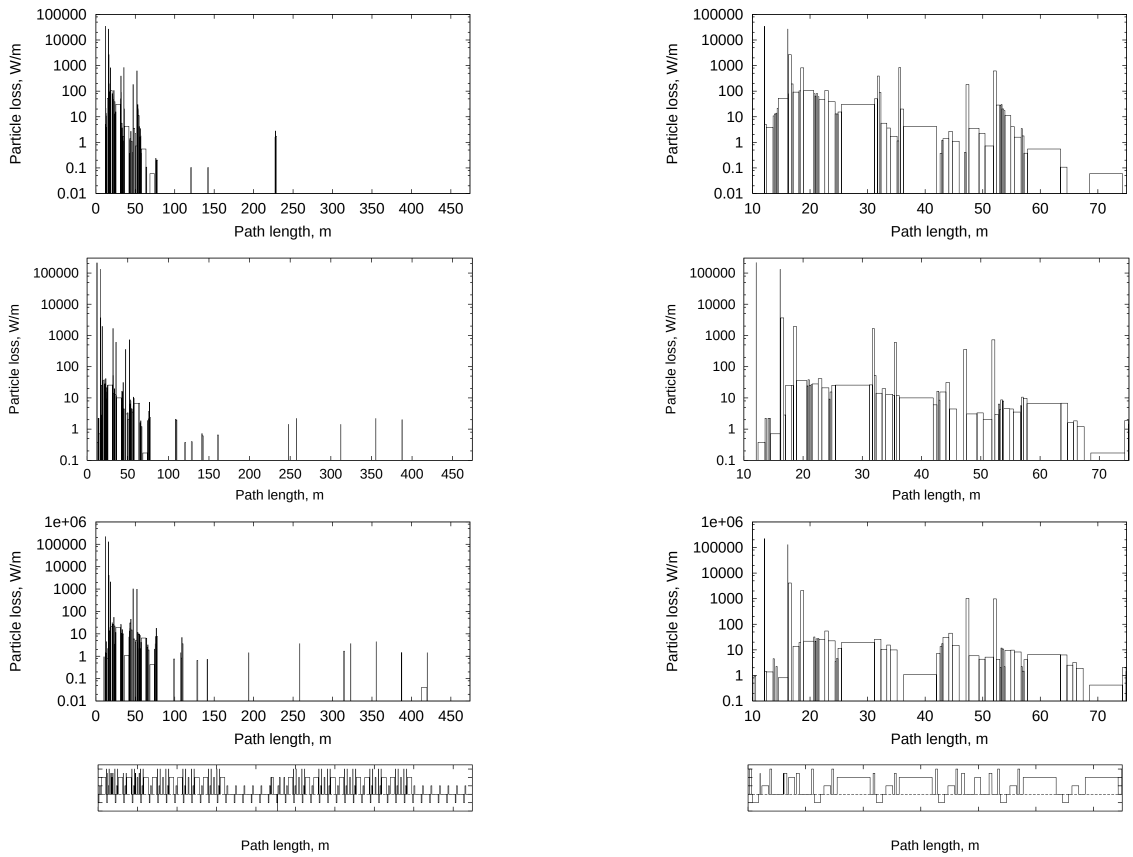

Figure 6.3. Beam loss distributions at injection (top) and at top energy with (middle) and without (bottom) supplementary collimators. The left group shows the entire machine and the right group shows the collimation region.

6.2.2. Mechanical design

The mechanical design of the secondary collimators is similar to that of those already built and installed in the Tevatron for Collider Run II [7]. The collimator jaws consist of two pieces 30-40 mm wide welded together in an 130-mm "L" configuration. Primary

Table 6.2. Total beam losses in the 58-m collimation section (P_{coll}) and in the rest of the lattice (P_{rest}) and peak beam loss rates in the rest of the machine (p_{peak}).

Primary collimator thickness	P_{coll} (kW)	P_{rest} (kW)	p_{peak} (W/m)
E_{kin} =8 GeV without collimation			
	0.310	4.489	5900
E_{kin} =8 GeV without supplementary collimators			
t = 0.1 mm	4.768	0.035	8
t = 0.3 mm	4.753	0.048	7
t = 0.5 mm	4.749	0.051	9
t = 1.0 mm	4.742	0.058	7
t = 1.5 mm	4.743	0.057	8
E_{kin} =8 GeV with supplementary collimators			
t = 0.3 mm	4.778	0.024	2
E_{kin} = 0.6 GeV with supplementary collimators			
t = 0.3 mm	3.596	0.005	0.2

collimators are made of tungsten 1 mm thick. Secondary and supplementary collimators are made of stainless steel or copper (choice will be the subject of further thermal analyses) 0.5 m (secondary) and 0.3 m (supplementary) long. These dimensions will accommodate the full beam size, after painting, as well as maximum impact parameters. Machining and assembly tolerances of 25 μm are easily met for the collimator jaws. All collimators will be in a fixed position during the machine cycle, but motion control is required in order to adjust collimators to their optimum position. The collimator assembly is welded inside a stainless steel box with bellows on each end (Fig. 6.4).

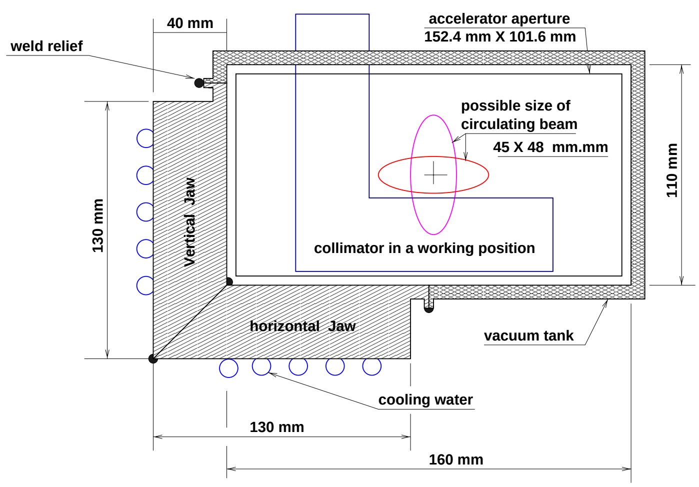

Figure 6.4. Collimator cross section.

The box assembly is supported by a cradle which is moved independently in the vertical and horizontal directions by stepping motors. Full range of motion is 50 mm in steps as small as 25 μm if required and a maximum speed of 2.5 mm/sec. The collimator speed can be increased if a larger minimum step size is acceptable. Position readback is provided by linear differential voltage transformers, although investigation into the radiation hardness of these devices is required. Mechanical damage is prevented by limit switches on all degrees of motion. The entire assembly, including bellows, will occupy approximately 1 m of lattice space.

The primary collimator assembly is identical to the secondary collimator assembly except that their "L" blocks are only 0.1 m in length. The 1-mm thick machined tungsten jaws are bolted to the stainless steel blocks. The blocks provide a good heat sink for energy dissipated in the tungsten. The entire assembly, including bellows, will occupy approximately 0.6 m of lattice space.

The motion controls for the collimators will be similar to the Tevatron system [7]. Up to 4 motors and 4 position readbacks will be controlled and monitored by a single MVME162 processor running VXWORKS in a VME crate in a nearby service building. Stepping motors and LVDT's are interfaced to the CPU via commercial IP's (Industrial Packs). The motor PS and motor controllers are also commercial hardware. A total of 3 "stations" – VME crate, motor controller crate, and motor PS will be required for the entire system of 10 collimators. A total of 8.4 kW of DC power (3.6 kW at injection and 4.8 kW at top energy) is expected to be dissipated in all the collimators. This power can be removed from each collimator by circulating LCW (Low Conductivity Water) through cooling channels on the outside of the collimator box. A flow of 1.6 gpm will remove the power with a temperature rise of 20°C. Good thermal contact between the stainless steel "L" blocks and the welded box is required.

6.3. Radiation Analysis

6.3.1. Collimation region

MARS calculations show that residual dose rates on the collimators and magnets of the 58-m collimation system significantly exceed the hands-on maintenance limits (Fig. 6.5(a)). To reduce these levels and protect ground water outside the tunnel walls, the entire region needs to be shielded. The proposed configuration, based on optimizational MARS calculations, consists of steel shielding uniform in two sections: first, 5-m long, starts 0.5 m upstream of the secondary collimator H1 and second is in the remaining downstream region. The first section is 1 m (vertically) and 1.3 m (horizontally) thick on each side of the secondary collimators and 0.6-m around magnets. The second section is 0.65-m (vertically) and 0.95-m (horizontally) thick on each side of the collimators, 0.25-m around dipoles, and 0.4 m (vertically) and 0.7 m (horizontally) around quadrupoles (Fig. 6.5(b)). This reduces residual dose rates below the limits (Fig. 6.5(a)) and provides adequate protection of cables and other components in the tunnel and ground water around the tunnel (Fig. 6.6(a)).

The shielding proposed equalizes (to some extent) the radiation source term outside the shielding and unshielded components further downstream. This allows for the uniform

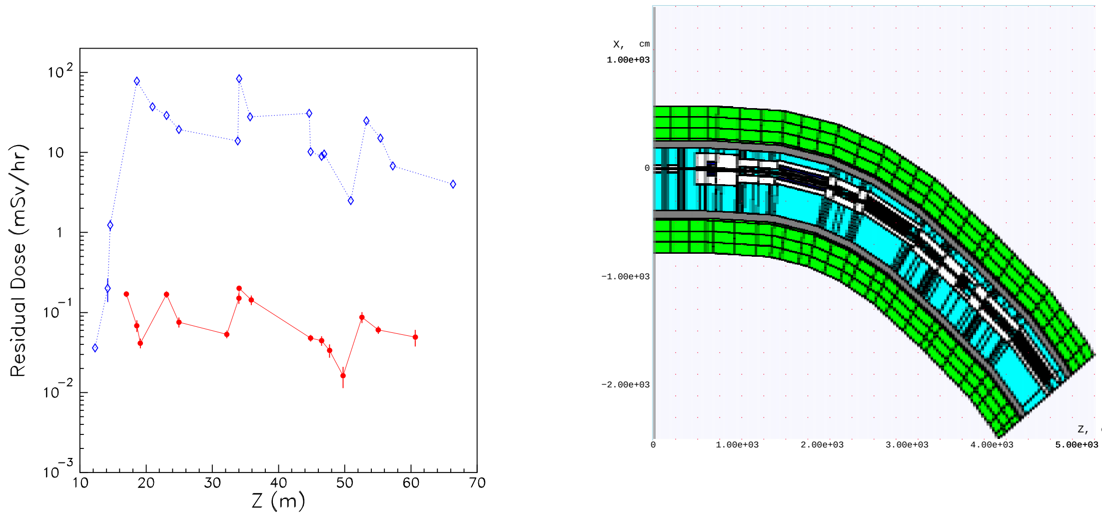

Figure 6.5. (a) Maximum contact dose on site surfaces of collimation section components (diamonds) and shielding (circles) (left). (b) MARS model of the 58-m collimation section with steel shielding (right)

.

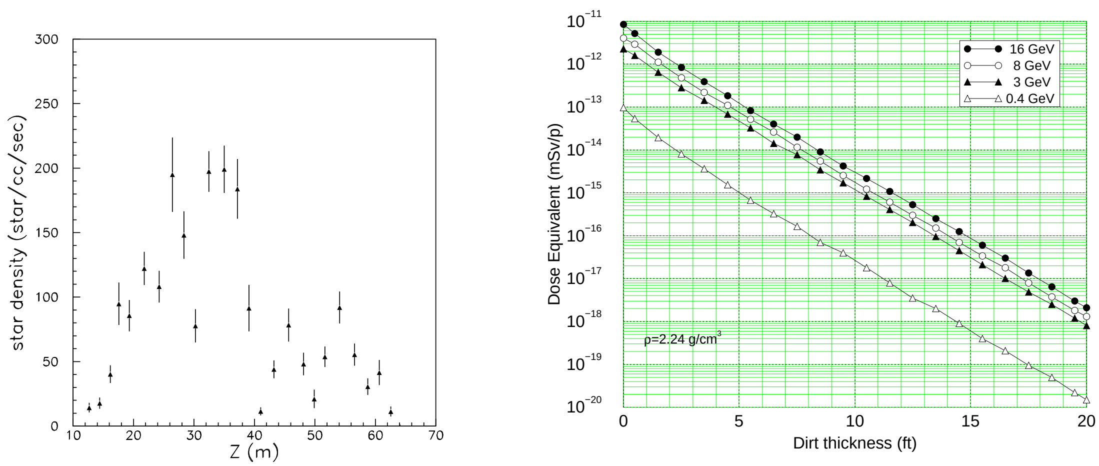

Figure 6.6. (a) Radiation load (star density) in the first 20-cm layer of dirt around the collimation section tunnel (left). (b) Prompt dose equivalent *vs* dirt thickness around the tunnel at a point-like proton loss at four energies (right)

.

approach to the dirt shielding calculation in the entire machine. The dose on the outer shielding surface depends on the beam energy in a complex way. Assuming a quasi-local beam loss in the magnet, the dose equivalent was calculated with MARS14 as a function of Fermilab wet dirt thickness ($\rho = 2.24$ g/cm^3) outside the tunnel walls. Fig. 6.6(b) shows this dependence for kinetic beam energies from 400 MeV to 16 GeV. The dose at high energies scales as E$^\alpha$, where α is about 0.8, while $\alpha \geq 1$ at E $\leq$ 1 GeV. In addition, a safety factor of three is applied in calculating a final shielding thickness.

To accommodate the collimation system, the first 58 meters of the arc downstream of the injection straight section have a tunnel 19-foot wide, 12-foot high. Its concrete walls are 27-inch thick. The ceiling and floor are 42-inch thick. Fig. 6.7 shows isoflux and isodose contours in the hottest dipole between the secondary collimators H1 and V1, its 1-m shielding and tunnel cross-section. With the shielding, radiation levels outside the tunnel wall are very close to those in the arcs (see below). Therefore, the same external shielding design both for normal operation and beam accident is applied. With a safety factor of 3, the thickness of dirt shielding above this 58-m long region is 19 feet. The maximum dose accumulated in the collimators and hottest spots of the magnet coils reaches 200 Mrad/yr. The maximum yearly dose at cable locations is about 150 krad per year.

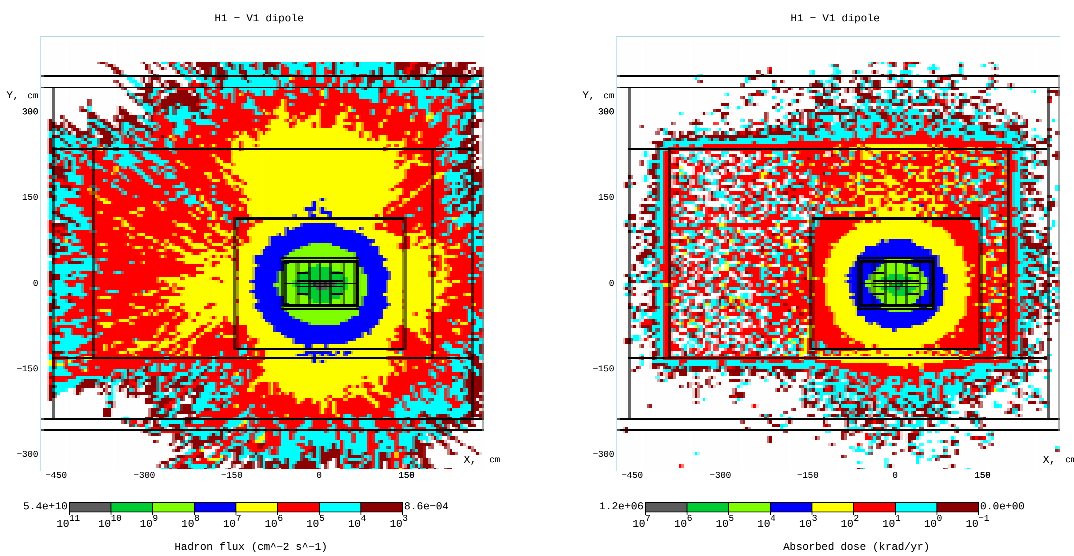

Figure 6.7. (a) Hadron (E>20 MeV) isofluxes (cm^{-2}s^{-1}) in the tunnel around the dipole between collimators H1 and V1 (left). (b) Yearly isodose contours (krad/yr) at the same location (right).

6.3.2. Linac and beam transport lines

In the Linac and injection beam line, assume a proton beam with E_{kin} = 600 MeV at 15 Hz of 2.8×10^{13} protons per pulse, 4.2×10^{14} protons per second with beam power of 40 kW. For a credible accident, the dose immediately outside the tunnel concrete walls is 6.3×10^{3} mrem/hr. This requires 11 feet of dirt to reduce the dose to 1 mrem/hr, or 12.5 feet with a safety factor of 3. In normal operation with a beam loss rate of 0.16 W/m, the required shield thickness is one foot less. At extraction, an accidental 8-GeV beam loss of 3.75×10^{14} (p/sec) requires 16 feet of dirt. An operational 8-GeV beam loss of 3.75×10^{8} (p/m/sec) = 0.48 W/m along a 1000-m long extraction beam line requires 13.5 feet of dirt. Assuming a safety factor of 3, the thickness of dirt shielding above the 8-GeV extraction beam line is 17.5 feet.

6.3.3. Long straight sections

Two long straight sections accommodate injection, extraction and RF systems. The tunnel width is 19 feet, its height is 12 feet, the concrete walls are 15-inch thick, ceiling and floor are 30-inch thick. Extraction will be one-turn fast extraction with very little loss at the extraction septum as in Ref. [1]. When the machine is well tuned, the extraction loss can be as low as the order of 10^{-4}, which has been achieved at the ISIS. As for the RF cavities with large apertures, our calculations show no noticeable beam loss in those regions. This implies that no local shielding is needed in the long straight sections. At this stage, shielding design and radiation requirements in these regions are assumed the same as in the arcs.

6.3.4. Arcs

The full arc lattice in a rectangular tunnel embedded into wet Fermilab dirt is implemented into the MARS calculation model. The tunnel width is 16 feet, its height is 9 feet, the concrete walls are 15-inch thick, ceiling and floor are 30-inch thick. Cable trays are positioned at the ceiling in the left and right corners of the cross-sections. The arc that follows the injection straight section is enlarged in the first 58 meters to accommodate the collimation system and is considered separately in the next sub-section. Because of non-uniform beam loss in the arcs (see Figs. 6.3) and the absence of self-shielding by magnet bodies, there are always pronounced radiation peaks of field around the long bare beam pipes. At some of these locations, the radiation levels are 2 to 4 times higher than the limits, requiring either further reduction of beam loss rates or a simple thin local shields. Around the magnets—due to absorption of radiation in their material—the flux and, as a result, all other radiation values are several times lower.

Despite the variation in beam loss distribution along the lattice and because the shield thickness is driven by accidental beam loss which can take place in an arbitrary lattice location, a uniform shielding design along the arcs is proposed. With a point-like accidental loss of 0.1% of the 1-hour beam intensity at 8 GeV, the shield thickness required is 17.5 feet of Fermilab wet dirt. During normal operation the earth shielding required to reduce the dose to 0.05 mrem/hr is $\sim$14 feet. This is based on the loss rate in the magnets normalized to 1 W/m. Assuming a safety factor of 3, the thickness of dirt shielding above the arcs, driven by accidental loss, is 19 feet.

The maximum dose accumulated in the coils is about 1 Mrad/yr which is acceptable with the use of appropriate materials for insulation. The maximum dose at cable locations is about 0.005 Mrad/yr around the hot spots in the magnets, and is about 0.05 Mrad/yr around long bare beam pipes at the same beam loss rate. At several locations, calculated peak residual dose rates near the bare beam pipes exceed the design goal for hot regions of 100 mrem/hr, being noticeably lower near the magnets due to significant absorption of soft photons in the dipole and quadrupole materials. The hands-on maintenance criterion gives about 3 W/m for a tolerable maximum beam loss rate in the lattice elements, except for the long bare beam pipes where one should decrease the loss rate to 0.25 W/m to reduce the dose to 100 mrem/hr. One needs further reduction to bring the dose down to a good practice value of about 10-20 mrem/hr. Alternatively, one can think of providing simple shielding around the bare beam pipes. With these measures, the above problem with ground water activation—if it exists at the site—is solved.

References

[1] "The Proton Driver Design Study" FERMILAB-TM-2136, December 2000.

[2] A.I. Drozhdin, O.E. Krivosheev, N.V. Mokhov, "Beam Loss and Collimation in the Fermilab 16-GeV Proton Driver", Proc. 2001 Particle Accelerator Conference, Chicago, p. 2572 (2001); Fermilab-Conf-01/128 (2001).

[3] N.V. Mokhov, A.I. Drozhdin, O.E. Krivosheev, "Radiation Shielding of the Fermilab Proton Driver", Proc. 2001 Particle Accelerator Conference, Chicago, p. 2578 (2001); Fermilab-Conf-01/132 (2001).

[4] I.S. Baishev, A.I. Drozhdin, N.V. Mokhov, "STRUCT Program User's Reference Manual", SSCL–MAN–0034 (1994); http://www-ap.fnal.gov/∼drozhdin/.

[5] N. V. Mokhov, "The MARS Code System User's Guide", Fermilab-FN-628 (1995); N. V. Mokhov and O. E. Krivosheev, "MARS Code Status", Fermilab-Conf-00/181 (2000); http://www-ap.fnal.gov/MARS/.

[6] "Fermilab Radiological Control Manual", Article 236, http://www-esh.fnal.gov/FRCM/.

[7] M. Church, A.I. Drozhdin, A. Legan, N.V. Mokhov, R. Reilly, "Tevatron Run-II Beam Collimation System", Proc. 1999 Particle Accelerator Conference, New York, p. 56 (1999); Fermilab-Conf-99/059 (1999).

Chapter 7. Injection and Extraction

7.1. Injection

A. Drozhdin, J. Holms, J. Lackey, C. Prior

7.1.1. Introduction

Injection Painting is required to realize uniform density distributions of the beam in the transverse plane for space charge effect reduction. Painting preserves emittance at injection. The system for injection painting is located at the end of the 75.4-meter long straight section of the machine. The Proton Driver beta functions and dispersion along the injection section are shown in Fig. 7.1. Table 7.1 lists the Proton Driver parameters that are relevant the painting system design.

Table 7.1. Proton Driver Parameters

Kinetic energy at injection	0.6 GeV
Injected beam normalized transverse emittance (95%)	3 π mm-mrad
Normalized transverse emittance after painting (100%)	40 π mm-mrad
Injected beam longitudinal emittance (95%)	0.1 eV-s
Circulating beam longitudinal emittance (95%)	0.2 eV-s
Injection painting duration	90 μs (45 turns)
Protons per bunch at injection	3×10^{11}
Total intensity at injection	2.5×10^{13}
RF frequency at injection	42.08 MHz
Revolution time at injection	1.996 μs
Harmonic number	84
Number of bunches	84
Full aperture ($2 \cdot A_x \times 2 \cdot A_y$)	152.4 mm $\times$ 101.6 mm
Horizontal betatron tune	11.415
Vertical betatron tune	7.303
Horizontal β at the foil	9.890 m
Horizontal α at the foil	-3.243
Horizontal dispersion at the foil	0.0 m
Vertical β at the foil	12.534 m
Vertical α at the foil	3.833
Horizontal beam size at injection in the foil	σ_x = 1.95 mm
Vertical beam size at injection in the foil	σ_y = 2.20 mm
Horizontal position of injected beam at the foil	27.00 mm
Horizontal angle of injected beam at the foil	9.529 mrad
Horizontal beam half-size at injection after painting	17.45 mm
Vertical beam half-size at injection after painting	19.64 mm

7.1.2. Injection PaintingScheme

Injection painting is performed by using two sets of fast horizontal and vertical magnets (kickers). The proton orbit is moved in the horizontal plane at the beginning of injection by 24.7 mm to the thin graphite stripping foil to accept the first portion of protons generated by H^- in the foil (Fig. 7.2). Three 1-m long kicker magnets are used to produce the orbit displacement (Fig.7.3). The maximum field of the kicker magnets is 0.19 kG. The horizontal kick at the beginning of injection is shown in Fig. 7.3. Gradual reduction of kicker strength permits "painting" the injected beam across the accelerator aperture with the required emittance. Vertical kicker magnets located in the injection line (not shown) provide injected beam angle sweeping during injection time, starting from maximum at the beginning of injection and going to zero at the end of painting process. Horizontal and vertical kickers produce abetatron amplitude variation during injection. This results in a uniform distribution of the circulating beam after painting. Painting starts from the central region of phase space in the horizontal plane and from the border of it in the vertical plane, and goes to the border of the beam in the horizontal plane and to the center in the vertical plane. This produces a so-called "uncorrelated beam" with elliptical cross section, thereby eliminating particles that have maximum amplitudes in both planes simultaneously.

A septum-magnet located upstream of the foil (Fig. 7.3) is used to separate the proton and H^- beams at the quadrupole upstream of the foil by 400 mm. This allows the H^- beam to pass outside the quadrupole body. The beam dump located behind the stripping foil is used for H^o interception. Injection kickers cause negligible perturbation of the β functions and dispersion at injection. Horizontal dispersion in the foil at injection is equal to -0.027 m.

Multi-turn particle tracking through the accelerator is done with the STRUCT [2] code. A stripping foil made of 300 μg/cm^2 (1.5 μm) thick graphite has the shape of a so-called corner foil, where two edges of the square foil are supported and the other two edges are free. The foil size is 1.6 cm × 3.0 cm.

The time dependence of kicker magnet strength is chosen to obtain uniform distribution of the beam after painting in both the horizontal and vertical planes. Eqs. 7.1 and 7.2 (horizontal) and Eq. 7.3 (vertical) are the equations for the optimal bump-magnet wave forms [3] as simulated in the STRUCT code. N is the turn number from the beginning of painting.

$$B = B_0\left[0.5815 + 0.4185\left(1 - \sqrt{\frac{2N}{45} - \left(\frac{N}{45}\right)^2}\right)\right] \qquad N < 45 \qquad (7.1)$$

$$B = B_0\left[0.5815 - \frac{N-45}{10.31.85}\right] \qquad N > 45 \qquad (7.2)$$

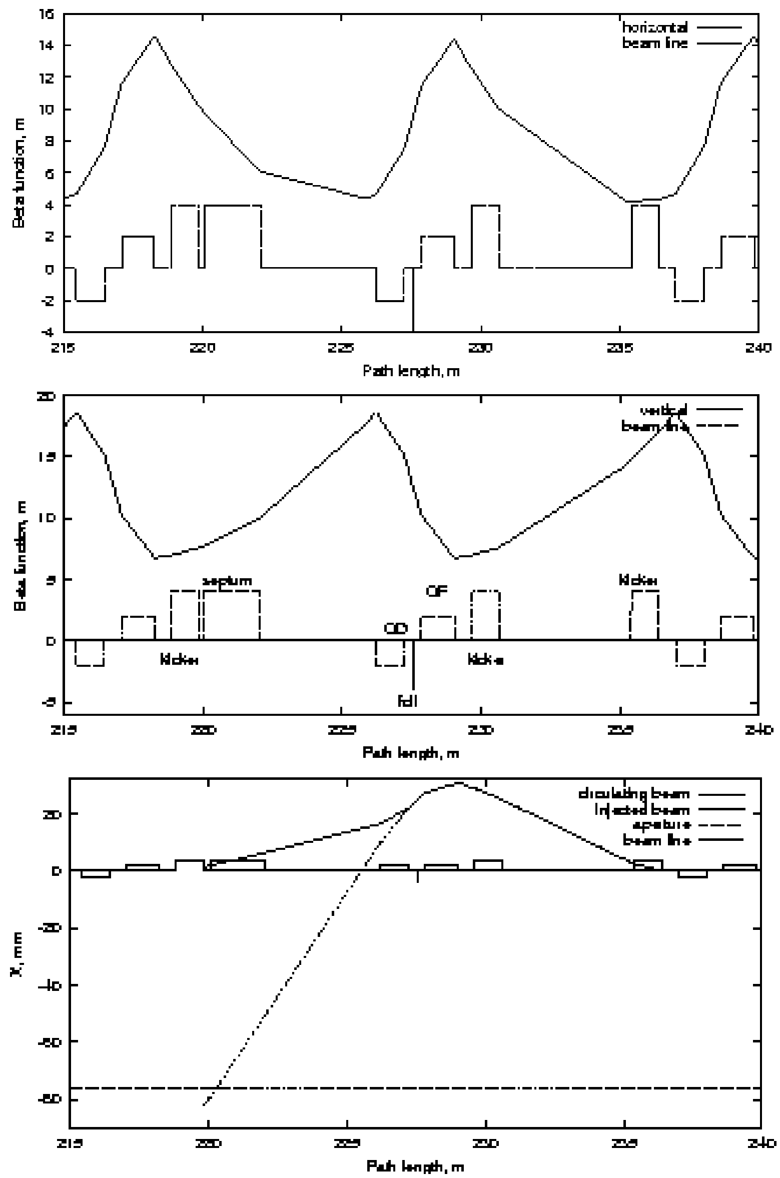

Figure 7.1. Horizontal (top), vertical (middle) beta functions, and painting bump (bottom) at injection.

$$Y^{'} = Y_0^{'}\sqrt{2\,\frac{45-N}{45}-\left(\frac{45-N}{45}\right)^2} \qquad Y_0^{'} = 1.0395\ mrad \qquad (7.3)$$

The horizontal and vertical phase planes of the injected beam in the foil are shown in Fig. 7.4. The emittance of the injected beam at 95% is equal to 3 π mm-mrad.

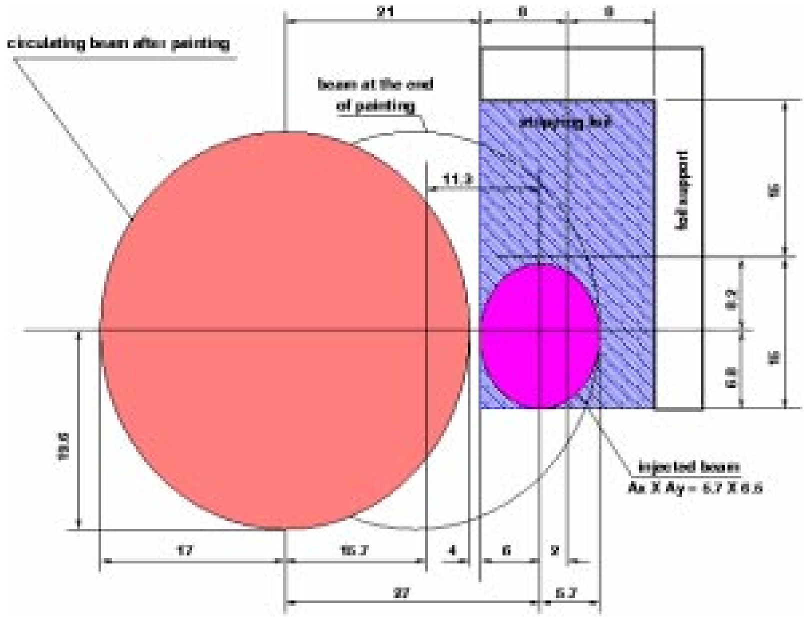

Figure 7.2. Injected and circulating beam locations in the foil at painting.

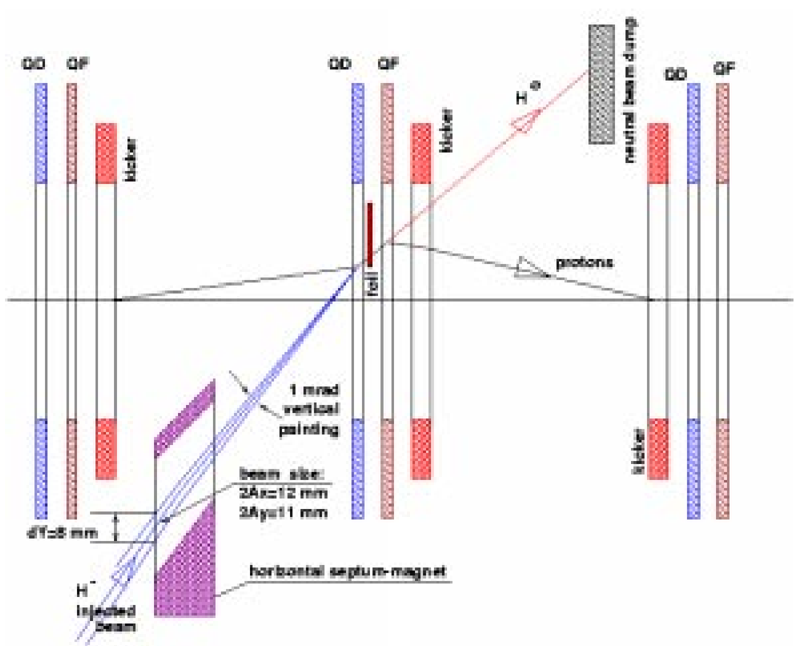

Figure 7.3. Injection painting scheme.

Painting lasts during 45 turns, and after painting the circulating beam moves out of the foil during 6 turns. In the simulations the horizontal bump amplitude at the foil is 27 mm = 11.3 mm (painting) + 15.7 mm (removing from the foil) (Fig. 7.2). Vertical angle variation is 1.0395 mrad. The horizontal and vertical phase planes of the circulating beam in the foil at 6^{th}, 45^{th}, and 51^{st} turns from the beginning of painting are presented in Fig. 7.5.

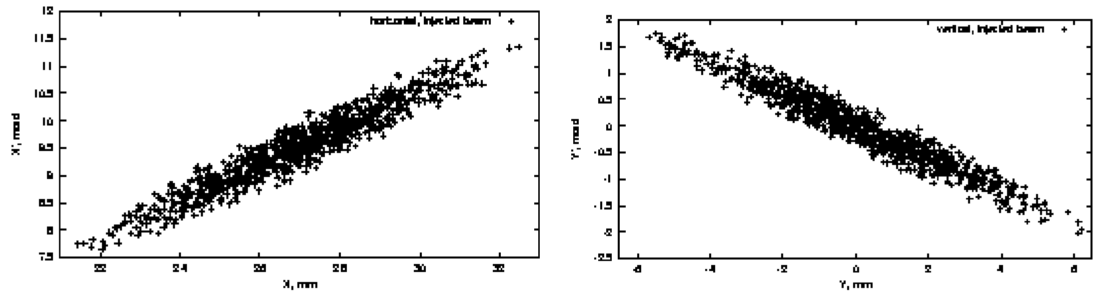

Figure 7.4. Horizontal (left) and vertical (right) phase plane of injected beam at the foil.

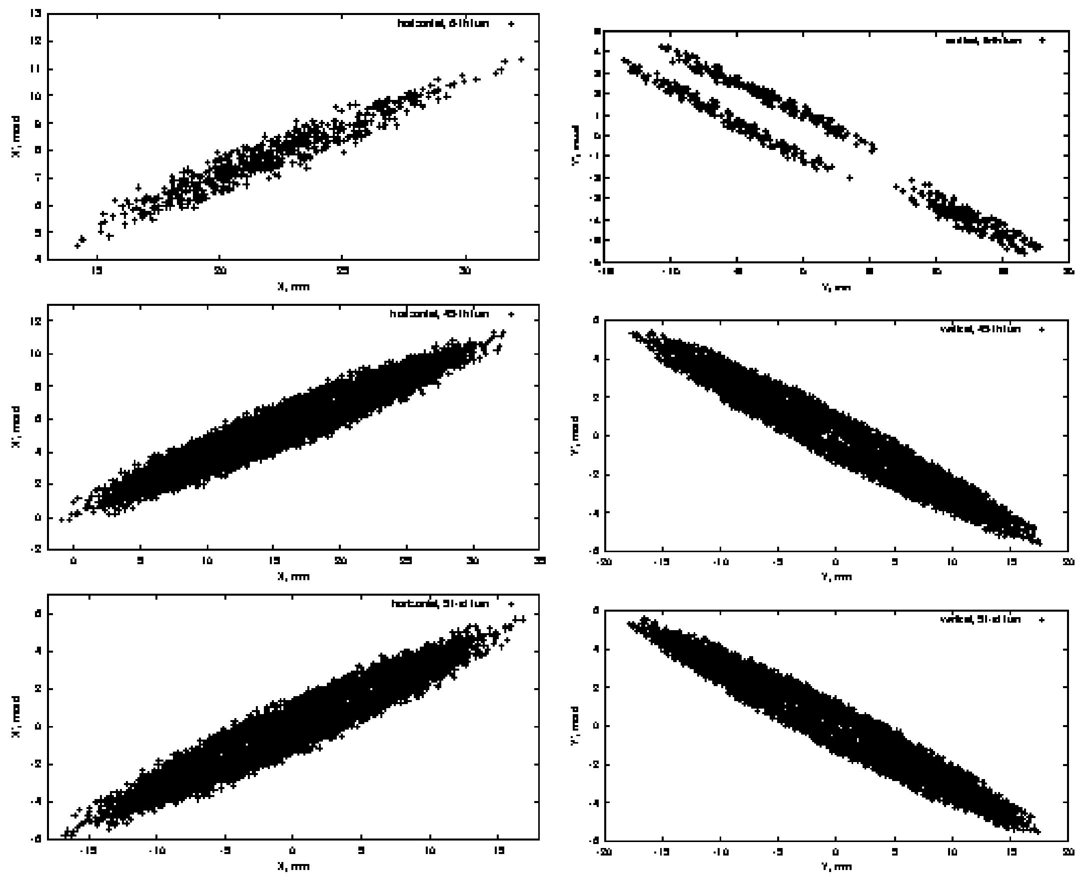

Figure 7.5. Horizontal (left) and vertical (right) phase plane in the foil at 6th (top), 45th (middle), and 51st (bottom) turn from the beginning of beam painting.

The horizontal kicker magnet strength and the vertical angle of the beam in the foil during injection are presented in the top part of Fig. 7.6. Particle transverse population and particle density distribution after painting at the foil location are shown in the middle and at the bottom of Fig. 7.6. Circulating beam after painting (51st turn) and particle population at the foil are shown in Fig. 7.7. Particle distribution at the foil is shown in Fig. 7.8.

The average number of hits upon the stripping foil for each particle is 5.22. This effects low-level nuclear interactions and multiple Coulomb scattering in the foil at injection, and because of this causes low-level particle loss at injection.

The circulating protons pass several times through the foil and some of them can be lost because of scattering in the foil. Multiple Coulomb scattering is very small because of small foil thickness. Particle energy loss in the foil at one pass is 1.6×10^{-6} of the initial energy. The total rate of nuclear interactions in the foil during the process is 2.0×10^{-5} of the injected intensity. The emittance of the circulating beam in the horizontal plane is small in the beginning of painting and it gradually reaches maximum at the end of painting. Therefore the particle horizontal amplitude, on average, is sufficiently smaller than the accelerator aperture. Particles can be lost only during the first few turns after injection, and only in the region of injection kick maximum where the beam is close to the accelerator aperture. At every subsequent turn after particles are injected, they move away from the aperture restriction because of the fast reduction in the painting kick amplitude. Simulations have shown that the rate of particle loss in the accelerator from interaction with foil is as low as 7.3×10^{-5} of the injected intensity.

The calculated stripping efficiency is 99.2% and the estimated yield of excited states $H^o(n)$ atoms with $n \geq 5$ is equal to 0.016% [4]. These atoms will be stripped into protons before they reach the dump and become a beam halo. The remaining excited atoms ($n \leq 4$) have a longer lifetime and they will go to the neutral beam dump.

7.1.3. Septum and Kicker Magnets Parameters

Septum and kicker magnets parameters are presented in Table 7.2. The septum is curved to reduce the pole-tip width.

Table 7.2. Septum and Kicker Magnets Parameters

Element	Field	Current	Inductance	Length	Poletip width	Pole-tip gap	Turns number	Septa thick.
Name	Gauss	Amps	μH	m	mm	mm		mm
Septum	2135	6720	2.538	2	40	40	1	15
kicker-1	108	37.98	126	1	152	102	8	-
kicker-2	92	22.48	126	1	152	102	8	-
kicker-3	212	74.40	126	1	152	102	8	-

7.1.4. Stripping Foil Design

Carbon stripping with densities between 300 and 600 μg/cm^2 have been in use in the Booster since the 400 MeV Linac upgrade. No foils have ever been lost because of beam damage. It should be pointed out, however, that the Booster uses nominally 11 injection turns per cycle and the Proton Driver will use up to 45 turns per cycle.

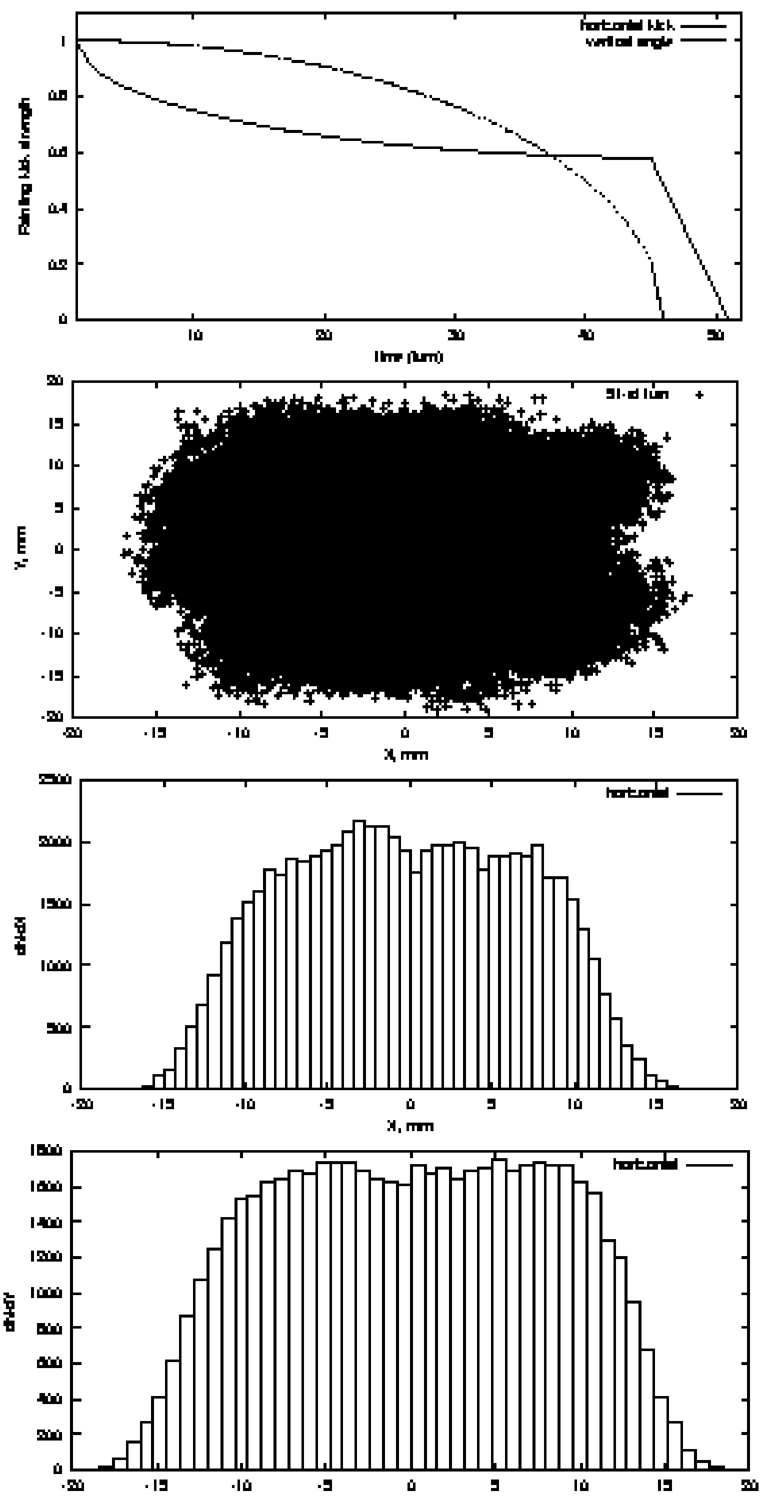

Figure 7.6. Horizontal kicker strength and vertical angle of the beam at injection in the foil (top). Particle transverse population (middle) and particle density distribution in the foil (bottom two figures) at 51st turn from the beginning of beam painting.

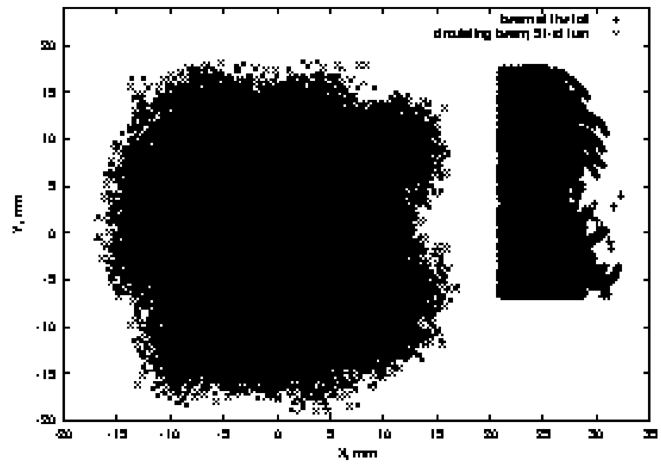

Figure 7.7. Circulating beam after painting (51st turn) and particle population at the foil.

The Booster also typically operates at a reduced duty factor, less than 1 Hz, whereas the Proton Driver will operate at 15 Hz continuously. The Booster operational repetition rate will change in the future with the Boone and NuMI experiments to as high as 10 Hz. It is possible that foil damage may become a factor and will have to be dealt with.

There are two basic concerns with the Proton Driver foils, heat dissipation and type of mount.

The stripping foil will reach temperatures of ~800 K. This temperature may be of concern in the mounting of the foil. The Fermilab Booster foils are simply bonded to a thin copper support with super glue. There has never been a problem with this kind of mounting. However the Booster has never run beam at 15 Hz for sustained periods, so average temperature rise has never been a problem. If the foil actually reaches sustained temperatures this high, another mounting technique may have to be used. Keep in mind that even though the foil may get very hot at the beam location, the foil is exceedingly thin and the amount of heat transmitted to the foil holder will be small. The metal holder will be capable of dissipating a large amount of heat relative to the foil so a simple glue bond may suffice. This is not considered a serious matter; however. there are many ways of mounting the foil.

The foil will have two free edges and this is also of some concern. (See Fig. 7.2 for the foil dimensions.) Carbon foils this thin have a tendency to curl up. If this proves to be the case then the foil may have to be mounted with only one free edge as done in the Booster. However this means the foil will be approximately twice as long. This is not desirable since there would be more interactions of the circulating beam with the foil. On the other hand, if necessary, it can be done.

7.1.5. Conclusions

An injection painting system, consisting of two sets of horizontal and vertical kicker magnets, produces the quasi-uniform density distribution of the circulating beam required for the beam space charge effect reduction and emittance preservation at injection.

The calculated stripping efficiency is 99.2%, and the estimated yield of excited $H^o(n)$ atoms with $n \geq 5$ is 0.016%. These atoms will contribute protons to the beam halo.

The temperature buildup during the injection pulse and steady state temperature of the foil are calculated from an analytical distribution of proton hits using ANSYS code. The instantaneous temperature buildup, calculated with contributions of multiple collisions, ionization loss from protons and electrons accompanying the stripping process, is a little less than 200 K.

With only emission as a cooling mechanism, the foil temperature reaches a steady state of ~800 K after about 10 cycles of injection, that is in less than one second.

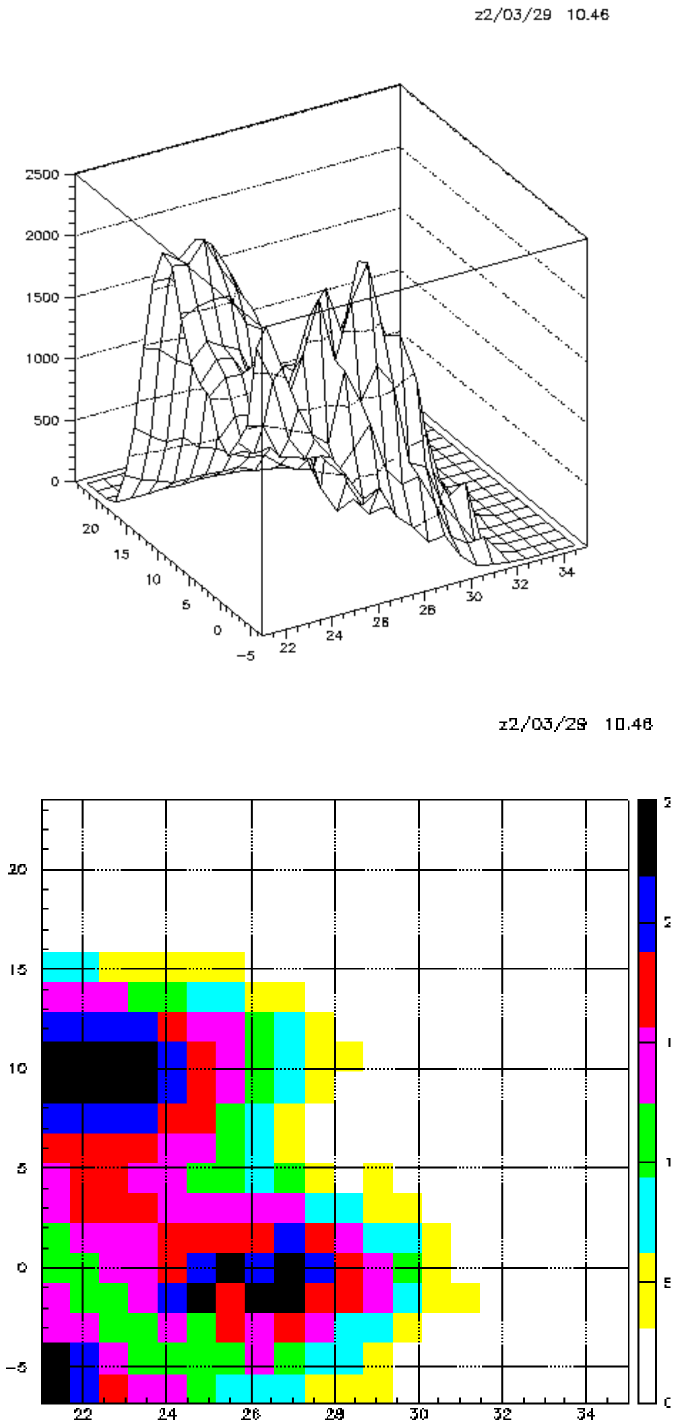

Figure 7.8. Particle distribution at the foil.

7.2 Extraction

J. Lackey

7.2.1 Introduction

The 8 GeV beam extraction is implemented using a standard single turn fast extraction system. The system presented here is the most compact system in terms of the amount of contiguous machine circumference required to accommodate the extraction equipment. Only the drift spaces of two adjacent cells are required for all of the extraction devices and the extraction system can be inserted into any two adjacent cells in either straight section. Possible other schemes discussed in section 7.2.6 would occupy more of the machine circumference but might have other beneficial properties such as faster kicker systems requiring a smaller notch in the beam or would allow the insertion of other required machine elements between the kickers and septum.

In order to avoid beam losses on the downstream extraction elements a notch or gap in the beam is required. This notch must be of a length equal to the effective rise time of the extraction kickers. It is assumed that the notch is created external to the machine.

7.2.2 Extraction System Elements

The extraction system consists of three primary elements: fast kickers, septum magnet and a system of orbit bump magnets to maintain the required circulating beam aperture with respect to the septum. The layout of the extraction system is shown in Figure 7.9. The layout of the septum and bump magnets is shown schematically in Figure 7.10.

7.2.3 Kickers

The kickers are a set of five 16.67-ohm transmission line type magnets. The impedance of the kickers is chosen to be equal to the impedance of three standard 50-ohm cables connected in parallel. The next usable impedance is 25 ohms but a choice of this impedance would require more kickers than can fit into the drift space of a single cell. The use of 25-ohm kickers is discussed in section 7.2.6.

The kickers are designed to kick the beam vertically. The transverse dimensions are chosen to allow for a reasonably thick walled non-metallic beam pipe presumably made of ceramic of some other appropriate material. A magnet length of one meter will allow five kicker magnets to fit comfortably in a single drift space. The strength of the kicker system is sufficient to kick a 90π mm-mrad beam across a 10 mm septum. The kicker parameters are listed in Table 7.3.

7.2.4 Septum

In this design report the use of a single septum magnet is assumed. The aperture of the septum is designed to be as large as is reasonably possible. The larger aperture is highly desirable since it reduces alignment tolerances and allows the extraction channel to accommodate some amount of halo in the beam. The septum parameters are listed in Table 7.3.

7.2.5 Orbit Bumps

A set of magnets designed to create a local orbit bump in the same drift space as the septum is required to maintain a desired circulating beam aperture with respect to the septum. Maintaining a large circulating beam aperture is necessary to insure that the collimators will intercept beam losses and the extraction elements will not become radioactive. These bump magnets are necessarily very short and very strong. Their design and implementation will have to be done carefully in order to avoid creating strong perturbations to the lattice because of high order field components. Two such systems are currently in use in the present Booster and their high order fields are significant, particularly the sextupole component.

The amplitude of the local bump sets the aperture with respect to the septum. At injection the bump pushes the beam a full 2 inches below the septum. The aperture is reduced as the beam energy increases but the design is such that the circulating beam aperture underneath the septum is 90π mm-mrad at extraction.

The design is done such that the magnets can be powered DC; ramping is not necessary. Ramping the bump magnets could potentially be beneficial but the cost would likely be prohibitive. The orbit bump magnet parameters are listed in Table 7.3.

7.2.6 Alternative Extraction Layouts

Other layouts for the kickers are possible. It would be possible to move the 16.67 ohm kickers upstream one cell. There the phase advance is more advantageous and the kickers could be run at lower voltages or fewer kickers could be used. However any equipment placed in the cell between the kickers and septum would have to accommodate the relatively large kick displacement of the extracted beam. The advantage of this layout is that other equipment *could* be put into the intervening cell if necessary.

One could also use lower impedance 25-ohm kickers. The advantage of lower impedance kickers is that the effective field rise time of the 25-ohm kickers is significantly shorter than the 16.67 ohm kickers and would require a shorter gap in which to rise. The cost is that at least two more kickers are required (for a total of 7) and would take up more longitudinal space in the machine.

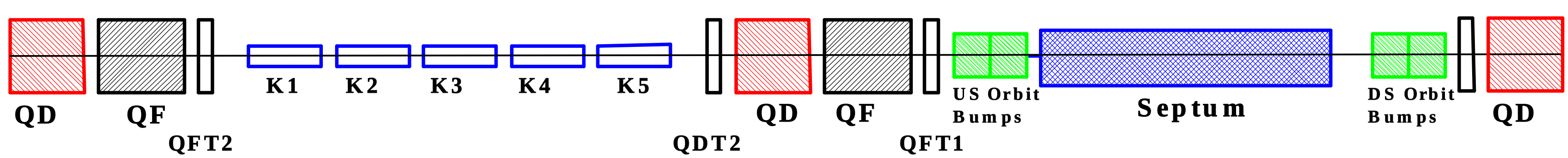

Figure 7.9. Vertical extraction system layout.

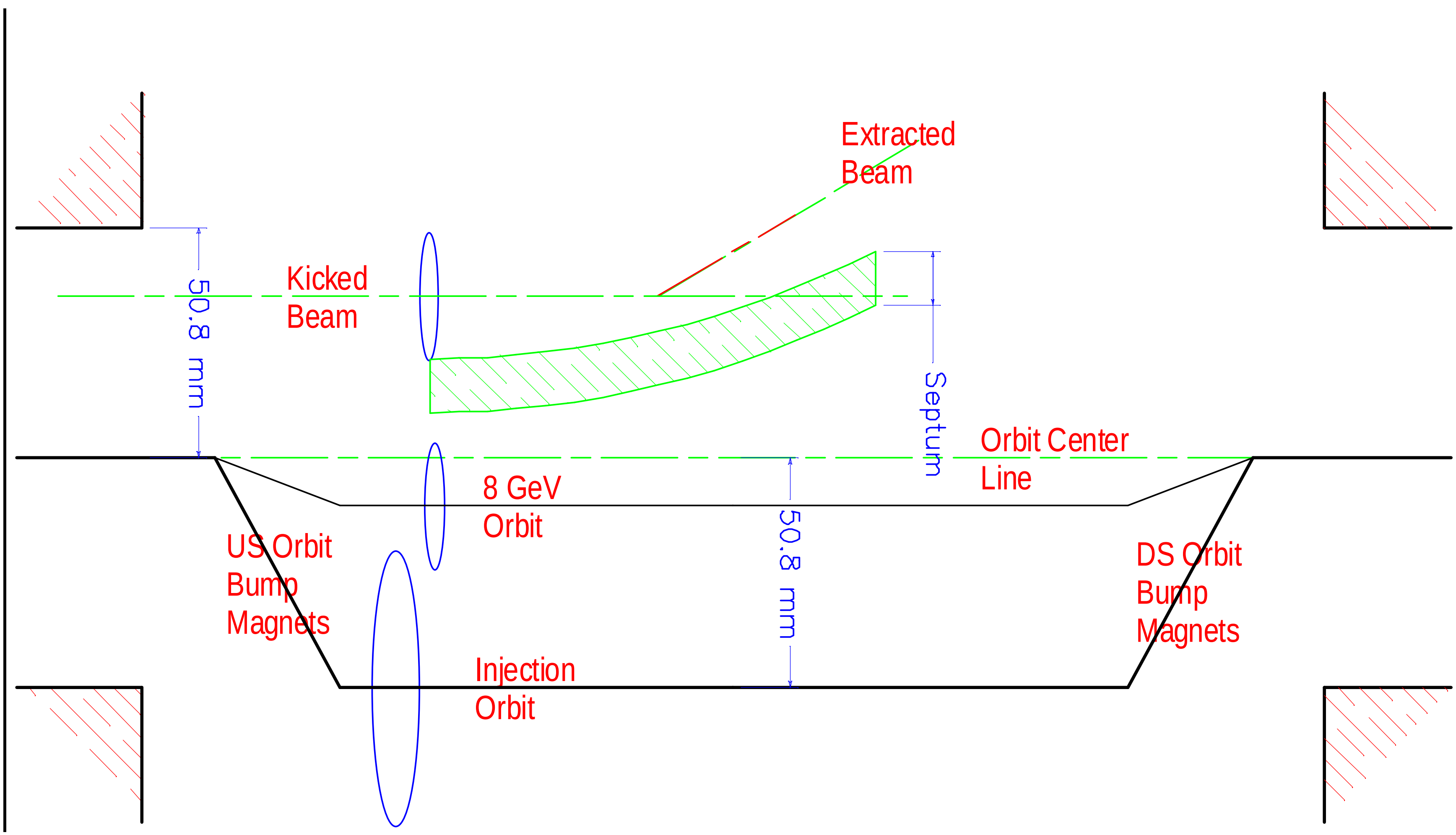

Figure 7.10. Orbit bump and septum in the extraction straight.

Table 7.3. Parameters of the Extraction System

	KICKERS	SEPTUM	ORBIT BUMPS
Number of Magnets	5	1	4
Magnet Length (m)	1	4	0.25
Insertion Length (m)	1.2	4.4	1 (2 magnets)
Effective Length (m)	1.16	4.025	0.415
Bend Center Spacing (m)	1.2	N/A	0.5
Pole tip Width (cm)	11.43	5.54	15.2
Pole tip Gap (cm)	16.51	2.54	16.51
Number of Turns	1	1	128
Inductance (μH)	791	10.96	7720
Nominal Current (kA)	2	21.56	0.98
Nominal Voltage (kV)	67	3	0.0202
Impedance (Ω)	16.67	N/A	N/A
B field (Tesla)	0.0223	1.08	0.941
Bend Angle (mrad)	0.75	145.5	96.02 @ 400 MeV
Current Pulse Length (μs)	1.6	250	DC
Magnet Fill Time (ns)	47.5	N/A	N/A
Current Rise Time (μs)	0.05	125	N/A
Field Rise Time (ns)	68.9	N/A	N/A

References

[1] The Proton Driver Design Study, Fermilab TM-2136, December 2000.

[2] I.S. Baishev, A.I. Drozhdin and N.V. Mokhov, STRUCT Program User's Reference Manual, SSCL-MAN-0034 (1994); http://www-ap.fnal.gov/~drozhdin.

[3] JHF Accelerator Design Study Report, KEK Report 97-16, JHF-97-10, March 1998, p3-67 - 3-71.

[4] A. Drozhdin, O. Krivosheev, “The Fermilab Proton Driver Painting Injection Simulations,” FERMILAB-FN-694 (2000).

Chapter 8. H^- Source and Linac Improvements and Upgrade

M. Ferguson, J. Lackey, E. McCrory, D. Moehs, N. Mokhov, A. Moretti, M. Popovic, M. Shea, R. Tomlin, R. Webber, D. Young

A substantial upgrade of the existing Linac will be required to meet the needs of the Proton Driver specified here. In particular, it is required that we provide 600 MeV H^- ions to the Proton Driver at a rate of 10^{18} ions per hour. Thus, an upgraded Linac with higher energy and a smaller and brighter beam is required.

8.1 Introduction

8.1.1 Impact of Requirements on Linac

The synchrotron proposed in this report will require that the Linac produce a beam as specified in Table 8.1.*

Table 8.1. Linac Parameters - Present and Upgrade

Item	Present	PD2	Units	Increase
Ion species	H^-	H^-		
Kinetic energy	401.5	601.5	MeV	1.50
Emittance	7	3	π mm-mrad	0.43
Beam current	50	50	mA	1.00
Brightness	1.0	5.6	mA/(π mm-mrad)^2	5.44
Pulse length	64	90	μsec	1.41
Ions per pulse	2.00×10^{13}	2.81×10^{13}	per 15 Hz pulse	
Pulses per hour	19,000	54,000		2,84
Uptime	0.8	0.8		1.00
Ions per hour	3.04×10^{17}	1.21×10^{18}		4.00

Thus, the Linac will be required to (1) add extra acceleration at the end of the existing Linac, (b) increase the pulse length (c) increase the overall repetition rate (e.g., use more of the 15 Hz pulses) and (d) decrease the losses in the Linac enough to allow continued hands-on maintenance.

8.1.2 H^- Source and Linac Parameter Table

We propose to build this 600 MeV Linac with a new injection scheme and with an extra segment of 200 MeV acceleration in the transfer line to the new synchrotron. The injection will consist of a new ion source, a 2.5 MeV radio frequency quadrupole (RFQ)

* The number of pulses per hour in this table takes into account the measured average number of pulses per hour requested of the Linac since January 1, 2001 (~1000) and the imminent request for 5 Hz operation of MiniBoone (18,000 per hour). The actual uptime measured over this period is only about 40%.

and a new 10 MeV drift tube tank at 201.25 MHz. All of these components need to accelerate over 50 mA of beam for 90 μsec. Table 8.2 details these specifications.

Table 8.2. Parameter Table for 600 MeV Linac and Ion Source

	Ion Source	LEBT/ Chopper	RFQ	Match Section	New Tank 1	DTL	CCL	HEBT	New CCL
Type	H^-	Electro-static	Vane	*TBD*	RGDTL	Drift-Tube	Coupled -Cavity		Coupled -Cavity
Output Energy (MeV)	0.05	0.05	2.5	2.5	10	116	401	401	601
Output Current (mA)	66	66	55	55	52	50	50	50	50
Emittance (π mm-mr, 95%)	1.0	1.2	2.0	2.6	2.8	2.8	3	3	3
Frequency (MHz)			201	201	201	201	805	805	805
Pulse Length	90	90	90	90	90	90	90	90	90

8.1.3 Pulse Length Requirements

In order to achieve the desired number of ions per pulse, it will be necessary to establish a longer beam pulse than is currently produced. We currently have 64 μsec available for accelerating beam. With trivial adjustments in the timing of the RF pulse, we can increase this by 32 μsec, which meets the required pulse length of 90 μsec.

This 90 μsec pulse is achieved by using most of overhead built into the system. The high-voltage systems in the new section of the Linac must be able to produce this 90 μsec with an overhead factor of 20%.

8.1.4 Achieving Acceptable Losses

The following table outlines our target level for the losses in the new machine.

Table 8.3. Linac Particle Loss Budget

Item	Present	PD II	Units	Change
Losses (Meas & tolerable)	2%	0.23%		9
Instantaneous Losses	1.00	0.12	millamps	9
Ave Current Lost@ 15 Hz	1.44	0.23	microamps	6
Ave current Lost in 1 hour	0.019	0.19	microamps	0.1

In the Linac, presently operating for the Tevatron in collider mode at about 1000 pulses per hour, the losses are acceptable. These are approximately a factor of ten lower than the generally accepted criterion for hands-on maintenance, which is 100 mrem/hour at 1 foot. Thus, we can tolerate a factor of 10 increases in activation without impacting our ability to work on the machine. With this criterion and taking into account the difference in the beam requests, we can tolerate a fractional loss in the Linac beam of about 0.23%—a factor of ten improvements over present-day levels.

Decreasing the transverse emittance in the Linac will reduce losses. The largest fractional increase in the transverse emittance of the present Linac beam is through Tank 1—we see an increase of about a factor of five from the ion source to 10 MeV. A redesign of the Linac up to 10 MeV for optimum emittance is therefore necessary. We estimate that a new ion source, coupled tightly to a 2.5 MeV RFQ, which itself is coupled tightly to a new, shorter "Tank 1" would yield an emittance under 3 π mm mrad—a factor of two improvement in emittance, and a factor of 5 improvement in brightness.

A detailed study of losses in the present Linac will need to be conducted. Most of the losses we see now are due to a mismatch in the capture between the 201 MHz and the 805 MHz segments, but significant transverse mismatches also exist. Moreover, extensive studies have been published in recent years detailing the calculations necessary to predict emittance growth in ion linacs. It will be necessary to understand these calculations and how they relate to our situation.

8.2 Low-Energy Improvements

The redesigned low energy section utilizes a single exchangeable ion source coupled closely to a single RFQ via an electrostatic transport region, which will also serve as an electrostatic chopper. Based on the SNS design, a double valve system will facilitate ion source exchange removing the need for two RFQs. Replacing the Cockcroft-Walton with this system allows for the possibility of improving the present H^- Magnetron ion source as well as considering other H^- sources with higher brightness.

8.2.1 Ion Source

Details of the development of negative hydrogen ions sources can be found in Ref. [1]. A modest increase in beam intensity and brightness is required here. It should be feasible to upgrade the Fermilab Magnetron Surface Plasma Source (SPS) for the required intensity, duty factor and beam quality without sacrificing the reliability and availability from its proven past performance. For matching to an RFQ a circular extraction aperture is proposed following the Brookhaven design. [2] An optimized system, including a suppression electrode, should produce longer pulses with higher beam intensity, better beam quality and some beam space-charge neutralization. Source lifetime will be a key element in this system and improved cathode and anode cooling may be necessary to handle the increased discharge pulse length and intensity.

To produce beams of the highest brightness it would be possible to use a SPS with a Penning discharge, also known as the Dudnikov-type source. Transition from a noisy mode of operation to a noiseless discharge can increase the brightness by a factor of 10 or more. The DESY RF type volume source is also a viable alternative. [3] A small injection of cesium and adjustment in the extraction system should give the desired intensity of 66 mA. Further discussion can be found in Ref. [1].

A 50 keV extraction voltage from the ion source is proposed for extracting sufficient current from the source and to allow for a short electrostatic focusing structure closely coupling the source to an RFQ. The increased energy of the H^- ions allows easier injection and greater transmission through the RFQ.

For ion source optimization and testing it will be necessary to resume operation of the ion source test stand and to upgrade the equipment. In prototyping new source equipment it will be possible to use previous developments from ANL, BINP, UMD, BNL, ISIS, and DESY. Testing of the DESY type source is possible using an RF proton source from NEC as a prototype.

8.2.2 Low Energy Beam Transport (LEBT) and Chopper

An ion beam from a compact ion source has a very high current density ($J \sim 1$ - $3\ A/cm^2$) and perveance. To transport these beams it is necessary to use deep space-charge neutralization (compensation) or very strong continuous focusing by electrostatic forces as in the RFQ. Sometimes both are required.

A detailed description of a strongly focused electrostatic lens designed to couple the beam to the RFQ along with discussion of the need and possibilities for additional chopping can be found in PD1. [1] Briefly, The last Einzel lens in the LEBT will be segmented and a pulsed voltage applied in order to excite a pair of these segments such that the beam from the source deflects enough to fall outside the aperture of the RFQ. LBL has designed and built a prototype chopper for the SNS using this technique. [4] However further development will be required to achieve good focusing for the 66 mA current required. Laser beam chopping may be the best second choice as it allows for a very short LEBT section.

8.2.3 Description of Radio Frequency Quadrupole (RFQ) Structure

Using the design code PARMTEQ, a one-section RFQ has been designed to transmit a 66 mA beam from 50 keV to 2.23 MeV. The transmission efficiency at this intensity is 98.8%. Table 8.4 lists the parameters of this RFQ.

8.2.4 Matching Section

The beam from the RFQ must be matched to the DTL acceptance for the design current in all three planes. There are at least two ways to match the beam to the DTL. The first consists of three quadrupoles and one RF gap or buncher. The virtue of this arrangement is that the elements are tunable which is desirable to accommodate a range of beam intensities. It also allows space for the insertion of beam diagnostic equipment. A second method requires four more RFQ cells at the end of the RFQ and a half-length quadrupole in the DTL. It may be desirable to use a combination of these two methods.

Table 8.4. Single Section RFQ Parameters

Type	Conventional Four-Vane	
Frequency	201.25	MHz
Input Energy	0.050	MeV
Output Energy	2.23	MeV
Input Current	66	mA
Aperture (r_0), (constant aperture design)	0.6	cm
Modulation	1.70	m
Intervane Voltage	129.3	kV
Maximum E Field (2.05 Kilpatrick)	30.17	MV/m
Duty Factor (90 μs, 15 Hz)	0.135	%
Peak Power	600	kW
Length	3.4	m
Transmission	98.8	%
Input Emittance (normalized, rms)	0.25	π-mm-mrad
Output Emittance (normalized, rms)	0.40	π-mm-mrad

8.3 Side-Coupled Cavity Modules From 400 MeV To 600 MeV

Additional acceleration to 600 MeV is required. Five new side-coupled cavity modules will be added to the transfer line to the new booster synchrotron, based on the design and techniques used for the Linac upgrade of 1993.

8.3.1. 400 MeV Beam Transport Line

The transfer line between the 400 MeV Linac and the additional 600 MeV modules has to satisfy several conditions:

- The line has to follow part of existing enclosure,
- The beam has to be cleanly extracted,
- The beam must be transported to the elevation of the new transfer tunnel and
- The beam must be matched to the accelerating structure.

It is assumed that beam is extracted using a DC magnet that fits between the 400 MeV Chopper and quadrupole Q2. The dipole magnet bends the beam by 20° and has a field of 7.4 kGauss with a bending radius of 4.25 meters. The extraction functionality of the present 400 MeV line is preserved. Two more horizontal bending magnets are needed to position beam next to the southern wall in the MuCool test area. The six quadrupoles in the line are used to control beam size as well dispersion in the horizontal plan.

To control the beam longitudinally, we will need two 3-cell bunching cavities. They will be positioned 22 meters away from the end of 400 MeV section and 5 meters before entrance to the new accelerating structure. To bring beam to the new elevation, two equal vertical magnets with opposite bends are used. The present design assumes that all bending magnet are the same, that quadrupoles are old “200 MeV quads” and that new accelerating modules will be copy of exiting design.

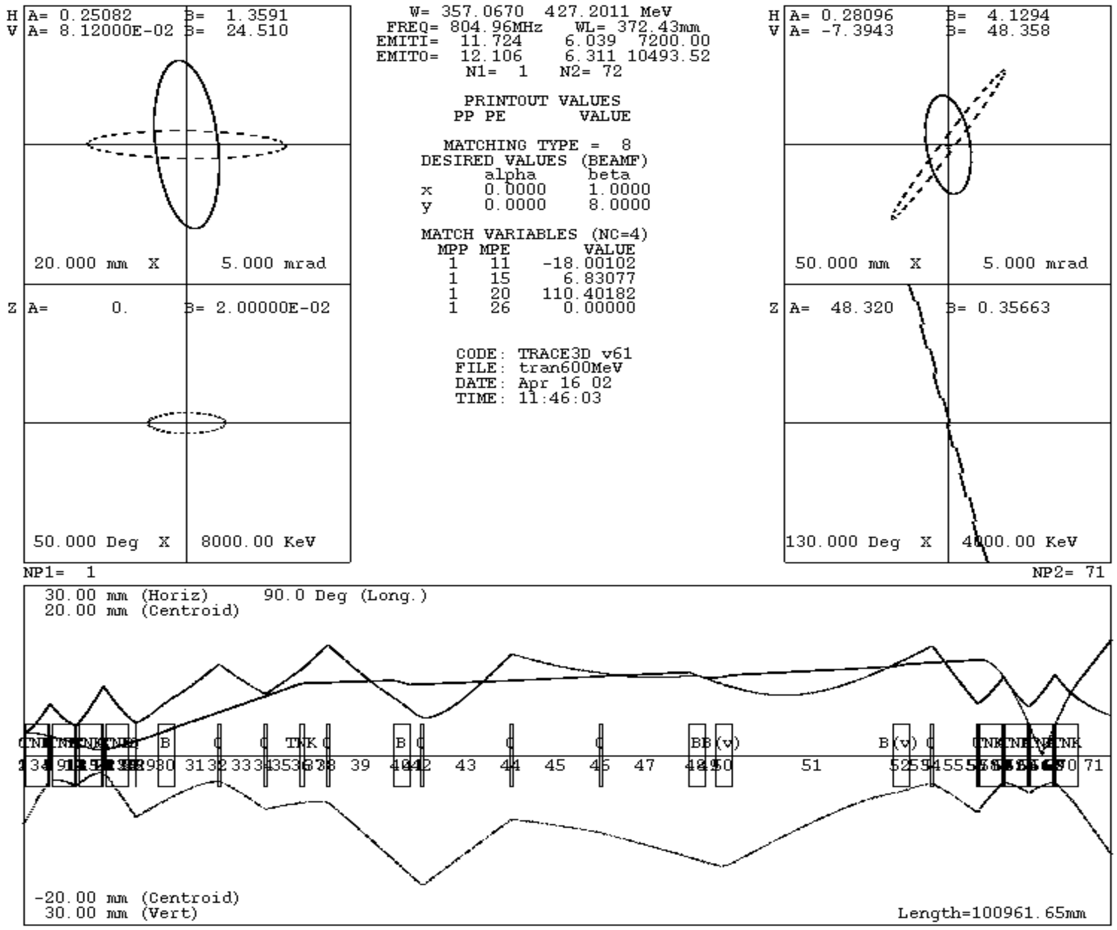

Figure 8.1. Trace-3D simulation of the 400 MeV beam transport line.

8.3.2 Options for Extending the Energy

The side-coupled structure and the Litton 12 MW klystrons used for the last ten years to extend the Linac energy from 116 MeV to 400 MeV have been satisfactory and reliable. Therefore, the choice of RF structure and power source to extend the Linac energy from 400 MeV to 600 MeV is to simply build more accelerating modules and use the same proven klystrons. The technology for constructing side-coupled cavities and building the RF systems was developed at Fermilab and the expertise exists to replicate the required systems for extending the Linac to this higher energy.

Using the more recent technology of superconducting accelerating cavities to extend the energy has been considered. If the long-range plan for the Linac were to ultimately extend the Linac energy beyond 1.0 GeV, then the development of superconducting accelerating cavities might be more favorably considered for the 200 MeV Linac extension. However the most cost-effective and simple solution is to replicate the existing Fermilab technology and this is what is proposed in this report.

8.3.3 Cavity Parameters

In order to extend the Linac energy by 200 MeV without exceeding the criteria for excessive sparking in the cavities, i.e. approximately 1.4 times the Kilpatrick limit of 26 MV/m at 805 MHz, 4 or 5 modules will be required. For this design a module is defined as four sections containing a fixed number of accelerating cells with the RF energy in the sections connected to each other via couplers of length 3/2 $\beta\lambda$. This space also allows the incorporation of quadrupole focusing elements within and between the modules. The RF power required for each module must not exceed the maximum RF power limit of the klystron used to excite the module. If these criteria are used in the design, then 5 modules of 40 MeV energy gain would be required. This segmentation of the structure results in a reduced peak surface voltage in the accelerating cavities, but this reduction would allow more stable operation (less sparking) for longer RF pulse-lengths and higher accelerated beam currents. Since these modules would be installed in a new enclosure containing the transport system to the synchrotron, the rigid sparking limits required in the old CCL modules would not be required.

At this stage of the design it is reasonable to use the same geometry of the accelerating cells that was developed for the lower energy side-coupled cavities. The program SUPERFISH was used to calculate the transit time factor T, the effective shunt impedance ZT^2 and the ratio of the maximum surface field and average accelerating field E_{max}/E_0 at several values of β corresponding to the energy range 116 to 400 MeV. Work was also done with the three-dimensional code MAFIA to confirm the results. Third order fits to the SUPERFISH results were made to derive the parameters necessary for the design of the accelerating sections. These data are used in the design of the modules from 400 to 600 MeV. These third order fits are:

$$ZT^2 = -34.700 + 266.92\,\beta - 247.07\,\beta^2 + 70.320\,\beta^3$$
$$T = 0.55963 + 1.2351\beta - 1.7236\,\beta^2 + 0.82560\,\beta^3$$
$$E_{max}/E_o = 1.5247 + 13.871\beta - 22.351\beta^2 + 13.507\beta^3$$
$$G/2 = -0.19017 + 4.1735\beta + 0.67878\,\beta^2$$

Using these parameters the design of the five modules to accelerate the beam from 400 to 600 MeV is shown in Table 8.5.

The grayed area displays the values for our existing Module 7, with the power numbers adjusted, through fudge factors on the shunt impedance and the total cavity power, to match the power measurements made on this operating cavity.

Table 8.5. CCL Module Parameters

Module #	Delta (KE)	KE(out)	Ave Beta	ZT**2	Lgth	E(max)	%E(k)	P(Cu)	P(cavity)	P(beam)	P(total)
7	44.4	401.5	0.70185	55.24	8.364	35.61	137%	7.6	7.6	2.22	9.79
8	40	441.5	0.72359	55.72	8.623	31.44	121%	5.9	5.9	2	7.91
9	40	481.5	0.74189	56.05	8.841	30.97	119%	5.7	5.7	2	7.73
10	40	521.5	0.75830	56.30	9.037	30.58	118%	5.6	5.6	2	7.58
11	40	561.5	0.77309	56.48	9.213	30.27	116%	5.5	5.5	2	7.46
12	40	601.5	0.78648	56.61	9.373	30.01	115%	5.4	5.4	2	7.35

Note that this table has very conservative values for the maximum electric field in the cavities: only about 20% over the Kilpatrick limit. The existing Linac was designed to a Kilpatrick factor of 140%, and the sparking rate is very acceptable. It is reasonable to redo this table with a more aggressive Kilpatrick factor and either (a) increase the energy out of this Linac segment (we estimate that an extra 5% of energy gain could be obtained in this way, to 630 MeV) or (b) reduce the number of cells in a section, thereby reducing the length of this addition.

8.3.4 RF Systems

The same Litton klystrons, locally built modulators/pulse-forming networks and computer controls will be used. The only change, other than modernization possibilities that may arise during the remanufacture of these items, would be a 20% increase in the pulse that the modulator/PFN can produce.

8.3.5 Maintenance Issues

The klystron gallery, containing the RF equipment, modulators, PFNs and controls for the five new 805 MHz cavities, should be built so that when the existing Booster is decommissioned, this new gallery may be connected to the exiting gallery. This will simplify the transfer of components between the galleries.

8.4 New Beam Diagnostics and Controls Requirements

The new Linac will need enhanced beam diagnostics and controls in order to measure the beam characteristics required to maintain the low losses specified in this proposal.

It will be necessary to include appropriate beam diagnostics in the 400 MeV transfer line to insure that the required bunching is maintained. Given the potential for a decrease by a factor of 10 in the losses in the existing Linac, it will be necessary to improve the character of the beam, our understanding of it and our ability to measure these losses.

The construction of this new accelerator will be an opportunity to upgrade and improve the Linac control system. For example, enhanced fast digitizers on all channels should be possible and would be desirable. Also, a simplified access to the data, possibly through the Web, should be considered.

8.5 Shielding Issues

The passive shielding that surrounds the existing Linac enclosure is, for the most part, inadequate for protecting adjacent areas from a sustained beam loss within the enclosure. A radiation safety system, utilizing 15 interlocked detectors, is installed to protect adjacent areas from excessive radiation levels. This same system will be sufficient for protecting the same areas for the proposed beam requirements, but modifications to the beam line component arrangement will likely require another shielding assessment to determine optimum interlocked detector locations. The 1991 and 1993 Linac Shielding Assessments can provide a description of the complex Linac passive shielding arrangement, and the associated interlocked detector arrangements.

Proposed modifications to the low energy end of the Linac may cause radiation levels near the existing 750 KeV end to increase. There is no passive shielding between the 750 KeV end of the Linac enclosure and the Pre-Accelerator enclosures. Depending on the positioning of the proposed RF cavities and RFQs, x-ray radiation levels in occupied areas may become excessive. In addition, it has been observed that varying amounts of backscattered radiation from the Linac enclosure finds its way into this area. This area is routinely monitored with an area film badge and these data show that doses in excess of 200 mrem/quarter, both for gamma and neutrons, are common.

The current proposal to have Linac beam re-directed at the south end of the existing Linac towards the new 600 MeV transport line will have to be done very cleanly to prevent beam from being inhibited by the 400 MeV labyrinth interlocked detector. The passive shielding above the existing, non-occupied utility portion of the Linac will be insufficient for the proposed transport line. Additions and modifications of the existing Linac Radiation safety system will have to be made.

The proposal for using 12.5 feet of passive earth shielding over the 600 MeV transport line will require a radiation safety system to limit beam loss within that enclosure. Consideration should be made to make the 600 MeV enclosure completely separate from the existing 400 MeV enclosure. This would require separate electrical and radiation safety systems, but would allow for the operation of the existing Linac while the 600 MeV portion is open for access.

8.6 Recent Measurements of the Losses in the Linac

Currently, we estimate losses in the high-energy segment of the existing Linac to be between 0 mA and 3 mA. The beam toroids do not measure any beam lost in the high-energy segment of the existing Linac. However, if we examine the loss monitors there carefully, there is possibility of a non-negligible loss in this segment. A measurement has been made recently to determine the correlation between the losses and the beam current lost. The sum of the loss monitors in the 805 MHz segment is correlated with the beam lost in this segment, as measured from the toroids, when we intentionally mistune an element at the beginning of the segment. We measure a correlation of about 20 “counts” on this sum per milliamp lost on the toroid. A constant reading of 54 “counts” on this channel, which is typical today, would correspond to 2.7 milliamps of beam lost in this segment of the Linac. This assumes that there is no offset in this loss reading. Naturally, the actual lost beam current is less than or equal to this value.

Assuming a constant loss throughout the 64 m 805 MHz segment of the Linac, then we observe at most 42 μA/meter of loss. At 116 MeV, this is a peak loss of about 5 kW; at 401 MeV, 16.8 kW. Normalizing to our beam-on duty factor of 0.09%, times our beam request duty factor of about 2% of the pulses actually being used, these losses become 0.1 to 0.3 W/m.

At this level of loss, we measure activation in the Linac to be as high as 12 mrem/hour at 1 foot, after 4 hours of cool down. The maximum activation measured in the 401 MeV transfer line to the Booster occurs at the Lambertson (which is scheduled for replacement in the summer of 2002) of 130 mrem/hour at one foot, after a 4-hour cool down. Thus, these levels are adequate for hands-on maintenance.

In conclusion, the upper limit for the beam lost in the 805 MHz segment of our existing Linac is 0.3 watts per meter. The peak activation is measured in the 805 MHz segment as 12 mrem/hr at 1 foot, measured at approximately 200 MeV, where the peak losses are less than 0.2 W/m.

<u>Appendix</u> 402 MHz Low-Energy Linac Replacement

Although not necessary for PD2, it would be highly desirable to consider the replacement of the entire drift-tube section of the Linac as part of the project for upgrade of the low-energy portion of the Linac. In the PD1 [1] arguments were made for the replacement of the Cockcroft-Walton preaccelerators by the more modern and accepted Radio-Frequency Quadrupole (RFQ) accelerating structure. Also it was pointed out that a large degradation in the quality of the accelerated beam occurs in the first drift-tube accelerating cavity, up to 10 MeV, as a result of the inferior alignment of the quadrupoles and the poor fabrication techniques used when this cavity served as a prototype for the fabrication of the other eight cavities in the Linac. The 200 MHz drift-tube section of the Linac is now over 30 years old and increasing operational demands are continually being requested.

The RF system for the DTL will soon require modifications to replace tubes that are no longer commercially available. The hard-tube modulators will require a redesign. The final power amplifier tubes are no longer available and rebuilding the failed tubes will be limited. For increased beam pulse-lengths, the power supplies for the pulsed quadrupoles will require replacement or extensive modification. Degradation of the elastomer seals on the drift-tube tanks will become a greater problem.

The technology of the design and fabrication of drift-tube accelerating structures has advanced considerably since the Fermilab Linac was constructed. Higher frequency structures powered by klystron-based RF systems are now the preferred choice. Permanent-magnet quadrupoles for radial focusing can be conveniently installed in the smaller drift-tubes. An example of a more modern DTL Linac was the one constructed for the Super-Conducting Super Collider Project. A commercial company fabricated this Linac. This company is routinely constructing DTL linacs that are mainly being sold for medical applications**.** [5,6] The technical specifications of one of their designs meet closely the requirements for a replacement for the Fermilab DTL. The budgetary cost estimate furnished at our request is considered a reliable estimate for the replacement cost of the Fermilab DTL.

The proposed system beyond the ion source and LEBT (Low Energy Beam Transport) consists of the following components:

- RFQ: A conventional four vane RFQ operating at 402.5 MHz to bunch and accelerate a 35 keV H^- ion beam up to 3.0 MeV is proposed. A matching section is built into the high-energy section of the RFQ to permit direct injection into the Ramped Gradient Drift Tube Linac (RGDTL) structure.

- RGDTL: The RFQ is close-coupled to a short section of a conventional DTL operating at 402.5 MHz. The fields in The RFQ are ramped to match the beam phase space from the RFQ at its input. The RGDTL accelerates the bunched 3 MeV beam from the RFQ up to 7 MeV for injection into the main DTL structure.

- DTL: A standard drift tube Linac operating at 402.5 MHz accelerates the H^- beam up to 70 MeV. This 20-meter length DTL consists of three tank sections with 102 drift tubes mounted in them. Each tank is made up of four sections and is driven by a 4 MW klystron RF system. RF power is fed to the tank through a waveguide window mounted on one of the tank sections.

- Matching Section: The Coupled Cavity Linac (CCL) structure used in the 400-MeV upgrade has a higher accelerating efficiency than the DTL above 70 MeV. The longitudinal phase of the bunched beam at 70 MeV in the 402.5 MHz DTL allows the beam to be matched into the 805 MHz CCL. And since the fabrication of CCL structure is well understood at Fermilab, it is a design choice to fabricate two CCL modules to extend the acceleration of the beam to 116 MeV where it would enter the existing CCL accelerating modules. The phase space of the 70 MeV H^- beam from the DTL is matched into the CCL using a 3.25 meter beam transport system containing two bunchers operating at 805 MHz and nine quadrupole magnets. The components used in the present system could be used in the lower energy matching system.

- Coupled Cavity Linac: The final stage of the system would be two side-coupled modules of conventional Fermilab design. This stage would consist of four sections of coupled cavities joined by 3/2 $\beta\lambda$ bridge couplers to accommodate the radial focusing quadrupoles and RF fed from the center-coupling cell of the module. These two modules would accelerate the beam to 116 MeV.

- Klystron/Modulator Systems: Three 4 MW, 402.5 MHz klystrons are used to power the constant gradient DTL tanks. The 10 MW RF systems for the CCL would be replicates of the existing 805 MHz RF systems in the Linac.

Table 8.6 lists the parameters of the proposed replacement DTL for the present Fermilab DTL.

Table 8.6. Parameters of the New 402 MHz Low-Energy Linac Section

			DTL				CCL		
		RFQ	Tank 1	Tank 2	Tank 3	Tank 4	Match Section	Mod 1	Mod 2
Input Energy	MeV	0.035	3	13.4	32.9	51.6	70.3	70.3	93.3
Output Energy	MeV	3	13.4	32.9	51.6	70.3	70.3	93.3	116.5
Delta E	MeV	2.965	10.4	19.5	18.7	18.7	0	23	23.2
Beam Current	mA	70	55	55	55	55	50	50	50
Frequency	MHz	402.5	402.5	402.5	402.5	402.5	805	805	805
Beam Pulse Length	usec	90	90	90	90	90	90	90	90
RF Pulse Length	usec	130	130	130	130	130	125	125	125
Rep Rate	Hz	15	15	15	15	15	15	15	15
RF Duty Factor		0.2%	0.2%	0.2%	0.2%	0.2%	0.2%	0.2%	0.2%
Average Axial Field	MV/m		2.4 to 4.6	4.6	4.6	4.6	7.5 to 7.35	8	8
Length	m		4.5	6	6.1	6.2	3.25	4.8	4.9
Structure Power	MW		1	1.75	2	2		5.4	5.4
Beam Power	MW		0.63	1.07	1.02	1.02		1.38	1.39
Total Klystron Power	MW		2.5	3.8	4	4		8.5	8.5

The cost estimate of this 402 MHz low-energy system in 2002 dollars is as follows (in K$):

Components, including the RFQ, RGDTL, DTL, matching section, CCL, DTL rf systems, matching section rf systems, beam diagnostics, and the control systems	24,649
Installation and commissioning	2,500
Building modifications	500
TOTAL (K$)	27,649

References

[1] "The Proton Driver Design Study," FERMILAB-TM-2136 (December 2000).

[2] J. Alessi, "Performance of the Magnetron H^- Source on the BNL 200 MeV linac", ICFA-HB2002 Workshop, April 8-12, 2002, Fermilab.

[3] J. Peters, Rev. Sci. Instrum., **69**, 992 (1998)

[4] J. Staples, et.al., “The SNS Front End Accelerator Systems”, PAC’99 Proceedings

[5] Private Communication from AccSys Technology, Inc.

[6] A. Lennox, R. Hamm, “A Compact Proton Linac For Fast Neutron Cancer Therapy”, Proceedings of the Third International Topical Meeting on Nuclear Applications of Accelerator Technology.

Chapter 9. 600-MeV and 8-GeV Beam Transport Lines

The synchrotron based PD2 study includes three new beam transport lines.

1) A 400 MeV line connecting the existing linac and the new linac extension. This line is about 90-m long and includes a vertical drop from the existing linac level (near the surface) to the new linac level (13.5 ft. deep).

2) A 600 MeV line connecting the new linac and the Proton Driver. It is about 254-m long and also includes a vertical drop from the new linac level to the Proton Driver level (27 ft. deep).

3) An 8 GeV line connecting the Proton Driver and the Main Injector. It has a total length of about 900-m and consists of two sections. The upstream section, about 420-m long, connects the synchrotron to the present MI-8 enclosure. It is followed by a 480-m section in the MI-8 enclosure. This beam line uses permanent combined function magnets, the same as the present MI-8 line.

The design of 1) is presented in Chapter 8. However, due to limited resources, the design of 2) and 3) has not been completed at the time of writing this report. This work will continue and will be included when this report is finalized to include the 8 GeV linac option.

Chapter 10. Civil Construction

R. Alber, R. Lackowski, E. McCrory, J. Sims

10.1 Introduction

This chapter outlines the civil conventional facilities required to house and support the proposed 8 GeV Proton Driver. An extension of the existing Linac Facility is required housing equipment to bring the beam energy from 400 MeV to 600 MeV. From the new Linac Extension, an enclosure will be required to inject the 600 MeV beam into the Proton Driver. In addition, an enclosure is necessary to carry the 8 GeV extraction line from the Proton Driver to the Main Injector.

10.2 Overview

10.2.1 Civil Construction

Civil Construction, for The Proton Driver, includes all below-grade beamline enclosures and all above-grade buildings, roads, parking, primary utilities, and primary services to accommodate the equipment for the operation of the Proton Driver on the Fermilab site.

The cost estimate for the civil construction, listed in Appendix 1 of this report, has grouped elements in a logical sequence as well as by facility function or type of construction work involved. While the cost estimate organization presents a reasonable construction scenario, it will not be identical with the actual subcontract packages nor is the final schedule of construction inflexible.

10.2.2 Site Construction

10.2.2.1 Wetlands Mitigation includes all of the compensatory floodplain construction.

10.2.2.2 Site Work and Utilities includes survey monuments, temporary power, construction access roads, tree protection, stream diversion, power and communication duct banks, 13.8 kV power feeders, and underground utilities including industrial cold water (ICW), primary cooling ponds, domestic water, sanitary sewer, chilled water supply and return, and final paving of all roads, and hardstand areas.

10.2.2.3 Landscaping includes construction yard removal, signage, site landscaping, and prevention of soil erosion.

10.2.3 Facilities Construction

10.2.3.1 Proton Driver Enclosure is a conventional below grade cast-in-place enclosure constructed to house the Proton Driver beamline.

10.2.3.2 Linac Extension is a conventional above and below grade building to house a new array of Klystrons.

10.2.3.3 Injection Enclosure is a conventional pre-cast enclosure constructed to house the injection beamline from the existing booster to the new Proton Driver enclosure. *A portion of this work must be accomplished during Booster beam off conditions.*

10.2.3.4 Extraction Enclosure is a conventional pre-cast enclosure constructed to house the extraction beamline from the new Proton Driver to the Main Injector enclosure. *A portion of this work must be accomplished during Main Injector beam off conditions.*

10.2.3.5 Proton Driver Service Gallery is an above grade service building used to house support equipment for the Proton Driver Enclosure.

10.2.3.6 Utility Support Building is an above grade utility building used to house equipment for process cooling equipment for the Proton Driver Enclosure.

10.2.4 EDI&A

10.2.4.1 EDI&A consists of all Engineering, Design, Inspection, and Administration costs associated with the Construction aspects of the project.

10.3 Detailed Facilities Descriptions

Construction of the Proton Driver Enclosure, Linac Extension, Extraction Enclosure, Injection Enclosure and above grade service buildings is similar to previously utilized and proven construction methods at Fermilab. Construction of all below-grade enclosures consists of conventional open cut type construction techniques. The architectural style of the new buildings reflects, and is harmonious with, existing adjacent buildings. Currently, the layout has been optimized for the accelerator. Future layouts will consider existing topography, watersheds, vegetation, natural habitat, and wetlands. All these aspects will be thoroughly addressed in the EA for this project.

Safety provisions for radiation, fire protection and conventional safety are included in this Project Definition Report. Energy-efficient construction techniques will be incorporated into all new structures. Quality assurance provisions will be part of all project phases including conceptual, preliminary, and final design, construction, and construction management.

10.3.1 Site Construction

10.3.1.1 Wetlands Mitigation

Detailed and specific definitions of the wetland area, floodplain and storm water management, archaeological concerns and ecological resources will be identified by environmental consultants resulting in the preparation, submittal and approval of a Floodplain/Wetland Assessment Report and an EA. All required permits will be obtained prior the start of construction. See Chapter 11 for environmental considerations.

After the environmental consultants report, modifications may be made on the location of roads, utilities or siting of structures to minimize the impact on the environment while still retaining the ability to construct this experiment in a cost effective manner.

10.3.1.2 Site Work and Utilities

Site Drainage will be controlled by ditches and culverts while preserving the existing watershed characteristics both during construction and subsequent operation. Permanent stream relocation of a portion of Indian Creek may be required for this project.

Minor road construction is anticipated for this project. The existing Kautz Road adjacent to the Antiproton complex will be out of service during construction of the Injection Enclosure. A temporary road will need to be installed to facilitate adequate traffic flow. Parking lots will be required at the Proton Driver Support Buildings.

Power, communications, and chilled water supply and return will tie in to existing systems at the intersection of the Main Injector Road and Kautz Road. These utilities will extend up to the Site.

Industrial Cold Water (ICW) will tie into existing utilities at the corner of Kautz and Giese roads. Primary cooling water will be taken from surrounding existing ponds.

Sanitary Service (SAN) and Domestic Water (DW) will tie into existing utilities at the intersection of Kautz and Giese Roads.

Natural Gas will tie into an existing gas line running along Giese road.

Excess and unsuitable spoil from the construction of the underground enclosures and caverns will be stockpiled on the Fermilab site in an appropriate manner. This material will then be used as nonstructural backfill for future projects.

10.3.1.3 Landscaping

Construction yards will be removed after completion of the construction phase of the project. All disturbed areas will be returned to a natural state or landscaped in a similar manner as found at other Fermilab experimental facilities. Erosion control will be maintained during all phases of construction.

10.3.2 Facilities Construction

10.3.2.1 Proton Driver Enclosure

The Proton Driver Enclosure is a cast in place enclosure 16 ft. wide and 9 ft. high with approximately 24.5 ft. of equivalent earth radiation shielding (26 ft. at all buildings). This region will house beam line components to accelerate protons to an energy of 8 GeV. See TDR-? and TDR-? for location and dimensions.

10.3.2.2 Linac Extension

The Linac Extension is a conventional above and below grade facility with approximately 26 ft. of equivalent earth radiation shielding. The below grade Linac Enclosure is a cast in place enclosure 12 ft. wide and 13 ft. high. The above grade Linac Gallery is approximately 30 ft. 4 in. wide and its height matches existing facilities.

10.3.2.3 Injection Enclosure

The Injection Enclosure is a conventional below grade 10 ft. wide by 8 ft. high precast concrete enclosure with approximately 24.5 ft. of equivalent earth radiation shielding. This enclosure will house the beamline components necessary to transport the 600 MeV beamline from the existing Linac to the proposed Proton Driver Enclosure.

10.3.2.4 Extraction Enclosure

The Extraction Enclosure is a conventional below grade 10 ft. wide by 8 ft. high precast concrete enclosure with approximately 24.5 ft. of equivalent earth radiation shielding. This enclosure will house the beamline components necessary to transport the 8 GeV beamline from the Proton Driver to the existing 8 GeV transport line enclosure. The existing 8 GeV transport line enclosure will be utilized to continue the beamline to the existing Main Injector.

10.3.2.4 Proton Driver Service Gallery

The proposed Proton Driver Service Gallery will consist of three above grade metal frame and wall panel buildings that house the equipment necessary to supply power, instrumentation and control the beamline components housed in the Proton Driver enclosure located below and adjacent to the service buildings. See TDR-? for building locations and dimensions. Total area of the building is approximately 50,000 sq-ft.

10.3.2.5 Utility Support Building

The Utility Support Building will be located in the center of the Proton Driver Service Gallery Campus. The above grade metal frame and wall panel building will house the equipment required for heat rejection and electrical distribution including chillers, pumps, and transformers. Total building area is approximately 12,000 sq-ft.

10.4 Civil Construction Issues for Linac Extension

10.4.1 Level of the new section of Linac

The level of the tunnel connecting the Linac to the new synchrotron should be lower than the existing Linac. Having it at the level of the new synchrotron may be too expensive. An intermediate level is indicated—the level of the current Booster seems appropriate.

10.4.2 Tunnel Dimensions

The tunnel that contains the new coupled-cavity modules for the new 200 MeV addition needs to be large enough to accommodate the cavities, room to move the cavities side-by-side down the tunnel, space for workers to navigate when two cavities are side-by-side and room to maneuver the wave guide from the penetrations to the cavities. Also, the tunnel should be large enough to accommodate conventional cavities or superconducting cavities, as a possible upgrade path. The existing Linac enclosure is artificially large because of the need to contain the massive 200 MHz Alverez structures.

The existing side-coupled cavity modules are about 7 feet 10 inches from the far wall and 3 feet 11 inches from the near wall. This smaller dimension translates to about 2 feet of walk-by space at the location of the wave-guide.

The stand for the modules is 29 inches wide, with an additional 5 inches for a small cable tray attached to the side or 34 inches total. It will be necessary to have two of these modules side-by-side in the tunnel. To maintain the 4-foot aisle on each side the overall width of the tunnel should be twice 4 feet plus 34 inches or a total of 13 feet 8 inches.

The wave-guide comes in from the wall at a top height of 9 feet 4 inches—this dimension would be difficult to reduce, so it will be retained. Thus, the new tunnel needs to be 10 feet high.

In summary, the dimensions of the tunnel should be about 13 feet wide and 10 feet tall.

10.5 Civil Construction Schedule

The following schedule is predicated on the assumption that <u>a funding profile to match the construction needs will be established and maintained</u>.

This schedule has been developed without consideration of the accelerator operation schedule. Work requiring accelerator beam off conditions is assumed to be accomplished during normal scheduled accelerator shutdowns.

	DURATION
Conceptual Design Complete	TØ - 0.25 yrs
Start Title I	TØ
Complete and submit Environmental Assessment (EA)	TØ + 0.25 yrs
Approved Finding of No Significant Impact	TØ + 0.50 yrs
Submit ACOE 404 Permit Application	TØ + 0.50 yrs
Title I Complete, Approval to start Title II	TØ + 1.00 yrs
Obtain ACOE 404 Permit	TØ + 1.50 yrs
Approval to Start Title III (Start Construction)	TØ + 1.75 yrs
Underground Enclosures Complete	TØ + 2.50 yrs
Above Grade Buildings Complete	TØ + 3.25 yrs
Civil Construction Complete	TØ +3.40 yrs
Shielding Assessment Approved - Project Complete	TØ +3.50 yrs

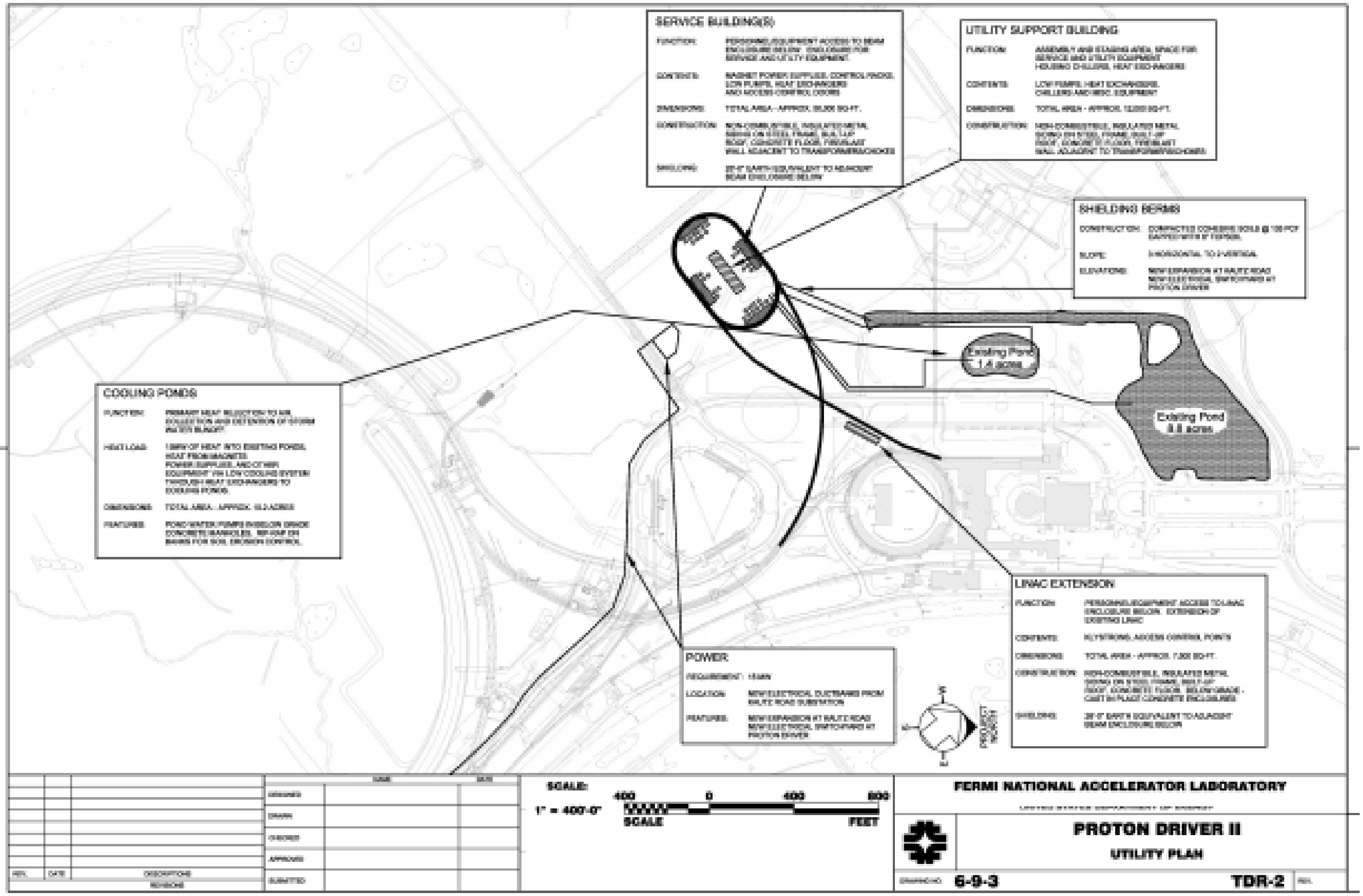

Figure 10.1. Proton Driver II (PD2) Utility Plan.

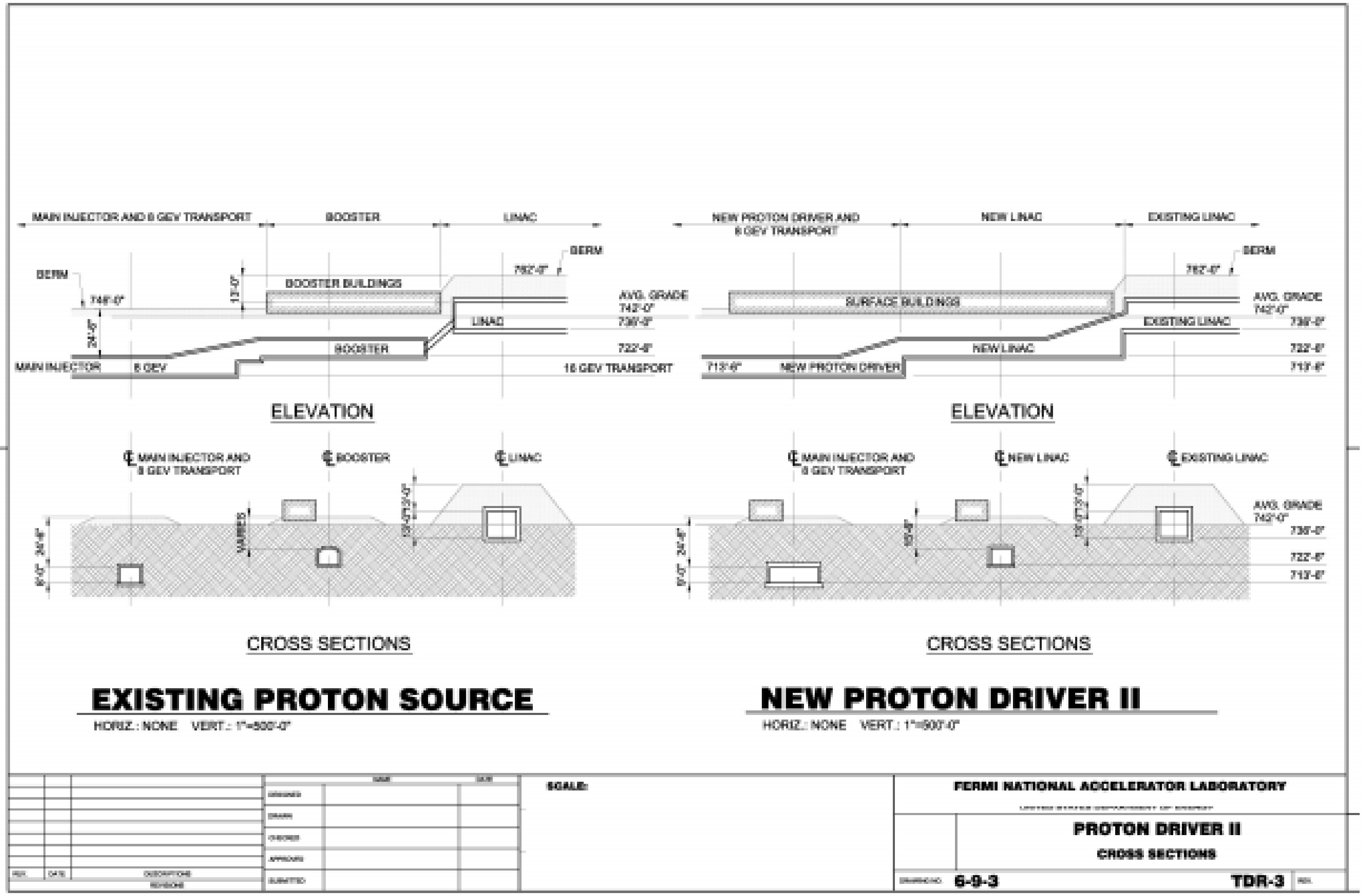

Figure 10.2. Proton Driver II (PD2) Elevation.

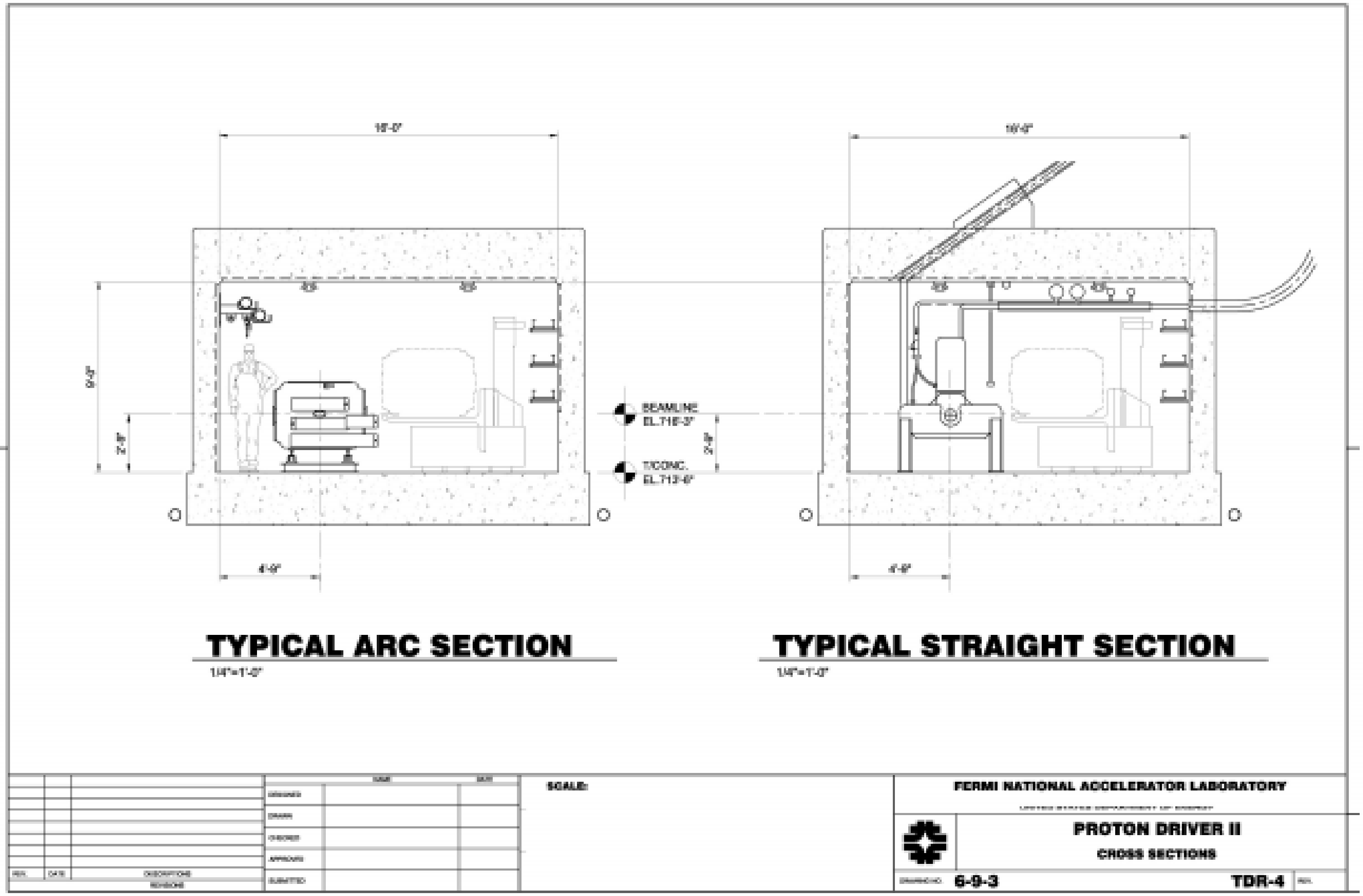

Figure 10.3. Proton Driver II (PD2) Enclosure Cross-Sections.

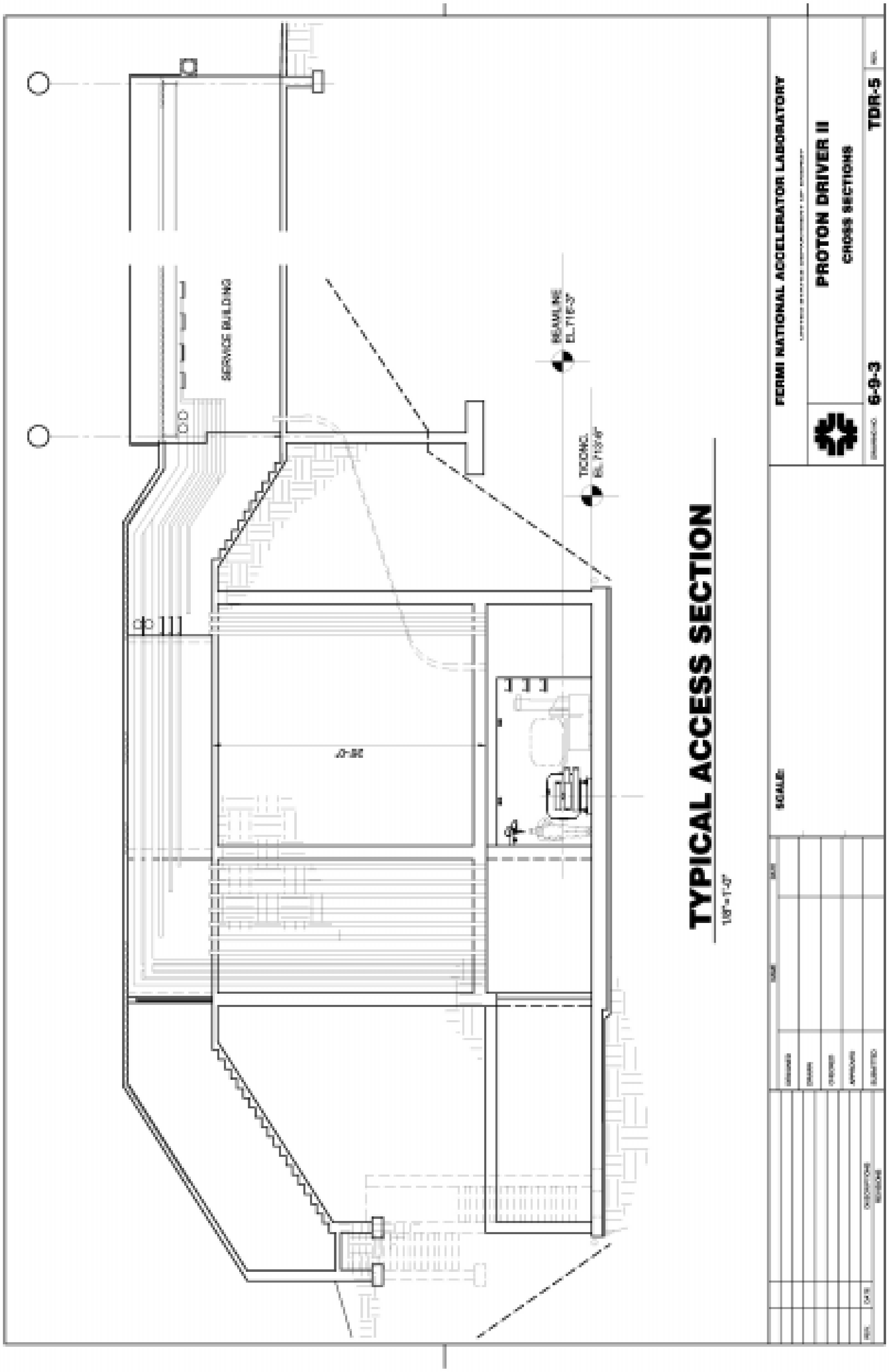

Figure 10.4. Proton Driver II (PD2) Access Section.

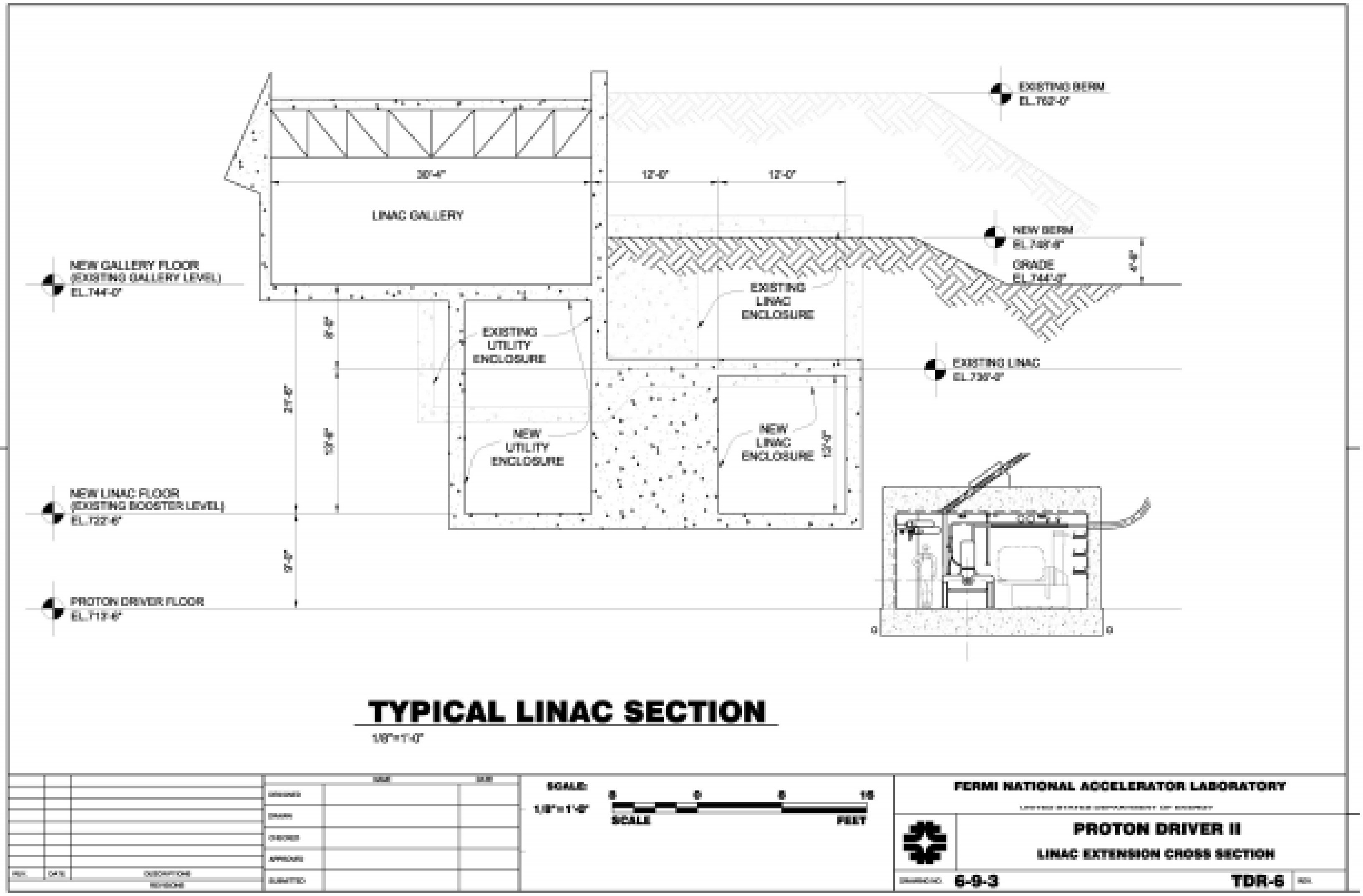

Figure 10.5. Proton Driver II (PD2) Linac Extension Gallery and Enclosure Cross-Section.

Chapter 11. Environment, Safety, and Health Considerations

D. Cossairt, K. Vaziri, and P. Kesich

11.1 Introduction

The Proton Driver, either utilizing a linac or a synchrotron, presents a number of challenges in environment, safety, and health. Here, we identify these challenges and provide a preliminary assessment of how they might be addressed and of their potential impact on the project. While many of these issues are very similar to those that have been encountered and solved during the construction and operation of other facilities at Fermilab and elsewhere, others are novel. The latter will require particular attention as the project proceeds to assure their timely resolution in a cost-effective manner that meets with the approval of the Department of Energy and the public. It is concluded that with adequate planning in the design stages, these problems can be addressed in a satisfactory manner. Future R&D needs related to environment, safety, and health are identified and summarized at the end of the chapter.

11.2 Overall View of Procedural/Regulatory Matters

The actual design, construction, and operation of the Proton Driver will have to meet a number of procedural/regulatory milestones in the area of environment, safety, and health to assure its success. Early attention to these matters is essential. These requirements are provided in Fermilab's Work Smart Standards in Environment, Safety, and Health [1].

11.2.1 Safety and Health Procedural/Regulatory Matters

The Laboratory will be required to prepare an assessment of the environment, safety, and health issues associated with this project in the form of a Safety Assessment Document (SAD). A Preliminary Safety Assessment Document (PSAD) will likely be needed first. Its purpose is to identify the relevant ES&H issues at an early stage and propose how they might be mitigated. The SAD, then, documents the resolution of the issues. DOE may employ an external review team to validate the analysis. Just prior to facility operation, a readiness review will be conducted in similar fashion. PSAD/SAD activities generally begin after funds are released. Fire Safety/Life Safety Code considerations, particularly those concerning egress conditions should be especially carefully thought out prior to the Title I design. DOE is presently "self-regulating" in the areas of industrial safety and occupational radiation protection, a condition that may change in the near-term future with consequences that are unknown at this time.

11.2.2 Environmental Protection Procedural/Regulatory Matters

All DOE projects are subject to the National Environmental Policy Act (NEPA). For a project of this scope, DOE will require an Environmental Assessment (EA). The required analysis is broad in scope and includes societal impacts, such as traffic and noise, along with the standard environmental protection topics. Also included would be investigation of archaeological and historic preservation sites located within the footprint. DOE will choose the methods used to involve the public. The conclusion of the environmental assessment process is either a Finding of No Significant Impact (FONSI) or the need to prepare an Environmental Impact Statement (EIS). The latter choice by DOE is plausible. The decision may hinge on how the Proton Driver is connected with other projects such as a neutrino source or a muon collider. Connection with some larger project, with perhaps more significant environmental impacts, logically will tilt the level of review toward that of an EIS. The completion of the EIS by DOE results in the issue of a formal notice called a Record of Decision (ROD). The process of preparing an EA from the beginning to the publication of the FONSI is estimated to take from one year to 18 months. Two or three years are likely needed, at a minimum, to complete an EIS. NEPA requirements must be completed prior to expenditure of project funds or any “detailed design.”

A significant part of the NEPA process consists of an analysis of alternatives to this proposal, identifying the environmental impacts of all of them, and demonstrating that the proposed project either has the least impact or that the impacts are justified by other considerations. Potential "hypothetical" alternatives must include the “no action” alternative, i.e., "making do" with the present Linac and Booster. Other alternatives that could be considered are to upgrade the present Booster in its current location or to place the Proton Driver in alternative locations on the Fermilab site. Alternative locations may have a substantial effect on the analysis of impacts. For example, locating the project in non-wetland areas (e.g., south of Giese Road, or west of the NuMI access road) may warrant serious consideration if it results in the alleviation of important environmental problems. Furthermore, any decontamination or decommissioning of portions of the accelerator complex that might be replaced by the Proton Driver (e.g., the 8 GeV Booster) should be included in the analysis.

Several environmental permits will be needed. Some of these apply during the construction stages, others apply to operations, and some apply to both. These permits include storm water discharges, discharges of cooling water, wetlands mitigation, releases of air pollutants for both non-radioactive pollutants and for radionuclides, and construction in any floodplains. Existing environmental permits issued to DOE and the Laboratory address some of these issues. However, modifications may be necessary to encompass the construction and operations of the Proton Driver. A prominent example is the need to secure a permit under the National Emissions Standards for Hazards Air Pollutants (NESHAP) to construct a new source of airborne radionuclide emissions [2]. The lead-time required for submittal of these permits is typically 180 days or longer. The permits all come with lists of "terms and conditions", enforceable by the regulatory agencies. It is important that these matters be carefully considered and realistically planned for early in the project to be properly funded to avoid problems later.

11.2.3 Wetlands Impact

The wetland impacts would be major for this project as it is currently envisioned with either choice of machine. At this early stage a great deal of the construction likely would be in jurisdictional wetlands (i.e., wetlands of a size of regulatory importance). Thus, an individual permit from the U.S. Army Corps of Engineers (CoE) must be obtained before the commencement of construction, with a minimum of a one-year lead-time. The permit is certain to require the replacement of the wetland acreage lost “in kind”. Unfortunately, the present wetlands that might be impacted are *forested*, and thus essentially impossible to replace “in kind.” Therefore, a ratio of 2:1 of replaced to lost acres is probable, with the likely necessity to create up to 60 acres of new wetland. The choice of a place on the Fermilab site for such a large wetland should be done carefully, since the new wetland becomes essentially untouchable for development in the future. At the time of this writing, replacement wetland typically costs about $50,000 per acre to build and manage. It must be monitored as a condition of the permit, typically for a period of five years, and failure to meet performance criteria would necessitate remediation. Efforts that can be made to reduce the size of the impacted wetlands are obviously worthwhile. The siting of any new cooling ponds is also a consideration here.

11.3 Environment, Safety, and Health Considerations During Construction

11.3.1 Occupational Safety During Construction of the Facility

These facilities all would be located within the glacial till, where construction is likely to proceed by the familiar "cut and fill" method. The Occupational Safety and Health Administration's (OSHA) regulations on the construction activities will be followed. Industrial radiography operations and any other work conducted using radioactive sources must be performed in compliance with State of Illinois requirements. Other routine radiological issues that might arise will be handled according to the *Fermilab Radiological Control Manual* (FRCM) [3]. Should alternative methods of construction such as underground tunneling be chosen, perhaps in order to minimize the size of impacted wetlands, further review may be necessary.

11.3.2 Environmental Protection During the Construction of the Facility

Erosion control measures similar to those employed elsewhere must be employed in accordance with good engineering practice and Federal and State regulations. Dust and runoff from any spoil piles must be kept under control. A National Pollutant Discharge Elimination System (NPDES) storm water permit for construction will be needed. This will include specific erosion and sedimentation controls that must be followed during the construction period. The usual precautions to prevent pollution from spills of regulated chemicals from the construction equipment will need to be taken. Noise from construction activities is not expected to be significantly more intense than that associated with normal civil construction activities in the vicinity of Fermilab. It is important to demonstrate adequate care for floodplains due to significant local public concerns about flood prevention. Also, due to the fact that Indian Creek runs through the proposed site, it is very likely that the construction would qualify as a "Class III" dam, a condition that would require a permit from the State of Illinois.

11.4. Environment, Safety and Health Considerations During Operation

11.4.1. Occupational Safety Hazards During Operations

The occupational safety hazards encountered at all other large particle accelerator facilities, including the present complex at Fermilab, will be found in this facility:

- The project will use high current electrical circuits in the magnets on a large scale.
- Radio frequency (RF) generation and distribution equipment will be used extensively.
- Large amounts of cables in cable trays, with associated fire protection implications, will be installed.
- Long tunnels will be present with corresponding egress and fire protection issues that need to be addressed.
- There will be movements and alignment of large, heavy components.
- There will be significant amounts of cooling water present.
- Cryogenics and superconductivity hazards will be present, if the linac option is chosen.

These issues have been successfully addressed in the past by the application of well-known technologies and safety practices that will be applied to this new facility. The incorporation of unusual materials in accelerator components or as target materials could pose industrial hygiene issues that will need proper evaluation and mitigation.

11.4.2 Ionizing Radiation Safety During Operation of the Proton Driver

The major issues related to ionizing radiation have been discussed elsewhere in this report and this detailed analysis will not be duplicated here.

11.4.2.1 Prompt Radiation Shielding

The Proton Driver will require massive amounts of hadron shielding similar in scale and type to that of other proton accelerators in this energy and intensity regime. It is clear that suitable combinations of steel, concrete, and earth shielding can meet the standard criteria for above ground shielding at Fermilab.

From the standpoint of machine reliability, it is inconceivable for a catastrophic loss of the full beam to continue for more than a short period of time. Likewise, long-term steady state losses must be kept very small. These limits on beam loss, if adequately analyzed and documented can be used to form the basis of the shielding assessment, which is needed to satisfy a Laboratory requirement [3].

Regulatory [4] and DOE [5] requirements pertain to radiation fields present on a DOE site. While Ref. [4] primarily concerns exposures to occupational workers and Ref. [5] pertains primarily to members of the public, these two standards, both incorporated into Ref. 1, are consistent in that the annual radiation dose equivalent must be kept below 100 mrem in locations where members of the public or employees who have not been specifically trained as "radiation workers" could be present. Fermilab has adopted policies that achieve this condition [3]. If the dose equivalent in an hour resulting from the maximum credible accidental beam loss can be constrained to be less than 1 mrem and if the dose equivalent due to normal operating conditions can be shown to result in a dose equivalent of less than 0.05 mrem per hour , the affected area needs no further controls.

Clearly, passive shielding can be used to achieve these objectives in a detailed design. The passive shielding should also consider muons. Fortunately, at these energies, the forward-peaked kinematical distributions and relatively short ranges (less than about 30 meters of earth) of the muons simplify their shielding. An especially welcome result of this project will be the elimination of the quite troublesome shielding problem associated with the present 8 GeV Booster and certain work places of high occupancy adjacent to it. Care in the detailed design should make it possible to avoid undesirable prompt radiation levels in various support structures by assuring that adequate passive shielding is used. Experience at nearly all accelerators, including the present Fermilab Booster, is that future upgrades nearly always are compromised or made more costly by having "occupied structures" located above or beside the accelerator enclosure. Provision should be made to assure that no such structures are placed at minimal distances from the accelerator enclosures. This is needed to avoid unnecessary constraints being placed on operations, necessitated by unexpected levels of beam loss. Otherwise, operational difficulties are likely due to the need to control radiation exposures in work places much more stringently than those required in "uncontrolled" areas, where one has options such as fencing available as fallback positions.

11.4.2.2 Residual Radioactivity of Components

Efforts should be made to keep residual radiation levels at contact with the beam pipe in unshielded portions of the lattice to less than approximately 100 mrem per hour while those at contact with magnets, etc. should be less than about 10 mrem per hour. This may require the achievement of average beam losses that are very small. The coupling of this issue with prompt radiation shielding is obvious. At levels of these magnitudes, the control of occupational radiation exposure during routine maintenance activities is possible, but difficult. To maintain total exposures to maintenance personnel at acceptable levels, considerations of maintenance activities in the design with a view toward keeping exposures as low as reasonably achievable (ALARA) is a necessity. Both residual and prompt radiation considerations are of sufficient importance to require continuous attention to beam loss during operations and careful planning of maintenance activities in order to keep occupational radiation exposures as low as reasonably achievable, in compliance with regulatory compliance [Ref. 4].

11.4.2.3 Airborne Radioactivity

Airborne radioactivity levels will largely be encountered either in areas where collimators are employed to limit beam loss or at the target stations (note: Target stations are discussed in Chapter 21) The design of the collimation system will include a calculation of the airborne radioactivity released, to support the permit requirements outlined in Section 11.2.2 and to assure compliance with regulations governing airborne radionuclide releases found in Ref. [2]. An early assessment of this issue will allow the inclusion of mitigation into the design of the facility.

11.4.2.4 Radioactivity in Soil and Groundwater

As the shielding design proceeds, the production of radioactivity in soil and the consequences of its migration to groundwater resources must be carefully considered so that the regulatory requirements of Ref. [1] are met. For "ordinary" sections of machine lattices, the allowable amounts of beam loss, especially those expected on a steady-state basis, need to also be compatible with the needs of prompt radiation levels external to the shielding and residual activity levels within the enclosure. Depending on the analyses of radioactivation of soil/groundwater, monitoring wells may be in place, requiring a sampling and maintenance schedule. These considerations are quite similar to those encountered at other Fermilab facilities located in the glacial till.

11.4.3 Non-Radiological Environmental Protection Issues During Operations

Efforts should be made to prevent the creation of regulatory mixed wastes and to control spills. Surface water discharges must be managed in accordance with Laboratory policies and any State and Federal environmental permits that are in place.

The cooling water requirements for the Proton Driver synchrotron are significant. These requirements should be examined to determine if the impact on Fermilab's industrial cooling water (ICW) system and any new discharges to "waters of the state" (i.e., Indian Creek) requires modifications to the Laboratory's current National Pollutant Discharge Elimination System (NPDES) permit under which these systems are operated. Any chemical additives to these systems must be approved within the framework of existing permits.

11.5 Summary

The Proton Driver provides a number of challenges in the area of environment, safety, and health. Many of these have been encountered, and effectively addressed, at Fermilab and other accelerators. Some of the problems are common to technological advances in other accelerators worldwide. For these, collaborative efforts should continue to develop and improve the solutions. This project raises a few new issues that must be addressed. Continued attention to these issues is anticipated as the project proceeds.

11.6 Need for Work on Environmental and Safety Issues

A. The Fire Safety/ Life Safety Code considerations need to be carefully addressed prior to Title I design (Section 11.2.1).

B. The needed environmental permit applications should be developed and submitted at the earliest possible stage (Sections 11.2, and 11.3.2). Specific time requirements for each permit application process are available from the ES&H section, but all permits must be assumed to take at least 180 days.

C. The alternatives to be studied as part of the NEPA process must be identified (Section 11.2.2).

D. Archaeological/historic sites within the footprint project will need to be surveyed (Section 11.2.2).

E. The potential size/type of impacted wetlands and floodplains should be further investigated before the "footprint" of the project becomes completely defined by other constraints (Section 11.2.3). Modifications to the footprint should be considered that would minimize the impacted areas.

F. The cost of environmental compliance, maintenance, monitoring, and oversight must be included explicitly in early planning/budgeting processes. This is especially true for projects of this magnitude, where such costs could be several million dollars, and the efforts needed extend for years beyond actual construction. Significant funds may also be necessary to complete studies for preliminary environmental work (e.g., wetland delineations, wildlife surveys, groundwater investigations) prior to project funding *per se* (Sections 11.2.2, 11.2.3, and 11.3.2).

G. The trade-off between control of beam loss and additional lateral shielding needs to be better understood (Section 11.4.2.1).

H. The support structures should be located so that they are not above any part of the accelerator enclosures and are shielded by more than "the minimum" amounts of lateral shielding to allow for uncertainties in shielding calculations and to accommodate future upgrades (Section 11.4.2.1).

I. Calculations of airborne radionuclide releases are needed concerning the beam collimation system to establish permitting requirements and demonstrate that operations will be within established regulatory requirements (Section 11.4.2.3).

J. A hydrogeological survey in the vicinity of the planned facility should be conducted to better refine the parameters relevant to groundwater activation prior to the finalization of the design (Section 11.4.2.4).

References

[1] "Fermilab Work Smart Standards Set," Fermi National Accelerator Laboratory, http://www-lib.fnal.gov/library/worksmart/worksmart.html, current version.

[2] United States Code of Federal Regulations, Title 40, Part 61, Subpart H, "National Emissions Standard for Hazardous Air Pollutants (NESHAP) for the Emission of Radionuclides other than Radon from Department of Energy Facilities," current version.

[3] *Fermilab Environment, Safety, and Health Manual,* and *Fermilab Radiological Control Manual*, http://wwwesh.fnal.gov/pls/default/esh_home_page.page?this_page=10, current version.

[4] United States Code of Federal Regulations, 10 CFR 835, "Occupational Radiation Protection," current version.

[5] DOE Order 5400.5, "Radiation Protection of the Public and the Environment," January 1993.

Chapter 12. Future Upgrade

W. Chou

The baseline design of the PD2 synchrotron provides 0.5 MW proton beams at 8 GeV. Chapters 1 through 11 are a detailed description of the PD2 synchrotron design concepts and technical components. A possible siting within Fermilab is identified. The design and the choice of the site also provide the potential to upgrade the beam power to 2 MW in the future. This can be achieved by a further increase in the linac energy from 600 MeV to 1.9 GeV.

Beam power is the product of beam energy E, number of protons per cycle N, and repetition rate f_{rep}:

$$P_{beam} = E \times N \times f_{rep}$$

Because the peak dipole field in the PD2 design is 1.5 Tesla, it would be difficult to increase the beam energy above 8 GeV. The 15 Hz repetition rate would also be difficult to increase because of eddy current losses in the laminations and coils of the magnets. Therefore, in order to raise the beam power, a logical step is to increase the number of protons per cycle.

Space charge is a major concern in high intensity proton machines. The effect scales as $\beta\gamma^2$, the relativistic factor. When the linac energy is increased from 600 MeV to 1.9 GeV, this scaling factor increases by a factor of 4. Therefore, for the same space charge effect, the beam intensity can be increased by a factor of 4. The number of protons per bunch increases from 3×10^{11} to 1.2×10^{12} and the number of protons per cycle increases from 2.5×10^{13} to 1×10^{14}. Consequently, the beam power increases from 0.5 MW to 2 MW. Table 12.1 lists these parameters.

Table 12.1. Parameters of PD2 Upgrade

Parameters	PD2 Baseline	PD2 Upgrade
Linac energy (MeV)	600	1900
Synchrotron peak energy (GeV)	8	8
Protons per cycle	2.5×10^{13}	1×10^{14}
Protons per bunch	3×10^{11}	1.2×10^{12}
Repetition rate (Hz)	15	15
Beam power (MW)	0.5	2

In the PD2 design, the 600-MeV beam transport line is about 254-m long. This leaves enough room for another 1.3 GeV accelerating structure to bring the linac energy up to 1.9 GeV. When one takes this upgrade path, one should consider using superconducting (sc) rf cavities for the additional 1.3 GeV acceleration. This technology is making rapid progresses thanks to the SNS Project and R&D work at other labs (DESY, CERN, CEA/Saclay, ANL, JLab, etc.). Compared to room temperature rf linacs (e.g., the 800 MeV linac at LANL), sc rf linacs have higher accelerating gradient and probably also cost less. One issue that needs to be addressed when adopting an sc linac is the proton beam pulse length. An sc linac works well for long pulses (1 msec or longer). Whether it is an appropriate choice for short pulse operations (e.g., 360 μsec in the PD2 upgrade) need further investigations.

In the PD2 upgrade, the existing normal conducting CCL rf system will be reused, because this is a relatively new system in the Fermilab accelerator complex, built about 10 years ago. However, the pulse length of this system must be raised. When the beam intensity is increased by a factor of 4, the number of protons injected from the linac also increases by the same factor. Assuming the linac peak current remains the same as in the PD2 design (50 mA), the pulse length needs to be quadrupled, from 90 μsec to 360 μsec. The existing CCL structures (from 110 MeV to 400 MeV) can only give a maximum pulse length of about 100 μsec (see Ch. 8). These structures need to be modified. Although the klystrons may be able to operate at longer pulses, the modulators and pulse transformers must be replaced. Moreover, the CCL cavity-sparking rate has a strong dependence on the pulse length. This also needs to be studied.

Chapter 13. Introduction

W. Chou

13.1. Overview

In Proton Driver Study II (PD2), in addition to the study of both an 8 GeV synchrotron-based design and an 8 GeV linac-based design, the Director's charge (Appendix 3) also requests a study of necessary modifications and upgrades of the Main Injector and associated beam lines in order to take full advantages of either option for an 8 GeV Proton Driver. Specifically the charge sets the following goals:

- To increase the Main Injector beam intensity by a factor of 5 (from 3×10^{13} to 1.5×10^{14} protons per cycle);
- To reduce the Main Injector cycle time by 20% (from 1.867 s to 1.533 s);
- To increase the Main Injector beam power by a factor of 6 (from 0.3 MW to 1.9 MW).

Part B of this report (Chapters 13 - 21) presents a detailed discussion of the required system modifications and upgrades in order to reach these goals.

In the baseline design of the Main Injector, the beam intensity was rather moderate (3×10^{13} protons per cycle, about a factor of two higher than what was achieved in the previous Main Ring at Fermilab). [1] However, a previous study showed that, with appropriate modifications and upgrades, much higher beam intensity in the MI would be possible. [2] The present Booster can deliver 6 batches of protons to the MI at a maximum intensity of 5×10^{12} protons per batch. This matches the MI baseline design. When a Proton Driver replaces the Booster, however, the situation will change dramatically.

From Table 2.1 in Ch. 2, it is seen that a synchrotron-based Proton Driver will be able to deliver 2.5×10^{13} protons per batch to the Main Injector. The circumference ratio between the Proton Driver synchrotron and the MI is 1:7. Thus, the MI can take six Proton Driver batches for a total of 1.5×10^{14} protons, which meets the intensity goal. In the 6-batch operation, the present MI cycle time is 1.867 s (28 Booster cycles). In order to reach the 1.9 MW beam power goal, this cycle time needs to be reduced to 1.533 s (23 Proton Driver cycles). Table 13.1 lists the main parameters in the Main Injector upgrade.

An upgraded Main Injector will be a powerful machine. At present, the highest beam power from a synchrotron is at the ISIS/RAL, U.K., which provides 160 kW pulsed proton beams. The highest beam power from a cyclotron is at the PSI, Switzerland, which delivers a 1 MW dc beam. The nearly 2 MW beam power from an upgraded MI will be higher than any existing proton machine. It will also be comparable to the two large accelerator projects currently under construction, i.e., the SNS project in the U.S., a 1.4

MW machine, and the JHF project in Japan, which has both a 1 MW 3-GeV synchrotron and a 0.75 MW 50-GeV synchrotron.

Table 13.1. Main Injector Upgrade Parameters

Parameters	**Present**	**Upgrade**
Injection kinetic energy (GeV)	8	8
Extraction kinetic energy (GeV)	120	8 - 120
Protons per cycle	3×10^{13}	1.5×10^{14}
Cycle time at 120 GeV (s)	1.867	1.533
Average beam current (μA)	2.6	16
Beam power (MW)	0.3	1.9

Compared to these other high beam power proton machines, a unique feature of an upgraded Main Injector is that it can provide proton beams up to 120 GeV, an advantage for a number of important physics experiments. For example, the long baseline neutrino experiment, NuMI, requires high intensity proton beams with a tunable energy. As NuMI evolves to increase the precision and sensitivity of its measurements, more MI beam intensity will be needed. An upgraded MI can meet this requirement. The upgraded MI will provide about 2 MW at 120 GeV. When the beam energy is reduced, the cycle time will also decrease. The beam power will remain high over the extracted beam energy range of 8 - 120 GeV and only be slightly reduced due to the "overhead" in the cycle time (e.g. injection time, parabola in the ramp waveform, flat top, and overshoot for resetting the magnets).

In this study, two beam lines - NuMI and MiniBooNE - have been investigated in some detail. The former uses the MI 120-GeV beams, the latter the Booster 8-GeV beams. Both experiments benefit from PD2 because high beam intensities from the MI and the Proton Driver will be made available. Other beam lines, e.g., the antiproton transport lines, are not in the scope of this study. (Note: It is expected that the increase of the antiproton production will be proportional to the increase of the MI proton intensity provided that the target, beam lines and stochastic cooling system of the present antiproton source will be upgraded accordingly.)

13.2. Main Injector Modifications and Upgrades

At high intensities, beam instabilities and space charge become a major concern. Beam dynamics studies on these problems, employing both analytical and simulation methods, have been carried out and are described in Chapter 14.

In order for the Main Injector to operate at 2 MW, most of the technical systems need to be upgraded. Some of these upgrades are major, some moderate. Here is an overview:

- RF: To accelerate 5 times more particles in a shorter period, the rf system requires a major upgrade. The number of cavities needs to be increased from 18 to

20. The number of power amplifier of each cavity also needs to be doubled from one to two. (Chapter 15)

- Gamma-t jump system: Transition is crossed in the MI during the acceleration cycle. Presently there is no gamma-t jump system in the machine. But this system will be necessary in PD2 due to high intensity operation. A detailed design of the gamma-t jump system is given in Chapter 16. This system can provide a $\Delta\gamma_t$ from +1 to -1 within 0.5 ms. This gives a jump rate of 4000 s^{-1}, about 17 times faster than the normal ramp rate (240 GeV/s).

- Large aperture quadrupoles: In the baseline design of the Main Injector, it was known that a physical aperture bottleneck is at the quadrupoles upstream of the Lambertson magnets in several straight sections: MI-10, MI-30, MI-40, MI-52 and MI-62 (and also MI-60 when the NuMI extraction beam line is in place). In order to reduce beam losses at these locations, large aperture quadrupoles need to be installed replacing the regular quadrupoles. Their aperture will be increased from 83.48 mm in diameter to 102.24 mm, i.e., 4 inches. (Chapter 17)

- Passive damper and active feedback: To suppress coupled bunch instabilities, both a passive damper and active feedback are investigated in Chapter 18. The former places nonlinear lossy materials (e.g., a special ferrite of which the loss parameter μ'' is frequency dependent) in the rf cavity to damp the higher order modes (HOMs) while leaving the fundamental mode unaffected. The design of a longitudinal feedback system is also presented. A transverse feedback system exists in the MI but needs improvement.

- Radiation shielding and collimation: The shielding of the MI appears to be adequate for the upgrade. However, a collimation system is required in order to minimize the uncontrolled beam losses in the machine to reduce residual radioactivity so that hands-on maintenance can be performed. (Chapter 19)

- Other technical systems: (Chapter 20)
    - Magnets: The MI magnets will function adequately in the upgrade and modifications are unnecessary.
    - Power supplies: A shorter cycle requires an increase of the maximum ramp rate from 240 GeV/s to 305 GeV/s. A modest upgrade of power supplies is needed.
    - Mechanical and utility: The cooling capacity for magnets and power supplies appears to be sufficient in this upgrade. But the cooling system capacity for the rf system and cavities need to be doubled.
    - Kickers: A major upgrade is needed. The MI beam pipe has a vertical aperture of 2-inch everywhere except at the kickers, which is 1.3-inch. In order to eliminate this bottleneck, the kicker aperture needs to be enlarged.
    - Beam dump: With a modest upgrade, the present beam dump at MI-40 can absorb five times more protons.
    - Controls: Only minor changes are needed.

It is foreseen that several other systems will be required for the MI upgrade, e.g., a stop band correction system. The design of this system is not yet finished.

For the option of an 8-GeV superconducting proton linac, the MI needs a new 8-GeV H^- injection system. This will be discussed in Part C of this report.

13.3. Beam line Upgrades

In chapter 21 are discussed some details about the NuMI and MiniBooNE beam line upgrades. The major issues are shielding and cooling in the target halls, decay pipes and hadron absorbers. The ground water problem is a concern but there is a reasonable solution.

For the option of an 8-GeV superconducting proton linac, the present extraction system of the MiniBooNE cannot be used. Either the Main Injector or the Recycler will be used to transport beams from the 8-GeV linac to the MiniBooNE.

Finally, in chapter 21 there is a brief discussion on the 120-GeV beam lines in the old Meson experimental area. More shielding will be necessary but calculations have not yet been done.

13.4. Conclusion

The Main Injector and beam line upgrades can be implemented in two possible ways. They can be included in the Proton Driver project. Or these upgrades can be accomplished through a series of accelerator improvement projects (AIPs). The cost estimate (Appendix 1) shows that most of the systems upgrades cost around $1M or below, except the for the rf system. This makes them appropriate candidates for AIP funding.

These upgrades will not only meet the requirements on the MI with a new Proton Driver, but also greatly benefit the on-going physics program at Fermilab, including Run II and NuMI.

References

[1] "Fermilab Main Injector Technical Design Handbook," Fermilab (1994).

[2] W. Chou, "Intensity Limitations in Fermilab Main Injector," PAC 97 Proceedings, pp. 991-993; also see FERMILAB-Conf-97/199.

Chapter 14. Beam Dynamics

14.1. Space charge and beam stability

K.Y. Ng

14.1.1. Tune shifts

The *betatron tunes* ν_z, $z = x$ or y, of transverse oscillations of charged particles in the beam moving with axial velocity $v = \beta c$, c being the velocity of light, are mainly determined by the applied focusing forces due to quadrupoles. With finite beam current the tunes are shifted, both by direct space charge and by image forces due to induced voltages in the surrounding structure impedances. Due to the relativistic nature of the beam, $\gamma = (1-\beta^2)^{-1/2} = 8.939$ even at injection, the space charge forces are reduced as a result of the compensation of the electric and magnetic components.

The *coherent* and *incoherent tune shifts* of a beam with half width a_x and half height a_y consisting of N_p protons are [1]

$$\Delta\nu_{\mathrm{coh},z} = -\frac{N_p r_p R}{\pi\nu_z\gamma\beta^2}\left[\left(\frac{1}{\gamma^2 B_f}+\beta^2\right)\frac{\xi_{1z}}{h^2}+\beta^2\frac{\epsilon_{1z}}{h^2}+\mathcal{F}\beta^2\frac{\epsilon_{2z}}{g^2}\right], \tag{14.1}$$

$$\Delta\nu_{\mathrm{incoh},z} = -\frac{N_p r_p R}{\pi\nu_z\gamma\beta^2}\left[\left(\frac{1}{\gamma^2 B_f}+\beta^2\right)\frac{\epsilon_{1z}}{h^2}+\beta^2\frac{\epsilon_{1z}}{h^2}+\mathcal{F}\beta^2\frac{\epsilon_{2z}}{g^2}+\frac{2\epsilon_{\mathrm{spch},z}}{\gamma^2 a_y(a_x+a_y)B_f}\right], \tag{14.2}$$

where r_p is the classical radius, B_f is the bunching factor, and R is the mean radius of the accelerator ring. The *coherent Laslett image coefficients* $\xi_{1,2z}$ and *incoherent Laslett image coefficients* $\epsilon_{1,2z}$ describe the strength of image forces for a particular geometry. For the elliptical vacuum chamber of the Main Injector with full height $2h=5.08$ cm and full width $2w=12.3$ cm, they are $\xi_{1x}=0.0049$, $\xi_{1y}=0.6114$, $\epsilon_{1x}=-\epsilon_{1y}=-0.2032$. The magnet pole gaps are approximated by two infinite plates separated by $2g=5.31$ cm covering $\mathcal{F}=0.5$ of the ring, giving $\epsilon_{2x}=\epsilon_{2y}=-\pi^2/24$. Assuming a uniform transverse distribution, the self-field space charge coefficients in the last term in Eq. (14.2) are $\epsilon_{\mathrm{spch},y}=a_y/(a_x+a_y)$ and $\epsilon_{\mathrm{spch},x}=a_y^2/[a_x(a_x+a_y)]$. The tune shifts are calculated at every moment of the ramp cycle according to the rf voltage table for the NuMi cycle and are plotted in Fig. 14.1. The bunching factor B_f is also shown in a different scale. It is computed from the bunch area which is assumed to be 0.15 eV-s throughout the cycle. The beam radii are computed from the 95% normalized emittance of $\epsilon_{N95\%}=40\times10^{-6}\,\pi$m. We see a dip for every curve at the time when transition is crossed. Because of bunch-by-bunch injection, all the tune shifts have their maximal values near injection. At their maximal values, we can write

$$\Delta\nu_{\mathrm{incoh},x}=-0.059+0.113=-0.054\,,\quad \Delta\nu_{\mathrm{incoh},y}=-0.060-0.117=-0.178\,, \tag{14.3}$$

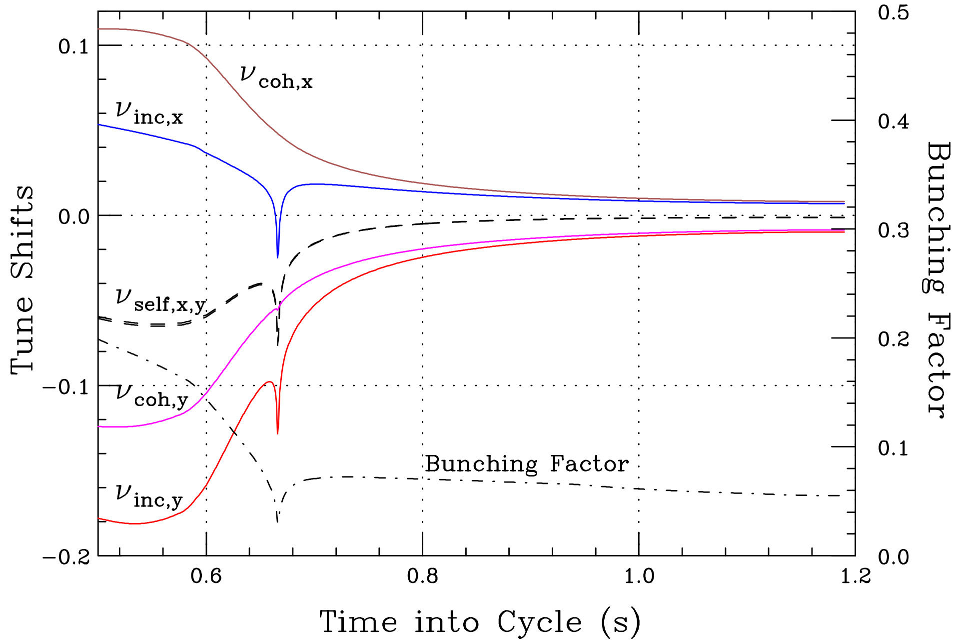

Figure 14.1. (color) Coherent and incoherent betatron tune shifts of the upgraded Main Injector.

where the first terms in the middle correspond to self-force contributions and the second image contributions. It is obvious that space charge contributions, denoted by $\nu_{\mathrm{self},x}$ and $\nu_{\mathrm{self},y}$ in the figure, are not so dominating. Here, the coherent tune shifts have their maximal values $\Delta\nu_{\mathrm{incoh},x} = +0.110$ and $\Delta\nu_{\mathrm{incoh},y} = -0.124$. It is well-known that only the coherent tune shifts are responsible for parametric resonances [2]. Although the space charge self-force does not contribute to the dipole coherent tune shifts, it contributes to the quadrupole coherent tune shifts. The symmetric coherent quadrupole mode will be shifted by $2 \times \frac{3}{4}$ of the incoherent dipole shift, or $\nu_{\mathrm{quad}} = 2\left[\nu_{\mathrm{dipole}} - \frac{3}{4}|\Delta\nu_{\mathrm{incoh}}|\right]$. Therefore, $2\nu_x$ is shifted from 2×26.425 to 2×26.494 and $2\nu_y$ is shifted from 2×25.415 to 2×25.253. With the bare tunes $\nu_x = 26.425$ and $\nu_y = 25.415$, the vertical tune will pass through the third order stopband.

14.1.2. Single Bunch Instability

Keil-Schnell limit for longitudinal microwave instability is [3]

$$\left|\frac{Z_0^{\|}}{n}\right| < \frac{|\eta| E_0}{e\beta^2 I_{\mathrm{pk}}} \left[\frac{\Delta E}{E_0}\right]^2_{\mathrm{FWHM}} F_{\|} \,, \tag{14.4}$$

where I_{pk} is the peak current, η is the slip factor, E_0 is the nominal beam energy, and the energy spread ΔE at FWHM is computed according to a parabolic distribution. The form factor $F_{\|}$ is near unity for the real and inductive parts of the impedance, but is large for the capacitive part of the impedance. The stability limit is depicted in the left plot of

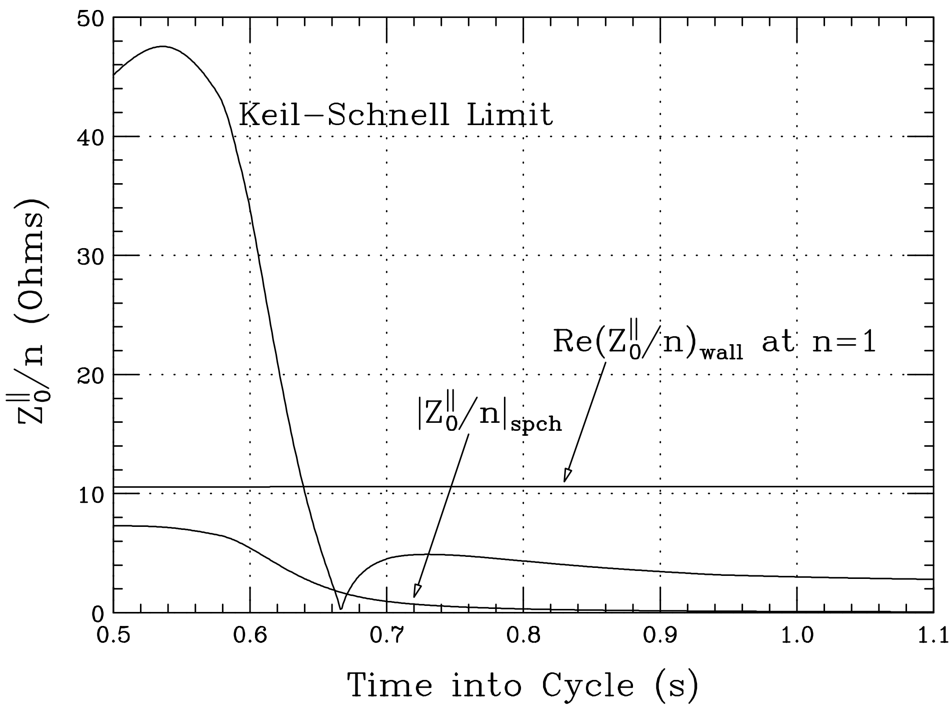

Figure 14.2. Longitudinal microwave instability limit for the upgraded Main Injector.

Fig. 14.2. Alongside, we also show the space charge impedance of the beam inside the elliptical vacuum chamber. The longitudinal resistive-wall impedance is

$$Z_0^{\parallel}\Big|_{\text{wall}} = [1 - i\,\text{sgn}(\omega)]\,\frac{\rho R}{h\delta_s}F_{\parallel}^{\text{wall}}\ , \tag{14.5}$$

where δ_{skin} is the skin depth for resistivity ρ and $F_{\parallel}^{\text{wall}} = 0.927$ is a form factor which takes care of the fact that the beam pipe cross section is elliptical. The beam pipe is constructed of stainless steel with $\rho = 7.4 \times 10^{-6}$ Ωm. The real or imaginary part of the resistive-wall impedance amounts to $10.6\ \Omega$ at the revolution frequency. In fact, except for space charge, the impedance of the Main Injector vacuum chamber is $|Z_0^{\parallel}| \lesssim 1\ \Omega$ according to the Main Injector Handbook, and is well below the Keil-Schnell limit.

The Keil-Schnell-like limit for transverse microwave instability is [4]

$$|Z_1^{x,y}| < \frac{4\nu_{x,y}E_0}{e\beta RI_{\text{pk}}}\left[\frac{\Delta E}{E_0}\right]_{\text{FWHM}}|S_{x,y}|F_{x,y}\ , \tag{14.6}$$

where the *effective chromaticity* is $S_{x,y} = \xi_{x,y} + (\hat{n} - [\nu_{x,y}])\eta$, with $\xi_{x,y}$ the chromaticity, $\hat{n} = n + \nu_{x,y}^I$, n a revolution harmonic, $\nu_{x,y}^I$ and $[\nu_{x,y}]$ the integral and decimal parts of the betatron tune. Instability occurs only for *slow waves* when $\hat{n} > [\nu_{x,y}]$. The form factor $F_{x,y}$ depends on the transverse particle distribution, about unity for the real part of the impedance but is rather large for the reactive dominated impedance. Since this is a coasting-beam theory, it is applicable only when the wavelength of the perturbation is much less than twice the total bunch length. In the ramp cycle of the Main Injector, this perturbation frequency should be $f > 83$ MHz or $n > 1750$ corresponding to a bunch area of 0.15 eV-s. Except around transition, this translates into the stability limits of $|Z_1^{x,y}| \lesssim 6.5\ \mathrm{M}\Omega$/m. The transverse impedances at 83 MHz are $\mathcal{R}e\, Z_1^{x,y} = 0.17$ and $i0.34\ \mathrm{M}\Omega$/m, respectively, which are well below the stability limits. The space charge impedances at injection, however, are $Z_1^{x,y} = i24.3$ and $22.6\ \mathrm{M}\Omega$/m, which are above the stability limits. Fortunately, most of the impedances at injection are space charge, which are reactive and will not drive an instability.

14.1.3. Coupled-bunch Instability

The resistive-wall impedance can drive the transverse coupled-bunch instability with a growth rate

$$\frac{1}{\tau_\mu^{x,y}} \approx \frac{eMI_bc}{4\pi\nu_{x,y}E_0}\,\mathcal{R}e\, Z_1^{x,y}(\nu_{x,y}^c\omega_0)F\ , \tag{14.7}$$

where the form factor is $F \sim 0.811$ if sinusoidal modes are assumed and the instability is worst at injection. For $\nu_y = 24.415$, $[\nu_y] = 0.415$, $\nu_{x,y}^c = [\nu_{x,y}] - 1 = -0.585$ and $\mathcal{R}e\, Z_1^{x,y}(\nu_y^c\omega_0) = -18.9\ \mathrm{M}\Omega$/m. The growth rate is $815\ \mathrm{s}^{-1}$ or growth time 1.22 ms or 110 turns. Because the bunch intensity has been increased 5 fold, the growth rate will be 5 times faster. This instability can be damped by operating at a negative chromaticity below transition and a positive chromaticity above transition. An octupole system and/or a mode damper will also be helpful.

Coupled-bunch instabilities, longitudinal or transverse, driven by the higher-order modes of the rf cavities will have growth rates five times faster than before. Passive de-Qing of the annoying modes as well as the introduction of mode dampers are highly recommended.

14.1.4. Transition Crossing

Just after transition, $Z_0^\parallel$ is dominated by space charge, which drives the microwave instability until η is large enough. The growth rate without damping is

$$\frac{1}{\tau} = \omega_0\sqrt{\frac{n|\eta||Z_0^\parallel|I_{\rm pk}}{2\pi\beta E_0}} = n\omega_0\sqrt{\frac{|\eta||Z_0^\parallel/n|I_{\rm pk}}{2\pi\beta E_0}}\ . \tag{14.8}$$

The geometric factor g inside $(Z_0^\parallel/n)_{\rm spch}$ behaves roughly like $g(n) \approx g_0/(1 + n/n_{1/2})$, where $g_0 = 1 + 2\ln(b/a)$ is the familiar geometric factor at low frequencies and the half-value revolution harmonic is roughly given by $n_{1/2} = \gamma R(1.60/b + 0.52/a)$. From Eq. (14.8), the growth rate increases linearly with frequency and exhibits a maximum at $n_{\rm max} = n_{1/2}/\sqrt{3}$ or 88.6 GHz, where the vertical half beam-pipe radius $b = 2.54$ cm and average beam radius $a = 6.13$ mm have been assumed. Notice that at beam-pipe cutoff frequencies, the seeds are big but the growth rate is slow. However, at high frequencies, the seeds coming from Schottky noise are small, but the growth rate is huge. The total growth is given by $\exp\left[\int dt\ (\text{growth rate})\right]$, where the integration is performed from the time transition is crossed to the moment when η is large enough to regain stability. Hardt [5] postulated that *beam blowup* occurs when $\hat{c} \gtrsim 1$, where

$$\xi\, n_{\max} \left(\frac{r_p}{R}\right)^2 \left(\frac{E_{\rm rest}^{5/2}\beta_t^{7/6}}{h^{1/3}\omega_0^{4/3}\gamma_T^{2/3}}\right) \left(\frac{N_b^2 g_0^2 |\tan\phi_s|^{1/3}}{S^{5/2}\dot{\gamma}^{7/6}}\right) = \hat{c}E_{\rm crit}\,, \tag{14.9}$$

$$\xi = \frac{3^{25/6}\pi^2\Gamma\left(\frac{2}{3}\right)}{2^{41/6}}\left(1-\frac{\pi}{4}\right) = 2.44656\,, \quad E_{\rm crit} \approx \frac{1}{2}\left[\ln N_b - \ln\left(\frac{2k_{b\frac{1}{2}}}{3}\sqrt{\frac{\pi}{\ln N_b}}\right)\right]\,,$$

γ_T is the transition gamma, $k_{b\frac{1}{2}} = n_{1/2}\widehat{\Delta\phi}/(\pi h)$ is the bunch mode at $n_{1/2}$ with $\widehat{\Delta\phi}$ being the half bunch width in rf radians, and $h = 588$ is the rf harmonic. It is important to point out that blowup in this context implies violent breakup of the bunch and there will be a modest increase in bunch area even if there is no blowup. Figure 14.3 shows the variation of the parameter $\hat{c}$ with the bunch area at various bunch intensities and ramp rates. At present, transition is crossed at $\dot{\gamma} = 240$ s^{-1}. The plot shows that there should be no blowup when the bunch area is larger than 0.081 eV-s at the present intensity of $N_b = 6\times10^{10}$ per bunch. For the 5-fold upgraded bunch intensity, however, it appears that the bunch area has to be increased to larger than 0.29 eV-s to avoid a blowup. Also shown are the situations when a transition jump is installed with 10, 15, and 20 times the present crossing rate. The prediction is that the situation will be the same as present if the crossing rate is increased by 15.8 fold.

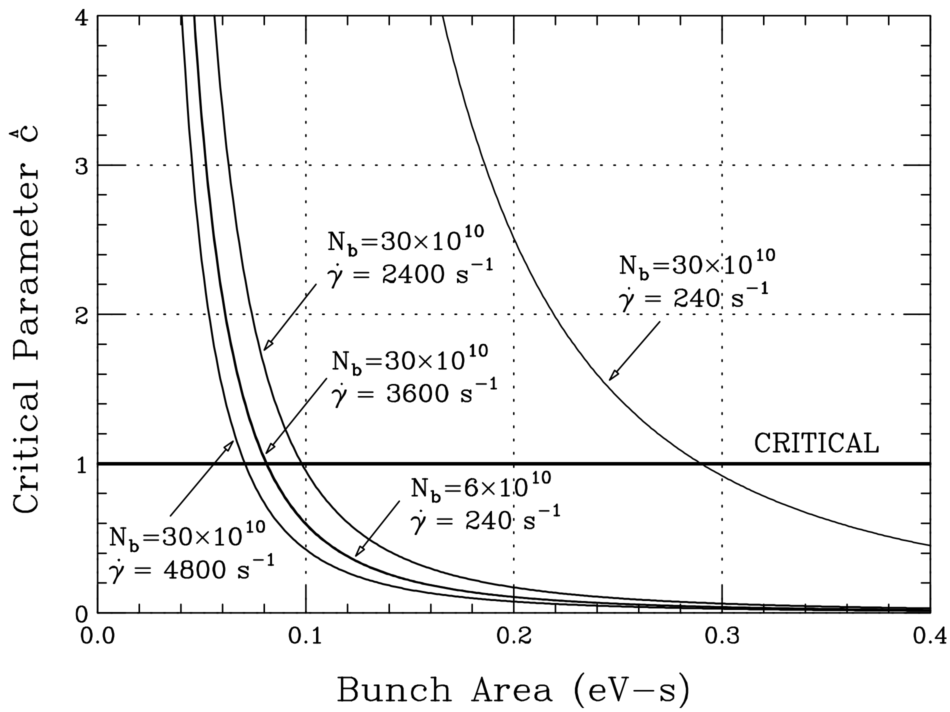

Figure 14.3. Possible negative-mass blowup of a bunch while crossing transition for the present intensity of 6×10^{10} at the present rate of $\dot{\gamma} = 240$ s^{-1}. Also shown are possible blowups at the upgraded intensity of 30×10^{10} crossing transition at 1, 10, 15, and 20 times the present rate.

14.2. Longitudinal Dynamics

Ioanis Kourbanis, James MacLachlan, and Zubao Qian

To operate the MI at 1.5×10^{14} protons per pulse will require the suppression of many of the known instability types, some in several modes. Detailed threshold estimates and designs for damping will be required in a comprehensive upgrade design. The following remarks take a qualitative first step, identifying problem areas and promising cures. At this conceptual stage, experience with existing machines like the Brookhaven AGS, the Los Alamos Proton Storage Ring, or Rutherford Laboratory's ISIS provides a more useful foundation for vetting proposed performance specifications than that provided by existing calculations for the MI, despite the very different nature of these machines. Because the worst effects of beam current are usually manifest at low energy, these exemplars are very relevant, and their variety lends an element of generality to conclusions derived from them.

14.2.1. Injection

The 8 GeV linac and the rapid cycling synchrotron versions of the Proton Driver present the MI with entirely different injection conditions. The transfer from the synchrotron is intended to be synchronous and matched both longitudinally and transversely. The procedures and difficulties are much the same as for the present Booster with, of course, the major complication of five times the charge per bunch. Injection from the linac has numerous variants involving choices on injection time, transverse and longitudinal painting, upstream debunching, etc.

The predicted longitudinal distribution from the PD2 synchrotron has been taken directly from the calculation for the ramp called minimum $\dot{p}$ in Ch. 4 Sec. 2 without inductive inserts. The longitudinal matching goes from a 90 kV bucket (0.78 eVs) to a 1 MV bucket in the MI. The contours in the low voltage PD bucket are strongly distorted by collective defocusing, whereas the waiting MI buckets are of course normal. The resulting shape oscillation of the bunches results in a few percent emittance growth, but it is not significant compared to that in negotiating transition. The injection and acceleration calculations are a development of studies going back several years, differing principally in the new initial distribution. Although arguably not optimized for the PD, they are well worked out from earlier needs, and they demonstrate nicely that this mode of operation naturally fits the established pattern. However, the bunches from the PD synchrotron are incredibly bright and need to be diluted before transition. This controlled blowup has not yet been modeled, however. For consideration of transition, the tracking is started afresh with an elliptical bunch of appropriate emittance.

For injection from the linac, the most favorable assumptions are that painting establishes about the transverse emittance wanted at the end, which is then accelerated with little dilution; the longitudinal painting should provide an approximately uniform momentum distribution with a width set to give the desired longitudinal emittance after adiabatic capture. There is a MI specification that the longitudinal acceptance is 0.5 eVs, a number set by momentum aperture in a classic transition crossing. However, this number is really more like 0.4 eVs because of nonlinearities, and the relevant value when a γ_T-jump is used is not available. For 0.1 eVs bunches, the full width injected energy spread should be 5.3 MeV, only a bit bigger than one would get naturally from the linac without debunching. A classic adiabatic capture (adiabaticity 0.22) takes only 80 ms. However, 0.1 eVs bunches of 3×10^{11} will not get through a MI acceleration cycle without uncontrolled, and presumably unnecessarily large, emittance growth. What has been modeled so far uses a less textbook approach and looks like a perfectly reasonable starting point. Namely, the linac beam is taken without debunching. The rf bucket is turned on at the end of multiturn injection with a bucket height about three times the batch height. Naturally this leads to emittance dilution, to about 0.3 eVs in this case, but that is not so bad a value for the rest of the cycle, and the rf can be turned up to 1.5 MV in only 3.5 ms. Not only does this rapid turn on save time, but it quickly establishes some rf focusing to counter the space charge disruption of the bunch. The space charge force helps to smooth out the filamented distribution. The same trials of the full cycle made for the synchronous injection case were also made using this sudden-capture distribution. The fast voltage increase results in sparse tails in the energy distribution which get scraped at transition. If this 0.03 % scraping were the actual loss, it would be acceptable (and remarkable). However, the claim for this calculation is not that it exemplifies the optimum treatment of the problem; rather it is preliminary evidence that it will be possible to get adequate capture with some standard precautions.

If a technique is found for 53 MHz beam chopping somewhere before or along the 8 GeV linac, it is then possible to inject synchronously from the linac. Although this would be a very desirable development, there has been no effort to estimate the effectiveness; there exists no satisfactory scheme for such fast chopping. Sophisticated chopping and painting will be useful to consider as a standard for judging less elaborate expedients, but it is not evident that such an approach will be required ultimately.

14.2.2. Transition crossing

It is possible to summarize in a few words much of what is observed, expected from analysis, and simulated for transition crossing in the MI. The longitudinal acceptance of the MI is set by two limits that converge with increasing intensity, *viz*., negative mass instability limits the bunch size from below and nonlinear motion limits the bunch size from above. The upper limit is fairly stringent even for single particle motion but also has current dependence arising from increasing shape mismatch. The upper limit is about 0.4 eVs and is dropping slowly at the design intensity. The lower limit is nearly 0.3 eVs and is increasing rapidly. The usual assessment has been that the MI should work at or near its design intensity without special measures for crossing transition but that any significant intensity improvement would surely require some hardware upgrade. Alternative schemes have been considered, but the now well-established solution of a fast γ_T-jump responds to the widest range of transition region pathologies and has proved robust. Documentation supporting these assertions is spread across a number of papers from Fermilab and elsewhere; however, see Ref. [6] in particular.

The PD synchrotron does not pass through transition; therefore its bunches can be far brighter than MI bunches above transition, which are subject to negative mass instability (NMI). The bunches from the PD are just a bit over 0.1 eVs. The tolerable emittance for MI is estimated to be about 0.4 eVs using the analysis of W. Hardt [5]. Although Hardt's treatment includes several approximations, the threshold depends so strongly on emittance, $\propto \varepsilon^{-3}$, that minimum emittance should be well approximated. Future modeling can provide an independent estimate. The tactics of how the bunch dilution should occur is somewhat involved; possibly proceeding with the small bunch and accepting the disruption at transition will give as small a final emittance as any other approach. However, tracking models of NMI are extremely demanding of computer resources and have not yet been well validated. Thus, for this report one should accept that emittance will grow and take the Hardt estimate as a reasonable minimum.

Figure 14.4 shows a bunch of 0.35 eVs that has been accelerated from 8 GeV to 42 GeV on a $\dot{p}_{\max} = 300$ GeV/c/s ramp. The model includes the perfectly conducting wall impedance and a broadband $Z_{\|}/n = 3$ Ohm; 14.4 (a) is a result without a γ_T-jump and 14.4 (b) shows the effect of the jump. The jump consists of two units change in γ_T over 0.5 ms, thirteen times the maximum ramp rate. Both examples show filamentation resulting from imperfect shape matching; the problem is less serious in the jump case and may be open to improvement by careful matching after the jump. The normal crossing case shows a characteristic second tail resulting from the nonadiabatic motion, which can not be remedied by post-transition matching. The preceding paragraph indicates 0.35 eVs may not be quite large enough to avoid NMI. However, at the given $\dot{p}$, there is not bucket area for a much larger bunch. Even with a γ_T-jump, the same sorts of shape matching problems that plague normal transition crossing exist at a reduced level and lead to losses without some margin in bucket area. Thus, by pushing for a factor of five in intensity one gets back to the same sort of squeeze that exists for the present MI at design intensity. Table 14.1 gives results for final rms emittance and percentage beam loss for a number of combinations of initial emittance, γ_T-jump, and inductive insert. The insert, chosen to cancel the net imaginary impedance at transition, does have a marginal benefit, evident in the table. However, the small gains may not be worth the extra complication. The γ_T-jump does permit 0.4 eVs bunches to cross transition without loss; it appears, therefore, that NMI should not prevent operation of the MI at 1.5×10^{14} protons/cycle.

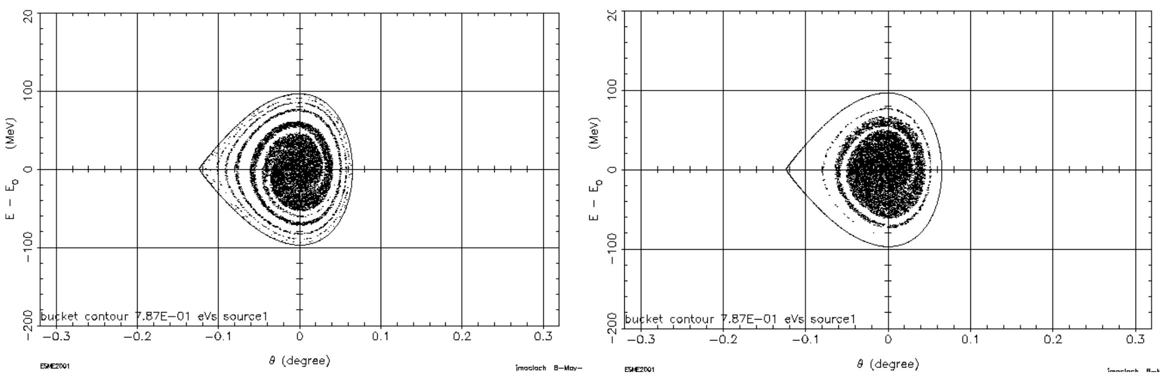

(a) normal transition crossing
$\varepsilon_\ell = 0.101$ eVs (rms)

(b) transition crossing with a jump of two units in γ_T
$\varepsilon_\ell = 0.077$ eVs (rms)

Figure 14.4. MI bunches at 42 GeV on a 300 GeV/c/s ramp. The bunches were 0.35 eVs elliptical distributions (0.069 rms) at injection.

14.2.3. Extraction

For injection into the Tevatron or for most Sec. counter experiments, the main concern is control of bunch-to-bunch regularity and duty factor. The likely difficulties include coupled bunch instability and fundamental beam loading. Extraction losses will also depend on how broad and regular the final momentum spread is. However, such questions are transverse dynamics in first order with momentum distribution as a possible complicating factor. They may be expected to be far more challenging with five times the current to handle, but they are familiar at some level.

Table 14.1. RMS emittance and percentage survival for 300 GeV/s MI ramps with/without γ_T-jump and with/without inductive insert to cancel imaginary impedance at transition. The effect of negative mass is *not* included.

Initial ϵ_ℓ [eVs]					
100%	rms	γ_T-jump	L insert	Final rms ϵ_ℓ	Loss %
0.30	0.060	N	Y	0.084	0.09
		Y	Y	0.066	0.00
0.35	0.069	N	N	0.101	0.74
		N	Y	0.095	0.40
		Y	N	0.077	0.00
		Y	Y	0.078	0.00
0.38	0.075	N	N	0.104	1.39
		N	Y	0.102	0.87
		Y	N	0.084	0.00
0.40	0.079	N	N	0.107	1.94
		N	Y	0.106	1.31
		Y	Y	0.089	0.00

PD2 is foremost an injector for the MI which is the final stage of a proton driver accelerator chain. As in the original Proton Driver study, the ability to deliver very narrow bunches has important potential for such applications as a ν factory. Although not designed to proton driver specifications, the MI does have a large momentum aperture — 2 % nominal, 1.6 % present operational. Therefore, it will be possible to get very short bunches by bunch rotation. The bunch emittance at 120 GeV is about 0.44 eVs. If the rf voltage is dropped in the final parabola of the ramp to maintain a bucket area near 0.75 eVs, it will reach 150 kV in the last 100 μs or so. Jumping the voltage as quickly as possible to 4.4 MV results in a quarter synchrotron oscillation during that time to a full width of 1.5 ns and energy spread of ± 250 MeV. The bucket height is ± 510 MeV, however, so the rotation is rather linear. The final momentum spread is only about ± 0.2 % . An energy-azimuth phase plane plot of the rotated bunch is shown in Fig. 14.5. The result is significantly cleaner than the 8 GeV result shown in Fig. 4.9 because the bunch height to bucket height ratio is lower and because $\Delta p/p$ is much lower.

At minimum bunch width, the collective voltage from space charge and 5 Ohm $Z_{\|}/n$ is about 0.65 MV, a warning on the need to control all sorts of sources of longitudinal coupling impedance. It is, however, small compared to the 20 MV induced at that time by the beam in the MI accelerating cavities. The bunch rotation period presents by far the greatest beam loading problem. If the fundamental beam loading correction systems have both the necessary reserve current and effective gain approaching 40 dB, the synchronous phase wander during the rotation is estimated to be acceptable. This wander was not however, included in the the modeling which resulted in Fig. 14.5. The character of this particular problem depends strongly on whether there is a full or partial circumferential filling.

14.2.4. Stability

There are existing treatments of MI stability issues from the design studies for the MI [7, 8]. Operational experience to date has added little new information. The references include most of the available threshold and impedance estimates plus speculations on the reasons for considerable discrepancies between some of them and available operating experience. From them one can conclude that quintupling MI beam current will encounter several stability problems, but it is not clear exactly which ones. For the longitudinal degree of freedom addressed here, it is abundantly clear that both passive damping of higher order cavity modes and bunch-by-bunch dipole mode damping or multichannel narrow band damping must be pursued vigorously. The narrow band approach has attraction for the possibility of using very similar hardware for quadrupole mode damping should that need arise.

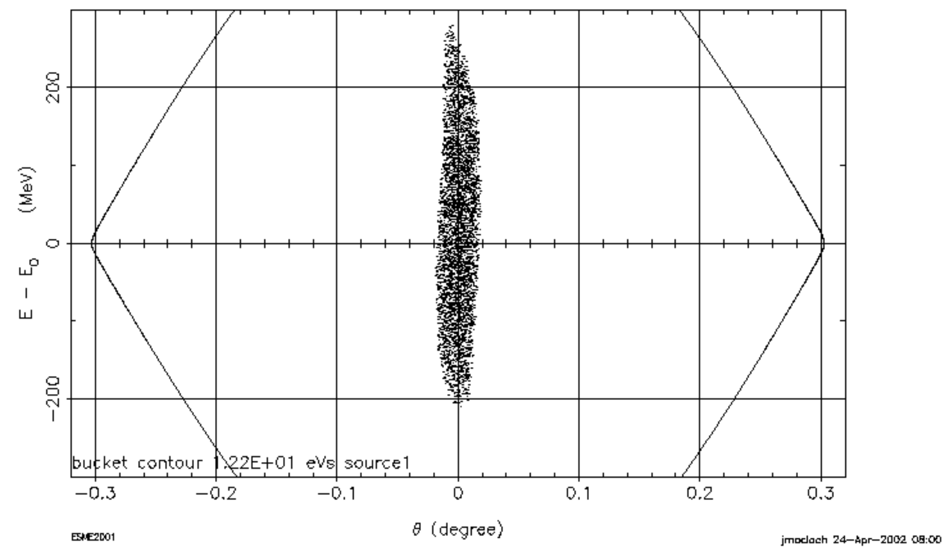

Figure 14.5. The phase space distribution of a bunch rotated with 4.4 MV of rf at the end of the ramp. The horizontal axis on this plot is just under 19 ns long; the units are first harmonic phase in degrees and energy in MeV. The momentum spread is about ± 0.2 %.

References

[1] L.J. Laslett, Proceedings of 1963 summer Study on Storage Rings, BEL-Report 7534, p. 324.

[2] F. Sacherer, *Transverse Space Charge Effect in Circular Accelerators*, Lawrence Rad. Lab. UCRL-18454 (PhD Thesis, University of California, 1968).

[3] E. Keil and W. Schnell, CERN Report TH-RF/69-48 (1969); V.K. Neil and A.M. Sessler, Rev. Sci. Instr. **36**, 429 (1965).

[4] B. Zotter and F. Sacherer, *Transverse Instabilities of Relativistic Particle Beams in Accelerators and Storage Rings*, Proceedings of the First Course of the International School of Particle Accelerators of ‘Ettore Majorana’ Centre for Scientific Culture, Erice 10-22 November 1976, p. 175.

[5] W. Hardt, *Gamma-Transition-Jump Scheme of the CPS*, Proc. 9th Int. Conf. High Energy Accel., SLAC, Stanford, 1974, p.434.

[6] “Transition Crossing Instabilities”, in *Proceedings of the Fermilab III Instabilities Workshop*, Eds. S. Peggs and M. Harvey, Fermilab, 1990.

[7] M. Martens and K. Y. Ng, *Impedance and Instability Threshold Estimates in the Main Injector*, Fermilab Report TM-1880, 1994, (MI Note MI-0103, 1994).

[8] “Impedances and Instabilities”, Sec. 2.9, *The Fermilab Main Injector Technical Handbook*, 1994.

Chapter 15. RF Upgrade

J. Griffin, J. Reid, D. Wildman

This chapter will examine the characteristics and properties of the existing Main Injector rf system with regard to its use, with appropriate modifications, at the beam intensity, acceleration rate, and longitudinal emittance specified in PD2. It will also give a brief description of a new rf system as an alternative approach.

15.1 PD2 RF Requirements

In the proposed Main Injector upgrade, six adjacent Proton Driver batches, each containing 2.5×10^{13} protons are to be injected into the Main Injector. The injected ensemble, containing 1.5×10^{14} protons, will span 504 of the h = 588 MI rf periods. Because each of the injected batches will contain fewer than 84 possible bunches, there will be a series of five small gaps in the injected ensemble. Assuming 500 filled buckets there will also be a larger gap of ~84 empty buckets in the injected ensemble. Bunches are to be injected into existing stationary buckets and each injected bunch is assumed to have longitudinal emittance (95%) ≤ 0.2 eV-s. Each bunch will contain $\sim 3 \times 10^{11}$ protons (4.8×10^{-8} Coulomb). The average steady state dc beam current (at mean rf frequency 53 MHz), will be ~2.54 A. The mean ring circumference is 3319.419 m. The rotation period ($\beta = 1$) is 11.07 μs. With $\beta \approx 1$ the effective accelerating voltage is $V\sin\varphi_s = (240 \times 10^9)(11.07 \times 10^{-6}) = 2.66 \times 10^6$ volts /turn.

With constant acceleration rate and rf voltage, the generated phase space bucket area above transition is minimum at $\gamma = \sqrt{3}\gamma_t$. Therefore, all calculations in this section will be done at 34 GeV ($\gamma = 36.2$). The longitudinal emittance of each bunch during acceleration is not expected to exceed 0.4 eV-s. Table 15.1 shows the requirements for the high power rf system to accelerate 1.5×10^{14} protons in the 1.867 s Main Injector cycle time.

Table 15.1. Summary of RF System Requirements

Frequency	52.813 MHz – 53.104 MHz
Maximum acceleration ramp slope	240 GeV/s (initially)
Beam intensity	1.5×10^{14} protons per cycle
Beam accelerating power	5.67 MW
Number of accelerating cavities	20
Cavity R/Q	120 Ω (unloaded)
Beam acceleration power per cavity	288 kW
Total Peak Power Amplifier power required (2 tubes) (beam + cavity + plate dissipation)	~ 800 kW (includes additional cavity loading)
Maximum cavity accelerating voltage	240 kV
Total accelerating voltage available	4.70 MV

15.2 Existing MI RF System

The existing rf system consists of eighteen stations, i.e. rf cavities, power amplifiers, power supplies, and ancillary systems. A sufficient number of spare rf cavities exist to allow expansion to twenty rf stations. The rf cavities are back-to-back folded resonators with a single accelerating gap, fabricated with OFHC Copper (cf. Sec. 15.5).

Ceramic vacuum seals are located at each end of an intermediate cylinder (not shown). Each cavity is tuned over the operating frequency range, 52.75 - 53.105 MHz, by two biased ferrite tuners inductively coupled symmetrically to the opposite lower cavity outer wall (i.e. outside of the inner vacuum chamber). The tuners and their coupling loops are water-cooled, as is the entire cavity.

At present each cavity is driven by a single Eimac 4CW150000 power tetrode mounted directly on the cavity. (The tube has been renamed Y567B because of slight geometry modifications required for this installation.) An important aspect of the cavity, incorporated into the original design, is that the tube anode is tightly coupled inductively to the cavity. The coupling loop is terminated by a symmetrically located capacitance equivalent to the tube output capacitance. The terminating capacitance is located within a top-hat mounted on a flange identical to the power amplifier mounting flange. This design anticipated the possibility of replacement of the terminating capacitance with an additional power amplifier tube with minimal cavity structure modification. An added benefit of the balanced loop coupling system is that the rf voltage at the fundamental frequency is zero at the center of the coupling loop so that the dc anode voltage can be applied at that point with minimum rf by-passing requirement. An additional benefit to this geometry is that if the dc voltage is supplied through a relatively small resistance (~50 Ω), energy from non-symmetric rf modes excited in the cavity (presumably by the beam current), can be coupled to the resistance, and the Q of such modes effectively damped. This technique is presently employed in cavity operation.

The installed (and available) rf cavities, with tuners attached and power amplifier in place, have effective shunt impedance $R_s \sim 7.8 \times 10^5\ \Omega$, $R_s/Q \sim 120\ \Omega$, and $Q \sim 6500$ (at frequencies away from injection). The voltage step-up ratio from anode to gap is 12.25:1. Each cavity is designed to operate at accelerating gap voltage 240 kV. The rf voltage at each vacuum seal is approximately 80 % of the half-gap voltage, i.e. ~ 100 kV.

The cavities have higher order mode dampers attached to vacuum seal cooling fans. Originally there were additional iris-coupled mode dampers containing frequency selective ferrite at each end wall. The iris ports may still be in place, but possibly covered with copper due to water leaks in the ferrite cooling plates backing the lossy ferrite.

15.3 RF Voltage, Power, Bucket Area, and Stability

Because of the increased beam intensity and acceleration rate contained in this proposal, it appears expedient to explore the improvements in performance and stability associated with increasing the number of rf stations to twenty, and the installation of an additional power amplifier on each rf cavity. Twenty of the existing Main Injector rf cavities, each powered by two of the presently used 150 kW tetrode amplifiers, should provide the rf voltage and power required by the proposed Main Injector upgrade.

Twenty rf cavities, each delivering 288 kW rf power to the beam, will deliver the requisite 5.76 MW. The cavities, each generating 235 kV, will provide total ring voltage 4.7 MV. The accelerating voltage $V\sin\varphi_s$ at 240 GeV/s is 2.66 MV. Consequently $\sin\varphi_s$ = 0.566, φ_s = 34.5°. The moving bucket factor $\alpha(\Gamma)$ (using the convention $\Gamma \equiv \sin\varphi_s$) is ~ 0.264. At γ = 7.75 the drift factor η = 0.0014. With these parameters the bucket area generated by 4.6 MV at 34 GeV is:

$$A_b = \alpha(\Gamma)\left[\frac{8R}{hc}\right]\sqrt{2E_s V/\pi h\eta} \approx 2.3 \text{ eV.s} .$$

Stability considerations will place stringent demands on the system capabilities, especially in the not uncommon circumstance where a cavity must be temporarily removed from service.

The frequency of the rf signal delivered to the rf stations is generated by a phase-lock system that locks the frequency to the beam bunch frequency. The rf voltage amplitude is controlled during acceleration by signals delivered to each station, calculated to generate the necessary power and bucket area. The phase of the rf signal is adjusted by an additional signal that makes small adjustments to correct for beam radial position errors. It is critically important that beam energy response to adjustments of the synchronous phase angle φ_s be stable and prompt. In addition to these global feedback loops, each rf station will have some element of local feedback to minimize transient and steady state beam loading effects. The gain, bandwidth, and performance of these feedback systems may be adversely affected by the physical length of the cabling necessary to implement them.

In conditions of heavy beam loading it is essential to consider the amplitude and phase of the voltage generated at each cavity gap by the rf component of beam current, in relation to that generated by the rf power generator. Because of the large bucket to bunch ratio proposed above, the relatively narrow beam bunch would have Fourier component approaching 2, so that the beam Fourier current and its image current will be near twice the steady state beam dc current. Here the beam rf current i_b is assumed to be 4.5 A.

It is convenient to represent the phase of the beam current on the positive real axis of a plot showing relative voltage and current phases. The equal and opposite image current i_i appears on the negative real axis. Also, it is common (though not absolutely necessary) to detune the rf cavity in such a way as to cause the phasor sum of the beam induced rf voltage and the rf power source voltage to be in phase with the source generator current. In this way the load presented to the amplifier is real and the anode dissipation is thereby minimized. Above transition (as is the case at 34 GeV), the cavity is tuned below its resonant frequency (so that it appears capacitive to the excitation current). This choice is consistent with one of the two Robinson stability requirements. [1,2] The rf cavity impedance presented to the generator and to the beam rf current is expressed:

$$Z_{cav} = R_{sh}\cos(\theta)e^{i\theta} \quad \text{where } \theta = \tan^{-1} 2Q\frac{\Delta\omega}{\omega_o} \quad \text{and} \quad \Delta\omega = \omega_o - \omega \quad .$$

The effective unloaded cavity shunt resistance R_{sh} is reduced by the parallel effect of additional components of real load, P_g, (exclusive of power delivered to the beam) referred effectively to the accelerating gap. The first instance of additional real load is the anode dissipation of the two amplifier tetrodes, ~280 kW. Added to the cavity dissipation, ~34 kW, the total 314 kW is larger than the 288 kW power delivered to the beam. This inequality (the requirement that the rf power source dissipation be larger than the power delivered to the beam) is in effect another of the Robinson stability criteria. The inequality is actually only a threshold for stability (see below). In order to increase the margin for beam loading stability it is proposed to deliver an additional 70 kW rf power to a water-cooled load from each operating cavity, increasing the real load at each gap to ~384 kW. The total rf power requirement per cavity becomes 672 kW, 336 kW per tube.

Using these parameters it is useful to define a resistance R_c in terms of the gap voltage V_g and the total real load P_g. A current, i_o, may be defined in terms of the resistance R_c and the gap voltage V_g. The ratio of the beam image current i_i and the defined i_o is expressed as Y.

$$R_c \equiv \frac{V_g^{\,2}}{2P_g}, \qquad i_o \equiv R_c/V_g, \quad \text{and} \qquad Y \equiv \frac{i_i}{i_o}.$$

The detuning angle required for a real load at the rf power source is Θ. The power source current necessary to deliver the required beam energy and to generate gap voltage V_g in the detuned cavity is i_g.

$$\Theta = \tan^{-1}\left(Y\cos(\varphi_s)\right) \qquad \text{and} \qquad i_g = i_o + i_i\sin(\varphi_s)\,.$$

For the conditions described here the loaded cavity R_c = 71.7 kΩ, i_o = 3.28 A. The detuning angle Θ = 48.5° and the generator current i_g = 5.83 A. The rf generator current developed by the two tubes is ~ 71.4 A. Transferred to the cavity gap by the step-up ratio 12.25, the generator current i_g at the accelerating gap is 5.1 A, slightly larger than the beam image current i_i. The cavity impedance $R_c\cos(\Theta)e^{i\Theta}$ is $47.4e^{i\Theta}$ kΩ. The gap voltage V_b developed by the beam image current i_i is 213.5 kV, and it lags the beam image current phase by the detuning angle Θ. A plot showing the relative magnitude and angular position of these voltages and currents is shown in Figure 15.1.

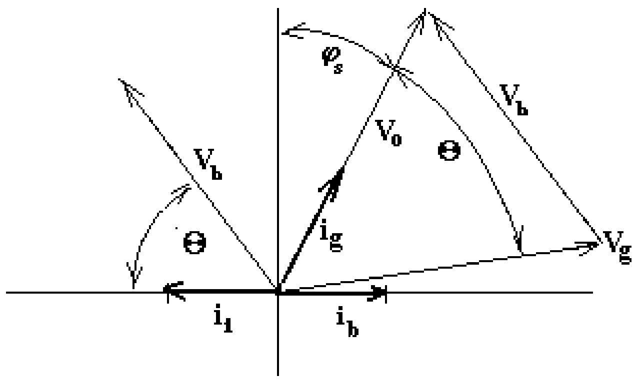

Figure 15.1. Relative phase and amplitude of gap voltages developed by the generator current i_g and the beam image current i_i. V_o is the effective resultant accelerating voltage.

The voltage phasor V_g, generated by the generator current i_g (and lagging it in phase by the detuning angle Θ), is nearly collinear with the beam current i_b. This phasor, added to the beam induced (actually decelerating) phasor V_b, creates the resultant gap voltage V_o at ($\pi/2$ - φ_s). If the focusing effect of the two phasors is considered separately, and if V_b moves in phase with a beam phase error, then the primary longitudinal focusing force is generated by V_g. If the angle ($\varphi_s + \Theta$) approaches $\pi/2$ then the beam bunches are riding at the peak of V_g, there is no longitudinal focusing force. The voltage response to a phase error ψ is (to 1st order in ψ)

$$V_g = V_o \sin\varphi_s + \psi V_o\left[\cos\varphi_s - Y\sin\Theta\cos\Theta_s\right] \quad .$$

The threshold for synchrotron phase oscillation stability under heavy beam loading is that the term in brackets cannot be negative, i.e.$Y\sin\Theta\cos\Theta/\cos\varphi_s \leq 1$. For the parameters developed above, $Y\sin\Theta\cos\Theta/\cos\varphi_s = 0.826$. This is the second of the Robinson stability criteria. [2] It is related to the rf power ratio stability limit through the definitions of Y and Θ.

When the rf cavity is delivering energy to the beam the amplifier must deliver 5.83 A to the cavity gap. This translates (through the 12.25:1 transfer ratio) to 71.38 A rf current from the amplifier, or 35.7 A per tube. This current is two times the tube average dc current multiplied by the Fourier transform of the tube anode current pulse. Tube screen grid voltages are set to +1500 V dc and the control grids set to -500 V dc. Each of the grids is grounded for rf by distributed capacitance. The desired anode current pulse (circles on Figure 15.2a), is obtained by driving the cathode with a 600 volt sinusoid delivered from a low impedance transistorized amplifier. The current conduction angle is $\pm 0.22\,\pi$ radians. The curve is well matched to the dotted function

$$i(t) = 78\left[1 - \left(\frac{4.6t}{T_{rf}}\right)^2\right]^{1.3} A\,, \qquad -0.22T_{rf} \leq t \leq 0.22T_{rf} \quad .$$

This function allows calculation of a normalized Fourier transform, Figure 15.2b.

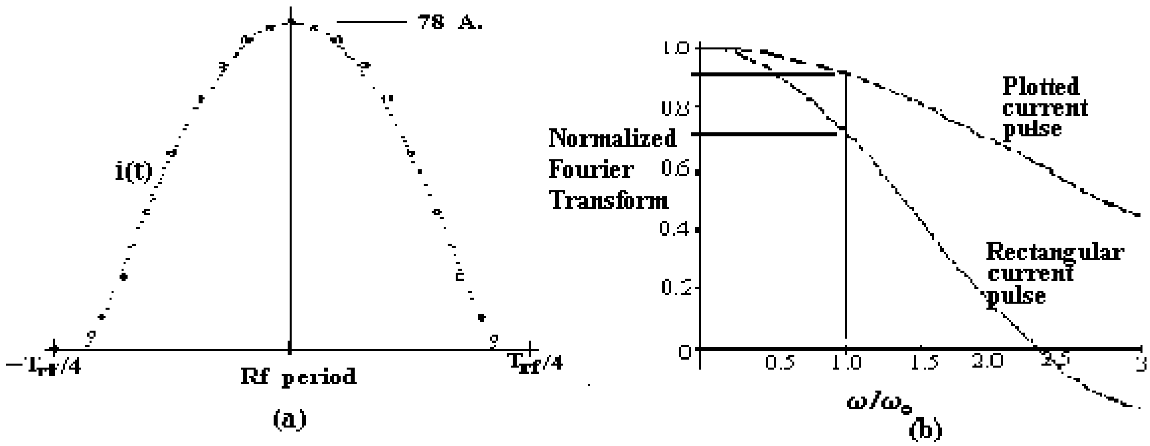

Figure 15.2. (a) Tube anode current for the grid bias and cathode drive level proposed. (b) Normalized Fourier transform for the matching calculated function (The transform of a rectangular pulse with the same area and width is shown for comparison.)

The normalized Fourier transform of the anode current pulse at the operating frequency is ~0.9. This translates to average anode current 39.6 A in each tube to develop the needed 71.4 A rf current. The anode dissipation, average tube current, and stability factor for the operating conditions proposed are:

$$\text{Anode diss.}\quad \frac{78}{2\cdot\pi}\cdot\int_{-1.3}^{1.3}\left[1-\left(\frac{x}{w}\right)^2\right]^{1.3}\left((23.-(19.2\cdot\cos(x)))+0.6\cdot\cos(x)+0.5\cdot\cos(5\cdot x)\right)dx = 139.81\ \text{kW},$$

$$\text{Average current.}\quad \frac{78}{2\cdot\pi}\cdot\int_{-1.3}^{1.3}\left[1-\left(\frac{x}{w}\right)^2\right]^{1.3}dx = 19.90\ \text{A.}\qquad \text{Stability factor.}\quad \left(\frac{Y\cdot\sin(\theta)\cdot\cos(\theta)}{\cos(\phi_s)}\right)=0.826\ .$$

15.4 Transient Beam Loading Considerations

In the course of normal operation the cavities must operate with a 1.6 μs beam current gap and several smaller gaps on each turn. The detuning angle Θ is usually generated by a feedback system that measures the anode voltage to cathode current phase angle and adjusts the tuner bias current to represent a real anode load. Due to the tuner inductive load and limited bandwidth of the tuner bias power supply this loop is relatively slow. As a result of the passage on each turn of the beam current gap, the sensing system would send a transient to the tuning system that may result is small errors in the phase of the rf buckets just following the gaps. It may be useful to disable the tuning feedback system during the gap passage by a programmed sample-and-hold technique.

If the cavities are not re-tuned at all during the gap, the phase and amplitude of the developed rf voltage will begin to move toward V_g, the phase shift being limited by the cavity time constant. This phase shift will again cause an rf phase error for bunches arriving just after the gap. If a fast phase shifter is installed in the cathode drive system, the rf drive phase could be shifted quickly to a point leading V_o by Θ so that the phase of the rf would remain correct during the gap. This phase shifter might be part of a feedback loop around each cavity and the loop performance could be augmented by a programmed feed-forward signal. Such a system would effectively minimize longitudinal dilution of those bunches just following the gaps.

15.5 Cavity Amplifier Upgrade Considerations

Several different scenarios have been considered to meet the upgrade requirement for about 800 kW of peak rf power to each rf station. The existing power amplifier on each cavity could be replaced by just one larger amplifier capable of developing ~800 kW. This would necessitate a complete redesign of the whole top half of the present cavity. This is by no means trivial and would require extensive redesign of the rf coupling loop geometry, top half of the cavity shell, anode dc voltage feed, water cooling, and probably cavity volume changes in order to re-establish the correct resonant frequency. A preferable approach to the single amplifier scenario is discussed in Section 15.9, where a new cavity-amplifier configuration is proposed.

The configuration to be considered is the installation of a second amplifier in place of the existing cavity balancing top hat capacitor. As shown in Figure 15.3, the cavities are already flanged for a second power amplifier, eliminating the need for redesign of the entire upper half of the cavity. The second amplifier can be added by replacing the original coupling loop with a new coupling loop, as shown in Figure 15.3. The second amplifier will be identical to the first, each capable of supplying approximately 400 kW of peak rf power.

The two-amplifier approach will require fabrication of new anode dc supply modulators, located upstairs in the equipment gallery. New rf driver amplifiers capable of supplying 25 kW (peak) rf drive to the cathodes of each power amplifier will be required. Larger capacity anode power supplies will be needed in order to supply the required anode currents (~40 amps per station). Cabling will have to be added to each station to support the second power amplifier and its driver. The existing cavity tuning ferrite bias power supplies need not be changed, as their requirements remain unchanged. However, these supplies are 32 years old, and at some point they will need to be replaced with updated units in order to maintain the long-term reliability of system components.

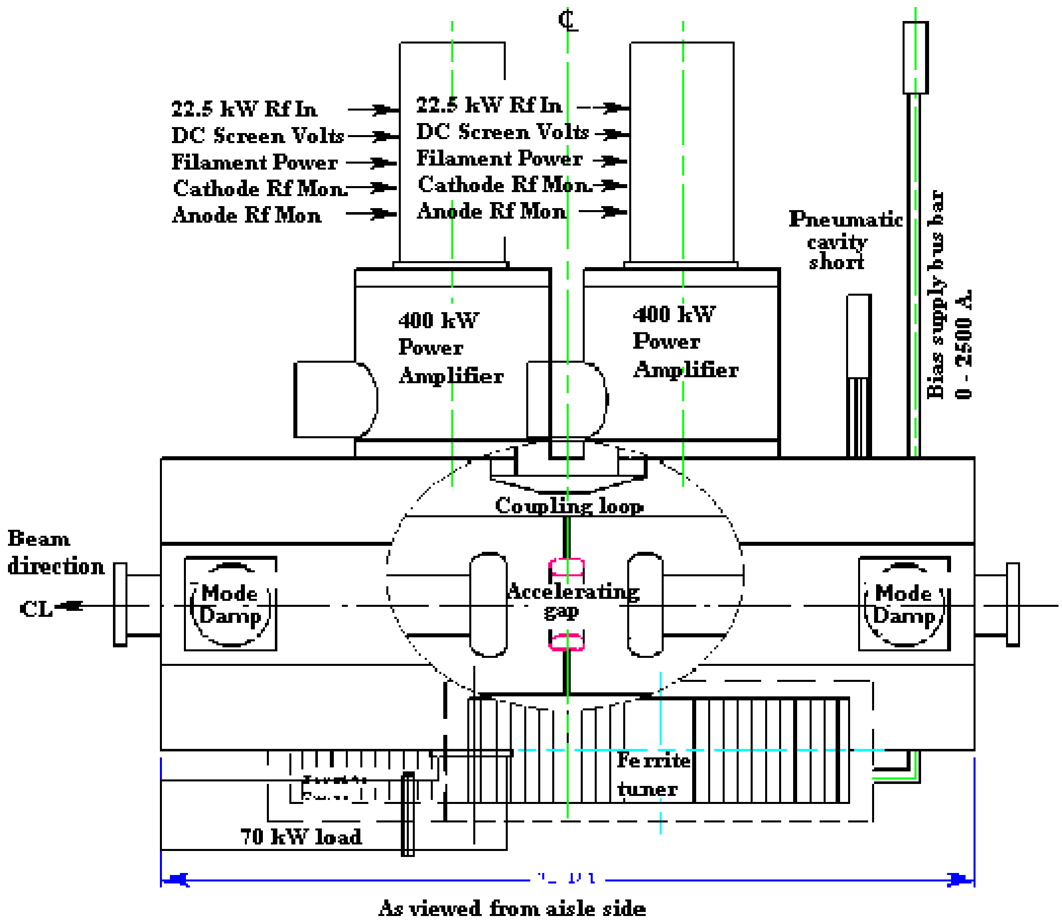

Figure 15.3. Modified Main Injector rf Cavity with two Power Amplifiers

15.5.1. Modulator requirements

A new anode voltage modulator design will be required to provide currents of 40 amperes at 21 KV to the two power amplifiers. Contained in these new modulators would be the screen, grid, and filament power supplies for the two power amplifiers along with a floating deck (electronic components operating at high voltage) and required power supplies. Because the modulator will have to supply two power amplifiers, a higher power (more plate dissipation) series tube will be used in the floating deck. This will probably result in a slightly larger cabinet, which will not be a problem in the existing equipment gallery. The present Main Injector modulators could be reused to upgrade the Booster's rf system. Another approach to a new modulator design would be to consider an IGBT.

15.5.2. Driver requirements

Because of the large rf drive power required in this configuration (25 kW per amplifier), a vacuum-tube driver will be necessary. This driver will need to be broadband and be driven by a few-hundred watt amplifier. Space in the equipment gallery is probably not a problem since it can take the place of the existing 4 kW solid-state drivers. However it would be highly desirable for these driver amplifiers to be located in the tunnel, thereby eliminating the long delay for the direct rf feedback (~ 300 ns). Minimization of cable delay is essential for maximum effectiveness of direct rf feedback This new driver amplifier will have power supplies (grid, screen, plate, and filament) located upstairs in the equipment gallery and multiple “Heliax” cables will carry the voltages from the remote power supplies to the tunnel.

15.5.3. Anode Supply requirements

Two choices are available to us. (1) Use the three existing anode supplies as they are to run three or four rf stations each. Build an additional three supplies (for a total of 6 supplies) to power the remaining stations. Since the three existing supplies are built as separate rooms off of the existing building, physical space for new supplies would have to be created. The 13.8 kV feeders that supply power to the anode supplies from the substation may require upgraded capacity. (2) Rebuild the three existing anode supplies with larger rectifier transformers capable of handling the ~6 MW peak power. This would also require upgrading the rectifier stack, capacitor bank, interphase reactor, water resistor, and possibly the fast 13.8 kV vacuum circuit breakers (step start contactors).

15.5.4. RF Controls requirements

Much of the rf controls would remain unchanged. A similar form of direct rf feedback would be employed unchanged, as in the present Main Injector system, along with transient beam loading (feedforward) compensation.

15.5.5. LCW requirements

Upgrade to the existing closed loop water systems at MI-60 that now provide LCW to the Main Injector’s rf systems will be required. There are currently two systems that supply water to the rf equipment, the 95^{o} F LCW and the 90^{o} F Cavity LCW systems. Table 15.2 shows the present requirements along with the upgrade requirements.

Table 15.2. LCW Requirements

95 degree (F) LCW	**Present Configuration 18 stations**	**Upgraded RF System 20 stations**
Ferrite Bias Supply	306 gpm	340 gpm
Series Tube Modulator	630 gpm	1400 gpm
Power Amplifier # 1	630 gpm	630 gpm
Power Amplifier # 2	0	630 gpm
Driver Amplifier	180 gpm	400 gpm
Anode Supplies	105 gpm	210 gpm
2.5 MHz Coalescing	72 gpm	72 gpm
Test Station	~200 gpm	~300 gpm
Total	**2123 gpm**	**3982 gpm**
Average Heat Load (50% DF)	~3.3 MW	~7.5 MW
90 degree (F) Cavity LCW		
RF Cavity	630 gpm	1300 gpm
Test Station	~100 gpm	~200 gpm
Total	**730 gpm**	**1500 gpm**
Average Heat Load (50% DF)	~0.5MW	~2.5 MW

15.6 Main Injector RF R&D Program

In order to reach the rf power levels necessary for stable operation at the proposed beam intensity and acceleration rate, several of the innovations described should be studied on the existing cavity test stand. This will require an increase in the cathode drive rf power and the anode dc power over that which is presently available. Following such a preliminary study it would be reasonable to modify one complete existing rf station with the necessary ancillary components and to install one modified cavity in the operating Main Injector.

The first step is a simple modification a power amplifier coupling loop, so that the top-hat can be replaced by an operational Y567 tetrode (cf. 15.5 above). The screen and control grids should be properly by-passed for rf and grounded through appropriate resistance (to prevent charging), and the cathode grounded through a small resistance (large dissipation). It should then be possible to operate the cavity at normal voltage and power level with a single amplifier, the newly installed amplifier providing only loop matching reactance. The installed amplifier will be supplied with correct anode voltage through the loop, but for this test the cathode filament may remain off.

If the filament of the installed tube is heated, but no rf drive supplied to the cathode, the effect of additional anode dissipation on the rf gap voltage may be measured for various settings of the screen voltage.

Subsequently the cavity can be excited with both amplifiers at presently available cathode drive levels. Unless the amplifiers are driven at reduced levels, rf power and voltage may become excessive unless additional rf loading is installed.

For study of cavity operation with additional rf loading, it may be possible to remove one or both of the tuners and replace them with transmission lines leading to 50 Ω water cooled loads. It may be necessary to reduce the coupling loop area in order to develop the desired load power at the water-cooled loads. This test must be done, of course, at constant frequency, reasonably near the normal operating frequency. Additional coupling ports and loops of appropriate area must eventually be installed and the loaded cavity tested again for proper frequency tuning.

Spurious mode properties of the modified cavities must be studied. It may be possible to re-activate and study the end-wall iris coupled dampers, possibly with different ferrite and improved cooling.

If some method of local rf feedback is to be considered, it may be possible to study transient beam loading by using one of the newly installed power amplifiers to inject beam transients into the cavity, while using the remaining tube with feedback to study dynamic response etc. In the same vein, it is attractive to consider the possibility of assigning one of the tubes the task of generating the desired no-beam-load gap voltage, while using the other tube with feedback and/or feed-forward simply to provide the necessary beam loading compensation.

In addition to these physical measurements and observations, a more detailed analysis of the adequacy of the stability margin should be studied. This may involve beam-tracking simulations using ESME with adjusted restoring force phasors. This may also be approached analytically by expressing the restoring force fields generated by the loaded cavity as a high order polynomial in a Laplace transform variable and analyzing the location of roots as a function of input variables.

The R&D program could start immediately with one of our spare cavities and the test station at MI-60. Even though the present MI rf cavity has provisions for a second amplifier, it has never been implemented as such. Engineering effort would be needed to carry out an operating life test. A final test could be done by installing this modified cavity in the tunnel and actually accumulate running time with beam.

15.7 Summary of Modifications to Existing RF Cavities

With moderate modification to the existing Main Injector rf cavities, and extensive additions to ancillary dc and rf power sources, the Main Injector rf system can be used effectively to meet the beam intensity and repetition rates proposed in the Main Injector

Upgrade program. The number of operating rf stations must be increased from eighteen to twenty. A sufficient number of spare rf cavities exist to meet this requirement. One additional rf final amplifier tube (with enclosure shell, tube socket and other components), must be added to each cavity. The additional dc power capability will have to be provided regardless of whether the existing cavities, or redesigned cavities with lower R/Q and larger tubes, are employed.

One advantage of this proposal is that work on the cavity system upgrade can begin immediately. Improvements in the cavity design can be used to advantage either in whole or in part in continued operation of the Main Injector in its present mode. This may become especially true if the total beam load in the Main Injector is increased in the future by slip stacking or barrier stacking of the injected Booster beam.

The question of whether modified Main Injector rf systems as proposed here might be used at even higher ramp rates (up to ~300 GeV/s) will become the subject of a further and more challenging analysis.

15.8 Increased Ramp and Repetition Rate

The rf parameters outlined in Section 15.5 indicate that twenty modified Main Injector rf stations, with two power amplifiers mounted on each cavity, can develop adequate rf voltage and power to meet the MI Upgrade requirements at an acceleration ramp rate of 240 GeV/s. Amplifier and cavity parameters were shown not to have exceeded maximum allowable levels at that ramp rate. The maximum reasonable acceleration rate, with additional cavity loading and maximized cavity and tube parameters, appears to be near 300 GeV/s. There is space in the MI lattice for two additional rf cavities similar to those in use.

At 34 GeV (minimum bucket area point), a 300 GeV/s ramp rate requires accelerating ring voltage $V\sin\varphi_s = 3.32$ MV per turn. The rf beam power required to accelerate 1.5×10^{14} is 7.2 MW. With twenty-two cavities installed the accelerating voltage and power requirements per cavity are 151 kV and 327 kW.

The existing MI rf cavities can be operated at 240 kV gap voltage. With 240 kV from 22 cavities (5.28 MV total ring voltage), the synchronous phase angle φ_s becomes 39°, the moving bucket factor $\alpha(\Gamma) = 0.222$, and bucket area ~2.0 eV-s is developed.

In order to deliver the requisite 327 kW of beam power, each amplifier tube is operated at the maximum allowed anode dissipation, 150 kW. With 120 kW of additional dissipation delivered to water-cooled loads, the detuning angle Θ is 41.3°. The stability sensitive voltage phasor V_g reaches $(\Theta + \varphi_s) = 80.3°$, approaching the stability limit (cf. Figure 15.1). In this mode of operation each amplifier delivers 392 kW rf power.

The most demanding parameter in this cavity-amplifier configuration is the gap excitation current i_g, which is required to reach 6.5 A. This implies that each amplifier tube must deliver 39.8 amperes rf current, very near the maximum cathode average current limit, 20 amperes, with the Fourier transform of the anode current i(t) forced as near to unity as possible. The required drive current may be generated by driving and biasing the amplifier tube to peak current 90 A. with the smallest possible conduction angle, ~130°. This can be done by adding a third harmonic component to the cathode drive power so that the cathode is driven by relatively narrow pulses superimposed on the fundamental excitation sinusoid.

It can be concluded that with all amplifiers on twenty-two installed rf cavities operating at or near maximum gap voltage, anode current, and dissipation, the Main Injector beam intensity and repetition rate goals can be approached using existing MI rf cavities with the proposed modifications.

15.9 Proposal for a New Main Injector rf Amplifier/Cavity System

An alternative approach to extensive modification of the existing MI rf system, described above, is to design an entirely new system. This new RF system has the advantage of solving the longitudinal beam stability and transient beam loading problems by addressing them at their source, the RF cavities themselves. The beam loading voltage, ΔV, An alternative approach to extensively modifying the existing MI RF system, described in induced by the passage of a high intensity proton bunch through N, RF cavities is proportional to the number of cavities times the charge in the bunch, dq, multiplied by the cavity shunt impedance, R_{sh}, divided by the cavity Q.

$$\Delta V \propto NdqR_{sh}/Q$$

In PD2, the Main Injector bunch intensity, dq, will be increased by a factor of five over the present operating conditions. If we were to lower NR_{sh} by a factor of five, the product $NdqR_{sh}/Q$ would then remain unchanged and the transient beam loading would remain equal to that experienced today in the MI. Since the present MI RF system can accelerate and store stable beam without any fast direct feedback to the cavities, the new system running at five times the current intensity will also be stable and will not require any additional feedback loops. From a beam stability viewpoint, the two situations are identical.

The proposed new RF system keeps $NdqR_{sh}/Q$ constant by reducing the number of cavities from 20 to 14 and lowering the R_{sh}/Q of each cavity from ~100 to 25 (while keeping Q constant). This change in the number of RF cavities requires that the peak acceleration voltage of each cavity be increased by a factor of 20/14 from 235 kV to ~350 kV. The above parameters, along with the tuning range of 52.813 MHz to 53.104 MHz, completely specify the new cavity.

For specification of the power amplifier, maximum and average power requirements are needed. One of the Robinson conditions for longitudinal beam stability is that, without fast feedback, the stability limit is reached when the power being delivered to the beam equals the power being dissipated in the RF cavity and power source. From section 15.1 the total power delivered to the beam will be 5.67 MW, or 405 kW/cavity. At the stability limit each amplifier must deliver twice this value, or 810 kW/cavity. Since the amplifiers will operate in the long pulse regime with a high duty factor, the amplifier specification calls for a cw output of at least 1 MW.

A sketch of one RF cavity and amplifier that meets the above design specifications is shown in Figure 15.4. The cavity is a single gap quarter wave coaxial structure with a characteristic impedance $Z_o = 20\ \Omega$. In order to achieve a shunt impedance $R_{sh} = 100\ k\Omega$ (Q = 4000) the main body of the cavity is made from stainless steel with water cooling jackets on both the inner and outer conductors. A 15 cm diameter beam tube is connected to the 10 cm accelerating gap. The cavity body is under high vacuum with connections to the rf drive, tuner, and higher order mode (HOM) dampers through high purity alumina coaxial windows. Unlike the body of the cavity, which is intentionally designed to produce high rf losses, the tuner is designed to minimize losses. It consists of a OFHC copper coaxial line filled with 30 Transtech G-810 yttrium garnets, 32 cm OD $\times$ 12 cm ID $\times$ 1 cm thick, separated by 0.5 cm. The garnets will be perpendicularly biased above resonance to obtain a Q > 20,000. During acceleration the perpendicular bias field on the garnets will be varied from 1.3 kG to 3 kG to produce a change in μ_r from 2.5 to 1.2. The maximum energy stored in the cores is approximately 0.047 J. The maximum rf magnetic field $B_{rf} = 42$ G with an average $B_{rf} = 25$ G. The peak power dissipated in the garnets is 300 W. The tuner will be both water and forced air-cooled. The single layer solenoid, which provides the perpendicular bias field, is wound from 60 turns of 1 cm square water-cooled copper bus. The solenoid has an inductance of 650 μH and requires a current of 1000 A to 2400 A. A magnetic flux return on the solenoid (not shown in the figure) along with magnetic shielding of the beam tube will be used to reduce stray fields at the beam axis.

The power amplifier is based on the EIMAC 8973 tetrode operated in the cathode driven, grounded grid configuration. The tetrode, rated to 110 MHz, has a maximum plate dissipation of 1 MW, and may be operated as a class C RF amplifier with an output power greater than 1 MW. The tube anode is coupled through a 2000 pf vacuum high voltage capacitor to the cavity input coupling loop. The cavity step-up ratio will be equal to 15, requiring an RF voltage swing of 20 kV on the tube anode. With dc anode voltage of 20.3 kV dc, screen voltage 1100 V, and dc grid voltage –300V dc, the 8973 has delivered a measured output power of 1050 kW for a 100 s pulse at 80 MHz. Under these conditions the plate current was 78 A, plate dissipation 550 kW. The required drive power was 38 kW. For transient beam loading compensation, the 8973 can supply peak current pulses greater than 400 A and an average current of 110 A for long pulses. Commercially available IGBT modulators will be used for the HV dc plate supplies, and the present MIRF power amplifiers will be used as drivers for the 8973 tetrodes.

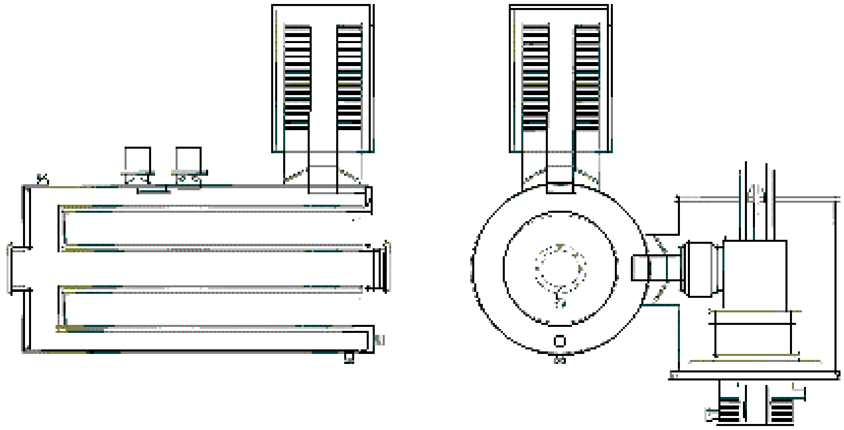

Figure 15.4. Side and end view of proposed low R/Q cavity with amplifier.

References

[1] D. Boussard, Theoretical Aspects of the Behavior of Beams in Accelerators and Storage Rings, CERN 77-13, (1977).

[2] K.W. Robinson, Cambridge Electron Accel. Report CEAL-1010, (1964) et. seq.

Chapter 16. Gamma-t Jump System

16.1. System Description and Lattice Layout

W. Chou

In the present Main Injector, the injection energy is 8 GeV and maximum energy 120 or 150 GeV (depending on the operation mode). Transition crossing is at $\gamma_t = 21.6$. In the MI baseline design, no γ_t-jump system was included. However, when the beam intensity is increased by a factor of five, as assumed in PD2, simulation shows that emittance dilution and beam loss will occur (see Section 14.2). Furthermore, from experience at other machines (e.g., the AGS at BNL, the CERN PS and the KEK PS), transition crossing could become a severe bottleneck in high intensity operation. Therefore, a γ_t-jump system is necessary when we plan to upgrade the MI beam intensity.

The conceptual design of a γ_t-jump system for the Main Injector was completed in 1997 and reported in Ref. [1]. It is a so-called first-order system employing local dispersion inserts at dispersion-free straight sections. The design goal is set as follows. The normal ramp rate of the MI is about 240 GeV/s. In order to have an effective γ_t-jump, the jump rate should be at least an order of magnitude higher. Thus the system was chosen to provide a $\Delta\gamma_t$ from +1 to -1 within 0.5 ms. This gives a jump rate of 4000 s^{-1}, about 17 times faster than the normal ramp rate.

The system consists of 8 sets of pulsed quadrupole triplets. Each triplet has two quads in the arc and one of twice integrated strength in the straight section, with a phase advance of π between each quadrupole. The perturbation to the original lattice is localized. In particular, the dispersion increase during the jump is small ($\Delta D_{max} \approx 1$ m), which is the main advantage of a first-order jump system. Each triplet is optically independent from the others and provides roughly 1/8 of the total required jump amplitude (i.e., $\Delta\gamma_t \approx 0.25$ per triplet). The power supply uses a GTO as the fast switch and a resonant circuit with a 1 kHz resonant frequency. The beam pipe is elliptical and made of Inconel 718. It has low electrical conductivity σ and high mechanical strength so eddy current effects are relatively small. (The eddy current effects scale as σd, where d is the pipe wall thickness. The σd value of Inconel 718 is about four times lower than that of stainless steel.)

An alternative to a γ_t-jump system is the focus-free scheme using a higher harmonic rf cavity. Although this scheme is believed to be good for tackling nonlinear effects during transition crossing, its effectiveness is unknown for curing collective effects (e.g., bunch length mismatch due to space charge, negative mass instability after transition). Therefore, it will not be discussed in this chapter.

The locations of the required 24 pulsed quadrupoles (PQ) are listed in Table 16.1 and shown in Fig. 16.1. Each triplet consists of three quads, marked as PQxxx, in which xxx is the nearest main quad number of the Main Injector. In Table 16.1, eight locations are marked with "ok," meaning that there is no conflict with the existing components in the ring. At fifteen of the locations notes indicate measures needed in order to fit the pulsed quadrupoles into the ring. However, one location (PQ322) in MI-32 may have to be excluded because of the antiproton beam transport line from the Recycler (which did not exist when the design was carried out in 1997). There are two possible solutions to this problem. One is to use 7 triplets instead of 8. This would lead to a reduction of 1/8 in jump amplitude, which is acceptable. Another is to find a new location for this triplet, which is yet to be studied.

Table 16.1. γ_t-Jump System Pulsed Quadrupole Locations

PQ104 – relocate a multiwire monitor
PQ108 – remove a sextupole
PQ112 – ok

PQ226 – shorten BPM by 1-inch or eliminate the bellows
PQ230 – same as PQ226
PQ302 – relocate a Schottky detector

PQ322 – interference with the MI-32 antiproton line from the Recycler
PQ326 – same as PQ108
PQ330 – ok

PQ334 – ok
PQ338 – ok
PQ400 – move the abort kicker downstream by 1 m

PQ404 – ok
PQ408 – same as PQ108
PQ412 – ok

PQ526 – same as PQ226, plus relocate an LLRF pickup
PQ530 – same as PQ526
PQ602 – relocate the Desert Air box

PQ622 – move the antiproton extraction kicker by 1 m
PQ626 – same as PQ108
PQ630 – remove a trim quad

PQ634 – ok
PQ638 – ok
PQ100 – move the γ_t quad downstream by 40-inches to avoid SQA852

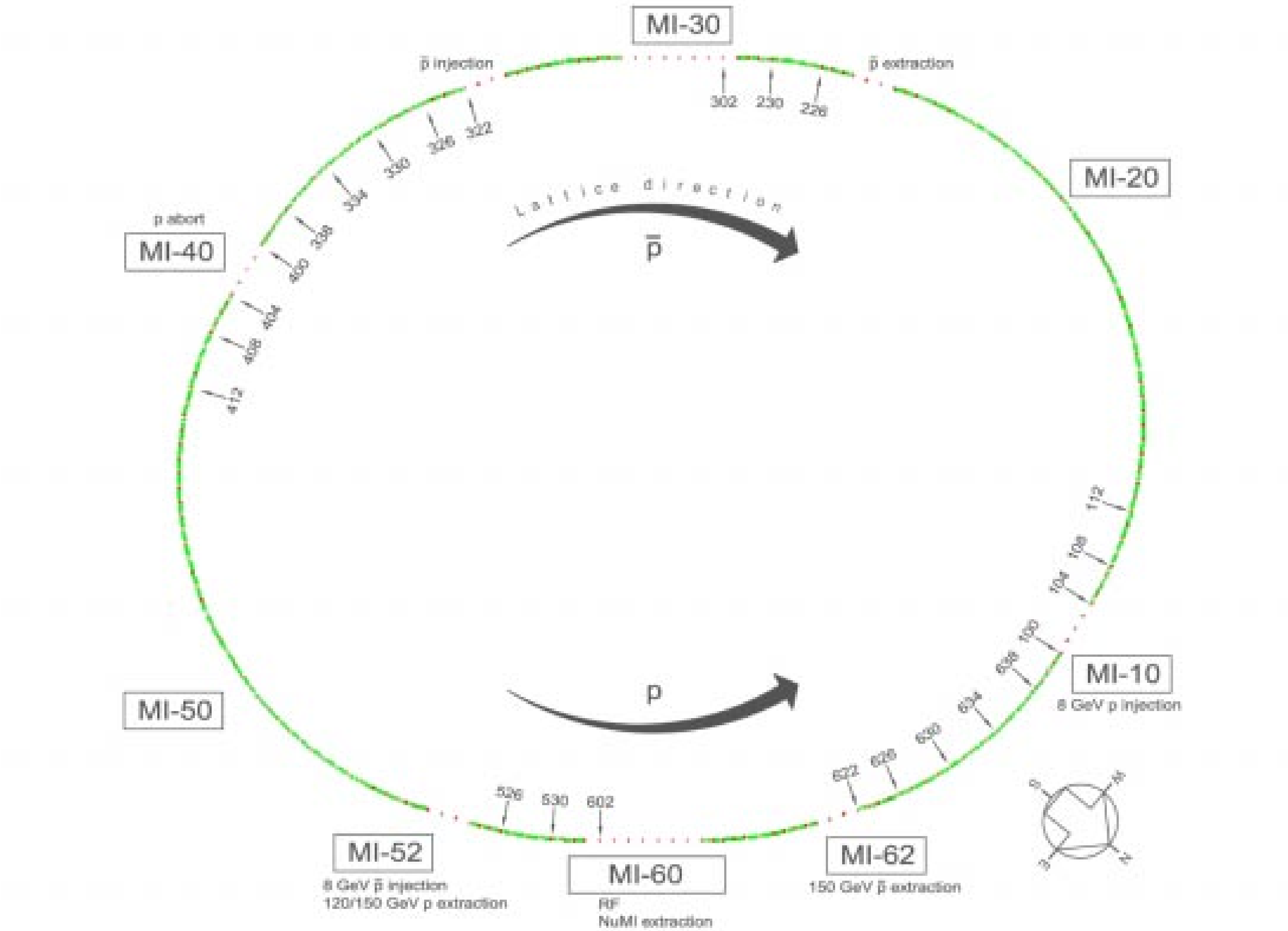

Figure 16.1. Gamma-t jump system lattice layout - Locations of the 24 pulsed quads in the Main Injector. (Red indicates the MI main quadrupoles, green the main dipoles.)

16.2. Pulsed Quadrupoles

I. Terechkine

16.2.1. Introduction

This section describes the pulsed quadrupole design for the Main Injector gamma-t jump system. Preliminary design criteria were described by B. Brown [2] and W. Chou [1] and provide a starting point for this section. Attention is paid to power losses in the quadrupole core, coil and vacuum pipe, because these losses will influence the power supply design and performance. The main feature of the quadrupole is its operational frequency requirement. The maximum frequency in the current pulse spectrum is about 1 kHz. The bipolar current pulse consists of three parts: a relatively slow current rise (about 3 ms) until maximum current is achieved, a fast current drop (0.5 ms) with current polarity reverse, and then a slow current decay (3 ms). The current pulse is to be applied to the quadrupole only once during the acceleration cycle, so heating is not so important. Nevertheless, eddy currents induced in the steel core (if the core is made from steel laminations), copper wire and stainless steel vacuum pipe can change significantly the current pulse parameters. That's why it is necessary to analyze the effect of these eddy currents on the magnet equivalent circuit parameters. Relevant system requirements are listed in Table 16.2.

Table 16.2. Pulsed Quadrupole System Parameters

Required integrated gradient (T)	0.85
Vacuum pipe cross-section (elliptical) (inch.)	2.4×1.125
Field quality within 1 inch radius circle	2%
Maximum quadrupole length (inches)	17
Maximum current (A)	200
Maximum voltage (V)	ALAP

16.2.2. Magnetic design

It is desired to keep the voltage as low as possible (ALAP). This necessitates reducing the total volume of magnetic field. It is possible to achieve the required field quality using an unsymmetrical pole design and simple flat coil fitted around the vacuum pipe. Figure 16.2 shows one quarter of a quadrupole cross-section, and Table 16.3 gives core cross-section base point coordinates.

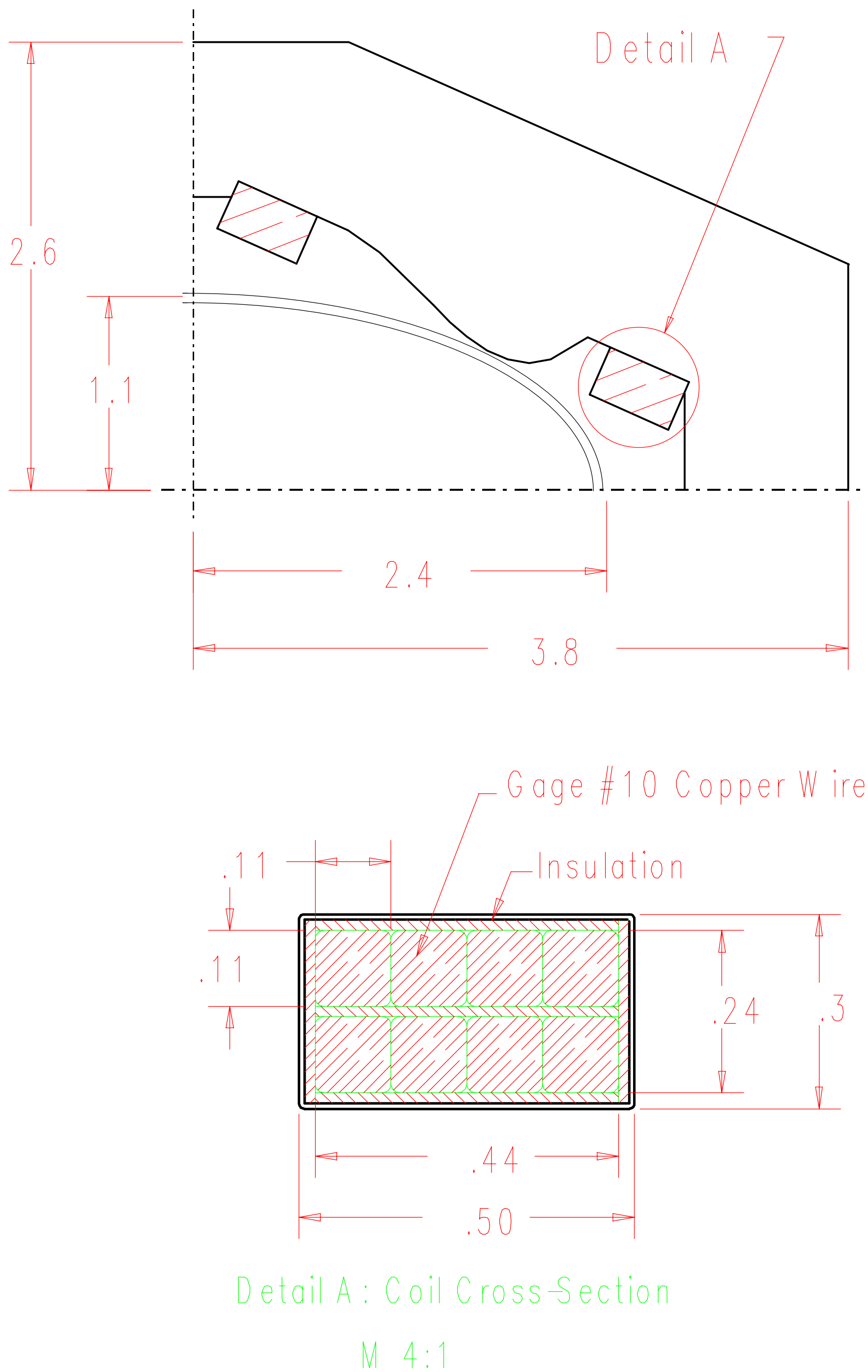

Figure 16.2. Pulsed Quadrupole Cross-Section Layout

Because the coil in this design plays a rather significant role in shaping the field, it should be epoxy impregnated to provide necessary rigidity and reproducibility of cross-section dimensions. Coil positioning tolerances are about ±0.010 inches, not a big problem for this kind of coil.

Table 16.3. Core Cross-Section Base Points Coordinates

X (in)	Y (in)	X (in)	Y (in)	X (in)	Y (in)	X (in)	Y (in)	X (in)	Y (in)
0.0	1.7	1.08	1.38	1.825	0.76	2.879	0.626	0.9	2.7
0.222	1.7	1.394	1.07	1.95	0.735	2.85	0.561	0.0	2.7
1.263	0.791	1.491	0.97	2.075	0.76	2.85	0.0	0.0	1.7
0.719	1.588	1.587	0.89	2.29	0.888	3.80	0.0		
0.9	1.508	1.706	0.81	2.422	0.829	3.8	1.3		

With total Ampere-turns in the coil Iw = 1623.8 A (corresponding to 20,000 A/in^2 of coil average current density), the gradient G = 560 Gauss/in; so about 15.2 inches of a core length is required to meet the integrated strength requirement. Figures 16.3 and 16.4 show the field distribution, and Figure 16.5 shows field quality for horizontal and vertical axes.

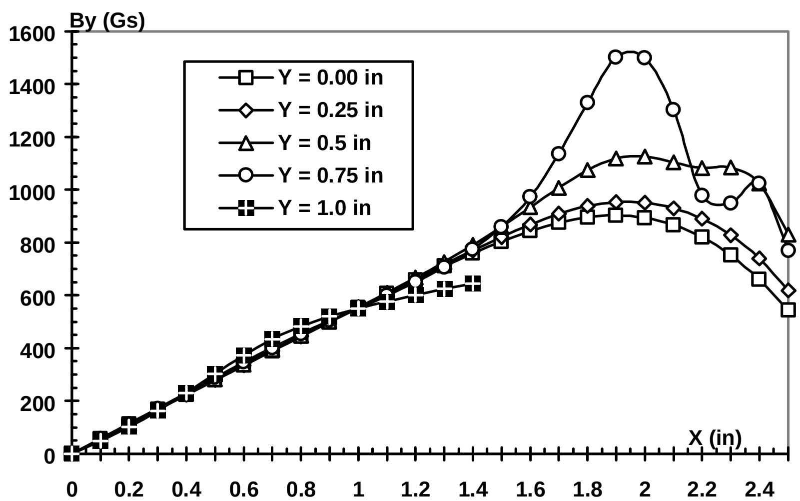

Figure 16.3. Vertical magnetic field distribution in the quadrupole cross-section.

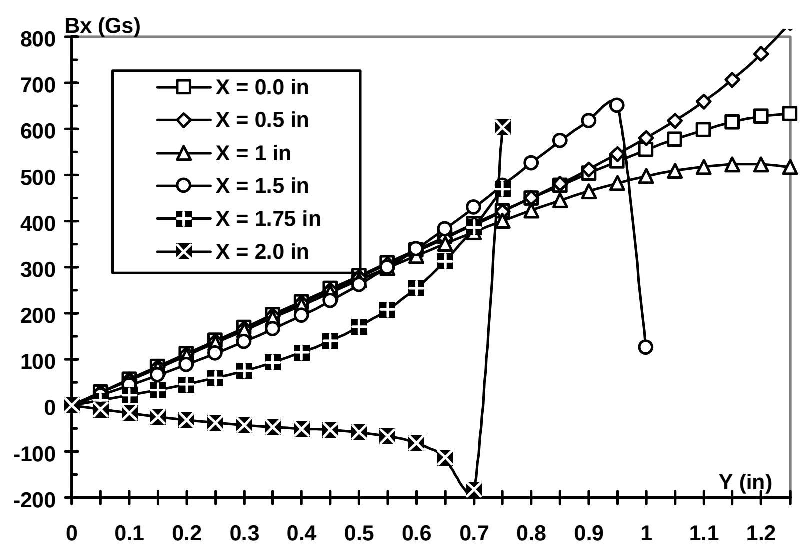

Figure 16.4. Horizontal magnetic field distribution in the quadrupole cross-section.

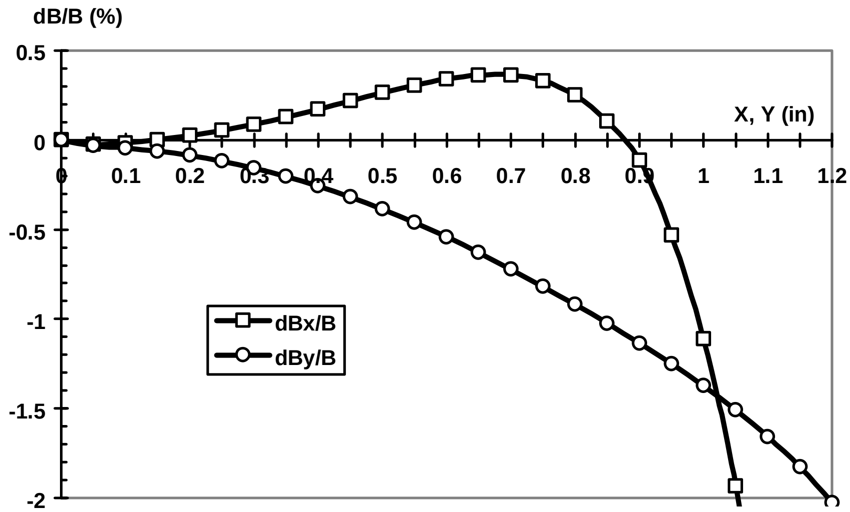

Figure 16.5. Quadrupole field quality

The magnetic flux for one pole at nominal gradient is 2530 G-in^2 per 1 inch of the magnet length, or 0.0025 Tm^2 for the 15.2 inch length quadrupole. Table 16.4 contains data used to choose coil parameters based on the required integrated strength.

Table 16.4. Quadrupole Parameters

Number of turns per pole	6	8	10
Inductance (μH)	225	400	620
Current (A)	270	200	160
Voltage (V)	375	500	630
Resistance (mOhm)	12	20	32

To choose coil wire gauge, it is useful to calculate the copper skin layer thickness. This is about 0.09 inch, so the wire thickness cannot be significantly larger than 0.18 inch. Fig. 16.2 and Table 16.4 use #10 square copper wire, which has thickness about 0.1 inches.

16.2.3. Eddy Current Losses

To form the required current pulse, the power supply described in [2] made use of LCR resonant circuits. The quality factor of this circuit is affected not only by the coil wire resistance, but also by power losses due to eddy currents induced in the vacuum pipe, in the steel core, and in the coil itself. To compare power losses due to eddy currents in different magnet parts, it is convenient to describe these losses in terms of an equivalent parallel resistance R. Then wire losses caused by the excitation current can be described by an equivalent parallel resistance R_{wire} that can be found if we know the wire series resistance r_{wire} (Table 16.4):

$$R_{wire} = \omega^2 L^2 / r_{wire}$$

This formula gives R_{wire} = 315 Ohm at 1000 Hz for an 8-wire pole coil. (L is the total magnet inductance). For comparison, the magnet impedance ωL = 2.5 Ohm.

16.2.3.1. Vacuum pipe power losses

In order to find vacuum pipe losses, it is necessary to know the current density distribution in the pipe wall. To calculate the current density distribution, the normal magnetic field distribution was found along the pipe circumference using the OPERA-2D magnetic modeling program. Figure 16.6 shows the normal magnetic field distribution for a vacuum pipe made of flat surfaces that approximate an elliptical cross-section. In this picture, s is the distance along the pipe wall beginning from the point (0, 1.1) counterclockwise to the point (2.4, 0) (see also Fig. 16.2). The field distribution is shown only for one quarter of the cross-section.

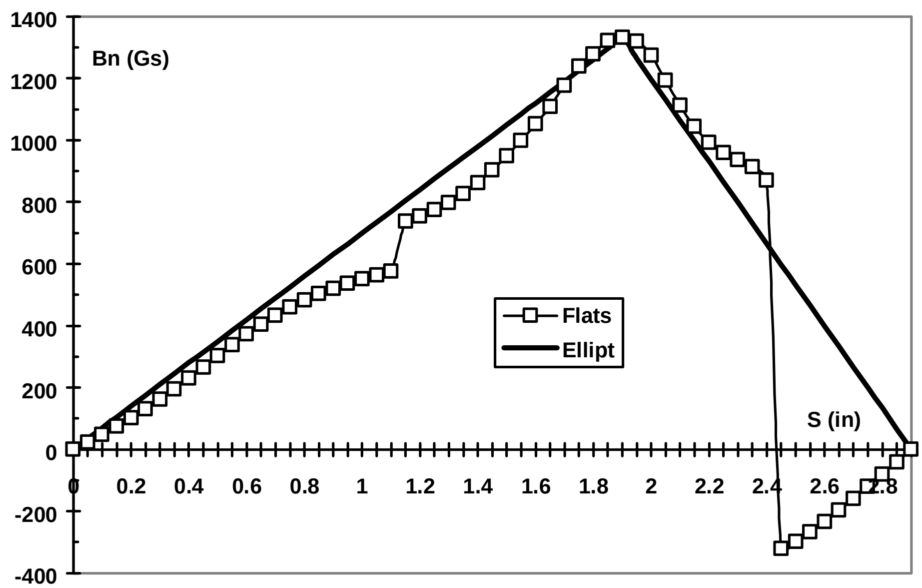

Figure 16.6. Normal magnetic field distribution along the vacuum pipe

To simplify the problem a linear normal field distribution was used along the pipe cross-section border:

B_n (G) = 700 s if s < 1.9 inches,
B_n (G) = 3857 - 1330 s if s > 1.9 inches.

This distribution is the solid line in Fig. 16.6. Converting inches to meters and Gauss to Tesla gives:

B_n (T) = 2.756 s (m) if 0 < s < s1,
B_n (T) = 0.3857 - 5.236 s (m) if s1 < s < s2.

In this expression s1 = 0.04826 m is the point with the maximum magnetic field B_m, and s2 = 0.07366 m is a quarter of the vacuum pipe perimeter. Using the simple expressions for the normal magnetic field distribution above and applying the condition that the total current in the pipe is zero, we find the pipe wall current distribution:

$$j(s) = 1/6\cdot\omega\cdot B/\rho\cdot(2\cdot s2 - s1 - 3\cdot s^2/s1) \qquad \text{if } s < s1,$$
$$j(s) = 1/6\cdot\omega\cdot B/\rho\cdot(3\cdot s^2 - 6\cdot s\cdot s2 + s1^2 + 2\cdot s2^2)/(s2 - s1) \qquad \text{if } s > s1.$$

This distribution is shown in the Fig. 16.7.

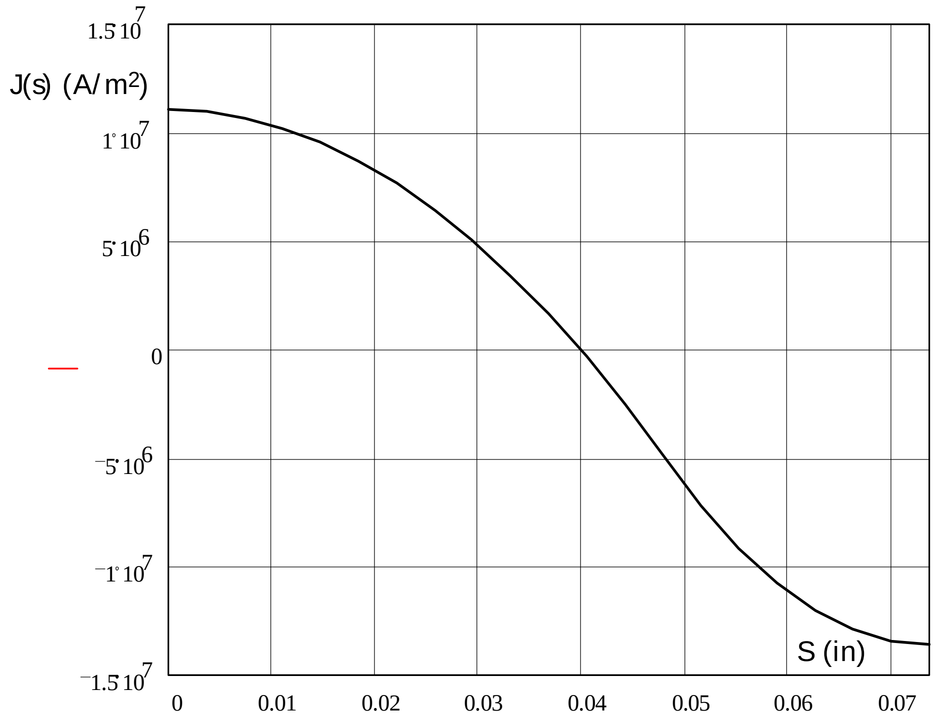

Figure 16.7. Current density distribution in the vacuum pipe wall

Now it is easy to find total power in the pipe wall:

$$P = l\cdot t\cdot\rho\cdot\oint_p j^2 ds\ ,$$

where l is the magnet length and t the wall thickness. Integrating over the vacuum pipe perimeter gives for a 25-mil wall Inconel 718 pipe ($\rho = 1.25 \times 10^{-6}$ Ohm·m) the maximum instantaneous power:

$$P \approx 7{,}300 \text{ W}$$

The parallel resistance that corresponds to this power loss $R_{pipe} = U^2/P \approx 34$ Ohm. Comparing this loss resistance value to the quadrupole intrinsic impedance (2.5 Ohm) gives the circuit quality factor $Q \approx 13.5$.

16.2.3.2 Core power losses

If the magnet core is assembled from steel laminations, two factors cause power losses: steel eddy currents and hysteresis. Because hysteresis losses scale proportionally to the operation frequency, and eddy current losses grow as the square of the frequency, we can expect at 1000 Hz eddy current losses will dominate.

Two different parts of the magnetic flux generate the steel eddy currents. The first is the main flux that goes along the laminations; the second is the end flux that is perpendicular to the lamination surface.

Main flux

Eddy current maximum instantaneous power losses in a laminated core can be estimated using the expression:

$$P_{st} = 1/12 \cdot \omega^2 \cdot B^2\, t^2/\rho \cdot V,$$

where V is steel volume and B stands for steel magnetic field. With B = 0.14 T, the average steel magnetic field from magnetic calculations, and choosing M-15 silicon steel ($\rho = 5 \times 10^{-7}$ Ohm·m) with lamination thickness t = 0.014 inch (0.355 mm), we have P_{st} = 120 W. Parallel resistance that accounts for this loss component is R_{st} = 2100 Ohm. Because the main flux loss resistance is rather high, we can use a thicker lamination. But this would reduce the steel effective stacking factor because flux is not distributed equally through the cross-section. Skin layer thickness for the silicon steel at 1000 Hz can be calculated as

$$\delta^{-1} = (\omega\mu\mu_0/2\rho)^{1/2}$$

Using μ = 5000, a typical value for silicon steel at low field level, we have δ = 0.15 mm; so a lamination thickness t = 0.3 mm is close to optimal.

End flux

Because it is practically impossible to make a coil that exactly follows the magnet pole edge (current density limitations), part of the magnetic flux goes perpendicular to the magnet end plane. Eddy currents induced in laminations result in a limitation on axial flux penetration thickness, but this thickness is not equal to the thickness of the skin layer. Magnetic modeling shows that if the coil is located near the pole end, it is possible to calculate the depth of axial field penetration using a linear magnetic field drop along the coil thickness d:

$$j \approx H_m(1/c-1/d),$$

or

$$j \approx B_m/\mu\mu_0(1/c-1/d).$$

Permeability μ should be taken close to 1 because most of the magnetic field circulation circuit passes through air, and only part of it goes inside the core. On the other hand, current density

$$j = U/(\rho\cdot p),$$

where $U = \omega\cdot F$ is voltage generated by changing flux F through the pole surface S, and p is the pole perimeter. To calculate end flux, we approximate the pole as a trapezoid with small side $w_0 = 0.5$ inches, base side $w_1 = 2$ inches, and height equal to the coil thickness (see Fig. 16.2). Then the total flux F through the pole is:

$$F = \int B_m(1-y/d)(w_0+3\cdot w_0\cdot y/d)dy,$$

where integration is performed along the pole height (0 to d). Calculation gives $F = 1.3 \times 10^{-5}\ Tm^2$, about 0.5% of the total magnet flux. Combining these equations, we have a simple estimate for the equivalent eddy current penetration depth c:

$$c^{-1} = 1/d + \omega\cdot\mu_0\ F/(B_m\cdot p\cdot\rho)$$

Because the flux F can be written as $F = k^{-1}\ S\ B_m$, where k is a coefficient depending on details of coil positioning and pole shape, we can rewrite the above equation as

$$c^{-1} = d^{-1} + \omega\cdot\mu_0/(k\cdot\rho)\cdot S/p$$

For our specific coil-pole case, we have $S = 0.375\ in^2$, $p = 2$ in, and $k = 2.56$. Substituting into the above equation we have c = 6.25 mm (0.25 inches).

On the other hand, the end flux is taken from the nearest lamination layers. The total thickness of this layer is approximately equal to half of the magnet gap, about 1 inch for this quadrupole. The effect of eddy currents on field distribution is a reduction of axial field near the pole and an increase of the gap field near the magnet end.

Comparing the two numbers for border layer thickness: 0.25 inches and 1 inch, we conclude that in the case of our magnet eddy currents change the steady state end magnetic field distribution. Taking this into the account, and providing an additional margin by choosing the maximum number for end flux penetration depth, the distribution of the axial magnetic field near the magnet end can be written as:

$$B_z\ (y,z)= B_m\ (1-y/d)\ (1-z/c),$$

where c = 1 inch.

When we know the normal magnetic field distribution, we can calculate the induced current density in the pole. To simplify the problem, we use a rectangular pole shape with width w and the same end surface area. This gives more power than with the real pole because a larger volume is carrying a larger current density. We also assume that only the x current component is present and that the steel resistivity is zero in the region where the magnetic field is zero (beyond the pole tip). Then the current density can be found by solving a system of field equations and boundary conditions:

$$\mathrm{rot}\ E = -\,dB_z/dt,$$
$$j = E/\rho,$$
$$E = E_x,$$
$$j_x = 0 \quad \text{if } y \geq d.$$

The solution gives the current density:

$$j_x = \omega B_m d/2\rho\cdot(1-z/c)\cdot(1-(y/d)^2).$$

Power losses can be found easily if we know the current density distribution:

$$P_{end} = \frac{\omega^2\ B_m{}^2 d^2 w}{2\,\rho}\cdot\int_0^c dz\cdot(1-\frac{z}{c})^2\cdot\int_0^d dy\cdot(1-\frac{y^2}{d^2})^2$$

After integration we have finally:

$$P_{end} = 0.04\cdot\rho^{-1}\cdot d^3\cdot c\cdot w\cdot\omega^2\cdot B_m{}^2$$

Power loss per pole is about 25 W and total power losses per magnet

$$P_{tot} \approx 200\ \mathrm{W}$$

The effective equivalent resistance for end losses is $R_{end} \approx 1250$ Ohm.

16.2.3.3 Coil eddy current losses

Because coil turns are located in the space between the quadrupole poles, the pole flux partially penetrates into the coil volume and induces an eddy current that is an additional source of power losses. To make an estimate of these losses we assume that the flux enters perpendicular to the coil wire surface. We can write down the expression:

$$dP_{Cu} = 1/12\cdot\rho_{Cu}{}^{-1}\ \omega^2\cdot B_w{}^2\ t^2\cdot dV_w\ ,$$

where B_w is the magnetic field that penetrates the wire. Applying Ampere's law to find B_w along the coil surface and integrating over all quadrupole coil wires, we have:

$$P_{Cu} \approx 1/36\cdot\omega^2\cdot(Iw)^2\ \mu_0{}^2/\rho_{Cu}*t^4\cdot l_w/h_w{}^2$$

where t is square copper wire thickness, Iw is the coil Ampere-turns, h_w stands for maximum distance from coil wires to the quadrupole plane of symmetry, and l_w is total wire length. With Iw = 1630 A and l_w = 35 m for #10 square copper wire (t = 0.1 inches), we have $P_{Cu} \approx 760$ W and R_{Cu} = 330 Ohm.

Taking all the above into the account, we may represent the magnet as an equivalent circuit. It consists of an inductance with impedance ωL. It is connected in parallel to several resistive elements with resistance values shown in the Table 16.5.

Table 16.5. Parameters of the Magnet Equivalent Circuit

Element	Inductance	Wire Resistance	Vacuum Pipe	Core Lamination	Core Ends	Wire Eddy
Symbol	ωL	R_w	R_p	R_c	R_e	R_{Cu}
Impedance	2.5	315	34	2100	1250	330

Clearly the main power loss is due to eddy current losses in the vacuum pipe. Nevertheless, the quality factor of circuit is about 13.5 and allows use of a resonant pulse-forming circuit.

16.2.4. Conclusion

The design of a pulsed quadrupole for the MI gamma-t jump system is feasible. Field quality can be maintained within required limits, the core shape can be optimized to reduce significantly end eddy current losses, and the coil can be designed to meet current requirements. If four quadrupoles are connected in series, about 5000 V of test voltage is required to insure adequate magnet insulation. This requirement can be significantly weaker if bi-polar power supply is considered. Wire resistance losses and core and coil eddy current losses are low enough to allow magnet operation in a resonant circuit. The major part of power losses occur in the Inconel-718 vacuum pipe, but even these losses allow use of a pulse-forming circuit as suggested in [2].

16.3. Power Supplies

D. Wolff

The MI gamma-t jump power supply system consists of 8 power supplies. Each power supply drives a four-magnet quadrupole string. The power supply design is shown in Figure 16.8.

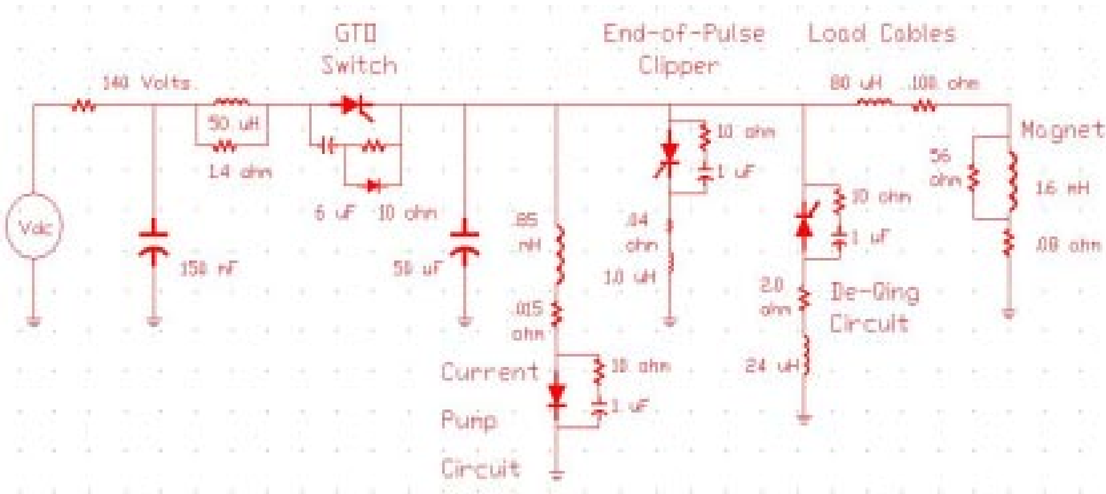

Figure 16.8. Circuit diagram of the MI gamma-t jump power supply system.

Figure 16.9 shows the various magnet current waveforms that can be produced by the power supply:

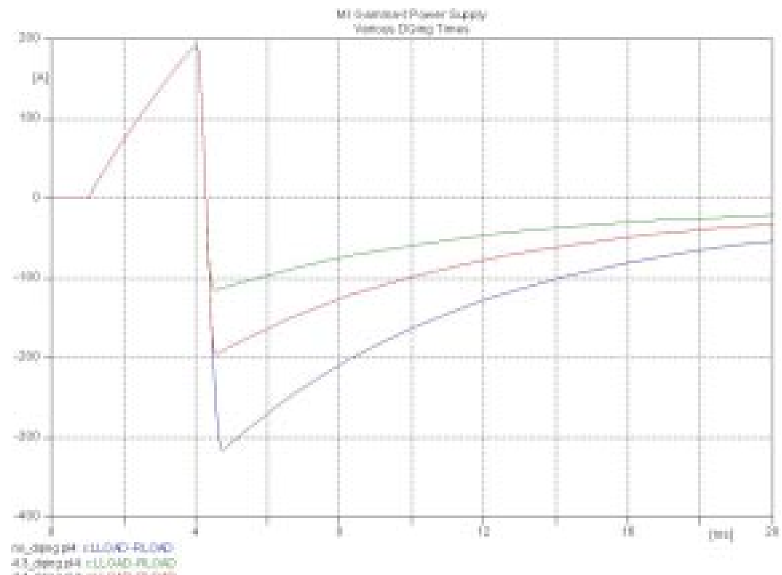

Figure 16.9. The magnet current waveforms for various De-Qing times.

A short description of circuit operation follows. The pulse begins when the GTO (gate turn-off thyristor) is turned ON. This applies 140 volts to the load and charges the load current to 195 amps in 3 ms. At this time the GTO is turned OFF and the magnet load acting as a resonant circuit with the 50 μF capacitor rings through one half cycle.

Turning ON the End-of-Pulse clipper SCR allows the magnet current to return to zero following the L/R time constant of the load and load cables. To control the peak negative current, the De-Qing circuit SCR can be turned ON before the pulse reaches its maximum negative value. The current will then return to zero as mentioned above. The waveforms in Figure 16.3.2 show two such De-Qing events at –200 amps and –120 amps. The current pump circuit is charged while the GTO is ON. When the GTO is turned OFF the current in the pump circuit adds to the negative load current thereby producing the maximum desired negative current.

16.4. Beam Pipes

A. Chen

The beam pipe of the MI gamma-t jump system will be made of thin metallic vacuum tight beam tubes. [4] Inconel 718 is chosen because it has excellent mechanical strength and high electrical resistance so that it can minimize the eddy current effects within a pulsed magnetic field. It can also be machined and welded without special cares. The parameters are listed in the following table 16.6:

Table 16.6. MI Gamma-t Jump System Beam Pipe Parameters

Material of Tube	Inconel 718, 0.025” Sheet
Material of End Flange	Inconel 718, 3/16” Sheet
Lengths of Tube	0.5 m (16 sections), 1.0 m (8 sections)
Major Diameter	4.89 inches
Minor Diameter	2.09 inches
Material of transition flanges	S.S. 316

The thin Inconel sheet will be cut into proper size, and then be rolled into round tube followed by electron beam welding. The round tubes will then be pressed to achieve an elliptical shape and heat-treated to increase mechanical strength. The tubes will then be welded to Inconel 718 flanges. These flanges and the stainless steel transition flanges are formed into a single piece.

16.5. Controls

M. Shea

The gamma-t jump system planned for PD2 consists of eight sets of magnets with their associated pulsed power supplies spaced around the Main Injector. This system would require an IRM at each of the eight locations to provide the analog control, timing triggers and data acquisition needed to operate the power supplies and to return readings to the Accelerator Network (ACNET) consoles. Timing requirements do not appear to be stringent and should be satisfied by the Tevatron-clock-based delay timers normally supplied by a Linac-style Front End computer. Analog control, slow analog readings of power supply parameters and snapshot readings of power supply waveforms will be provided by an IRM at each of the eight locations.

References

[1] W. Chou, et al. "Design of a Gamma-t Jump System for Fermilab Main Injector," PAC 1997 Proceedings, pp. 994-996.

[2] B. Brown, Beams Division, Fermilab, private communication.

[3] T. J. Gardner, private communication.

[4] J.R. Leibfritz, "FNAL Main Injector Gamma-t Jump System Beamtube Design," PAC 1997 Proceedings, p. 3601.

Chapter 17. Large Aperture Quadrupole

V. Kashkhin

In several straight sections of the Main Injector, i.e., MI-10, MI-30, MI-40, MI-52 and MI-62, (and also MI-60 when the NuMI extraction beam line is in place) the quadrupoles upstream of the Lambertson magnets limit the physical aperture; the beam is deflected at these locations during injection and extraction. In order to reduce beam losses at these locations, Large Aperture Quadrupoles (LAQ) will be installed replacing the regular quadrupoles. These LAQs have an identical design to regular Main Injector quadrupoles, but the aperture is increased from 83.48 mm in diameter to 102.24 mm and the number of turns per pole from 4 to 6. The main LAQ parameters are listed in Table 17.1.

Table 17.1. Large Aperture Quadrupole Parameters

Aperture diameter	102.24	mm
Length	2.134	m
Strength	19.6	T/m
Integrated strength	41.87	T-m/m
Turns/pole	6	
Peak current	3630	A
RMS current	2000	A
Winding resistance	7.3	mΩ
Inductance	1.5	mH
Peak power	96	kW
RMS power	29	kW
Conductor dimensions	14.35×25.4	mm
Conductor hole diameter	6.35	mm
Number of water circuits	4	
Water pressure drop	4	atm
Water flow	16	l/min
Water temperature rise	27	˚C
Weight	5800	kg

Figures 17.1 and 17.2 show the magnetic field distribution and field quality of the LAQ. These LAQs will be on the same bus as the regular quadrupoles. The relative gradient change of the regular quadrupole and the LAQ is shown on Figure 17.3. The LAQ has higher iron saturation in the pole area because of its larger aperture. This ~1% difference between regular quadrupole and LAQ can be compensated by an additional correction coil. Figures 17.4 and 17.5 show the cross-section and end view of the LAQ.

The LAQ is based on MI regular quadrupole materials and technology and will use the same copper conductor, the same low carbon laminated steel and electrical insulation. Nevertheless the separate coil vacuum impregnation technique will be used for better reliability.

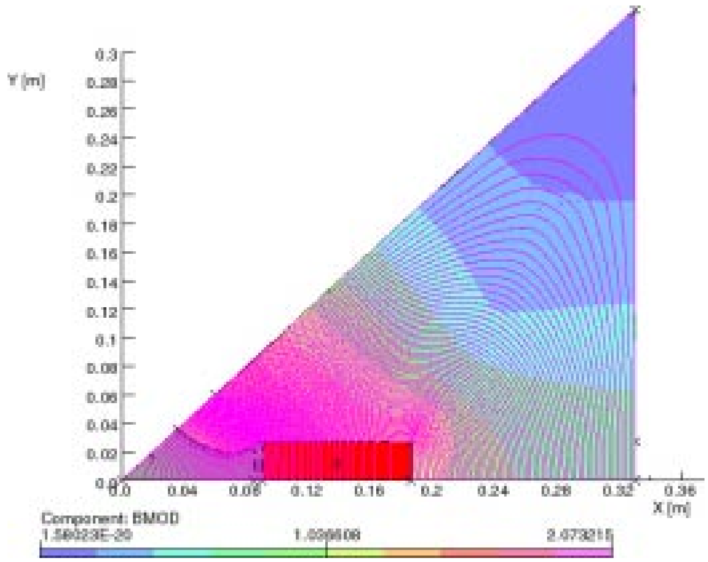

Figure 17.1. Flux lines and flux density distribution.

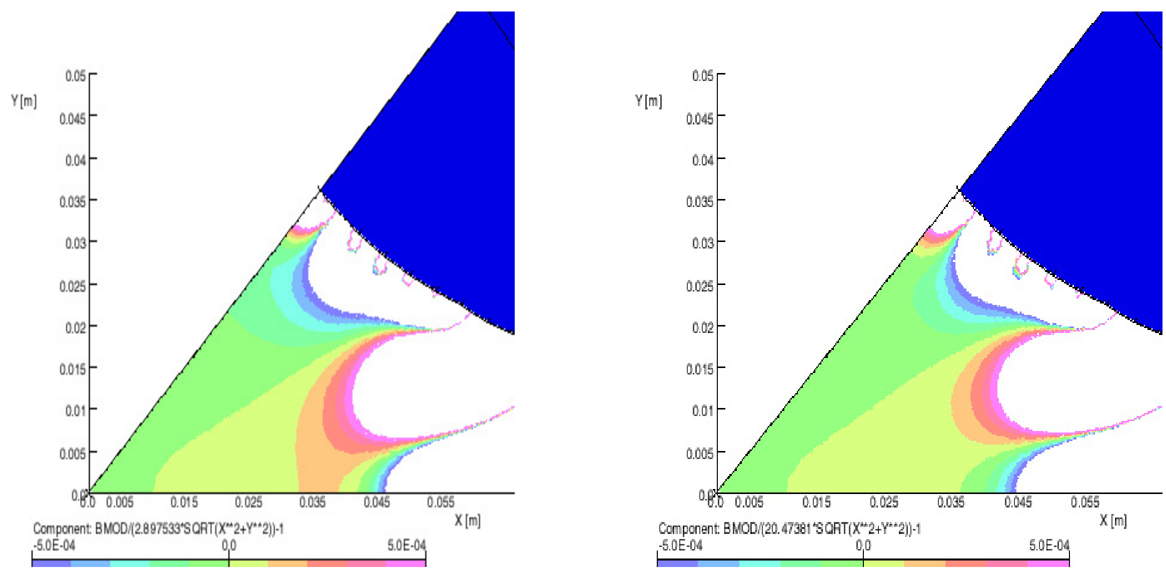

Figure 17.2. Field quality at injection (left) and maximum current (right)

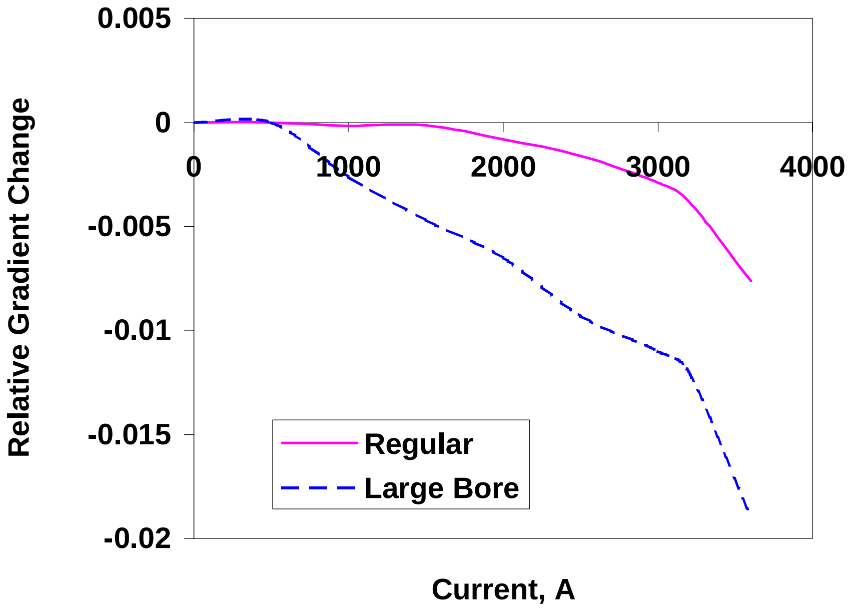

Figure 17.3. Relative gradient change of the regular MI quadrupole and Large Aperture Quadrupole

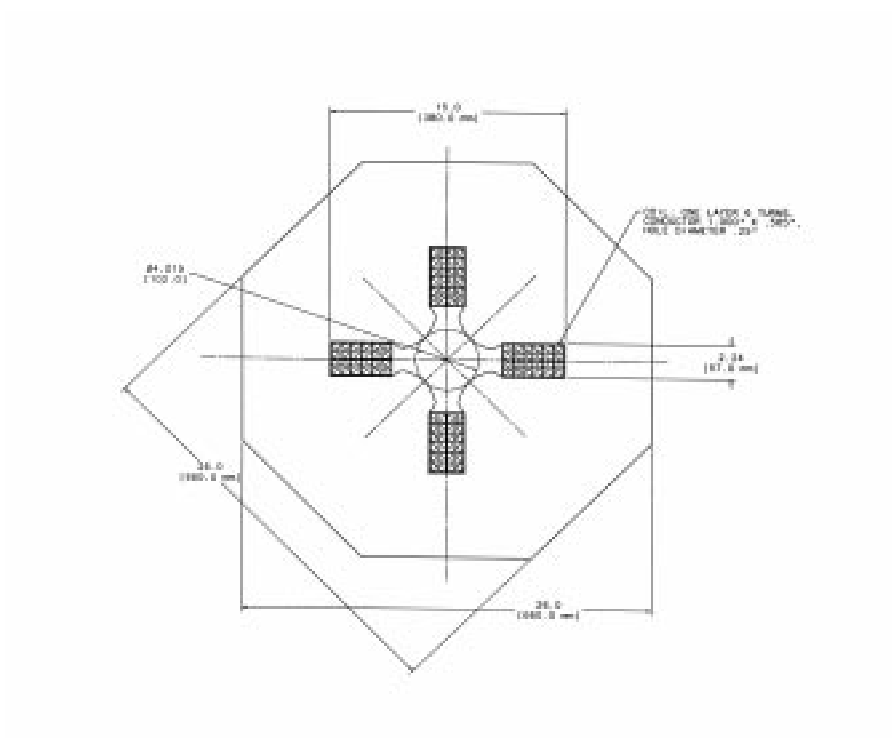

Figure 17.4. Large Aperture Quadrupole cross-section

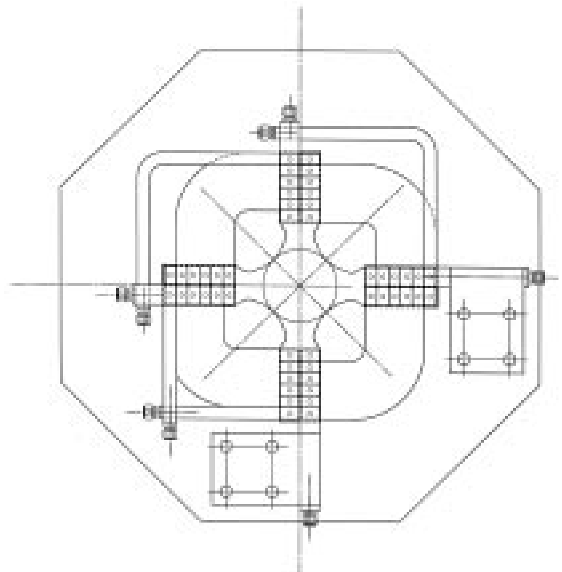

Figure 17.5. Large Aperture Quadrupole end view

Chapter 18. Passive Damper and Active Feedback

18.1 RF Cavity Passive Spurious Mode Damping

J. Griffin

With the large beam intensity increases proposed, spurious resonant modes in the rf cavities (and elsewhere in the lattice), present increased sources of longitudinal instability. The existing rf cavities have higher order mode dampers attached to vacuum seal cooling fans. These dampers are effective at two predominant offending cavity modes: 128 and 225 MHz. Originally there were additional iris-coupled mode dampers containing frequency selective ferrite (Indiana General Q2), at each end wall. The iris ports may still be in place, but possibly covered with copper due to water leaks in the ferrite cooling plates backing the lossy ferrite. Improved ferrite cooling could be implemented if measurements indicate that the iris dampers can contribute to stability.

The cavity revisions proposed in Ch. 15 will probably change the offending cavity mode frequencies so that they will have to be remeasured, along with any additional modes that appear to have potential for causing beam instability.

There is an additional feature of the upgraded cavity design that may be turned to advantage in the area of spurious mode damping. In Ch. 15 it is proposed to couple 50 - 70 kW additional rf power out of each cavity, to be dissipated in matched water-cooled terminations. The additional power dissipation is primarily for the purpose of establishing an adequate margin of stability against the Robinson beam loading instability. However, if rf power output coupling devices (inductive loops or possibly capacitances), are selectively located and properly configured they may effectively be used to also damp spurious cavity modes.

The effectiveness of reinstituting iris coupled damping, the location of new spurious modes, or the location of damping power output coupling devices should be studied to the extent possible using cavity modeling programs such as enhanced versions of MAFIA.

18.2. Longitudinal Feedback and Damping

D. Wildman

Before discussing longitudinal feedback in the Main Injector, it is necessary to understand the different responses of the modified (see Section 15.5) and the new rf systems (see Section 15.9) to transient beam loading. Both the modification of the existing MI rf system and the design of an entirely new system aim to increase beam stability by lowering the rf cavity shunt impedance, R_s, by increasing the power dissipated in the cavity. Modifying the existing system would lower R_s by reducing Q by connecting a 150 kW rf load to the cavity. The new system would lower R_s by reducing the cavity's characteristic impedance, Zo, while leaving Q unchanged. In the steady state beam-loading limit, the two approaches give essentially the same results. However, transient beam loading effects are quite different in the two options. Consider the case of a single high intensity bunch passing through an rf cavity. The voltage induced in the cavity after the passage of the bunch is proportional to the R_s/Q of the cavity. In the modified system, R_s/Q remains unchanged since R_s was lowered by changing Q. In the new system R_s/Q is lowered by a factor of four (R_s decreased by lowering Z_o, Q remains unchanged.) This means that transient induced voltages (on time scales short compared to $2Q/\omega$) will be four times smaller with the new rf system.

As previously mentioned in Ch. 15, the cavity tuning feedback system will not be able to change the cavity tuning angle on the time scale of a 1.6 µs Booster batch. Therefore, there will be a shift in the phase of the total rf cavity voltage with respect to the beam as the Booster batch transverses the cavities. For the modified version of the present cavities, assuming narrow proton bunches of 3×10^{11} per bunch, the beam induced voltage in a single rf cavity after the passage of 84 bunches $\approx 84\omega\Delta q R_s/Q = 140$ kV. At injection, the maximum cavity voltage is limited to 110 kV due to sparking in the tuners. Under these conditions the total phase shift θ observed would be $\theta = \arctan$ (140 kV/110 kV) $\approx 52°$ and beam will be lost from the machine as the trailing bunches try to gain energy by moving to a new synchronous phase angle, ϕ_s. Beam loss will occur since the last bunch loses 140 keV/turn while it can only gain 110 keV/turn from the rf voltage. For the completely new rf system, the transient induced voltages will be lower by a factor of four (140 kV/4 = 35 kV) due to the lower R_s/Q. The new system is also designed to run at a higher voltage at injection. If the new cavities were operated at 150 kV at injection, this would result in a total phase shift of $\theta = \arctan$ (35 kV/150 kV) = 13°. This 13° phase shift corresponds to that presently observed in the MI at injection.

The above example illustrates the important difference between a modified and a new rf system. If the present MI system is modified, a fast feedback loop around each individual rf cavity will be absolutely necessary for beam stability in the face of transient beam loading effects. The new rf system, without any fast feedback, would give performance comparable to the present MI.

A fast feedback loop around each rf station would be designed as a direct feedback loop in the tunnel around each rf cavity. A fraction of the detected cavity gap voltage would be summed with the cavity drive signal to reduce both amplitude and phase excursions.

The damping of longitudinal coupled-bunch motion will be required in PD2. If the present rf cavities are modified for use in the new machine, the three existing higher order mode (HOM) passive dampers will have to be redesigned to provide more coupling to the HOMs and allow for greater HOM power dissipation. Likewise, effective HOM dampers must be included in any new rf cavity design. Even if all the HOMs of the accelerating cavities are successfully damped, other resonant structures in the ring might have sufficiently high impedances to excite coupled-bunch instabilities. In this case an active longitudinal damper will be required. Since the amount of power that will be required for damping coupled-bunch oscillations is unknown, a modular active damping system is proposed. Each module would consist of a 50 Ω broadband rf cavity driven by a commercially available 10 kW solid state amplifier. Each cavity/amplifier module will generate peak gap voltages up to 1 kV over the frequency range of 100 kHz to 250 MHz. The drive to the amplifier will be derived from the existing resistive wall monitor signal. Initially, one module will be inserted in the ring for testing and damping studies. During commissioning, as the machine intensity is raised to its design value, additional modules could be inserted, if needed, to provide increased damping.

Chapter 19. Radiation, Shielding and Collimation

A. Drozhdin, D. Johnson, K. Vaziri

19.1. Radiation and Shielding

19.1.1. Introduction

This chapter explores how the Main Injector (MI) radiological issues will be affected with the Proton Driver (PD) as its injector. For simplicity, it is assumed that the PD will provide about 6.5 times more protons per hour than in the original MI design. [1] Data obtained from measurements and calculations are then scaled and compared to the MI design. Reasonable solutions are suggested, where possible, to mitigate the problem areas.

The current safety envelope for the MI and the original projected losses are given in Tables 19.1 and 19.2. [1,2]

Table 19.1 Main Injector Design Beam Intensities [2]

Description	Protons/hr During Operation	Type of Occupancy
MI-8 beam line	5.7×10^{16}	Unlimited
MI	5.7×10^{16}	Unlimited
P150 beam line: 8 GeV 120 GeV 150 GeV	 5.7×10^{16} 3.9×10^{16} 3.3×10^{16}	 Unlimited Unlimited Unlimited
A150 beam line: 150 GeV protons 150 GeV anti-protons	 3.3×10^{16} 3.3×10^{16}	 Unlimited Unlimited
F0 to AP1 beam line: 8 GeV 120 GeV	 2.9×10^{17} 3.9×10^{16}	 Minimal Minimal
Meson 120	3.9×10^{16}	Unlimited/Minimal
Recycler Ring (RR)*	1.5×10^{16}	Unlimited
MI-40 beam absorber: 150 GeV (protons/year)	 1.0×10^{19}	 Unlimited

* Number of protons or anti-protons in the RR will be administratively controlled to be less than 1.5×10^{16} per hour to allow access to the F0 region of Tevatron during a RR store.

Table 19.2. Projected Losses Based on the Current MI Design

Category	Energy	Protons	
Operational Losses	8 GeV 120 GeV	1.0×10^{19}/ year[#] 4.1×10^{18} / year	1.67×10^{15} / hr 6.83×10^{14} / hr
Accidental Losses	8 GeV 120 GeV	5.7×10^{16} / accident 8.5×10^{15} / accident	

We assume 1 year = 6000 operational hours

The radiological issues are ground water contamination, activated air emissions, residual activation in equipment and cooling water systems, and shielding.

19.1.2. Ground Water Contamination

Radiation leaking out of enclosures can induce radioactivity in the soil. Activated products will seep through the ground and reach the aquifer. Federal regulation limits the concentration of tritium in groundwater to less than 20 pCi/ml. There are regulatory limits on the other radioisotope levels, which could lower the above limit if present in the groundwater. However, other radioisotopes leach to a much lesser extent than tritium. Depending on many geological factors, the amount of radioactivity that reaches the ground water will be reduced due to dispersion and decay. Several important loss locations around the MI were chosen for geological characterization. Based on data obtained from these locations, a reduction factor was calculated for each area using a geological contaminant transport code. [3]

Table 19.3. Calculated Reduction Factors around the Main Injector

Location	Reduction factor due to seepage
MI-62	1.0×10^{-9}
MI-52	6.5×10^{-9}
MI-40	1.1×10^{-7}
MI-30	6.7×10^{-7}
MiniBooNE target area (vicinity of MI injection)	$< 9.7 \times 10^{-15}$

As shown in Table 19.3 the smallest reduction in the soil radioactivity is 6.7×10^{-7}, which is around MI-30. These results indicate that ground water contamination will not be an issue for the MI with PD intensities. There are limits on the concentration of radionuclides discharged to the surface waters as well, which should be considered for the sump discharges. However, the results of measurements of tritium concentrations in the sump samples from 17 locations around the MI, over the last few years, have shown no concentration levels above 0.1 pCi/ml. [4] Therefore, an upgrade to PD intensities would not cause a problem.

19.1.3. Activated Air Emissions

The level of radioactivity in the air is expressed in DAC (Derived Air Concentration). The DOE regulatory limit for allowed access into an area where radioactive air is present is 0.1 DAC. [5,6] Table 19.4 shows the PD era expected air activity obtained by scaling from measurements and the expected 2% beam loss at different MI locations.

Table 19.4. Calculated Radioactive Air Concentrations in the MI in PD Era

Expected beam extracted per hour	E (GeV)	DAC (current MI)	PD2 (DAC × 6)	PD2 DAC (1-hour delay)	PD2 DAC (2-hour delay)
5.70×10^{16}	8	0.33	2.01	0.14	0.02
3.90×10^{16}	120	1.74	10.46	0.74	0.08
3.30×10^{16}	150	1.74	10.46	0.74	0.08

Note the activity in the fourth column is immediately after the beam is turned off. More than 95% of the activity is from the ^{11}C and ^{13}N isotopes, which have half-lives of 20 minutes. and 10 mins, respectively. Imposing delays before entering these areas will be sufficient to meet the DOE requirement. Currently, the release of activated air from the MI is insignificant. During the PD era, measurements should be made to determine if additional sealing of air leakages is needed [7].

19.1.4. Residual Activity

Measurements on MI beam line equipment show that at some locations residual activity is above the predicted levels (Table 19.5).

The 622 kickers and the 100 kickers almost always show rates ranging from 20 - 50 mrem/hr. These are right next to their respective Lambertson magnet (MI-10 and MI-62), and dose rates from Lambertsons always dominate the area. If the loss rates scale linearly with the proton intensity, the extrapolated dose rates at some places are of the order of rem/hr. Radioactive decay curves for iron/steel show that most of the short lived isotopes decay within the first hour after irradiation. Waiting a few more hours would only lower the dose rates by a factor of two. If MI beam optics is not improved, access and repairs will become more difficult and time consuming.

The activity levels in the cooling system water will also increase with intensity and loss rate, which will require additional shielding, containment measures and reposting of the MI buildings where these systems are located.

Table 19.5. Residual Dose Rate History of the MI Components in mrem/hr at 1 ft, One Hour after Beam-Off [8]

Survey Date	MI10 LAM	Q105	Q109	Q112	Q113	Q114	Q313	321 LAM	MI40 LAM	MI52 LAM	MI62 LAM	Q626
2/21/2002	30	30	40	NR	50	NR	NR	400	40	150	100	NR
1/9/2002	60	NR	30	NR	40	NR	NR	125	20	150	150	20
11/18/2001	50	NR	NR	NR	NR	NR	NR	NR	NR	NR	60	20
10/7/2001	70	NR	NR	NR	NR	170	NR	100	40	200	100	25
7/10/2001	50	NR	NR	40	NR	NR	50	70	40	30	120	40
1/15/2001	50	NR	NR	NR	NR	NR	NR	60	30	20	50	60
11/6/2000	70	NR	NR	NR	NR	NR	NR	160	80	50	200	350
9/5/2000	150	NR	NR	NR	NR	NR	NR	100	100	50	70	130
7/5/2000	100	NR	NR	NR	NR	NR	NR	120	100	50	100	200
6/23/2000	200	NR	NR	NR	NR	NR	100	175	120	60	100	300
3/16/2000	150	NR	NR	NR	NR	NR	NR	150	100	45	25	20
2/23/2000	130	NR	NR	NR	NR	NR	NR	NR	100	50	NR	NR
2/7/2000	200	NR	NR	NR	NR	NR	NR	NR	NR	100	50	35
1/22/2000	500	NR	NR	NR	NR	NR	NR	300	150	200	75	90

(NR: < 20 mrem/hr or not surveyed)

19.1.5. Shielding

If the dose rates outside the shielding go up by a factor of six, there are generally two mitigation options available: [5]

(a) The design soil equivalent shielding thickness is about 24.5 ft. This is in accordance with the Preliminary Safety Analysis Report of the Main Injector. [1,2] However, the enclosure is built to support a soil weight of 26.5 ft, available for future MI intensity upgrades. Two extra feet of soil shielding provides about 5.2 times more attenuation, which would almost be sufficient to keep the current postings of the berms.

(b) Currently, most of the MI berms are classified as "Unlimited Occupancy"; the dose rate is less than 50 micro-rem/hr. A factor of 5 higher dose rate will make it a "Controlled Area", with limited occupancy. This means we have to add posting to the berms. There are a few places that will have higher radiation fields. These may have to be fenced and posted as a "Radiation Area"; the MI-8 service building may be such a place. Operational access procedures may have to change at places such as AP2 and the MI-8 cross over. This option is much less costly than option (a).

19.1.6. Shielding Conclusion

Use of the PD as an injector for the MI, will not significantly affect MI operations. As discussed above, most issues can be handled by revising operations, procedures and postings. Residual activity in the beamline equipment is the only issue that requires further R&D. No significant expenses are required in any of the mitigative options discussed.

19.2. Collimation

19.2.1. Requirements

The combination of a very high amount of Proton Driver beam power injected into the MI (~0.13 MW), tight MI aperture defined by the extraction and injection Lambertson magnets, as well as a complicated set of orbit bumps during the cycle, imposes serious constraints on beam losses. All eight MI straight sections are occupied by rf cavities, and injection and extraction systems. The horizontal orbit bumps used for a closed orbit displacement at the Lambertson magnet septa do not permit the installation of horizontal collimators close to the beam in the straight sections occupied by the extraction and injection systems. The only straight section that can be used for beam collimation is MI-30. Currently a kicker magnet is located at the center of MI-30 which is used both for beam extraction from the MI to the Recycler and injection from the Recycler to the MI. There is also a horizontal closed orbit bump (Figure 19.1), which is used for a kicked beam displacement reduction in the region from MI-22 to MI-32. To resolve this conflict the primary and secondary collimators will be retracted from the accelerator aperture in those cycles used for antiproton beam recycling.

Zero-dispersion at the straight sections of the accelerator complicates the problem further. This may require special measures such as “beam-in-gap-cleaning” (suggested for SNS) for off-momentum particle collimation.

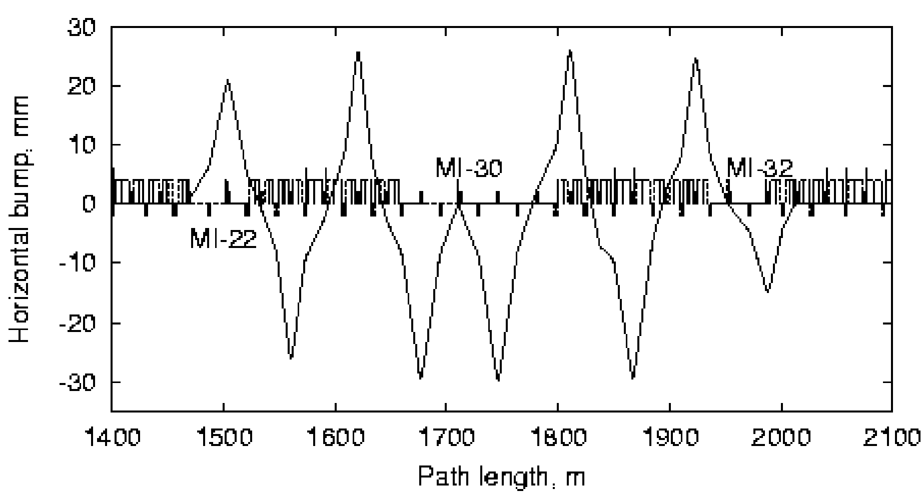

Figure 19.1. Horizontal closed orbit bump used for a kicked beam displacement reduction in the MI-30 section and beam displacement at the injection and extraction Lambertson magnets in the MI-22 and MI-32.

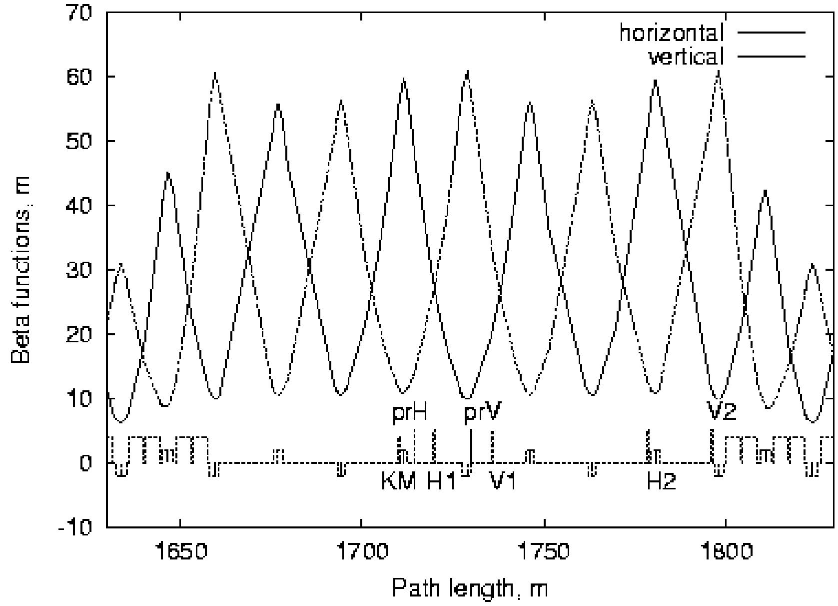

Figure 19.2. Beam collimation system location and beta function in the MI-30 straight section. PrH and PrV are primary collimators and H1, H2, V1 and V2 are secondary collimators.

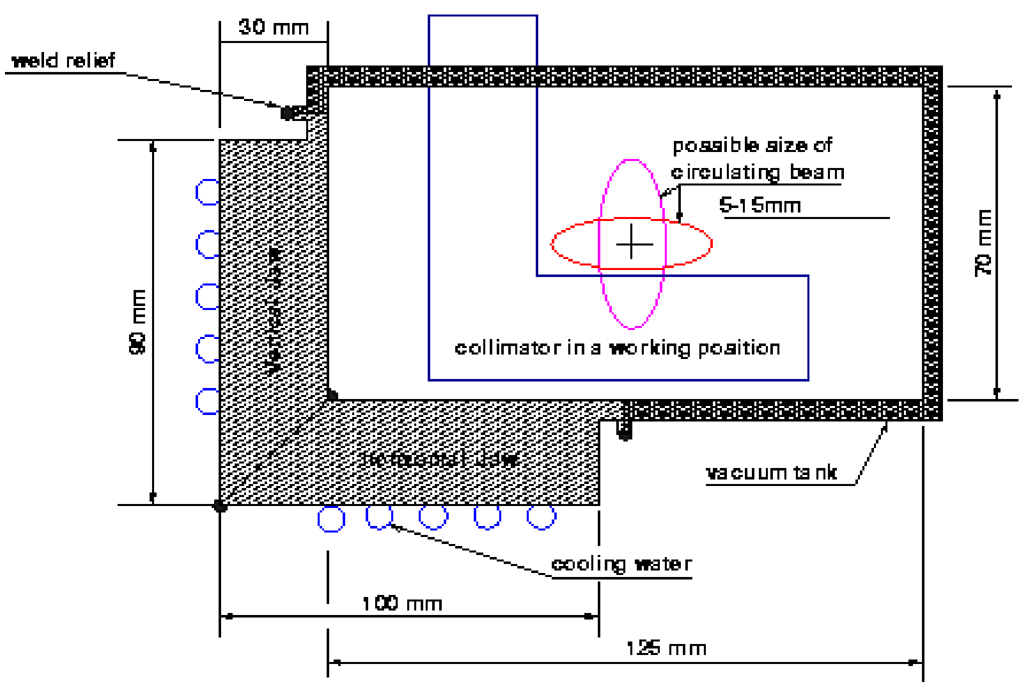

Figure 19.3. Secondary collimator cross-section.

19.2.2 Collimation System Parameters

A possible location for a two-stage collimation system is shown in Fig. 19.2. The system consists of one primary and two secondary collimators for both horizontal and vertical planes. Secondary collimators are located in an optimal phase advance location, downstream of the primary collimators. This provides for halo particle collimation at the secondary collimators during the first turn, after interaction with the primary collimator. Assuming that 1% of the beam is collimated at injection and 0.5% at the top energy, simulations show that most of the power is intercepted by the two secondary collimators (about 5 kW each). The total power intercepted is 11 kW. This requires local steel shielding ~1 m thick and ~2.5 m long, which covers the secondary collimators and the first quadrupole downstream.

The entire collimation system is concentrated in the downstream 2.5 periods of the MI-30 straight section. This leaves 1.5 periods for the electron cooling system and Recycler kicker magnet in a low radiation region upstream of the collimation system.

A system with collimators distributed around the accelerator at the necessary phase advance, in available free drift spaces, can be investigated. However, the required level of power interception by the collimators, makes this solution much more complicated and expensive.

The mechanical design of the secondary collimators and targets will be similar to those already built and installed in the Tevatron for Collider Run II. Those collimators consist of 2 pieces of stainless steel, 0.5 m long, welded together in an "L" configuration (Fig. 19.3). The collimator assembly is inside a stainless steel box with bellows at each end. Full range of motion is 50 mm, in steps as small as 25 μm if required, and a maximum speed of 2.5 mm/sec. Linear differential voltage transformers provide position read-backs. The primary collimator assembly is identical to the secondary collimator assembly, except that the target "L" blocks are only 0.1 m long. The 1 mm thick, machined-tungsten primary collimator jaws are bolted to the stainless steel blocks. The blocks provide a good heat sink for energy dissipated in the tungsten. The entire assembly, including bellows, occupies approximately 0.6 m of lattice space.

Circulating standard low conductivity water through cooling channels on the outside of the collimator box, can remove 11 kW of DC power from a single collimator. A flow of 2.2 gallons per minute, will remove this power with a temperature rise of 20°C. Further investigations should be done for collimation system efficiency and optimization.

References

[1] C.M. Bhat, P. Martin, and T. Leveling, “Main Injector and Recycler Ring Shielding Assessment”, MI Note-0225, Jan. 14, 1998. C.M. Bhat, P. Martin, and T. Leveling, “Main Injector 8 GeV Beamline Shielding Assessment”, MI Note-0205, Feb. 10, 1997.

[2] S. D. Holmes, "Main Injector Safety Assessment Document," July 1998. R. D. Swain and C.M. Bhat, "A Preliminary Analysis of Ground-Water and Surface-Water Radioactivity Around the Main Injector Extraction and Injection Regions," MI Note-0225, Nov., 1997.

[3] E. A. Sudicky, T. D. Wadsworth, J. B. Kool, and P. S. Huyakorn, "PATCH3D-Three-Dimensional Analytic Solution for Transport in a Finite Thickness Aquifer with First-Type Rectangular Patch Source." Prepared for Woodward Clyde Consultants, HydroGeologic Inc. Herndon, Va., January 1988.

[4] Gary Lauten, Beams Division ES&H Dept., private communication.

[5] Code of Federal Regulations, 10 CFR 835, "Occupational Radiation Protection," current version. *Fermilab Radiological Control Manual current version.*

[6] DOE Order 5400.5, "Radiation Protection of the Public and the Environment," January 1993.

[7] United States Code of Federal Regulations, Title 40, Part 61, Subpart H, "National Emissions Standard for Hazardous Air Pollutants (NESHAP) for the Emission of Radionuclides other than Radon from Department of Energy Facilities," 1989.

[8] Matt Fergusen, Beams Division ES&H Dept, private communication.

Chapter 20. Upgrade of Other Technical Systems

20.1 Magnets

D. Harding

The properties of the magnets themselves do not impose a limit to running the Fermilab Main Injector at its design rate of 240 GeV/sec with a 1.467 second cycle time. Shorter cycle times, down to as little as one second, appear viable, though tests should be considered before running at a ramp rate significantly faster than the design. We address that highest ramp and repetition rate here; anything between that and the design is also good.

It should be noted that there are about two dozen different kinds of magnets in the Main Injector complex. We concentrate here on the most numerous of them, as they would require the largest effort to modify.

20.1.1. Voltage to Ground

The doubling of the ramp rate required to execute a one second cycle time doubles the inductive voltage across each magnet, the dominant factor for the ring magnets.

1. <u>Dipoles.</u> The typical operating voltage to ground for the dipoles with the nominal ramp ranges up to 500 V and the coil to through bus reaches 1000 V. In fault conditions the coil to ground voltage can reach 1000 V. Doubling the ramp rate approximately doubles these numbers with the existing bus configuration.

   The magnet insulation was designed to withstand a DC voltage of 5000 V to ground and 10,000 V between coil and through bus, and in production every magnet was tested at these voltages with a limit of <5 μA leakage current. In practice the current was below the 0.05 μA limit measurable with the test equipment.

   AC operation imposes more stringent conditions on devices due to the potential for partial discharge. In September 2000 Chez Jach measured one spare MI dipole and found an extinction voltage of about 535 V. While this suggests that the magnets are safe under current operating conditions, it may be worth looking more closely if a higher ramp rate is desired. Examining more than a single sample would give a better picture of the distribution of behavior across the ring. Localizing the discharge might reassure us of the triviality of the location or suggest a relatively uncomplicated improvement to extend the magnet lifetime.

2. <u>Quadrupoles.</u> In order to double the ramp rate, additional quadrupole power supplies would be necessary. Spacing them around the ring leaves the voltage to ground as it is now. Corona tests on old and new Main Injector quadrupoles would be useful.

3. <u>Sextupoles.</u> The sextupoles were tested to 1500 V during production.

4. Other magnets. All other magnets run in such short strings that the total voltage to ground does not become an issue even with the higher ramp rate.

20.1.2. Magnet Field Quality

We do not expect the field shape due to the magnet steel to vary with ramp rate during acceleration, although a small change in the strength and sextupole component of the dipole field at injection is possible. (See the Fermilab Main Injector Technical Design Handbook section 3.1, page 15 and the references therein.) These changes are small enough to be easily accommodated by small operational changes in the dipole and sextupole bus currents.

20.1.3. Beam Tube Eddy Currents

Eddy currents in the beam tubes will double with the doubling of the ramp rate, with two effects - heating and field distortion.

The heating is negligible at these ramp and repetition rates; the beam tube is in intimate contact with the pole, which serves as an excellent heat sink.

The field distortion is primarily the generation of a sextupole component. The sextupole system, magnets and power supply, were designed to compensate for the sextupole from the saturation of the dipole magnets at 150 GeV. The increased effect of the eddy currents in a 120 GeV ramp is minimal compared to that saturation (MI-Note 0100) so the present sextupole system can compensate adequately.

20.1.4. Magnet Heating

The ramp rate is not yet high enough to induce significant eddy current heating in the magnets. All the ring and beam line magnets are designed to run DC at their peak current, so even if the rms power dissipation increased substantially they would not suffer as long as the water system continues to provide cooling water at the nominal pressure and temperature. The shorter cycle time actually decreases the rms power compared to the design antiproton production cycle, let alone the design slow spill cycle, so cooling should not be an issue.

20.2 Power Supplies

D. Wolff

20.2.1 Present Power Supply Capability

The available voltage from the power supply rectifier stations determines the limit on the ramp rate of the Main Injector. The following table lists the maximum voltage available for each bus:

BUS	RAMP	INVERT
Bend Bus	12.0 kV	-10.8 kV
QD Bus	2.9 kV	-2.6 kV
QF Bus	2.9 kV	-2.6 kV

Given these limitations, a ramp with a total cycle time of about 1.5 seconds was developed, (The goal is 1.533 seconds.) while minimizing changes to the existing $23 ramp, the one for 6-Booster batch injection for NuMI. Figure 20.1 and its associated table show the segment-by-segment ramp description and the resulting bend bus power supply waveforms.

Time	Momentum	Pdot	Pddot
0.34550	8.889	0.00	0.00
0.36367	8.98	6.00	252.62
0.40521	9.5	20.00	337.04
0.48212	22	305.00	2706.00
0.69862	85	277.00	-129.22
0.84538	115	121.00	-1034.60
0.92706	119.7	0.00	-1557.55
0.94706	119.7	0.00	0.00
1.03615	105	-330.00	-2704.08
1.17901	60	-300.00	210.00
1.26747	11	-220.00	424.49
1.40656	6.7	0.00	5627.91
1.45521	7.7945	45.00	925.08
1.50385	8.889	0.00	-925.08
1.50485	8.889	0.00	0.00

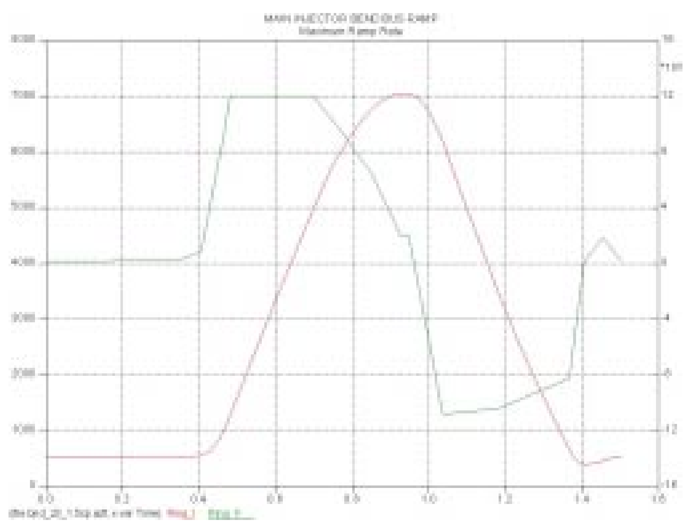

Figure 20.1. Bend bus current and voltage waveform for 1.5 seconds cycle.

The following is a list of the changes to the $23 ramp that were made to achieve this cycle time:

1. The injection time was reduced from 0.5 s to 0.34 s.
2. The 22 GeV ramping segment was increased from 240 GeV/s to 305 GeV/s.
3. The 85 GeV ramping segment was increased from 230 GeV/s to 277 GeV/s.
4. The flattop time was reduced from 98 ms to 20 ms.
5. The 105 GeV invert segment was increased from -300 GeV/s to -330 GeV/s.
6. The 60 GeV invert segment was increased from -280 GeV/s to -300 GeV/s.

While the above ramp cycle time of 1.5049 seconds meets the goal, the power supplies would be operating at their limits. During certain times of the year, particularly on hot summer days, the AC mains may sag and that could result in losing the exacting current regulation required for successful accelerator operation. Studies should be performed to measure the voltage regulation margin in the power supply stations while operating with this new ramp. If the margin is considered too small, a fairly inexpensive solution exists. One power supply in each of the buses could be upgraded to gain a nominal increase in voltage output. Such a modification was completed a couple of years ago for one power supply in each of the quadrupole busses when it was determined that the power supplies were having trouble achieving the 1.5-second cycle rate required for antiproton stacking.

20.2.2. Power Supply Modifications Required to Operate at a 1.0 Second Cycle Rate

To operate at a 1.0-second cycle major modifications need to be made to the power supply system. Basically, twice as much voltage is needed for a 1.0-second ramp compared to the 1.5-second ramp. To accomplish this, we propose to add to every Main Injector service building two additional bend power supplies and one additional quadrupole power supply. This will double the operating voltage-to-ground on the bend bus but keep the quadrupole busses the same. Figure 20.2 and its associated table show the proposed ramp description and bend bus waveforms:

Time	Momentum	Pdot	Pddot
0.34000	8.889	0.00	0.00
0.41037	30	600.00	8526.36
0.52801	100	580.00	-168.67
0.59656	119.7	0.00	-8538.07
0.61686	119.7	0.00	0.00
0.66763	105	-580.00	-11442.18
0.82893	15	-550.00	188.33
0.85711	8.7	0.00	18222.69
0.90575	7.7945	45.00	925.08
0.95440	8.889	0.00	-925.08
0.95540	8.889	0.00	0.00

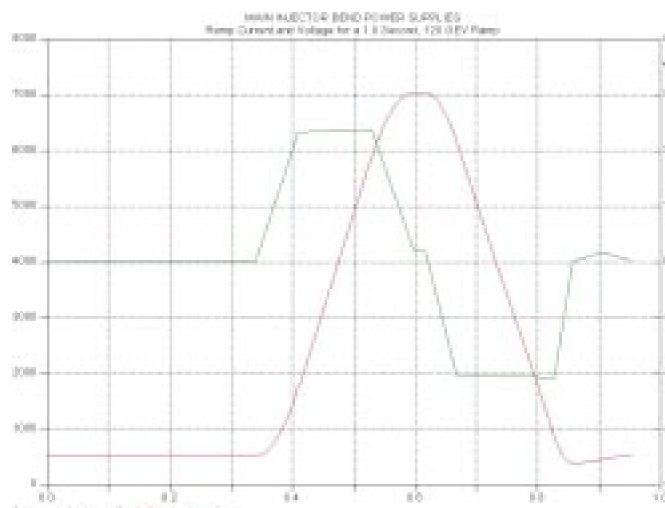

Figure 20.2. Bend bus current and voltage waveform for 1.0-second cycle.

For this ramp we needed to abandon the parabolas as defined in the present $23 ramp and allow the power supplies to ramp to their maximum voltage as fast as possible while still maintaining good voltage regulation. Whether the proton beam will behave well with such a ramp is unknown.

In addition to the power supplies themselves, the high-current DC bus, the AC feeders, the service buildings, and the Kautz Road substation will all need major modifications. The following summarizes the changes that are needed:

1. Main Injector service buildings:

* Buildings themselves need to be enlarged to accommodate two additional bend power supplies and one additional quadrupole power supply.
* Power supply transformers, pads, and additional feeder work need to be added outside each building.
* One additional high-current DC quadrupole bus (to the tunnel) will need to be installed at each building.

2. Main Injector Feeders:
   The number of power supply feeders will have to double. Sufficient duct bank space should be available in most areas around the ring. The bank by the MI 60 service building may need to be expanded.

3. Kautz Road Substation:
   * Two additional 345 kV transformers will be needed.
   * The substation building will need to be expanded to accommodate additional breakers and relaying equipment.
   * Two additional harmonic filters will need to be installed.

20.3. Mechanical and Utility

A. Chen

20.3.1 Mechanical & Utility Requirements

As the Main Injector repetition rate increases from 0.54 Hz to 0.65 Hz (the cycle time reduced from 1.867 s to 1.533 s), the change of total heat load in magnets is insignificant. The heat load for power supplies can still be handled by existing capacity at the service buildings, which have about 20% margin. However, the heat load due to the rf system upgrade will be increased dramatically as shown in Table 20.1. It becomes the main issue from the mechanical point of view.

Table 20.1. LCW requirements for RF System Upgrade

	Present	Upgraded
Flow rate for 95° F rf	2100 gpm	4000 gpm
Heat load for 95° F rf	3.3 MW	7.5 MW
Flow rate for 90° F cavity	730 gpm	1500 gpm
Heat load for 90° F cavity	0.5 MW	2.5 MW

To meet these requirements, it is necessary to upgrade the MI-60 pump room and most of present piping for rf power supplies and its cavity system. Meanwhile, MI cooling ponds have already been run at their full capacity so extra cooling pond area will be needed.

20.3.2 LCW System upgrade

20.3.2.1. MI60 Pump Room

a) 95° F LCW for rf power supplies:
Adding one more heat exchanger will increase the capacity from 6.6 MW to 9.9 MW. In order to fit the third heat exchanger into the fully occupied room, some modification of the building is necessary. This includes removing the swinging door, widening the garage door, and relocating pumps and manifolds. The four pumps would be upgraded to deliver the doubled flow rate.

b) 90° F LCW for rf cavities:
Its current heat exchanger has a design capacity of 3 MW. But it has served about 30 years and some channels are partially clogged so it may be necessary to replace it with a new one at the same or higher capacity in order to take the 2.5 MW load. (Currently the load is 0.5 MW.)

20.3.2.2. Piping

The flow rate for both the rf power systems and its cavity needs to be doubled. We can either run another pipe at the same size as the current ones or replace them with larger sizes. It will cost less to run another pipe as long as there is space for it. At the penetrations, it can only be done by replacing the existing 10-inch pipe with a larger pipe.

20.3.2.3. Cooling pond

The MI cooling ponds are almost running at their full capacity now. The 5 MW extra heat load will need extra cooling surface. We can either create a new pond of about 5 acres in the region of the MI or utilize existing Tevatron cooling ponds. The MI rf is close to the Tevatron Ring. It needs less than 1000 feet of piping to connect the MI rf LCW to Tevatron Pond 24. Pond 20, 21, 22, 23, 24 together can provide more than 5 acres of surface area with minor modification of their channels. These ponds are designed for the cooling needs of Tevatron Sector E, which has a very low heat load. However, it would cost about $400 K to construct 5 acres new pond at the MI region. The costs of their auxiliary systems are the same in either way.

20.4. Kickers

C. Jensen

Most of the MI kickers were designed to handle a 1.467 second cycle time for antiproton production, so changing to a 1.5 second cycle time is a non-issue for all but the MI-60 (NuMI) 6-batch extraction kickers and the MI-52 (120/150 GeV proton extraction) 6-batch kickers. For the NuMI kickers it is a simple matter to purchase a larger charging supply to charge the pulse-forming network (PFN) in a shorter time (currently 1.833 second cycle time). For the MI-52 kickers the problem is more fundamental. While a larger charging power supply would charge the PFN in a shorter time, the PFN was not designed for continuous operation at 1.5 seconds. If indeed the 6-batch beam was needed down the P1 and P2 line, the PFN at MI-52 would need to be completely rebuilt to be reliable at that higher repetition rate. In addition, the magnet would need substantially more cooling of the high voltage load.

Another issue is kicker magnet apertures. They are approximately 1.3 inch V × 3.2 inch H (33 mm V × 81 mm H) for all MI kickers (as shown in Figure 20.3) except at MI-10 where the kicker has an aperture of approximately 1.75 inch V × 3.75 inch H (44 mm V × 95 mm H). The kickers at MI-30, MI-52 and MI-60 could be increased to an aperture of approximately 1.55 inch V × 3.5 inch H without magnet or power supply redesign. This is because the physical aperture in the magnetic material is approximately 2.05 inch V × 4.25 inch H. The MI-40 and MI-62 magnets (which are identical) were moved from the old Main Ring and have less room for a larger vacuum chamber. They would probably have to be rebuilt from scratch. Currently, there is a low level effort to investigate replacement materials for the ceramic vacuum chambers. Two possibilities are Pyrex and PEEK (a high temperature plastic). The PEEK alternative would probably fit with the MI vacuum requirements.

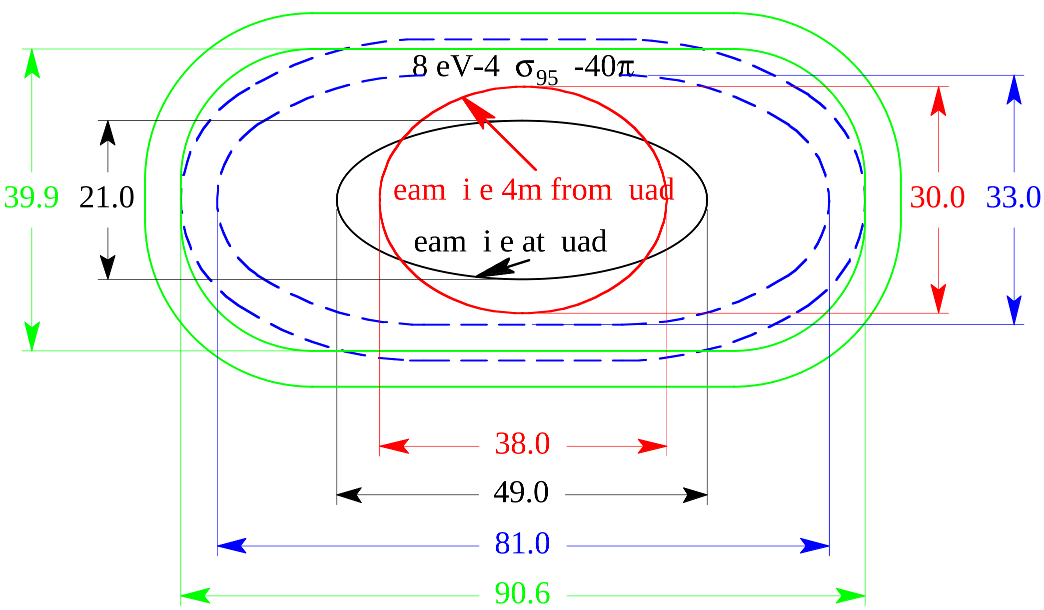

Figure 20.3. Existing (dashed) and proposed (solid) vacuum chamber cross sectionandthe typical beam si e at kicker locations (units in mm).

20.5. Beam Abort Dump

N. Mokhov

With five times more protons on the abort dump, the concerns are instantaneous temperature rise in the graphite core, its integrity and cooling, and radiation levels above grade. These issues have been addressed in detailed Monte Carlo calculations with the MARS code. [1] The following parameters were used in these studies: maximum extraction beam energy of 120 GeV and 1.5×10^{14} protons per pulse with a 1.533 s cycle time, corresponding to 1.9 MW beam power. For a normalized emittance of 40 π mm-mrad, the rms beam spot size at the dump at top energy is $\sigma_x = 4.88$ mm and $\sigma_y = 1.52$ mm. The abort dump, its shielding and enclosure geometry and materials from Ref. [2] were implemented into the MARS model. The graphite core made of 6-in $\times$ 6-in graphite blocks is 2.4 m long, encased in a water-cooled aluminum box. This assembly is surrounded by steel and concrete shielding.

Figure 20.4 shows the calculated absorbed dose distribution in the setup. The corresponding dose on the outer surface of the berm is -- just proportionally -- 5 times higher than now and should not cause a problem. The peak-absorbed dose in graphite can reach 10 Mrad per pulse, which again seems to be acceptable for the assumed beam abort scenario. Figure 20.5 shows the instantaneous temperature after a 120-GeV beam abort on the axis of the beam dump core. The peak temperature in graphite is 290°C, much lower than the ~1000°C in the Tevatron dump graphite core which has been successfully operated since 1980. At the same time the temperature is 186°C in the aluminum box, and 386°C on the axis of the downstream steel. To avoid overheating of the cooling water and structural damage in metals -- especially in a case of successive aborts -- these values need to be reduced by at least a factor of two. This can be provided by increasing the graphite core length (in the upstream open region towards the incoming beam) from 2.4 m to about 3 m. One should also perform a thermal analysis to check if a significant fraction of deposited energy is adequately removed by the existing cooling system prior to the next abort.

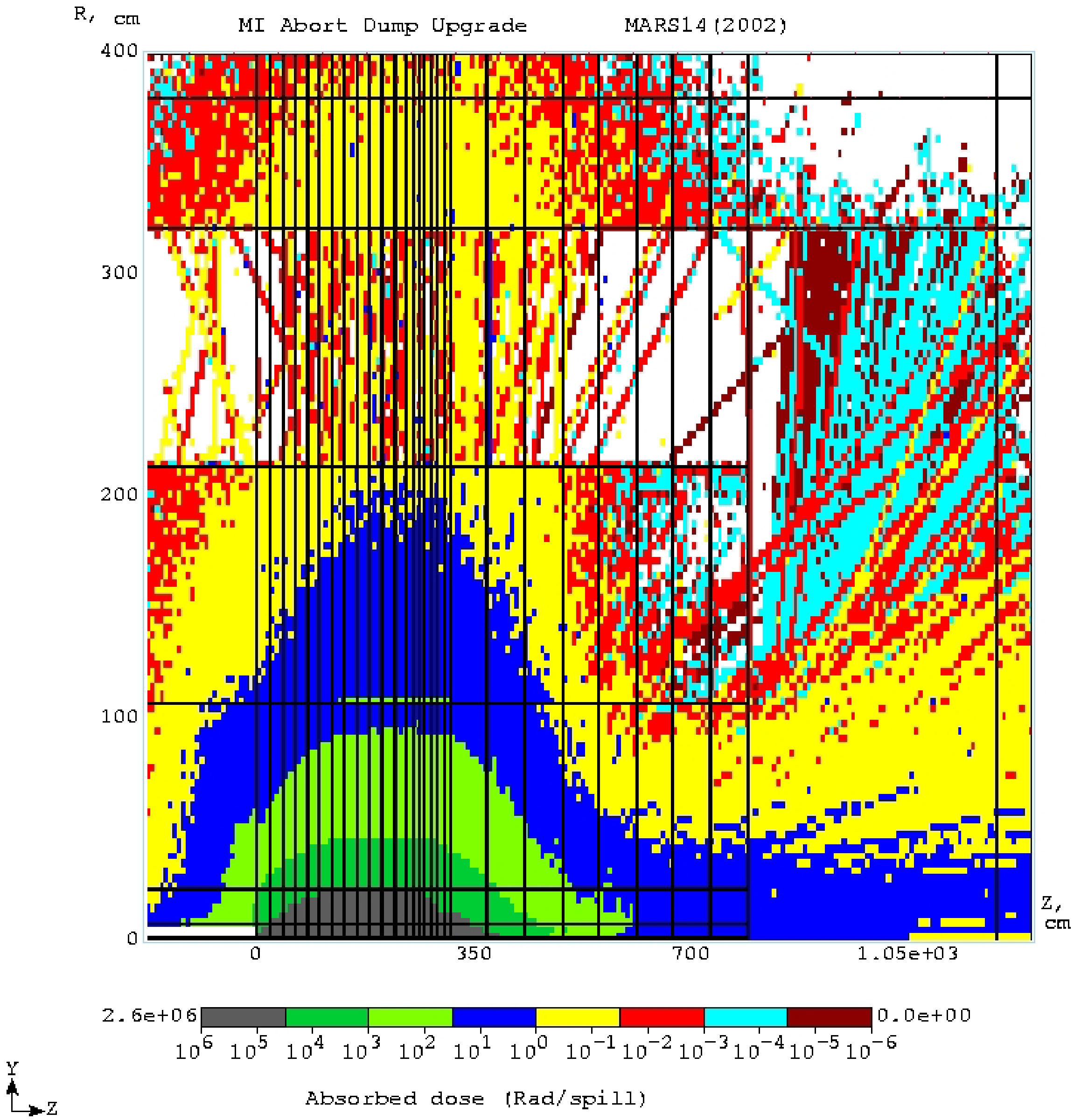

Figure 20.4. Isodose contours (Rad per pulse) in the beam abort setup.

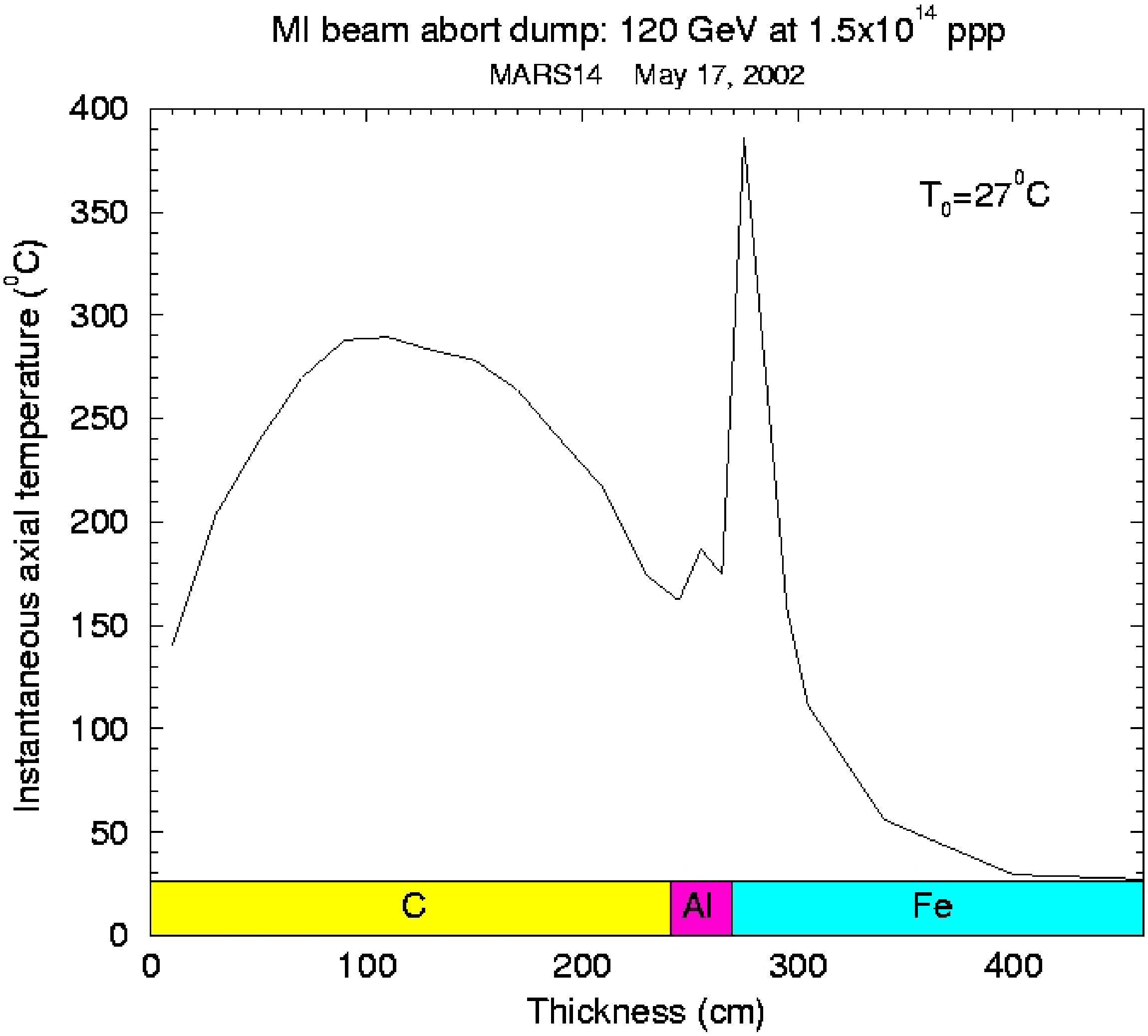

Figure 20.5. Maximum instantaneous temperature on the beam axis in the abort dump.

20.6. Controls

M. Shea

20.6.1. Decreased Main Injector cycle time

Decreasing the Main Injector cycle time to 1.5 sec will require a large increase in the rf accelerating system, changes to the main magnet power supplies, and more capacity for the water cooling system. A new gamma-t system would also be added. Although the ring magnet power supplies will be much different, the ramp control will be patterned after the Tevatron and Main Injector ramp controllers. This type of controller was included in PD1.

20.6.2. Main Injector RF Controls

Existing Main Injector high-level rf stations are controlled and monitored using an IRM (Internet Rack Monitor) for each rf station. The option of adding a second power tube to each of the Main Injector rf cavities will require 18 more IRMs and their associated cable interface chassis.

20.6.3. Main Injector Cooling System

Changes in the rf system and magnet power supply will add to the cooling requirements for the Main Injector. In all, the amount of cooling will be roughly double the present capacity. Controls for the present cooling system are PLC (Programmable Logic Controller)-based and PLC controls will be added to accommodate the added cooling equipment.

References

[1] N.V. Mokhov, "The MARS Code System User's Guide," Fermilab-FN-628 (1995); N.V. Mokhov and O.E. Krivosheev, "MARS Code Status," Fermilab-Conf-00/181 (2000); http://www-ap.fnal.gov/MARS/.

[2] "Fermilab Main Injector Technical Design Handbook," Fermilab (1994).

Chapter 21. Upgrade of Beamlines

21.1. NuMI Beamline

N. Grossman, D. Harris

21.1.1 Introduction

It should be pointed out that there is a difference in beam intensity and beam power between the NuMI baseline and the Main Injector baseline parameters. For the former, they are 4×10^{13} protons per cycle and 0.4 MW, respectively; for the latter, 3×10^{13} protons per cycle and 0.3 MW, respectively.

The NuMI beamline (see Figure 21.1) is designed to handle 0.4 MW of proton power, and it will not be trivial to upgrade it to withstand a proton power of 2 MW. In this chapter we describe which elements would survive such an upgrade, and which elements would need to be modified. Where possible, rough estimates have been made for how much those modifications cost; these are tabulated in Appendix 1.

The neutrino beam at NuMI is created when 120 GeV protons from the Main Injector strike a 0.94 m graphite target located roughly 40 m below ground in the NuMI tunnel. Secondary mesons are then focused in a two-horn focusing system, and directed towards a 675 m long decay pipe. The uninteracted protons and particles that did not decay hit a hadron absorber located about 725 m from the upstream edge of the first horn. Finally, there are beamline monitors both upstream and downstream of the absorber, as well as in two alcoves embedded in the dolomite following the absorber alcove. The target, the horns, and the decay pipe itself all must be water cooled, and the entire beamline has an impressive amount of shielding to prevent groundwater contamination.

The design parameters for the primary beam for both the NuMI design and the proton driver upgrade are given in Table 21.1. In the following sections, we will address what major items would or would not need to change for this new set of parameters. Smaller aspects of the experiment that also would need to change are not addressed.

21.1.2 Primary Beam

The NuMI primary beamline is designed to match the dynamic aperture of the Main Injector. Therefore, although the protons per cycle will increase by almost a factor of 4, the primary beam optics should not need to be changed. This assumes that the losses per minute can be maintained at the same level as for nominal running, or the fractional losses per pulse have to be reduced by a factor of 5. To do this may require the addition of collimators in the NuMI beamline. With the 1.5 second repetition rate, the power supplies on the primary beam optics (ramps, controls) also should be adequate, with the exception of the kicker power supply, which would need a larger charging power supply. Thus, the LCW for this system, assuming the optics does not change, can also remain the same.

Table 21.1. NuMI Baseline Design Parameters vs. Proton Driver Era Parameters

	NuMI Baseline	Proton Diver Era
Beam Energy (GeV)	120	120
Protons per cycle	4×10^{13}	1.5×10^{14}
Cycle Time (sec)	1.87	1.53
Protons per second	2.13×10^{13}	1×10^{14}
Average Beam Current (mA)	3.4	16
Target Beam Power (MW)	0.41	1.9
Normalized Transverse Emittance (mm-mrad)	40π	40π
Longitudinal Emittance (95%, eV-s)	1	0.2
Momentum acceptance	$\pm 0.7\%$	$\pm 0.7\%$
Dynamic Aperture	Matches that of the MI	$>80\pi$

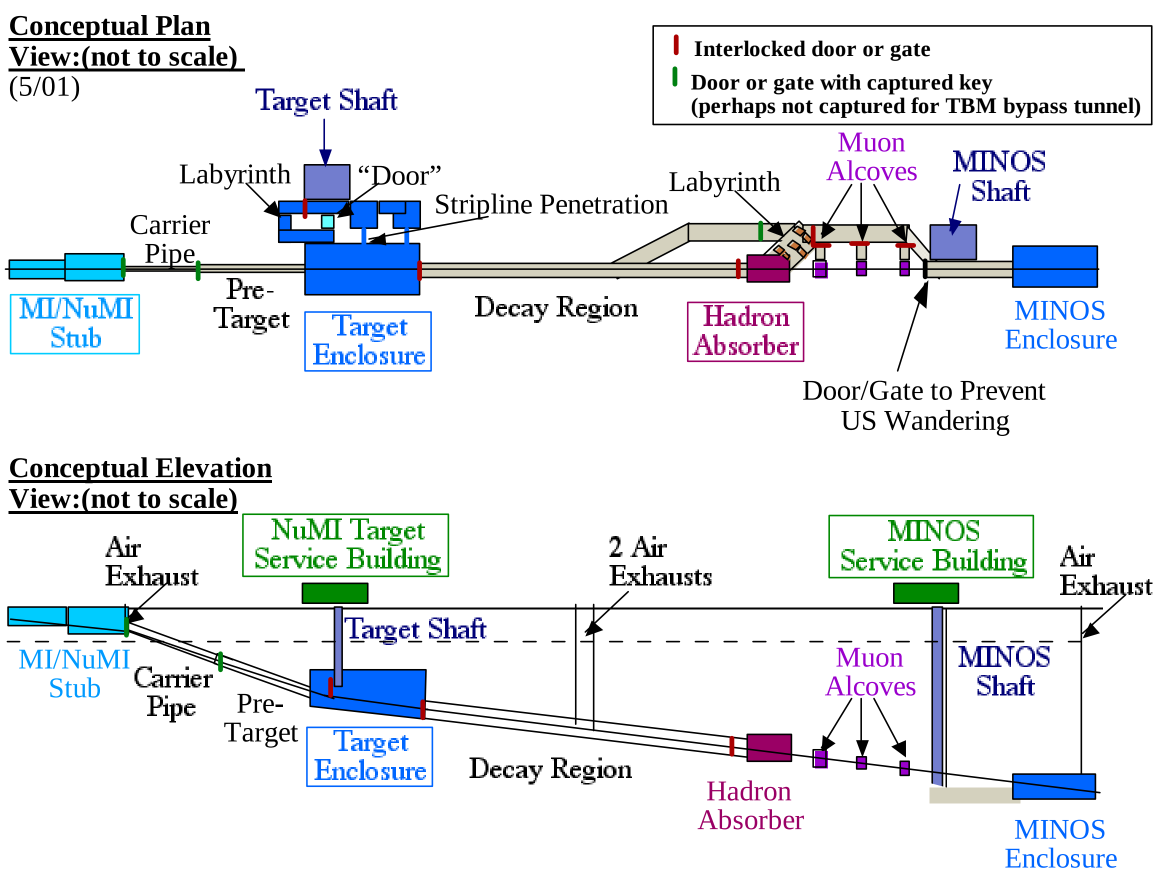

Figure 21.1. Conceptual Diagram of the NuMI Beamline

21.1.3 Target and Horns

If the proton beam were to maintain the same spot size, then the current design of the NuMI target would not withstand the increased proton power, because the temperature of the graphite would be too high. However, it has been shown that if the proton spot size were three times as large, and the target were also three times larger in the transverse direction, then the graphite would not yield for 2 MW proton power. In this case a different scheme for cooling the target would also have to be designed.

The horns could probably handle the increased pion flux and the increased repetition rate, although the life expectancy for a given horn might be reduced. In fact most of the wear and tear on the horns is due to the pulsing, not the passage of the produced particles. The life expectancy for a NuMI horn pulsed at 1.87 seconds is at least one year; so the lifetime for a horn in the upgrade might be reduced to 9 months. The NuMI prototype horn has been pulsed 1 year equivalent of pulses with no problems, and once the experiment is running the true lifetime of these horns will be much better known. The horn power supply could be modified to operate at a higher repetition rate at minimal cost.

21.1.4 Target Area Cooling

The cooling for the horns and target area (which has a total extent of about 48 m) is one of the hardest things to upgrade. Right now the target area is being cooled by a very high flow rate of air through the region. With 5 times the proton power it is likely that the region will have to be water cooled instead. Rebuilding this area for water-cooling will take a large amount of planning, since that region will be extremely radioactive after NuMI runs. We estimate ~$5.5 million to re-design, fabricate, de-install and re-install the Target Hall cooling and shielding to accommodate the increased heat load.

21.1.5 Decay Pipe and Cooling

The decay pipe window has aluminum in the center, surrounded by an outer ring of steel. This design was adapted over a solid one-material window design because if there were to be an accident where the proton beam missed the target and hit the upstream window of the decay pipe several times, the window would break. Replacement of this window, due to the high level of radioactivity, would be difficult. If the proton intensity were increased by a factor of 4 without changing the spot size on the target, then it is likely that the dual material window would not survive. From the target studies, however, we know that the target would not survive either, so it is likely that the proton spot size would be considerably larger in a proton driver upgrade scenario. If the proton spot size increases by a factor of three in both the horizontal and vertical directions, and the proton intensity only increases by a factor of 4, then the upstream vacuum window of the decay pipe would not need to be changed. The downstream window of the decay pipe is not a concern and would not have to be changed regardless of the proton beam spot size.

The most challenging aspect of an upgrade would be the decay pipe itself. Here the heat loads will increase by a factor of five. The existing cooling lines are conservatively designed for the NuMI heat load, and measurements with NuMI running would need to be made (and planned for by design) in order to determine what upgrades are needed. One can expect the bulk temperature of the cooling water in the current design to increase to 60° F and the mean metal temperature in the decay pipe steel to increase even more dramatically. If additional cooling were needed, it would be needed for a fraction of the decay pipe's length. The costs for the additional cooling for the decay pipe are very roughly estimated at a million dollars.

21.1.6 Hadron Absorber

The Hadron Absorber for NuMI consists of a water-cooled Aluminum core, surrounded by un-cooled steel blocks. The temperature rise in the hottest module in the aluminum core in normal running is 60° C above the cooling water, and in the first steel block downstream of the aluminum, the temperature rise is about 300° C above the cooling water. An increase in the proton beam intensity alone would be acceptable for the aluminum core, but the first steel block after the absorber may be too hot. Thus some modification of the Hadron Absorber would be needed. If the proton spot size and target increases in size by a factor of 3, then taking into account multiple scattering in the target, the area of the beam at the absorber would be about 3.5 times bigger, and an integrated rate 5 times higher. This would minimize the modifications needed for the Hadron Absorber cooling.

21.1.7 Beamline Monitors

Because of the high radiation rates that are expected in the monitoring locations for nominal running conditions, the beamline monitors are being constructed entirely of radiation-hard materials: ceramics or metals. In nominal running the muon monitors will see tens of Megarads, while ceramic has been tested to above the Gigarad level. Therefore an increase in the proton power of a factor of 5 should not be a problem. At the expected fluxes in nominal running, the monitors are not expected to saturate, and even at these higher levels (increase in pulse per spill of a factor of 4) they should at the worst only be saturating by a few percent.

21.1.8 Radiation Safety

21.1.8.1 Groundwater

Groundwater activation has been a big issue for the NuMI Beamline due to the majority of the beamline being located in the aquifer, which is considered a "Class I" groundwater resource. Contamination limits for drinking water supplies and for Illinois "Class I" groundwater resources (water that potentially could be drinking water) are the same. The radionuclides of concern are ^{3}H (12.3 year half-life) and ^{22}Na (2.67 year half-life). Table 21.2 lists the limits for these radionuclides for both surface and drinking water. For mixtures of radionuclides, a weighted sum is used. The annual average concentrations must be below the limits.

Table 21.2. Regulatory Limits for Accelerator Produced Radionuclides in Drinking and Surface Waters

Regulation	Water Use Type	Annual Dose Equivalent (mrem)	^{3}H (pCi/ml)	^{22}Na (pCi/ml)
40CFR Part 141/35 IAC 620	Drinking	4	20	0.4 (inferred)
DOE Order 5400.5	Surface	100	2000	10
DOE Order 5400.5	Drinking	4	80	0.4

For NuMI, conservative estimates have been made of the expected concentrations relative to these limits, including uncertainties, to ensure that the levels produced by the NuMI beamline will be below them. For the Proton Driver upgrade, measurements from NuMI running will be available from which one can extrapolate. We do not expect any measurable levels of ^{3}H or ^{22}Na in the groundwater monitoring wells due to NuMI operation. Extrapolating from these measurements will show that an intensity increase of a factor of 5 will similarly show negligible levels relative to the regulatory limit in the monitoring wells. Similarly, measurements will be made of the levels of radionuclides in the water pumped from the NuMI tunnel and released to the surface waters. These levels are expected to be at least a factor of 20 below the surface water limits. Thus with an intensity increase of a factor of 5, we would still be below the surface water limits.

The main area of concern for groundwater activation is in the "interface region" between the glacial till and the dolomite. This is where the NuMI primary beam is in the lined carrier tunnel. Here the water is in the aquifer and the tunnel is lined and the water flows at the rate of the regional gradient towards the Fox River. Normal operational losses in this region drive the groundwater concerns, not accident conditions. In most areas of the NuMI primary beamline, the estimated upper limit on normal loss levels for NuMI operation is 2.1×10^{9} p/sec, either due to groundwater activation concerns or residual activation concerns. In the carrier tunnel interface region, the upper limit is estimated at 2.1×10^{7} p/sec. The calculations assume a constant loss at this level. For other beam intensities, these loss rate limits would still apply. As a result, depending on the Proton Driver beam parameters, Main Injector collimators may be necessary to reduce beam halo to keep losses in the beamline to a minimum.

Not related to radiation safety, but of concern, is the temperature of discharged water to surface waters. Temperatures of 60° - 90° F are expected for NuMI, and will be higher with the Proton Driver intensities. Most likely additional cooling ponds will be needed.

21.1.8.2 Airborne Activation

The air within the Target chase is the main source of air activation for NuMI. This air is sealed within the chase and re-circulated. Still, some amount will leak out. For 5 times the intensity, the chase would need to be much better sealed in order for NuMI to keep the release rate below ~40 Ci/yr, the agreed upon level. The air permit that FNAL has with IEPA could be modified to allow larger annual releases for the laboratory as a whole and this would relax the requirements on NuMI as well as other areas at Fermilab. Another way that releases for NuMI could be reduced is by decreasing the ventilation rate from the Target Hall to the vent and from the Hadron Absorber to the vent. This would increase the humidity levels in the decay tunnel and reduce the air-cooling in that region. To know the extent to which these measures would need to be taken, measurements with NuMI operation need to be made. The cost estimate listed in Appendix 1 for upgrading the Target Hall cooling and shielding includes the cost for increased sealing of the target chase. Similarly the Hadron Absorber upgrade cost also includes required additional sealing to keep the activated air contained.

21.1.8.3 Prompt Radiation, Labyrinths and Penetrations

The area to the Target Hall upstream shaft side of the equipment door may become a radiation area. Since people would not need to be in the area for any length of time with the beam on, this does not present a problem. Similarly, the dose rate through the transmission line penetration to the power supply room may be above 5 mrem/hr. There is also little reason to work in this area extensively with the beam on.

The portion of NuMI in the Main Injector would need additional earth shielding, as would the Main Injector. When the Main Injector shielding in this area is upgraded for increased intensity, the NuMI portion will also be upgraded as part of the Main Injector.

21.1.8.4 Residual Dose Rates

Residual dose rates above the Target Hall shielding would still most likely be below 5 mrem/hr in most areas. There may be some hot spots where localized shielding would need to be increased by an additional layer of 1.5 ft. concrete blocks if one wished to have rates below 5 mrem/hr everywhere. Below the concrete cap, where people would need to connect and disconnect water, electricity, etc. to the horn, the dose rates in most places would be below ~50 mrem/hr. Localized hot spots could be shielded when the concrete cap is removed.

Dose rates along the emergency egress pathway along the decay tunnel might reach 500 mrem/hr. This is due to the activated concrete and rock. The concrete and rock will cool down relatively quickly. The emergency egress is not envisioned to be occupied except for maintenance and search and secure. The Hadron Absorber area will be ~100s of mrem/hr. The concrete side will cool down quickly. The steel portions will be hotter and not cool down significantly. They might need to be covered in concrete, depending on access needs.

Clearly all components in the chase (horn, target, T-blocks) and the Hadron Absorber core would be highly radioactive and very difficult to work on. Present estimates range from 100 R/hr to several thousand R/hr (for the target and horns). These estimates would have to be increased by a factor of about 5. Once NuMI runs, measurements will be made of the residual dose rates from various components. These can then be used to more accurately extrapolate to 5 times the intensity and thus more accurately determine the upgrades needed.

21.1.9 Operation at 1-second Repetition Rate

Operation at a 1 second repetition rate and five times the intensity would require major changes to the beamline power supplies, cooling systems, horns, target etc. This would be a large investment that one cannot begin to quantify at this stage without a large engineering effort.

21.1.10 Summary

The main upgrades needed to the NuMI beamline are those associated with cooling. The Target Hall shield pile, decay pipe, and Hadron Absorber cooling would all need to be upgraded. A new target would also need to be designed, built and installed. Due to air activation concerns, the Target Hall and Hadron Absorber shielding would need to be more tightly sealed. Some minor upgrades would be needed for the kicker power supply and perhaps the primary beamline would need a few collimators. Radiation safety issues do not drive any costs. The overall cost for the upgrade to 5 times intensity and 1.5 second repetition rate would be between \$5 and \$18 million dollars, with an estimated expected cost of \$9 million. The cost breakdown is listed in Appendix 1. To then be able to run at a 1 second repetition rate and the same intensity would be a significant additional cost.

21.2. MiniBooNE Beamline

P. Martin

The MiniBooNE target station is comprised of the following main elements (Figure 21.2):

- beryllium target
- horn
- horn power supply
- target pile
- decay region
- beam absorber

The baseline design for the MiniBooNE target station is a 1.6 μsec beam pulse of 5×10^{12} protons at an average rate of 5 Hz. This corresponds to a beam power of 30 kW. The beam is delivered by energizing a switch magnet at the downstream end of the MI-8 beamline. In addition to the issues of the target station elements themselves, air activation and groundwater are two major concerns that need to be addressed when considering an intensity increase. Beam-on radiation in the MI-12 Service Building and over the decay region are also issues requiring discussion.

21.2.1 Spill duration impact on MiniBooNE

The horn and horn power supply were designed for operation with a 1.6 μsec beam spill, at a repetition rate of 7.5 Hz (with operations expected at 5 Hz.) The current pulse is a

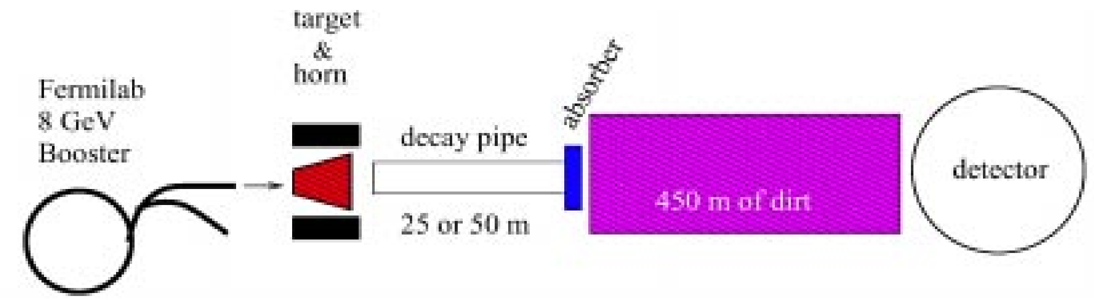

Figure 21.2. MiniBooNE Beamline Layout

half-sine wave with a width of 140 μsec. Changing the beam spill to 10 μsec has little impact on the horn focusing; the current is still uniform over the spill to better than 1%. A 1-msec long pulse of beam delivered directly from an 8 GeV linac would require a total redesign of the horn power supply. The present cooling is near the limit of what can be achieved with sprayed-water cooling and precludes a high repetition rate. In addition, the longer pulse duration would seriously impact the experiment, which relies upon a short spill time for signal to background enhancement.

21.2.2 Intensity impact on MiniBooNE

The target itself absorbs around 1 kW of beam power. Increasing this five-fold (as will be discussed below) requires a new target design with a larger surface area for cooling, and a larger beam size to reduce the peak energy density. A new cooling system may also be required to remove the higher heat load.

The larger target requires a new horn design with a larger inner diameter. Joule heating from the current pulse dominates the horn temperature rise. Beam heating is a minor factor at the nominal baseline design of 2.5×10^{13} protons per second. A larger diameter alone should be adequate to provide the additional cooling for the higher beam power since it provides a larger area for cooling, and the smaller resistance (for the same wall thickness) reduces the Joule heating. If necessary, reducing the horn current by a few percent also reduces the total power absorbed.

The target pile absorbs around 10 kW of the beam power in the baseline design. Increasing this five-fold should be possible. The steel is cooled on three surfaces by water-cooled panels. While the temperature in the interior of the pile will rise, there are no concerns in this regard.

The decay region and the beam absorbers capture over half of the beam power. This heat is removed by a series of cooling pipes surrounding the decay pipe. These pipes are used to circulate air that removes the heat through an air-to-air heat exchanger. The system was designed to remove 15 to 20 kW of beam power. Increasing this five-fold may be possible with the existing system, although the temperature of the decay region would rise considerably. To go beyond a factor of five would probably require changing to using water as the cooling medium. This may be possible, but there would be some reluctance to introducing water in these lines due to their close proximity to the decay pipe and the resulting activation of the water if there were any leaks in this system.

21.2.3 Radiation issues

Beam-on Radiation. The expected levels in the MI-12 Service Building are expected to be on the order of 0.1 mrem/hr. Increasing this five-fold is not a problem. The levels on the berm over the decay region are expected to be about 1 mrem/hr; increasing this to 5 mrem/hr would require fencing the entire region.

Air activation. Calculations indicate that MiniBooNE will release around 10 Ci/yr. Until there is some experience with how difficult it is to achieve this level, one can only speculate that with additional effort, it would be possible to reduce this by a factor of five to handle the increased beam power.

Groundwater. The decay region is surrounded by a double-walled liner to exclude water from the vicinity of the decay pipe. Although this liner has failed at the bottom, presumably due to inadequate compaction of the underlying soil adjacent to the MI-12 enclosure, a plan is in place to dewater this region by using the monitoring wells to continuously pump water. Calculations indicate that the level of activation of any water that accumulates in the lower portion of this region will reach the levels of what is permissible for discharging to surface waters. An increase of a factor of five in beam power may require this water to be pumped into holding tanks and sampled before being released, or, if the levels are too high, of disposing as liquid waste. This would be very expensive for the tanks and manpower for sampling, and prohibitively expensive to dispose of the waste if required. Again, until there is experience with the system at the baseline design intensity, once can only speculate as to what the pumping volumes and activation levels will be.

Horn changing procedure. Another issue to consider is the need to change a failed horn. The residual activation of the horn will scale with the beam intensity. A much longer cooldown period may be required before changing the horn. Here again, experience with the baseline intensity will help clarify the magnitude of this problem.

21.2.4 Summary

There are a number of areas in which a large intensity increase begins to have substantial impact. Foremost among these are air and groundwater activation, and cooling of the decay region. One could reasonable expect that these aspects could be handled for a five-fold intensity increase, but that is probably near the limits of what can be done.

21.2.5 Cost considerations

The beam is delivered to the MiniBooNE target by a beamline that begins near the end of the MI-8 beamline, just before injection into the Main Injector. The extraction is presently accomplished by energizing a pulsed “switch magnet” just downstream of quad Q851 in the MI-8 line.

Major modifications to this portion of the beamline would be required for any scheme of proton driver that does not utilize the existing MI-8 beamline for injection. In particular, in the proposed 8-GeV superconducting linac scheme, one must assume that a new means of extracting to the MiniBooNE target must be developed.

Extracting from the Main Injector. To extract from the Main Injector directly, a kicker would need to be placed just downstream of Q100 and a Lambertson magnet after Q102. This would be followed by a beamline with much harder bend than presently exists to point beam towards the target hall. While no optics design has been done, it is assumed that a solution may exist, but such a solution may require design and fabrication of new magnets for this bend, to achieve the ~60 degrees of bend in a shorter space than presently exists. This would require demolition of the MI-10 Service Building, excavation and demolition of some portion of both the MI and MiniBooNE beamline enclosures, and the reconstruction of the enclosures and building. A rough estimate for the cost of this work would be $8 M. A major drawback of using the Main Injector for this purpose is that this will require dedicated use of the Main Injector during the period of time the beam is being delivered to MiniBooNE, roughly one-third of the time at the assumed 5-Hz average spill rate.

Extracting from the Recycler. To extract from the Recycler, it may be possible to avoid demolition of the MI-10 Service Building and the MiniBooNE beamline enclosure, but a section of the Main Injector enclosure in the vicinity of quads Q636 - Q100 would need to be excavated, demolished and reconstructed with a larger enclosure to accommodate a new transfer line connecting the Recycler into the MiniBooNE beamline before it enters the jacked pipe. This will be considerably cheaper than the option above, but would still cost several million dollars. Again, no optics design has been done, but it is assumed a solution may exist. A major drawback of using the Recycler for this purpose is that this will require dedicated use of the Recycler. In addition, either the proton driver must also be capable of injecting directly into the Recycler, or the Main Injector must also be dedicated to MiniBooNE operations for one-third of the time. Table 21.3 compares the proton pulse length and protons per pulse for the two schemes: Synchrotron at 5 Hz (1.25×10^{14} protons per second, or 5 times MiniBooNE design), and Linac at 1 Hz (1.5×10^{14} protons per second, or 6 times MiniBooNE design).

Table 21.3. Proton pulse length and protons per pulse

8 GeV synchrotron	1.6 μsec pulse	2.5×10^{13} protons/pulse
8 GeV linac, via MI or RR	~ 10 μsec pulse	1.5×10^{14} protons/pulse

21.3. The Meson, Neutrino, and Proton External Beam Areas

C. Brown

During the 1990s, the Tevatron routinely delivered, via the External Beams Switchyard, up to 1×10^{13} /min. 800 GeV protons to the Meson, Neutrino and Proton Experimental Areas. During FY2002, the F-sector Main Ring Remnant and the Switchyard are being modified to transport 120 GeV protons from the Main Injector to the Meson Area. Due to shielding limitations in many places along the 1.5-mile journey from the MI to the Meson Area, the intensities delivered to the Meson Area will be limited to 5×10^{12} protons per 3-second MI cycle.

In a Proton Driver era, it would be relatively easy to deliver 120 GeV protons to any or all of the existing Meson, Neutrino, and Proton Areas through the existing Switchyard. If the full intensity capabilities of the Proton Driver were needed for some experiment in one of these areas, shielding upgrades would be needed. Until the current Shielding Assessment Document for the Meson 120 GeV beam project is completed, and until the details of a high intensity experiment in one of the three External Beam Labs are known, the extent of the shielding modifications required cannot be reliably estimated.

Appendix 1. Cost Estimates

R. Alber, T. Anderson, A. Chen, W. Chou, J. Crisp, A. Drozhdin, N. Grossman,
D. Harding, C. Jach, C. Jensen, J. Lackey, P. Martin, E. McCrory, J. Reid, M. Shea,
I. Terechkine, D. Wildman, D. Wolff, D. Young

A1.1 Introduction

The cost of a synchrotron-based Proton Driver and of the modifications and upgrades of the Main Injector and associated beam lines have been estimated using the "bottoms up" method. After the design of each technical system is completed, it is given to an experienced engineer who has built similar systems before who makes a cost estimate that contains sufficient details based on previous work. In this Appendix, however, we only list the cost estimate of each technical system without including these details. We believe this is sufficient at this stage of the design study. The cost estimate for civil construction is done in the same way. A Work Breakdown Structure (WBS) is not incorporated but will be produced when it is required.

This is the so-called "unloaded" cost estimate. In other words, it does not include G&A (lab overhead) and contingency. These items will be added later following guidelines provided by the Fermilab Director and the DOE. The ED&I costs are included in the cost estimates and are assumed to be 17% across the board.

All the figures are in FY 2002 U.S. dollars. No inflation is included.

A1.2 Cost Estimate of a Synchrotron-based 8 GeV Proton Driver

Table A1.1 lists the cost estimate of a synchrotron-based 8 GeV Proton Driver. It includes an 8 GeV synchrotron, a 200 MeV linac extension (to bring the total linac energy to 600 MeV), a 600 MeV beam transport line, an 8 GeV beam transport line, improvements in the present H^- source and Linac, and civil construction. The total cost is about \$170M. Compared with PD1 (of which the cost is about \$242M), the saving is about \$72M. This saving mainly comes from the magnets, power supplies and civil construction. This is because the machine size is smaller; the number of magnets and magnet aperture are also reduced. An additional cost item of PD2 is the conventional construction required for the linac extension (technical systems and a gallery), about \$20M, which is not required by PD1.

(Note: In the Appendix of Chapter 8 we discussed an upgrade of the aging original 1972 DTL linac; the cost of such an upgrade is not included here since although desirable it is not required by PD2.)

It should be pointed out that a result of this cost saving is a reduction of the proton beam power. In PD1, the Proton Driver is a 1 MW machine. In PD2, it is reduced to 0.5 MW.

A1.3 Cost Estimate of the Main Injector and Beam Lines Upgrades

Table A1.2 lists the estimated costs of the required modifications and upgrades of the Main Injector and associated beam lines in order to make the Main Injector a 2 MW machine. Included are the rf system and power supply upgrades, a gamma-t jump system, four large aperture quadrupoles, major modification of the kickers, a longitudinal feedback system, collimators, upgrade of the MI-40 beam dump, and controls and utilities upgrades. The table also includes the cost estimate of the NuMI and MiniBooNE upgrade in order for these beam lines to take full advantage of the higher beam power that would be available from the upgraded Main Injector and Proton Driver. Upgrades to the NuMI and MiniBooneNE detectors are not included.

The main cost item in the MI upgrade is the rf system. Most other items cost around $1M or below. There are two possible ways to implement the MI upgrade. It can be done as a single "all-included" Fermilab project. Or the upgrade can be accomplished through a series of accelerator improvement projects (AIPs).

There is a large uncertainty in the cost estimate for the NuMI beam line upgrade to 2 MW. A lot of the data that are necessary for making a reliable cost estimate are not available at this time. The actual cost could be twice as high or 50% lower than that listed in the table (about $9M).

Table A1.1. Cost Estimate of a Synchrotron-based 8 GeV Proton Driver (in K$)

1	**Technical Systems**			115,813
1.1	8 GeV Synchrotron		92,426	
1.1.1	*Magnets*	27,329		
1.1.2	*Power supplies*	25,968		
1.1.3	*RF*	5,115		
1.1.4	*Vacuum*	6,061		
1.1.5	*Collimators*	325		
1.1.6	*Injection system*	938		
1.1.7	*Extraction system*	2,189		
1.1.8	*Instrumentation*	2,393		
1.1.9	*Controls*	2,468		
1.1.10	*Utilities*	4,931		
1.1.11	*Installation*	1,280		
1.1.12	*ED&I*	13,429		
1.2	Linac Improvements and Upgrade		20,475	
1.2.1	*Front end and RFQ*	3,000		
1.2.2	*New drift tube Tank #1*	1,000		
1.2.3	*Transfer line to new CCL*	1,800		
1.2.4	*New CCL modules and klystrons*	11,100		
1.2.5	*Controls and diagnostics*	600		
1.2.6	*ED&I*	2,975		
1.3	600 MeV Transport Line		1,053	
1.3.1	*Magnets*	720		
1.3.2	*Power supplies*	180		
1.3.3	*ED&I*	153		
1.4	8 GeV Transport Line		1,859	
1.4.1	*Magnets*	1,271		
1.4.2	*Power supplies*	318		
1.4.3	*ED&I*	270		
2	**Civil Construction**			43,468
2.1	8 GeV Synchrotron		17,500	
2.1.1	*Enclosure*	7,000		
2.1.2	*Service buildings*	7,000		
2.1.3	*Utility support building*	3,500		
2.2	Linac extension		2,500	
2.3	600 MeV Transport Line		1,800	
2.4	8 GeV Transport Line		2,200	
2.5	Site work		4,800	
2.6	Subcontractors OH&P		5,760	
2.7	ED&I		5,875	
2.8	Environmental controls and permits		3,033	
3	**Project Management**			10,000
	TOTAL ($k)			169,281

Table A1.2. Cost Estimate of Main Injector and Beam Lines Upgrades (in K$)

1	**Main Injector Upgrade**			23,502
1.1	RF system		14,238	
1.1.1	*Modulator*	3,400		
1.1.2	*Power amplifier*	1,390		
1.1.3	*Anode supplies*	1,098		
1.1.4	*Cavity modifications*	1,250		
1.1.5	*Driver amplifiers*	3,600		
1.1.6	*Installation*	3,500		
1.2	Main power supplies		430	
1.2.1	*Bend bus*	210		
1.2.2	*Quad bus*	220		
1.3	Gamma-t jump system		490	
1.3.1	*Pulsed quads*	130		
1.3.2	*Power supplies*	320		
1.3.3	*Beam pipes*	40		
1.4	Large aperture quadrupole		710	
1.4.1	*Magnets*	360		
1.4.2	*Tooling*	350		
1.5	Kickers		1,060	
1.5.1	*PFN and cooling*	370		
1.5.2	*Magnets*	690		
1.6	Longitudinal feedback		625	
1.7	Collimators		325	
1.8	Beam dump		500	
1.9	Controls		303	
1.10	Utilities		1,406	
1.11	ED&I		3,415	
2	**NuMI Upgrade**			8,920
2.1	Collimators		180	
2.2	Target and cooling		750	
2.3	Kicker and horn power supplies		90	
2.4	Target Hall chase cooling		1,000	
2.5	Target Hall shielding		3,000	
2.6	Install Target Hall shielding		1,000	
2.7	Install Hadron Absorber		500	
2.8	Hadron Absorber cooling		1000	
2.9	Decay pipe cooling		1,000	
2.10	Additional cooling ponds		400	
3	**MiniBooNE Upgrade**			250
4	**Project Management**			3,000
	TOTAL ($k)			35,672

Note: For the option of an 8 GeV superconducting proton linac, one needs to add two more items:

- A new H^- injection system in the Main Injector;
- A new extraction scheme for the MiniBooNE experiment.

The cost of these two items is not included in this table.

Appendix 2. R&D Program

W. Chou

A2.1. R&D for a Synchrotron-based 8 GeV Proton Driver

The R&D required to build the Proton Driver has been discussed in PD1 (see Chapter 19 of Ref. [1]). In that study, the R&D is divided into three categories. Category A includes those items that are not only needed by the Proton Driver but will also be useful for improving the performance of the present proton source. Therefore, they have the highest priority. Category B is the R&D work that is critical to the Proton Driver and is currently underway (partially supported by the US-Japan Accord for Joint R&D on High Intensity Proton Facilities). Category C lists other R&D items that are necessary for the Proton Driver but may have to wait until more resources are available. This itemization of R&D items is still valid for PD2. Although several major design parameters in PD2 differ from PD1, most R&D items are the same with only a few exceptions. For example, the stranded conductor coil study is no longer needed due to changes in the magnet design. Here we highlight those R&D items that should be given high priority:

- Booster 53 MHz rf cavity modification. Enlarge the central pipe aperture from 2-1/4-inch to 5-inch and increase the voltage per cavity from 55 kV to 66 kV. These modifications would also benefit the present Booster. This work is making good progress (see Chapter 5.1).

- Space charge study in the present Booster. A study group has been formed for this purpose. It consists of experts in theoretical modeling, computer simulations and machine experiments. Several physicists from the Oak Ridge National Laboratory and Rutherford Appleton Laboratory have also joined this study.

- Inductive inserts study in the present Booster. From the experience at the PSR at Los Alamos National Laboratory and simulations on the Proton Driver as well as on the Booster, it is expected that inductive inserts would effectively reduce the potential well distortion due to space charge and thus reduce beam losses at high intensity. Two ferrite modules, each one-meter long, were installed in the Booster. No adverse effects have been observed on the beam. It is planned to install 8 more modules during the next scheduled machine shutdown in October 2002.

- Booster magnet dc and ac field measurement in E4R. A test stand has been set up in the E4R area. It has two spare Booster magnets and a 15 Hz resonant power supply. Two measurement techniques have been employed. One uses a stretched wire. Another uses a rotating coil (a mole). The data will be compared with those from machine experiments (e.g., chromaticity measurements).

- Dual resonance power supply test in E4R. It is planned to add another choke and another capacitor to the 15 Hz resonant power supply to add a 12.5% 30 Hz component to the magnet current waveform. The would lead to a 25% reduction in maximum dB/dt. Since the peak rf power is proportional to dB/dt this is then also reduced.

- Linac front-end improvements. These include the development of high brightness H^- sources (i.e., producing high intensity low emittance beams) as well as a 200 MHz RFQ. Both are described in detail in Chapter 13 of Ref. [1].

A2.2. R&D for the Main Injector Upgrade

Since the Main Injector is an existing machine, R&D on it can be performed as Accelerator Improvement Projects (AIPs). Each successful R&D project will improve the MI performance. Here we list those R&D projects specified in this PD2 study.

- Gamma-t jump system. This system has been designed. R&D is required to fabricate a prototype triplet (two 0.5-m and one 1-m quadrupoles), a pulsed power supply and several Inconel pipes, and to carry out magnetic field measurements.

- Dual power amplifier rf system test in MI-60. This is a major part of the R&D in the MI upgrade. There is no experience in operating an rf cavity using two amplifiers. It must be tested. Furthermore, the reliability of the Y567B tetrode operating at 800 kW at high duty cycle is also an untested territory. To ensure this scheme will work, an rf test stand in the MI-60 building for this study should be a high priority item.

- Large aperture quadrupoles (LAQs). A 4-in. LAQ needs to be fabricated and its field measured. Because these LAQs will be on the same bus as the regular quadrupoles, the fields must track each other during the ramp.

- Large aperture kickers. There is on-going R&D to use PEEK pipes replacing the ceramic ones presently used for the kickers. This would increase the vertical aperture from 1.3 in. to 1.6 in. However, this is not enough. The goal of this R&D needs to be aimed at a 2-in. aperture, the aperture of the beam pipe in the Main Injector. Both PEEK and ceramic materials will be investigated.

- Collimators. The design of a 2-stage collimation system is presented in this report (Ch. 19.2). The primary and secondary collimators need to be manufactured and installed in the MI ring for a beam test.

- Passive damper and active feedback. A spare MI rf cavity will be used for a passive damper experiment. Active feedback is an on-going activity and will continue.

References

[1] "The Proton Driver Design Study," FERMILAB-TM-2136. (December 2000)

Appendix 3. Charge from the Director

Fermilab

January 10, 2002

To: Bill Foster and Weiren Chou

From: Mike Witherell

SUBJECT: DESIGN STUDY OF PROTON DRIVER OPTIONS FOR THE MAIN INJECTOR

The HEPAP Subpanel report is expected to identify a modest energy, high average power, proton facility as a possible candidate for a construction project in the U.S. starting in the middle of the current decade. Fermilab represents an attractive location for such a facility and we need to identify options that could be presented to the DOE and U.S. community over the next few years if the physics is determined to warrant construction. One such option has been identified, the 8-16 GeV Proton Driver described in Fermilab-TM-2136, and another concept has recently come to light, an 8 GeV superconducting linac.

I would like the two of you to prepare a common document that would outline the two possible approaches to a Proton Driver at Fermilab and required modifications to the Main Injector to accommodate the increased intensity. In both cases I would like you to work with the following parameters:

Peak (Kinetic) Energy	8 GeV
Protons per Main Injector acceleration cycle	1.5×10^{14} (=1.9 MW @ 0.67 Hz)
Protons per second at 8 GeV	3.0×10^{14} (=380 KW)

For each option the report should include a description of the design concept and the technical components, identification of possible siting within Fermilab, and a preliminary cost estimate. In addition I would like you to provide a description and cost estimate for upgrades to the Main Injector, including its existing beamlines, and to the MiniBoone beamline required to support the performance defined above.

To the extent that you have the time and ability to do so I would like you to identify options for subsequent upgrades that could provide enhanced capabilities further into the future, including:

- Higher beam power at 8 GeV
- Higher beam power at energies up to 120 GeV, specifically through the implementation of reduced cycle time in the Main Injector

- An accumulator or compressor ring that could be used to achieve the performance required of the driver for a Neutrino Factory
- Utilization of the linac-based facility as an 8 GeV electron source

In general I would like to see each of these two options brought to a comparable state of development in this report. Because of the significant prior effort expended in the synchrotron-based proton driver, I expect that the development of the linac-based proton driver concept will require the bulk of the effort. Steve Holmes will provide Directorate guidance and support on this, including defining primary reference design parameters.

I would like to receive an interim report on progress prior to the ICFA Workshop at Fermilab on April 8-12 and a final report by May 15, 2002. Preparation of this report will require support of personnel in both the Beams and Technical Division. You should identify required resources and then work with the Divisions/Sections to secure support, consistent with their commitments to Run II. Both the Division/Section heads and Steve Holmes can help you in this task.

The identification of promising ventures utilizing hadrons and building upon Fermilab infrastructure and expertise is an important part of planning for the future of U.S. HEP. A Proton Driver could represent a strong candidate for a construction project in the intermediate term future with strong potential links to the longer-term future. Both Steve and I look forward to working closely with you and the participating divisions in defining the possibilities.

cc

G. Brown
B. Chrisman
J. Cooper
S. Holmes
M. Kasemann
R. Kephart
P. Limon
J. Marriner
D. Nevin
M. Shaevitz
K. Stanfield
E. Temple